Surface uplift, fluvial incision, and geodynamics of plateau evolution, from the western margin of the Central Andean plateau

by

Taylor F. Schildgen

B.A. in Geosciences, Williams College, 2000
M.Sc. in Geographical Information Science, University of Edinburgh, 2001

SUBMITTED TO THE DEPARTMENT OF EARTH, ATMOSPHERIC AND PLANETARY SCIENCES IN PARTIAL FULFILLMENT OF THE REQUIREMENTS FOR THE DEGREE OF

DOCTOR OF PHILOSOPHY IN GEOLOGY

AT THE

MASSACHUSETTS INSTITUTE OF TECHNOLOGY

JUNE 2008

Signature of Author: _____
Department of Earth, Atmospheric and Planetary Sciences
February 14, 2008

Certified by: _____
Kip V. Hodges
Professor of Geology
Thesis Supervisor

Certified by: _____
Kelin X Whipple
Professor of Geology
Thesis Supervisor

Accepted by: _____
Maria T. Zuber
Professor of Geophysics and Planetary Science
Department Head

Surface uplift, fluvial incision, and geodynamics of plateau evolution, from the western margin of the Central Andean plateau

by

Taylor F. Schildgen

Submitted to the Department of Earth, Atmospheric and Planetary Sciences
on January 11, 2008 in Partial Fulfillment of the Requirements for the
Degree of Doctor of Philosophy in Geology

Abstract

The Colca-Majes and Cotahuasi-Ocoña rivers in southwest Peru that cut through the western margin of the Andean plateau en route to the Pacific Ocean incised canyons over 3 km deep in response to late Cenozoic surface uplift. This latest uplift represents a fundamental shift in the style and magnitude of surface deformation that had been ongoing since at least late Cretaceous time, but only relatively recently created what represents the only major barrier to atmospheric circulation in the Southern Hemisphere. Studying canyon incision history as a proxy for surface uplift offers a promising route to understanding how climate and tectonics have interacted throughout the evolution of the Central Andean plateau.

In this thesis, a combination of bedrock low-temperature thermochronology (apatite and zircon (U-Th)/He techniques), $^{40}Ar/^{39}Ar$ dating of valley-filling volcanic flows, and three-dimensional thermal modeling using a modified version of Pecube were applied to investigate the incision history of the rivers. Results suggested between 2.6 and 3.0 km of incision occurred in the deepest reaches of the canyons starting at ca. 10 to 11 Ma and ending between 2.3 and 3.5 Ma. The onset of surface uplift that is likely to have driven incision probably did not precede incision by more than one million years, although incision may have continued long after surface uplift ceased. The magnitude and timing of uplift that we infer is in broad agreement with uplift documented along the western margin in northern Chile, in the interior of the Andean plateau, and the eastern margin.

Additional work on the style of structural accommodation of this uplift provide important context for interpreting what potential geodynamic mechanisms may have been responsible for this latest tectonic activity. Structural mapping revealed an early history of predominantly reverse fault activity that probably generated the first significant topography in the Central Andes. This compressional period was succeeded by a phase of long-wavelenth warping deformation and normal kinematic movement on high-angle faults. This later activity appears to have continued through the latest phase of uplift documented through river incision history, hence was likely responsible for accommodating uplift. Given the broadly synchronous timing of late Cenozoic uplift across the Andean plateau and the style of structural accommodation documented on the western margin, two possible geodynamic mechanisms appear most feasible for generating this latest phase of uplift: lithospheric delaminantion, and redistribution of ductile material through mid- to lower-crustal flow. Our initial studies of coastal uplift suggest that each is likely to have played a role, although additional work is required to understand how important each may have been in generating uplift.

Thesis Supervisors:

Kip V. Hodges	Title: Professor of Geology
Kelin X Whipple	Title: Professor of Geology

Acknowledgments

I am indebted to my advisors, Kip Hodges and Kelin Whipple, for their guidance, patience, and good humor. They have given me a breadth of training as a scientist, teacher, and a writer that has served me well over the course of my studies, and I trust will form the solid foundation of my academic pursuits in the future. I thank many other faculty members at (or formerly at) MIT who have also contributed to my academic training and provided kind support over the years, including Sam Bowring, David Mohrig, Stephane Rondenay, Brad Hager, Lindy Elkins-Tanton, Clark Burchfiel, Wiki Royden, Tim Grove, and the 10th floor visitors: Kevin Burke, Arjun Heimsath, and John Geissman. A number of colleagues have also helped with their generous collaboration, advice, and encouragement. Arjun Heimsath and Jeannie Dixon lead me through my cosmogenic sample preparation at Dartmouth. Todd Ehlers and his students at the University of Michigan (particularly Dave Whipp and Jason Barnes) were tremendously helpful in getting me initiated with Pecube. Pete Reiners and Stefan Nicolescu helped with many of my (U-Th)/He sample analyses, and were always willing to help in any way they could despite the mayhem associated with all the people and labs moving from New England to Arizona. Matthijs van Soest produced data as fast as humanly possible from the new He lab at ASU. David Shuster generously agreed to give my samples a shot at $^4He/^3He$. Malcolm Pringle and Bill Olzscheski continually worked wonders to keep a steady steam data coming from the argon lab at MIT. My international colleagues, particularly Gerhard Wörner, Jean-Claude Thouret, and Mirian Mamani, were instrumental in getting my field seasons kick-started and helping me early on to understand the bigger picture of what has happened in the Andes.

The post-graduate, graduate, and undergraduate students are one of the most impressive aspects of MIT. There are far too many heartfelt memories to even attempt to do justice to here. Needless to say, I could not have survived, no less truly enjoyed my time here, without their boundless support, friendship, and guidance. I'm fortunate to call them my mentors, I'm excited to call them my future colleagues, I'm proud to call them my friends.

Thanks to a huge supporting cast, my field seasons in Peru were logistically simple, productive, and far too much fun to call "work." These include all the people at Cusipata who led/organized our white-water rafting trips: GianMarco Vellutino, Santiago Ibanez, Christian Duran, Pato Valsecchi, Diego Valsecchi, Sergio Cabada, Vincent Taylor, and Marc Goddard. Javier Bustamante was helpful in every possible way in Peru, arranging transportation, lodging, and continually looking out for our safety and well-being while in Peru. My field assistants were incredible: Tyson Smith my first year, Katrina Cornell for years two and three, plus her mom Julie Bradley for the third year. I can't thank them enough for all the time and effort they put in, and for putting up with me through failed sample-collecting excursions, terrible meals even stray dogs wouldn't eat, driving on (or digging through) sketchy roads with guys who brag about the trucks they've rolled, and one particularly scary canyon. Each of them has more patience and good-humored tolerance than I can ever hope for, and our times together in the field were among my fondest memories of graduate school.

The ultimate frisbee community has dominated my social life throughout my time in Cambridge. I thank the players and coaches on Smite, Brute Squad, and Lady Godiva for the good times on and off the fields, and all the lessons that extend far beyond sports. I particularly thank April Lehman and Ali Cohen, two women who's incredible athletic and intellectual abilities are only surpassed by their boundless loyalty to their friends; Tracy Woo, who continued to coordinate my social calendar long after I decided to devote all my time to thesis-writing; Nancy Sun, my hero; and Ted Munter, an angel if I've ever known one.

The people I've lived with over the years have been a big part my daily rejuvenation. I'll miss the hall feeds on Second East and the weird and fascinating community that is East Campus. I probably won't miss the 2-am courtyard explosions that I mistook for gunshots for my first two years. Cim, Abigail, Alysia, Arik, and Dang have been a great group of housemate-friends that saw me through the final trying months of finishing up.

Finally, thanks to my family for their love and everything they've done to give me the freedom to pursue whatever path I'd like. My parents have long preached the importance of finding a career I can love. I never imagined it could also come along with such an amazing group of colleagues and friends.

Table of Contents

Chapter 1:
Introduction

1. Motivation

Orogenic plateaus are dominant topographic features of many major tectonic provinces on Earth, including the India-Eurasian collision zone, the North American Cordillera, and the Central Andes. Despite the wide range of tectonic settings in which they occur, similarities in their lithospheric thicknesses, heat flow patterns, and deformation characteristics suggest that a common set of fundamental geodynamic processes may govern their development through time. These may include feedbacks between tectonic and surface processes. High plateaus act as barriers to atmospheric circulation and can exert first-order controls on climate patterns. Many studies have demonstrated linkages between development of these major topographic barriers and significant changes in climate. These include the onset of the Indian Summer Monsoon associated with uplift of the Tibetan plateau (e.g., Kutzbach et al., 1989; Molnar et al., 1993; Zhisheng et al., 2001; Liu and Yin, 2002; Harris, 2006), a pronounced shift in precipitation from the South American Monsoon and the onset of hyperaridity in the Atacama Desert associated with uplift of the Central Andean plateau (e.g., Alpers and Brimhall, 1988; Horton and DeCelles, 2001; Rech et al., 2006; Strecker et al., 2007), and the development of a pronounced rainshadow in the western United States associated with uplift of the Colorado plateau (e.g., Kutzbach et al., 1989; Mulch et al., 2006). Surface processes driven by climate change can in turn affect plateau evolution. Focused erosion on windward plateau margins can alter the style and pattern of tectonic denudation (e.g., Beaumont et al., 2001), while rainshadow effects can lead to aridification and sedimentation in plateau interiors (e.g., Sobel et al., 2003). Orogenic plateaus arguably provide the best opportunities to study how surface and deep crustal processes interact to shape the surface of the Earth.

The Central Andean plateau is in many ways an ideal natural laboratory for exploring the processes that contribute to plateau development. Its average elevations of 4000 m stretching over a region 350 km wide and almost 2000 km long make it the second largest orogenic plateau on Earth, yet it is considerably more accessible than many of the remote regions of the largest orogenic plateau in Tibet. Variations in precipitation patterns along its length provide excellent opportunities to study the effects of increased erosion on plateau development (e.g., Barnes et al., 2006; Strecker et al., 2007). The relative simplicity of the plate tectonic setting also helps to isolate processes specifically related to plateau development. Since at least late Cretaceous time (Pardo-Casas and Molnar, 1987), oceanic plate subduction beneath the South American continent created an active margin long

characterized by compression and crustal thickening in the overriding plate (e.g., Sheffels, 1990; Schmitz, 1994; Muñoz and Charrier, 1996; Baby et al., 1997; McQuarrie, 2002; Müller et al., 2002; Victor et al., 2004; Elger et al., 2005; Farias et al., 2005) with an absence of accreted terrains. This contrasts dramatically with the complex collision between India and Eurasia that created Tibet, and the long history of terrain accretion that slowly built the western United States.

Although interest in understanding plateau development has existed for decades, only relatively recently have quantitative tools advanced sufficiently such that the evolution of surface topography can be compared with records of changing climate, erosion patterns, and tectonic activity. Early estimates for topographic development in the Central Andes were primarily based on paleobotanical work, which used fossil records of changes in vegetation as a proxy for changes in temperature and elevation. Although these pioneering studies deciphered dominant patterns in the history of plateau growth, including approximately 2 km of late Cenozoic uplift (e.g., Singewald and Berry, 1922; Berry, 1939; Gregory-Wodzicki, 2000; Graham et al., 2001), uncertainties that approached ±1000 m in paleoelevation estimates were generally too large to guide interpretations of how plateau development may be related to the complex interactions of surface and deeper crustal processes. The relatively rapid response of fluvial systems to tectonic forcing provides a promising alternative direction to paleoelevation studies. Incised, dated paleo-fluvial surfaces on the eastern margin of the plateau suggested that 1000 to 2500 m of uplift started between 12 and 9 Ma (Kennan et al.1997; Barke and Lamb, 2006). More recently, oxygen and clumped-isotope records from the Central Andean plateau have documented the increased fractionation associated with growing topography and its orographic effects. Estimates for uplift magnitude based on these studies range from 2.5 to 3.5 km occurring between 11 and 6 Ma (Garzione et al., 2006; Ghosh et al., 2006).

Together, these studies suggested that plateau growth may be highly punctuated in time, rather than a more gradual uplift associated with isostatic balancing of compression-induced, slowly thickening crust. Late-stage orogenic processes such as lithospheric delamination of a high-density root may play a dominant role in surface uplift, though supporting evidence such as thinned lithosphere and widespread mafic volcanism is presently only documented at the southern (Puna) end of the plateau (Kay and Kay, 1993; Schurr et al., 2006). Regional uplift driven by ductile redistribution of material in the mid to lower crust is another alternative. Similarity of timing between the late Cenozoic pulse of uplift and the ca. 10 Ma initiation of Brazilian Shield underthrusting beneath the eastern margin of the growing plateau (e.g., Gubbels et al., 1993) suggests that this cratonic piston driving into the lower crust may have been responsible for regional uplift. Although the implications of late-stage surface uplift are intriguing, large and potential systematic errors in each of the paleoelevation studies requires that independent estimates be made. This is coupled with a need

for representative estimates throughout the plateau interior and margins in order to best approach the questions of how orogenic plateaus develop through space and time.

2. Approach

Chapters 2 through 4 in this thesis summarize our efforts to understand the tectonic and topographic development of the western margin of the Central Andean plateau in southwest Peru, particularly as they relate to geodynamic processes that governed growth of the entire plateau. In southwest Peru, the Cotahuasi-Ocoña and the Colca-Majes rivers cut two of the deepest canyons in the world through the western margin of the Central Andean plateau en route to the Pacific Ocean. These canyons, which exceed 3 km in depth, record a history of river incision response over a growing plateau margin. Through our studies of the river incision history and the style of structural deformation that accommodated uplift through time, we aimed to generate a tightly coupled study on surface uplift and tectonic history to help guide interpretations of the geodynamic processes responsible for plateau growth.

Chapter 2 introduces our approach of using river incision as a proxy for surface uplift. It describes the two primary methods we applied to learn about incision history: $^{40}Ar/^{39}Ar$ dating of valley-filling volcanic flows and low-temperature thermochronology. A date for a volcanic flow that entered the canyon gives a minimum time at which the canyon incised down to the level of the flow. A series of dated flows thus places general constraints on the timing of incision. Low-temperature thermochronology can potentially provide a much more detailed record of the timing and magnitude of incision by recording the depression of near-surface isotherms that occurred in response to canyon incision. As the lowest low-temperature thermochronometer in common use, the apatite (U-Th)/He system is most sensitive to the localized transient cooling that occurs beneath canyon bottoms. The valley-bottom bedrock sampling technique used in this study proved to be highly effective in deciphering the strong cooling signal induced by incision. We applied two main assumptions in interpreting our data. First, that the depth below a regional, well-preserved, uplifted paleosurface can provide a common reference frame for widely-dispersed samples. Second, that two key components of the data set are not significantly affected by lateral variations in the thermal field, topography, or exhumation: the timing of the onset of incision recorded by the transition from slowly- to rapidly-cooled samples, and the thickness of the rapidly-cooled zone as inferred on an age-depth plot. From these two components of the apatite data and simple 1-D thermal modeling, we estimated the minimum magnitude of the latest phase of incision. Together with constraints from valley-filling volcanic flows, we also bracketed the timing of incision. Several of the broad assumptions made in this chapter set the stage for the more detailed studies described in later chapters. These include the

effects of a spatially and temporally complex thermal field on thermochronology data interpretations, canyon incision processes and timescales of response, and the style of tectonic deformation along the western margin that is likely to have accommodated the latest phase of uplift.

In Chapter 3 we show how three-dimensional thermal modeling with a modified version of Pecube (Braun, 2003; Whipp et al., 2007) can refine interpretations of thermochronologic data in settings where the thermal field is characterized by complex spatial and temporal variations. Using both the valley-bottom transect data presented in Chapter 1, new data from four vertical transects, and constraints from modern-day heat flow determinations, we explore what range of topographic evolution scenarios are consistent with the modern-day pattern of thermochronologic data. This allowed us first to characterize the thermal field and regional exhumation rates that provide the backdrop for the cooling pulse that is later induced by canyon incision. We then explored the sensitivity of our interpretations to a range of parameters including incision onset time, incision completion time, and depth of the canyon prior to the latest phase of incision. Results presented encompass the best-fit scenarios for the timing and magnitude of this latest phase of incision, and also estimates for how well we can constrain these numbers given the precision of thermochronologic data and sensitivity to free parameters in the model.

We draw together results from these previous chapters with detailed structural mapping in Chapter 4 to try to understand the late Cenozoic phase of uplift in the context of an evolving orogenic plateau. Specifically, we attempt to discern what structures are responsible for accommodating the late Cenozoic phase of uplift documented by river incision. To do this, we present four detailed geological maps, cross-sections, and describe stratigraphic and geochronologic constraints on the timing and magnitude of movement on faults mapped in the region. This includes additional $^{40}Ar/^{39}Ar$ dating of volcanic units that cross over fault zones and transects of zircon (U-Th)/He data. The former bracket the timing of latest movement on structures, while the latter show patterns of bedrock cooling ages along valley bottoms and any discontinuities that may be associated with significant movement on a particular structure. We present evidence for changing styles of structural deformation through space and time that are strong indications of the likely geodynamic forcing mechanisms behind plateau development.

Chapter 5 presents a synthesis of all the work described in chapters 2-4. It draws together our studies of surface uplift documented through canyon incision, caveats to the linkage between canyon incision and surface uplift, and our structural evidence used to evaluate models of the geodynamic evolution of the western margin of the Central Andean plateau in particular, and by inference, the larger plateau region as well. This includes brief discussion of several remaining open questions in the Central Andes, and some possible paths to pursue them. We finish by discussing some wider

implications of what our work tells us about orogenic plateau development, not only in the Central Andes, but in also in other places in the world where large orogenic plateaus dominate the surface morphology.

References:

Alpers, C. N., and Brimhall, G. H., 1988, Middle Miocene Climatic-Change in the Atacama Desert, Northern Chile - Evidence from Supergene Mineralization at La-Escondida: Geological Society of America Bulletin, v. 100, no. 10, p. 1640-1656.

Baby, P., Rochat, P., Mascle, G., and Herail, G., 1997, Neogene shortening contribution to crustal thickening in the back arc of the Central Andes: Geology, v. 25, no. 10, p. 883-886.

Barke, R., and Lamb, S., 2006, Late Cenozoic uplift of the Eastern Cordillera, Bolivian Andes: Earth and Planetary Science Letters, v. 249, no. 3-4, p. 350-367.

Barnes, J.B., Ehlers, T.A., McQuarrie, N., O'Sullivan, P.B., and Pelletier, J.D., 2006, Eocene to recent variations in erosion across the central Andean fold-thrust belt, northern Bolivia; Implications for plateau evolution: Earth and Planetary Science Letters, v. 248, p. 118-133.

Beaumont, C., Jamieson, R.A., Nguyen, M.H., and Lee, B., 2001, Himalayan tectonics explained by extrusion of a low-viscosity crustal channel coupled to focused surface denudation: Nature, v. 414, p. 738-742.

Berry, E. W., 1939, The fossil flora of Potosi, Bolivia: John Hopkins University Studies in Geology, v. 13, p. 1-67.

Braun, J., 2003, Pecube: a new finite-element code to solve the 3D heat transport equation including the effects of a time-varying, finite amplitude surface topography: Computers and Geosciences, v. 29, p. 787-794.

Elger, K., Oncken, O., and Glodny, J., 2005, Plateau-style accumulation of deformation: Southern Altiplano: Tectonics, v. 24, no. 4.

Farias, M., Charrier, R., Comte, D., Martinod, J., and Herail, G., 2005, Late Cenozoic deformation and uplift of the western flank of the Altiplano: Evidence from the depositional, tectonic, and geomorphologic evolution and shallow seismic activity (northern Chile at 19 ° 30 ' S): Tectonics, v. 24, no. 4.

Garzione, C. N., Molnar, P., Libarkin, J. C., and MacFadden, B. J., 2006, Rapid late Miocene rise of the Bolivian Altiplano: Evidence for removal of mantle lithosphere: Earth and Planetary Science Letters, v. 241, no. 3-4, p. 543-556.

Ghosh, P., Garzione, C. N., and Eiler, J. M., 2006, Rapid uplift of the Altiplano revealed through C-13-O-18 bonds in paleosol carbonates: Science, v. 311, no. 5760, p. 511-515.

Graham, A., Gregory-Wodzicki, K.M., and Wright, K.L., 2001, Studies in neotropical paleobotany. XV. A Mio-Pliocene palynoflora from the Eastern Cordillera, Bolivia: implications for the uplift history of the central Andes: American Journal of Botany, v. 146, no. 3, p. 813-826.

Gregory-Wodzicki, K. M., 2000, Uplift history of the Central and Northern Andes: A review: Geological Society of America Bulletin, v. 112, no. 7, p. 1091-1105.

Gubbels, T. L., Isacks, B. L., and Farrar, E., 1993, High-Level Surfaces, Plateau Uplift, and Foreland Development, Bolivian Central Andes: Geology, v. 21, no. 8, p. 695-698.

Harris, N., 2006, The elevation history of the Tibetan Plateau and its implications for the Asian monsoon: Palaeogeography Palaeoclimatology Palaeoecology, v. 241, no. 1, p. 4-15.

Horton, B. K., and DeCelles, P. G., 2001, Modern and ancient fluvial megafans in the foreland basin system of the central Andes, southern Bolivia: implications for drainage network evolution in fold-thrust belts: Basin Research, v. 13, no. 1, p. 43-63.

Kay, R. W., and Kay, S. M., 1993, Delamination and Delamination Magmatism: Tectonophysics, v. 219, no. 1-3, p. 177-189.

Kennan, L., Lamb, S., and Hoke, L., 1997, High altitude palaeosurfaces in the Bolivian Andes: Evidence for Late Cenozoic surface uplift, in Widdowson, M., ed., Paleosurfaces: Recognition, Reconstruction and Paleoenvironmental Interpretation: Geological Society Special Publication, Geological Society of London, p. 307–324.

Kutzbach, J. E., Guetter, P. J., Ruddiman, W. F., and Prell, W. L., 1989, Sensitivity of Climate to Late Cenozoic Uplift in Southern Asia and the American West - Numerical Experiments: Journal of Geophysical Research-Atmospheres, v. 94, no. D15, p. 18393-18407.

Liu, X. D., and Yin, Z. Y., 2002, Sensitivity of East Asian monsoon climate to the uplift of the Tibetan Plateau: Palaeogeography Palaeoclimatology Palaeoecology, v. 183, no. 3-4, p. 223-245.

McQuarrie, N., and Davis, G. H., 2002, Crossing the several scales of strain-accomplishing mechanisms in the hinterland of the central Andean fold-thrust belt, Bolivia: Journal of Structural Geology, v. 24, no. 10, p. 1587-1602.

Molnar, P., England, P., and Martinod, J., 1993, Mantle Dynamics, Uplift of the Tibetan Plateau, and the Indian Monsoon: Reviews of Geophysics, v. 31, no. 4, p. 357-396.

Mulch, A., Graham, S. A., and Chamberlain, C. P., 2006, Hydrogen isotopes in Eocene river gravels and paleoelevation of the Sierra Nevada: Science, v. 313, no. 5783, p. 87-89.

Müller, J. P., Kley, J., and Jacobshagen, V., 2002, Structure and Cenozoic kinematics of the Eastern Cordillera, southern Bolivia (21°S): Tectonics, v. 21, no. 5.

Munoz, N., and Charrier, R., 1996, Uplift of the western border of the Altiplano on a west-vergent thrust system, Northern Chile: Journal of South American Earth Sciences, v. 9, no. 3-4, p. 171-181.

Pardo-Casas, F., and Molnar, P., 1987, Relative motion of the Nazca (Farallon) and South American plates since late Cretaceous time: Tectonics, v. 6, no. 3, p. 233-248.

Rech, J. A., Currie, B. S., Michalski, G., and Cowan, A. M., 2006, Neogene climate change and uplift in the Atacama Desert, Chile: Geology, v. 34, no. 9, p. 761-764.

Schmitz, M., 1994, A Balanced Model of the Southern Central Andes: Tectonics, v. 13, no. 2, p. 484-492.

Schurr, B., Rietbrock, A., Asch, G., Kind, R., and Oncken, O., 2006, Evidence for lithospheric detachment in the central Andes from local earthquake tomography: Tectonophysics, v. 415, no. 1-4, p. 203-223.

Sheffels, B. M., 1990, Lower Bound on the Amount of Crustal Shortening in the Central Bolivian Andes: Geology, v. 18, no. 9, p. 812-815.

Singewald, J. T., and Berry, E.W., 1922, The geology of the Corocoro copper district of Bolivia: John Hopkins University Studies in Geology, v. 1, p. 1-117.

Sobel, E. R., Hilley, G.E., and Strecker, M.R., 2003, Formation of internally-drained contractional basins by aridity-limited bedrock incision: Journal of Geophysical Research - Solid Earth, v. 108, 2344.

Strecker, M. R., Alonso, R. N., Bookhagen, B., Carrapa, B., Hilley, G. E., Sobel, E. R., and Trauth, M. H., 2007, Tectonics and climate of the southern central Andes: Annual Review of Earth and Planetary Sciences, v. 35, p. 747-787.

Victor, P., Oncken, O., and Glodny, J., 2004, Uplift of the western Altiplano plateau: Evidence from the Precordillera between 20° and 21° S (northern Chile): Tectonics, v. 23, no. 4.

Whipp Jr., D.M., Ehlers, T.A., Blythe, A.E., Huntington, K.W., Hodges, K.V., and Burbank, D.W., 2007, Plio-Quaternary exhumation history of the central Nepalese Himalaya: 2. Thermomkinematic and thermochronometer age prediction model: Tectonics, v. 26, TC3003. doi:10.1029/2006TC001991.

Zhisheng, A., Kutzbach, J. E., Prell, W. L., and Porter, S. C., 2001, Evolution of asian monsoons and phased uplift of the Himalayan Tibetan plateau since late Miocene times: Nature, v. 411, no. 6833, p. 62-66.

Chapter 2.

Uplift of the western margin of the Andean plateau revealed from canyon incision history, southern Peru

Taylor F. Schildgen[1]
Kip V. Hodges[2]
Kelin X Whipple[2]
Peter W. Reiners[3]
Malcolm S. Pringle[1]

1. Department of Earth, Atmospheric and Planetary Sciences, Massachusetts Institute of Technology, Cambridge, Massachusetts 02139, USA
2. School of Earth and Space Exploration, Arizona State University, Tempe, Arizona 85287, USA
3. Department of Geosciences, University of Arizona, Tucson, Arizona 85721, USA
Published in June 2007 issue of *Geology* (v. 35, no. 6, p. 523-526)

Abstract

We explore canyon incision history of the western margin of the Andean (Altiplano-Puna) plateau in the central Andes as a proxy for surface uplift. (U-Th)/He apatite data show rapid cooling beginning at c. 9 Ma and continuing to c. 5.1 Ma in response to incision. A minimum of 1.0 km of incision took place during that interval. The youngest apatite date and a volcanic flow perched 125-m above the present valley floor dated at 2.261 ± 0.046 Ma ($^{40}Ar/^{39}Ar$) show that an additional c. 1.4 km of incision occurred between c. 5.1 and 2.3 Ma. Thus we infer that a total of at least 2.4 km, or 75% of the present canyon depth was incised after c. 9 Ma. (U-Th)/He zircon data collected along the same transect imply that the western margin of the plateau was warped upward into its present monoclinal form, rather than uplift being accommodated on major surface-breaking faults.

1. Introduction

Understanding the development of the Central Andean plateau[1] is crucial to evolutionary models of both Andean geodynamics and regional climate patterns. Although episodes of central

[1] We use "Central Andean plateau" as defined by Allmendinger et al. (1997) to represent the region above the 3 km elevation contour between 13°-27°S. This includes the Altiplano and Puna plateaus and portions of the Western and Eastern Cordilleras.

Andean deformation are constrained in many regions, it is often difficult or impossible to discern the magnitude of plateau uplift based on deformation history alone. Different approaches for estimating paleoelevation or the existence of high topography have led to a broad range of proposed uplift histories, but precise constraints are lacking. Oligocene uplift probably generated less than half of central Andean relief seen today (e.g., Gubbels et al., 1993; Kennan, 2000). Numerous lines of evidence from the plateau and its eastern margin point to additional surface uplift starting at c. 10 Ma, with magnitudes ranging from at least 1 to as much as 3.5 km (e.g., Kennan et al., 1997; Lamb and Hoke, 1997; Barke and Lamb, 2006; Garzione et al., 2006; Ghosh et al., 2006). In northern Chile, Hoke (2006) and Nestor et al. (2006) estimate 1 to 1.4 km of western margin uplift after 10 Ma, and Wörner et al. (2000) argue for termination of uplift by 2.7 Ma. More recently, interpretations of oxygen and clumped isotope data have led to estimates that the plateau reached its present height by c. 6 Ma (Garzione et al., 2006; Ghosh et al., 2006). Uncertainties in all these estimates require that independent measures of surface uplift be made before we can accurately constrain uplift history.

In southwest Peru, large rivers cut deep canyons through the western margin of the Central Andean plateau. Cotahuasi-Ocoña Canyon is the deepest of these, incising more than 3 km below the plateau surface (Fig. 1). The western margin of the plateau has been characterized by a semiarid-hyperarid climate for at least the past 15 Myr (e.g., Hartley, 2003; Rech et al., 2006). As expected, given the arid climate and gentle slopes of the region, Kober et al. (2007) found that millennial-scale interfluve erosion rates are uniformly low, despite a gradual increase in erosion rate with elevation (<0.001 to 0.05 mm/yr). As predicted from these studies, and as seen in the field, little surface erosion has occurred on canyon interfluves in our study area, making canyon incision an excellent proxy for surface uplift. Incision depth provides a minimum estimate for the amount of surface uplift, while the onset of incision provides a minimum age for the timing of uplift. We use $^{40}Ar/^{39}Ar$ dates of volcanic flows and bedrock (U-Th)/He thermochronologic data to explore canyon evolution. Detailed information regarding geochronologic data and their interpretation are provided in the GSA Data Repository[2] (Tables DR1 through DR4).

2. Valley-filling volcanics

Dates of valley-filling volcanic flows give a minimum time by which the canyon had incised to the depth of the sampled flow. In the middle reaches of Cotahuasi-Ocoña Canyon, a whole-rock

---

[2]GSA Data Repository item 2007124, G23532A.1, is available online at www.geosociety.org/pubs/ft2007.htm, or on request from editing@geosociety.org or Documents Secretary, GSA, P.O. Box 9140, Boulder, CO 80301, USA.

$^{40}Ar/^{39}Ar$ date of 2.261 ± 0.046 Ma for a basaltic andesite flow sampled 125 m above the present valley floor (05TS38, Fig. 1) shows that ~96% of the incision in that section of the canyon (3.2 km total local incision) happened before 2.3 Ma. Farther upvalley, an ignimbrite (05TS25) perched c. 400 m above the present valley shows that ~75% of the canyon depth (1.6 km total local incision) was cut before 3.825 ± 0.016 Ma. Thouret et al. (2005) obtained a $^{40}Ar/^{39}Ar$ date of 3.76 ± 0.14 Ma for the same flow and interpreted it as a maximum age for most of the valley incision.

3. Low-temperature thermochronology

In this setting where background erosion rates are very slow, we expect thermochronometers to yield very old dates. However, canyons are sites of localized, potentially rapid exhumation. When a canyon is incised, perturbations to near-surface isotherms result in rapid cooling of bedrock below the canyon bottom (Fig. 2). Because the closure temperature isotherm for the apatite (U-Th)/He system is only c. 2–3 km below the surface (assuming a geothermal gradient of 20–30 °C/km, Farley, 2000), we expect to find young, rapidly-cooled apatites below this level in the deepest reaches of Cotahuasi-Ocoña Canyon. Their young ages should reflect both downward movement of the closure isotherm and relative upward advection of rock due to erosion of the surrounding surface, though the latter component is small in this setting as discussed above. The oldest date among this young suite of ages should reflect the initiation of the thermal response to canyon incision.

We collected most samples for apatite (U-Th)/He dating along a 75-km, canyon-bottom transect, far from the influence of volcanic activity (Figs. 1 and DR1). Additional samples were collected from the uppermost catchment where there are abundant volcanic flows dated at c. 1.4 to 3.8 Ma (Thouret et al., 2005). We constrained canyon depth by measuring the distance below a paleosurface that is preserved today as bedrock remnants beneath the regionally blanketing 14–16 Ma Huaylillas Ignimbrite (Thouret et al., 2005, and dates reported here). Positions of remnants exposed in valley walls were digitized and a spline surface warped to fit the points, giving an approximation for the bedrock surface (Fig. DR1). Samples were collected from c. 1 km below the paleosurface near the coast, down to c. 3.1 km below in the deepest reaches of the canyon.

The resulting dates are c. 60 Ma near the coast, and rapidly decrease to c. 9 Ma in the middle reaches of the canyon. Farther upvalley, there is a much more gradual change in dates with distance, with the youngest sample away from the volcanic-dominated upper catchment dated at 5.1 Ma (Fig. 3). Samples from the uppermost catchment (05TS07 and samples upstream from there) range from < 1 to 3.8 Ma. Because these samples are as young as the abundant volcanic flows in that region, we suspect their ages have been reset or partially reset by recent volcanism. For this reason, we focus the remainder of our discussion on samples from the middle and lower catchment, which we believe have

not been affected by reheating.

A plot of sample cooling age versus canyon depth (Fig. 4) can be interpreted the way that vertical profiles of thermochronologic data are typically interpreted: as indicative of how exhumation rates changed over the time interval represented by the measured ages. Although such an interpretation of Figure 4 may be compromised by variations in bedrock thermal structure, there is very little evidence of large lateral variations in upper crustal temperatures in this region of southern Peru. For example, reported variations in measured surface heat flow range only from 32 to 44 mW/m^2 (Henry and Pollack, 1988; Hamza and Muñoz, 1996; Springer and Förster, 1998).

Ignoring the minor influences of such variations in heat flow, our apatite data imply slow background erosion of only c. 0.7 km from c. 60 to 9 Ma (0.01 km/Myr), and a change to rapid incision of at least 1.0 km from c. 9 to 5.1 Ma (0.26 km/Myr). The latter is a minimum estimate because isotherm movement is damped compared to changes in surface topography. Additional incision must have occurred after 5.1 Ma to exhume this youngest apatite. Because a 2.3-Ma volcanic flow is perched 125 m above the valley floor in the middle reaches of the canyon, we know that the young apatite must have been exhumed from its closure depth to the near surface between 5.1 and 2.3 Ma. We explored probable erosion rates and depths to the closure temperature for this scenario using M. Brandon's computer code AGE2EDOT (summarized in Ehlers et al., 2005). Assuming typical thermal properties of the crust (Table DR5) and an initially uncompressed geothermal gradient between 20 and 30 °C/km, exhumation of the youngest apatite requires incision between 0.7 and 0.5 km/Myr, an effective closure temperature of 72 °C, and corresponding depths of 2.0 to 1.4 km to the closure temperature. Because we expect even greater compression of isotherms below a canyon compared to the compression expected from simply increasing erosion rate over flat topography as AGE2EDOT assumes, we choose the lower end of this range as an estimate. Thus, we infer that c. 1.4 km of material was removed in the middle reaches of the canyon between 5.1 and 2.3 Ma (average 0.5 mm/yr) to exhume the youngest apatite.

Collectively, the data suggest that the middle section of Cotahuasi-Ocoña Canyon was incised at least 1.0 km between c. 9 and 5.1 Ma and c. 1.4 km between 5.1 and 2.3 Ma. This represents incision of at least 75% of the total canyon depth since 9 Ma, and 44% since 5.1 Ma.

4. Interpreting surface uplift from thermochronologic data

Deciphering surface uplift from thermochronologic interpretations of canyon incision is complicated by several factors. First, incision can reflect a transient response to tectonically-driven uplift, and/or climatically-driven changes in sediment supply and fluvial discharge, provided prior surface uplift had produced sufficient topographic relief. We interpret the latest phase of incision to be

a response to uplift because it is the simplest explanation and there is no evidence for a climate change that could induce a pulse of incision at this time. The interpreted drying of climate starting at c. 15 Ma (e.g., Hartley, 2003; Rech et al., 2006) should have the opposite effect of deterring incision, rather than generating a pulse of incision into pre-existing topography. Also, our estimate for the onset of incision correlates well with tectonic evidence in northern Chile for surface uplift after c. 10 Ma (Nestor et al., 2006). Second, although incision magnitude is limited by uplift magnitude, incision rates are not necessarily closely tied to uplift rates. The incision history we interpret from thermochronologic data is offset from tectonically-driven uplift by lag times defined by both the geomorphic response time to uplift and the thermal response time to incision. Constraining these response times is critical in order to quantitatively extract uplift history from canyon incision.

By "geomorphic response time", we mean the timescale over which rivers respond to a pulse of uplift. When uplift occurs, a river steepens at its outlet. Over time, this steep segment migrates upstream at a rate that depends principally on whether incision is transport- or detachment-limited (Whipple and Tucker, 2002). In a detachment-limited system, the pulse of incision will move through the system vertically at a rate that approximates the new uplift rate (Niemann et al., 2001), which appears to be c. 0.5 mm/yr in Cotahuasi-Ocoña Canyon. In transport-limited systems, the incision pulse migrates upstream much more rapidly, resulting in essentially uniform onset of incision throughout the catchment on geologic timescales (Whipple and Tucker, 2002). Because we sampled from the trunk stream at large drainage area and thus both relatively low in elevation and most likely to approach transport-limited conditions, we expect incision across the sampled region to have a relatively short response time. Even if incision were detachment-limited, the highest bedrock sampled for apatite (852m) would imply a maximum lag time of 2 Myr.

We investigated the thermal response time to incision using M. Brandon's RESPTIME computer code (summarized in Ehlers et al., 2005). Although this code was written to evaluate thermal field transients resulting from changes in broad-scale erosion rates, it is also useful for exploring general effects of localized incision. We tested the thermal response time to a sudden increase in erosion rate from 0.01 mm/yr to 0.5 mm/yr. Using typical values for thermal properties of the crust (Table DR5), results show that after an initial slow response, the migration rate of the apatite He closure temperature isotherm reaches 75% of the incision rate 0.7 Myr after incision starts. Thus, isotherm migration is significantly slower than incision for the first c. 1 Myr.

Response time estimates show two ways in which our thermochronologic data do not directly reflect uplift. First, the age of the "kink" in the age-depth profile is likely to lag behind onset of uplift primarily as a result of geomorphic response time, which we expect to be a maximum of 2 Myr. Second, the damped response of isotherm movement in response to incision means that we derive only

a minimum estimate of uplift rate and magnitude. Given these limitations, our estimate for the onset of uplift is likely good to c. 2 Myr, and our estimate for uplift magnitude should be a robust minimum.

5. Style of tectonic deformation

Compared to apatite, the higher closure temperature to helium diffusion in zircon (c. 180 °C, Reiners et al., 2004) means that (U-Th)/He zircon ages are set much deeper in the crust (c. 7 km) where they are not significantly affected by localized, near-surface thermal effects of canyon incision. The pattern of zircon cooling ages should therefore reflect only regional exhumation and post-closure bedrock deformation. Zircon dates of samples collected along the same valley-bottom transect show a regular but scattered progression from older dates near the coast to younger dates farther upvalley (Fig. 3).

If the latest pulse of uplift recorded by canyon incision were accommodated through localized, surface-breaking fault movement, we would expect to see a step-change in the pattern of zircon cooling ages (Fig. 5). Although we see no evidence for a large step, the present data set cannot rule out the possibility of uplift accommodated on a series of small faults distributed over a wide region. We have not seen distributed faulting in the field, but we mapped a focused shear zone at the range front. A 16.12 ± 0.04 Ma ($^{40}Ar/^{39}Ar$) undeformed ignimbrite crossing what appears to be the equivalent shear zone 100 km to the southeast of the field area suggests that significant movement on this structure predates the inferred c. 9 Ma uplift. These thermochronologic data lead us to interpret the latest pulse of uplift as resulting from monoclinal warping of the western margin, consistent with interpretations presented by Isacks (1988).

6. Geodynamic implications and conclusions

One of the most important characteristics of the data presented here is the evidence they provide for onset of at least 2.4 km of river incision at c. 9 Ma, in broad agreement with the magnitude and timing of recent uplift of the Central Andean plateau estimated by different methods. If, as we suggest, this incision corresponds to a phase of surface uplift, what can the age range tell us about plausible causes of uplift? Upper-crustal thickening from shortening at the plateau margins mostly occurred prior to 10 Ma (e.g., Gubbels et al., 1993; Victor et al. 2004; Farías et al., 2005; Elger et al., 2005). The argument for uplift through lithospheric delamination is well supported at the southern end of the plateau, where thinned lithosphere and widespread mafic volcanism point to delamination as a plausible cause (Kay and Kay, 1993; Schurr et al., 2006). In the north, however, strong evidence is lacking. Seismic data (Beck and Zandt, 2002) suggests there may be thinned lithosphere beneath the eastern portion of the plateau, but not under the western region. There is also no evidence for a

volcanic flare-up close to the time of uplift (James and Sacks, 1999). Ignimbrite volcanism in southern Peru from c. 16 to 14 Ma may be related to a small delamination event, although we expect canyon incision would not lag more than 2 Myr behind significant uplift. Ductile thickening of the mid- to lower-crust provides a likely alternative, possibly triggered by displacement of material due to underthrusting of the Brazilian Shield beneath the eastern margin, as proposed by Isacks (1988). The c. 10 Ma initiation of underthrusting (Gubbels et al., 1993) correlates well with the latest phase of uplift inferred from our data. For these reasons, although the data we present on uplift timing and monocline deformation are consistent with either lithospheric delamination or lateral flow of lower crust, we favor the latter hypothesis to explain this latest phase of uplift.

Acknowledgments

We thank T. Smith, K. Cornell, and J. Bradley for help with fieldwork; S. Nicolescu for help with (U-Th)/He analyses; G. Wörner for discussions; T. Sempere, O. Oncken, and an anonymous reviewer for constructive reviews. This work is supported by NSF Tectonics Division grant EAR-0409359.

References Cited

Allmendinger, R.W., Jordan, T.E., Kay, S.M., and Isacks, B.L., 1997, The evolution of the Altiplano-Puna plateau of the central Andes: Annual Review of Earth and Planetary Sciences, v. 25, p. 139-174.

Barke, R., and Lamb, S., 2006, Late Cenozoic uplift of the Eastern Cordillera, Bolivian Andes: Earth and Planetary Science Letters, v. 249, p. 350–367, doi: 10.1016/j.epsl.2006.07.012.

Beck, S.L., and Zandt, G., 2002, The nature of orogenic crust in the central Andes: Journal of Geophysical Research, v. 107, no. B10, doi: 10.1029/2000JB000124.

Ehlers, T.A., Chaudhri, T., Kumar, S., Fuller, C.W., Willett, S.D., Ketcham, R.A., Brandon, M.T., Belton, D.X., Kohn, B.P., Gleadow, A.J.W., Dunai, T.J., and Fu, F.Q., 2005, Computational Tools for low-temperature thermochronometer interpretation: Reviews in Mineralogy and Geochemistry, v. 58, p. 589–622, doi: 10.2138/rmg.2005.58.22.

Elger, K., Oncken, O., and Glodny, J., 2005, Plateau-style accumulation of deformation: Southern Altiplano: Tectonics, v. 24, p. TC4020, doi: 10.1029/2004TC001675.

Farías, M., Charrier, R., Compte, D., Martinod, J., and Hérail, G., 2005, Late Cenozoic deformation and uplift of the western flank of the Altiplano: evidence from the depositional, tectonic, and geomorphic evolution and shallow seismic activity (northern Chile at 19°30'S): Tectonics, v. 24, TC4001, doi:10.1029/2004TC001667.

Farley, K.A., 2000, Helium diffusion from apatite: General behavior as illustrated by Durango fluorapatite: Journal of Geophysical Research, v. 105, no. B2, p. 2903–2914, doi: 10.1029/1999JB900348.

Garzione, C.N., Molnar, P., Libarkin, J.C., and MacFadden, B.J., 2006, Rapid late Miocene rise of the Bolivian Altiplano: Evidence for removal of mantle lithosphere: Earth and Planetary Science Letters, v. 241, p. 543–556, doi: 10.1016/j.epsl.2005.11.026.

Ghosh, P., Garzione, C.N., and Eiler, J.M., 2006, Rapid uplift of the Altiplano revealed through ^{13}C-^{18}O bonds in paleosol carbonates: Science, v. 311, p. 511–514, doi: 10.1126/science.1119365.

Gubbels, T.L., Isacks, B.L., and Farrar, E., 1993, High-level surfaces, plateau uplift, and foreland development, Bolivian central Andes: Geology, v. 21, p. 695–698, doi: 10.1130/0091-7613(1993)021<0695:HLSPUA>2.3.CO;2.

Hamza, V.M., and Muñoz, M., 1996, Heat flow map of South America: Geothermics, v. 25, no. 6, p. 599–646, doi: 10.1016/S0375-6505(96)00025-9.

Hartley, A.J., 2003, Andean uplift and climate change: Journal of the Geological Society [London], v. 160, p. 7–10.

Henry, S.G., and Pollack, H.N., 1988, Terrestrial heat flow above the Andean subduction zone in Bolivia and Peru: Journal of Geophysical Research, v. 93, no. B12, p. 15153–15162.

Hoke, G.H., 2006, The influence of climate and tectonics on the geomorphology of the western slope of the central Andes, Chile and Peru [Ph.D. thesis]: Ithaca, NY, Cornell University.

Isacks, B.L., 1988, Uplift of the Central Andean plateau and bending of the Bolivian Orocline: Journal of Geophysical Research, v. 93, no. B4, p. 3211–3231.

James, D.E., and Sacks, I.S., 1999, Cenozoic formation of the Central Andes: A geophysical perspective, *in* Skinner, B.J., ed., Geology and Ore Deposits of the Central Andes: Society of Economic Geology Special Publication 7, p. 1–26.

Kay, R.W., and Kay, S.M., 1993, Delamination and delamination magmatism: Tectonophysics, v. 219, p. 177–189, doi: 10.1016/0040-1951(93)90295-U.

Kennan, L., Lamb, S., and Hoke, L., 1997, High altitude palaeosurfaces in the Bolivian Andes: Evidence for Late Cenozoic surface uplift *in* Widdowson, M., ed., Paleosurfaces: Recognition, Reconstruction and Paleoenvironmental Interpretation, Geological Society Special Publication, v. 120, Geological Society of London, p. 307–324.

Kennan, L., 2000, Large-scale geomorphology of the Andes: Interrelationships of tectonics, magmatism and climate, *in* Summerfield, M.A., ed., Geomorphology and Global Tectonics, John Wiley, New York, p. 167-199.

Kober, F., Ivy-Ochs, S., Schlunegger, F., Baur, H., Kubik, P.W., and Wieler, R., 2007, Denudation rates and a topography-driven rainfall threshold in northern Chile: Multiple cosmogenic nuclide data and sediment yield budgets: Geomorphology, v. 83, p. 97-120, doi: 10.1016/j.geomorph.2006.06.029.

Lamb, S., and Hoke, L., 1997, Origin of the high plateau in the Central Andes, Bolivia: South America: Tectonics, v. 16, no. 4, p. 623–649, doi: 10.1029/97TC00495.

Nestor, P.L., Jordan, T.E., Blanco, N., Hoke, G.D., and Tomlinson, A.J., 2006, Evidence for late Miocene uplift by long-wavelength rotation of western flank of Altiplano segment of Central Andes 20°30' – 20°30'S, Chile in Proceedings, Geological Society of America and Asociación Geológica Argentina, Backbone of the Americas Conference, Mendoza, Argentina.

Niemann, J.D., Gasparini, N.M., Tucker, G.E., and Bras, R.L., 2001, A quantitative evaluation of Playfair's law and its use in testing long-term stream erosion models: Earth Surface Processes and Landforms, v. 26, p. 1317–1332, doi: 10.1002/esp.272.

Rech, J.A., Currie, B.S., Michalski, G., and Cowan, A.M., 2006, Neogene climate change and uplift in the Atacama Desert, Chile: Geology, v. 34, no. 9, p. 761-764, doi: 10.1130/G22444.1

Reiners, P.W., Spell, T.L., Nicolescu, S., and Zanetti, K.A., 2004, Zircon (U-Th)/He thermochronology: He diffusion and comparisons with $^{40}Ar/^{39}Ar$ dating: Geochimica et Cosmochimica Acta, v. 68, no. 8, p. 1857–1887, doi: 10.1016/j.gca.2003.10.021.

Schurr, B., Rietbrock, A., Asch, G., Kind, R., and Oncken, O., 2006, Evidence for lithospheric detachment in the central Andes from local earthquake tomography: Tectonophysics, v. 415, p. 203-223.

Springer, M., and Förster, A., 1998, Heat-flow density across the Central Andean subduction zone: Tectonophysics, v. 291, p. 123–139, doi: 10.1016/S0040-1951(98)00035-3.

Thouret, J.-C., Wörner, G., Singer, B., and Finizola, A., 2005, The Central Andes in Peru: 'Old' valleys in a 'young' mountain range? *in* Proceedings, 6th International Symposium on Andean Geodynamics, Barcelona, Extended Abstracts, p. 726–729.

Victor, P., Oncken, O., and Glodny, J., 2004, Uplift of the western Altiplano plateau: evidence from the Precordillera between 20 and 21°S (northern Chile): Tectonics, v. 23, doi: 10.1029/2003TC001519.

Whipple, K.X, and Tucker, G.E., 2002, Implications of sediment-flux-dependent river incision models for landscape evolution: Journal of Geophysical Research – Solid Earth, v. 107, no. B2, 2039, doi:10.1029/2000JB000044.

Wörner, G., Hammerschmidt, K., Henjes-Kunst, F., Lezaun, J., and Wilke, H., 2000, Geochronology ($^{40}Ar/^{39}Ar$, K-Ar and He-exposure ages) of Cenozoic magmatic rocks from Northern Chile (18–22°S): implications for magmatism and tectonic evolution of the central Andes: Revista Geológica de Chile, v. 27, no. 2, p. 131–137.

Figure Captions

Figure 1. Location map and sample sites. Topography is shown as a grayscale DEM draped over shaded relief from 90-m resolution SRTM data. Inset shows location relative to South American geography. (U-Th)/He samples are collected from near river level. $^{40}Ar/^{39}Ar$ samples are from elevations noted in Data Respository.

Figure 2. Schematic interpretation of incision history based on (U-Th)/He apatite data. Gray zones are rapidly-cooled due to migration of the closure temperature isotherm (~70 °C) in response to incision. At least 1.0 km of incision occurred between 9 and 5.1 Ma, since this is the thickness of the rapidly-cooled zone between those ages on the age-depth plot. Post-5.1 Ma incision is equal to the depth of the closure temperature isotherm below the valley bottom at 5.1 Ma.

Figure 3. Zircon and apatite results plotted as distance measured perpendicular to coastline. Errors in age show 2σ uncertainty.

Figure 4. Apatite and zircon (U-Th)/He ages collected along valley at river level. Mean ages are weighted by the inverse of the variance of individual crystal ages. Errors in age are plotted as 2σ analytical errors only. Errors in depth below paleosurface are estimated at ± 100 m. Inset shows apatite data over the last 25 Myr.

Figure 5. Predictions for patterns of (U-Th)/He zircon ages for samples collected along river profile in various tectonic settings, assuming initially flat isochrons. The pattern of ages presented here best match the prediction resulting from a monocline.

Figure DR1. Creation of paleosurface reference layer. Left panel illustrates how points (black dots) were selected where bedrock outcrops beneath the regionally-blanketing Huaylillas Ignimbrite,

Elevations are defined by intersections with topographic contour lines. Right panel shows the surface spline fit to the selected points to create a representation of the (now deformed) paleosurface under the Huaylillas ignimbrite. This paleosurface shows a flat region in the upper catchment which then ramps down toward the coast. Also shown on left panel are valley-filling volcanic flows (bright red) we mapped in the field. Other volcanic units are shown in yellow. Low-temperature themochronology sample locations are shown (white dots) such that a comparison between sample locations and volcanic flows can be made. Young volcanics flows (c. 1.4 to 3.8 Ma, Thouret et al., 2005, and data presented here) dominate the landscape in the uppermost catchment and probably affected (U-Th)/He ages in that region.

Table DR1. Apatite (U-Th)/He individual crystal data.

Table DR2. Zircon (U-Th)/He individual crystal data.

Table DR3. $^{40}Ar/^{39}Ar$ data for valley-filling volcanic flows and Huaylillas ignimbrite.

Table DR4. Location and context for samples dated with $^{40}Ar/^{39}Ar$.

Table DR5. Parameters used in thermal model calculations and results.

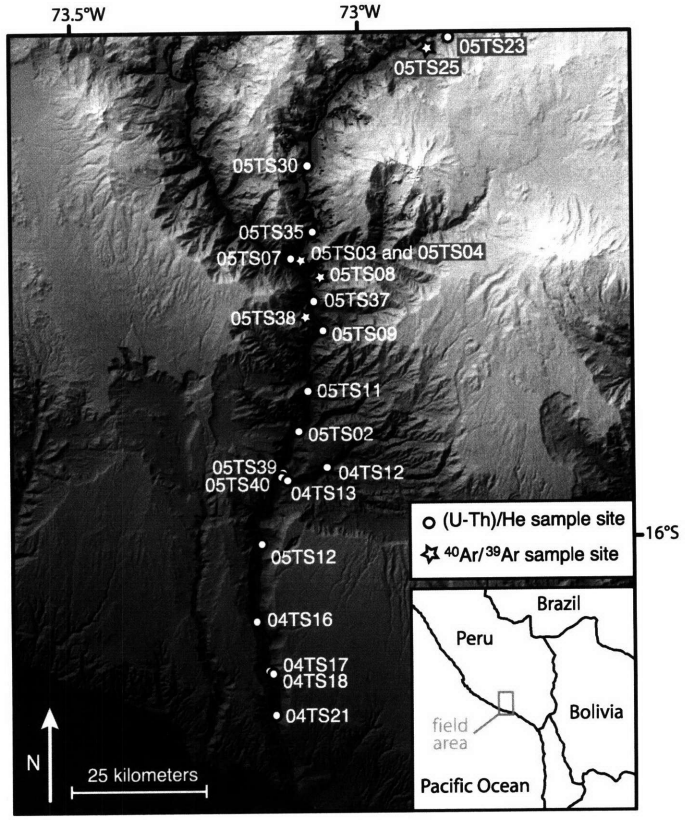
73.5°W
73°W
05TS23
05TS25
05TS30
05TS35
05TS07
05TS03 and 05TS04
05TS08
05TS37
05TS38
05TS09
05TS11
05TS02
05TS39
05TS40
04TS12
04TS13
05TS12
04TS16
04TS17
04TS18
04TS21
16°S
(U-Th)/He sample site
40Ar/39Ar sample site
Brazil
Peru
Bolivia
field area
Pacific Ocean
N
25 kilometers

Figure 1.

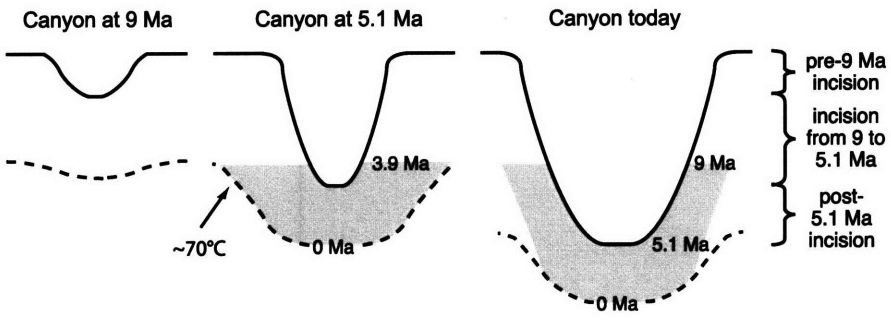
Canyon at 9 Ma
Canyon at 5.1 Ma
Canyon today
3.9 Ma
~70°C
0 Ma
9 Ma
5.1 Ma
0 Ma
pre-9 Ma incision
incision from 9 to 5.1 Ma
post-5.1 Ma incision

Figure 2.

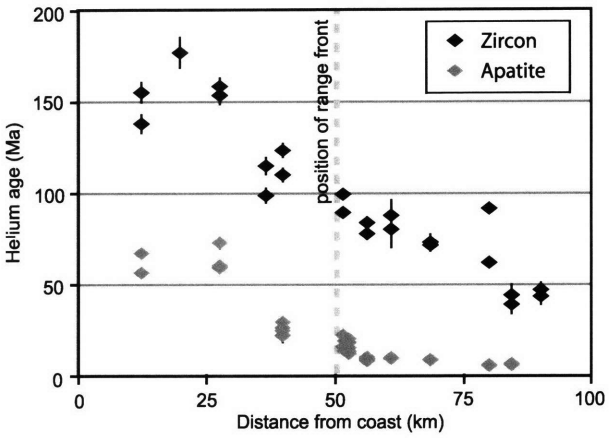
200
150
100
50
0
0
25
50
75
100
Helium age (Ma)
Distance from coast (km)
position of range front
Zircon
Apatite

Figure 3.

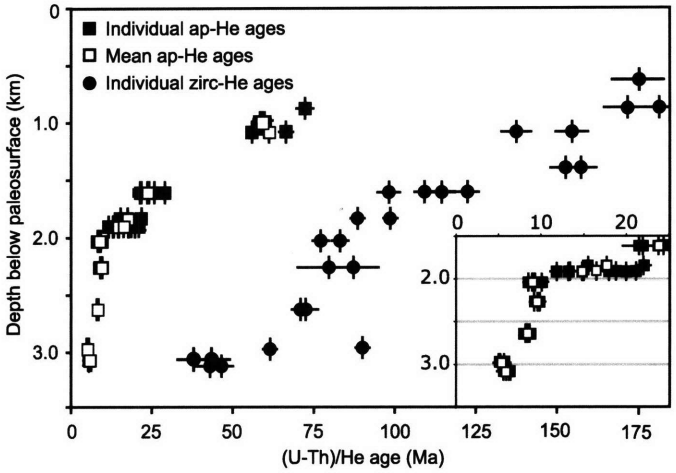
Individual ap-He ages
Mean ap-He ages
Individual zirc-He ages
Depth below paleosurface (km)
0
1.0
2.0
3.0
0
25
50
75
100
125
150
175
(U-Th)/He age (Ma)
0
10
20
2.0
3.0

Figure 4.

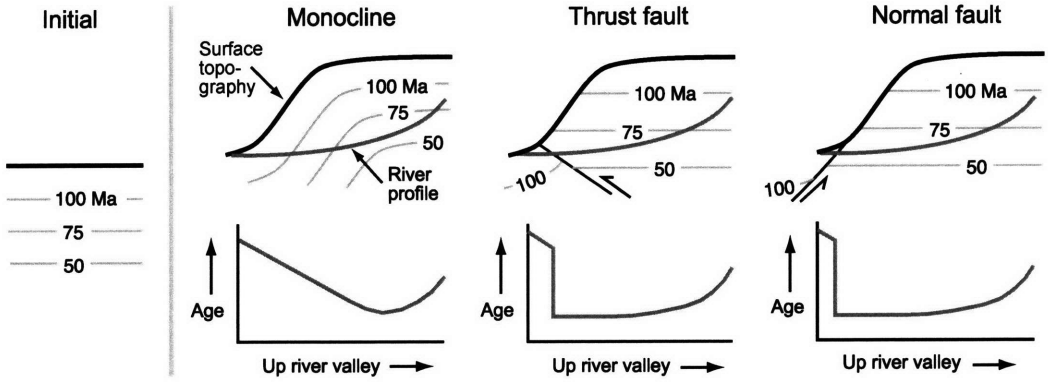
Initial
100 Ma
75
50
Monocline
Surface topo-graphy
100 Ma
75
50
River profile
Age
Up river valley
Thrust fault
100 Ma
75
50
100
Age
Up river valley
Normal fault
100 Ma
75
50
100
Age
Up river valley

Figure 5.

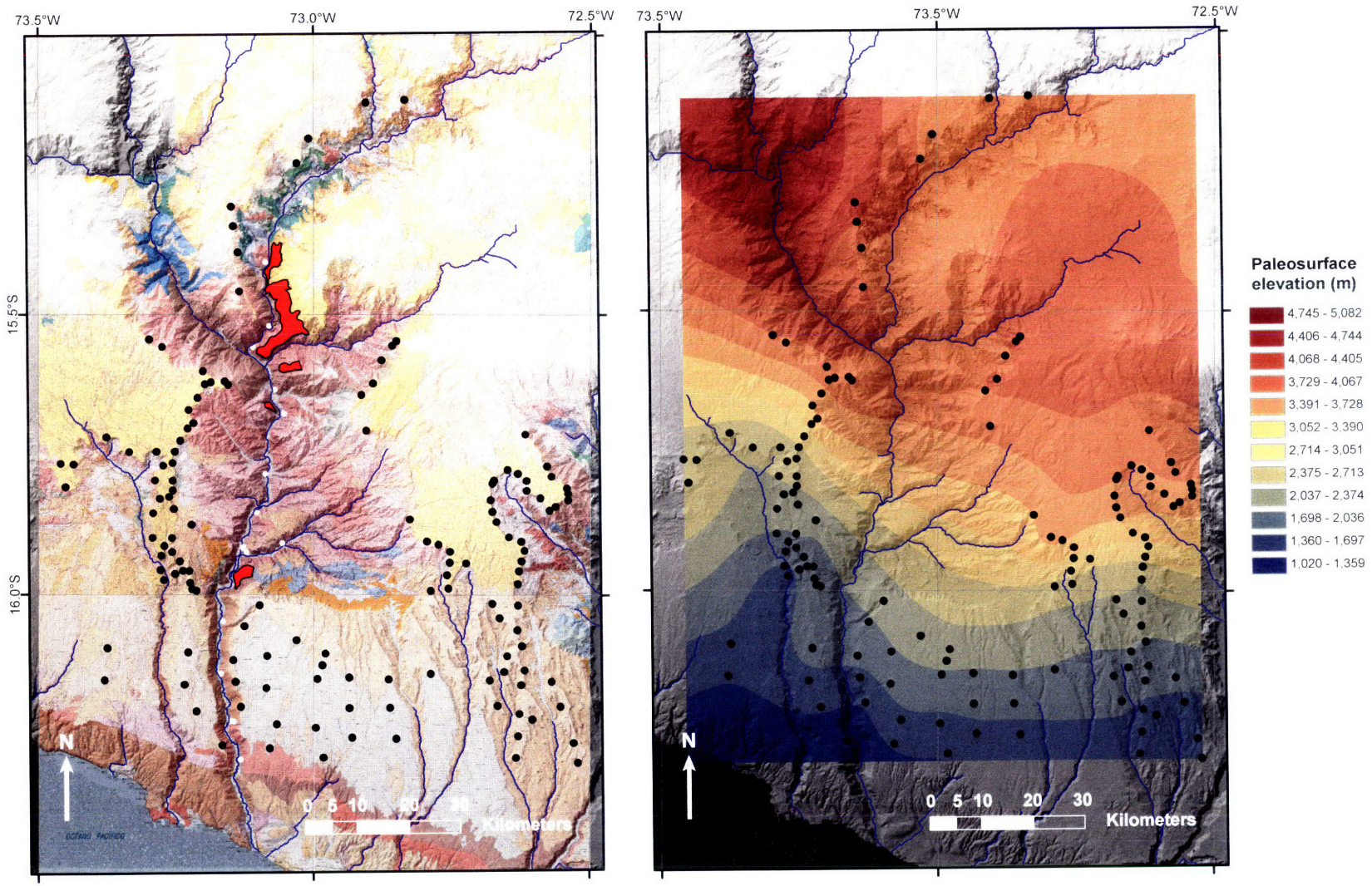
73.5°W
73.0°W
72.5°W
15.5°S
16.0°S
N
0 5 10 20 30
Kilometers
Paleosurface elevation (m)
4,745 - 5,082
4,406 - 4,744
4,068 - 4,405
3,729 - 4,067
3,391 - 3,728
3,052 - 3,390
2,714 - 3,051
2,375 - 2,713
2,037 - 2,374
1,698 - 2,036
1,360 - 1,697
1,020 - 1,359

Figure DR1.

TABLE DR1. APATITE (U-Th)/He INDIVIDUAL CRYSTAL DATA

Sample	Mass (μg)	Radius (μm)	U (ppm)	Th (ppm)	Sm (ppm)	4He (nmol/g)	Ft	Corrected age* (Ma)	2 σ† (Ma)	Depth§ (km)	Distance (km)	Elevation (m)
04TS12aA	6.67	63.5	148	106	187	6.28	0.79	8.54	0.31	2.04	56.4	702
04TS12aB	2.63	42.8	180	114	168	7.33	0.70	9.31	0.34	2.04	56.4	702
04TS12aC	1.15	34.3	174	143	152	7.14	0.63	10.1	0.37	2.04	56.4	702
04TS12aD	2.32	44.3	189	115	220	5.81	0.70		0.26	2.04	56.4	702
04TS12aE	1.11	32.5	197	107	165	6.82	0.62	9.18	0.35	2.04	56.4	702
04TS12aF	1.81	39.8	244	156	225	8.07	0.68	7.85	0.29	2.04	56.4	702
04TS13aA	1.08	32.3	84.8	53.8	179	7.17	0.62	22.1	0.83	1.85	51.7	552
04TS13aB	1.34	32.3	81.7	49.2	145	4.90	0.63	15.5	0.60	1.85	51.7	552
04TS17aA	4.42	47.0	9.39	100	309	7.76	0.71	60.0	1.98	1.01	27.7	290
04TS17aB	3.04	41.3	11.2	109	318	8.15	0.68	59.2	1.97	1.01	27.7	290
04TS17aC	2.53	45.3	14.7	98.0	283	10.1	0.69		2.32	1.01	27.7	290
04TS17aD	2.97	45.8	8.83	94.7	279	6.99	0.70	58.7	2.00	1.01	27.7	290
04TS18aA	2.21	40.3	4.72	31.8	138	1.31	0.67		1.25	0.89	27.7	415
04TS18aB	1.34	36.3	5.33	78.6	307	5.92	0.62	72.5	2.98	0.89	27.7	415
04TS21aA	1.02	37.3	258	148	221	67.6	0.64	66.7	2.48	1.09	12.4	73
04TS21aB	1.57	36.0	22.5	66.3	92.1	7.46	0.64	56.1	1.95	1.09	12.4	73
05TS02_A	2.40	46.7	64.9	140	309	3.70	0.71	9.86	0.41	2.28	61.1	590
05TS02_B	1.40	35.6	63.9	114	267	2.91	0.64	9.22	0.40	2.28	61.1	590
05TS02_C	1.43	37.1	62.9	113	274	3.09	0.65	9.81	0.42	2.28	61.1	590
05TS02_D	2.24	49.2	31.6	47.8	165	3.18	0.71		0.82	2.28	61.1	590
05TS09_A	1.86	39.7	111	110	233	2.85	0.68	5.68	0.25	2.99	80.1	816
05TS09_B	2.50	43.4	106	118	255	2.56	0.70	5.05	0.22	2.99	80.1	816
05TS09_C	1.77	41.1	97.8	85.8	217	2.22	0.68	5.11	0.23	2.99	80.1	816
05TS11_A	1.49	37.3	45.1	74.4	189	1.87	0.65	8.45	0.38	2.64	68.7	647
05TS11_B	2.11	45.1	74.4	145	258	4.57	0.70		0.47	2.64	68.7	647
05TS11_C	1.87	42.5	111	223	310	5.25	0.68	8.68	0.36	2.64	68.7	647
05TS11_D	1.27	38.6	126	239	327	5.25	0.65	8.19	0.34	2.64	68.7	647
05TS39_A	2.28	44.5	51.9	31.9	167	4.54	0.70	20.0	0.92	1.92	52.8	490
05TS39_B	2.47	47.5	90.2	48.3	169	5.21	0.72	13.2	0.59	1.92	52.8	490
05TS39_C	3.84	51.1	52.4	28.0	174	2.09	0.74		0.33	1.92	52.8	490
05TS39_D	2.48	40.8	84.7	50.9	112	5.44	0.69	15.0	0.55	1.92	52.8	490
05TS39_E	3.37	51.9	54.5	35.8	251	4.55	0.74	18.0	0.66	1.92	52.8	490
05TS39_F	2.31	48.6	56.7	26.6	124	2.90	0.72	11.9	0.56	1.92	52.8	490
05TS40_A	1.03	34.9	108	97.2	161	9.42	0.63	21.2	0.79	1.92	52.1	480

05TS40_B	1.40	39.2	119	98.2	139	6.82	0.66	13.4	0.49	1.92	52.1	480
05TS40_C	0.87	32.1	143	85.5	107	10.1	0.61	18.8	0.71	1.92	52.1	480
05TS40_D	1.12	32.6	141	49.6	112	5.24	0.62		0.40	1.92	52.1	480
05TS12_A	1.54	36.9	1.86	23.2	473	0.70	0.63	26.1	1.54	1.62	40.0	360
05TS12_B	1.41	40.7	2.79	22.5	356	0.36	0.65		0.70	1.62	40.0	360
05TS12_C	1.85	38.9	2.24	15.4	337	0.18	0.65		0.62	1.62	40.0	360
05TS12_D	1.80	46.3	2.43	8.24	330	0.38	0.69	21.5	1.64	1.62	40.0	360
05TS12_E	2.83	47.9	1.37	13.9	380	0.15	0.70		0.77	1.62	40.0	360
05TS12_F	3.12	49.9	3.22	16.9	434	0.88	0.72	29.2	1.68	1.62	40.0	360
05TS12_G	2.10	40.7	1.33	6.67	377	0.27	0.67	22.0	3.73	1.62	40.0	360
05TS12_H	3.03	50.4	3.37	24.7	369	0.91	0.72	24.4	1.23	1.62	40.0	360
05TS37_A	3.57	48.6	10.9	23.3	151	0.60	0.73		0.39	3.08	84.5	852
05TS37_B	3.26	42.4	12.6	32.2	186	0.48	0.70	6.26	0.24	3.08	84.5	852
05TS37_C	2.81	43.7	13.7	37.2	189	0.48	0.70	5.60	0.23	3.08	84.5	852
05TS37_D	1.88	40.8	8.01	15.9	134	0.28	0.68	6.42	0.52	3.08	84.5	852
05TS07_A	3.69	44.1	13.8	19.3	144	0.27	0.71	3.79	1.43	3.13	90.2	940
05TS07_B	2.93	42.3	14.9	16.4	85	0.26	0.70	3.66	1.40	3.13	90.2	940
05TS07_C	2.98	48.9	17.1	20.9	149	0.34	0.73	3.87	1.45	3.13	90.2	940
05TS07_D	5.62	51.4	8.33	10.7	104	0.18	0.75	4.10	1.50	3.13	90.2	940
05TS35_A	3.28	45.7	70.1	134	169	0.78	0.72	1.97	0.07	3.00	96.9	1028
05TS35_B	2.76	47.5	86.5	167	177	0.90	0.72	1.84	0.06	3.00	96.9	1028
05TS35_C	3.41	46.4	68.5	136	141	0.84	0.72	2.16	0.07	3.00	96.9	1028
05TS35_D	4.17	53.5	68.5	108	136	0.71	0.75	1.86	0.06	3.00	96.9	1028
05TS30_A	1.30	36.9	62.2	318	149	0.78	0.63	1.66	0.08	2.60	108.6	1355
05TS30_B	1.43	37.8	48.2	212	132	0.30	0.64	0.88	0.05	2.60	108.6	1355
05TS30_C	1.01	35.7	60.8	274	138	0.42	0.61	1.01	0.07	2.60	108.6	1355
05TS23_A	1.48	40.8	10.5	37.3	184	0.04	0.66	0.53	0.18	1.41	139.8	2580
05TS23_B	1.31	36.6	12.1	44.3	228	0.07	0.64	0.86	0.17	1.41	139.8	2580

*Alpha-ejection corrected age; values shaded gray are outliers not plotted in results. "Outliers" were defined based on microscopic inclusions or cracks that were suspected could affect the age; others did not have visible flaws but had ages that were far from the rest of the population of grains analyzed. This can come about for a number of different reasons, such as strong zoning in U and Th, errors in the alpha-ejection correction, radiation damage affecting diffusion characteristics of the grain, He-implantations from adjacent crystal phases in the host rock, etc.

†Error includes analytical precision only; in reality errors noted previously are likely to contribute to uncertainty.

§Depth below paleosurface. Error on this values is estimated to be +/- 100 m.

TABLE DR2. ZIRCON (U-Th)/He INDIVIDUAL CRYSTAL DATA

Sample	Th/U	Mass (μg)	Radius (μm)	U (ppm)	Th (ppm)	^{4}He (nmol/g)	Ft	Corrected age* (Ma)	2 σ† (Ma)	Distance (km)	Depth§ (km)	Elevation (m)
04TS13z_B	0.47	2.92	38.3	233	106	90.9	0.73	88.9	4.50	51.7	0.19	552
04TS13z_A	0.63	3.31	37.5	277	169	125	0.73	99.0	4.95	51.7	0.19	552
04TS16z_A	2.79	14.7	59.8	94.5	257	110	0.82	158	7.28	27.7	0.14	225
04TS16z_B	0.55	14.7	65.3	170	91.4	134	0.84	153	7.67	27.7	0.14	225
04TS18z_A	2.78	7.80	56.8	56.5	153	74.3	0.81	182	8.34	27.7	0.89	415
04TS18z_B	1.31	6.82	57.3	122	156	121	0.81	173	8.23	27.7	0.89	415
04TS20z_A	1.16	2.22	37.5	200	227	210	0.72	210	9.86	20.0	0.66	650
04TS20z_B	1.46	4.14	51.5	123	174	123	0.78	177	8.13	20.0	0.66	650
05TS02z_A	0.83	14.5	54.7	206	166	87.3	0.82	79.9	3.78	61.1	2.28	590
05TS02z_B	0.48	8.21	50.4	340	160	143	0.80	87.5	4.29	61.1	2.28	590
05TS07z_A	0.52	13.3	55.3	228	115	53.0	0.82	46.7	2.25	90.2	3.13	939
05TS07z_B	0.43	12.5	54.3	195	80.8	40.7	0.82	43.1	2.13	90.2	3.13	939
05TS09z_A	0.63	12.4	63.9	365	223	116	0.83	61.7	2.99	80.1	2.99	816
05TS09z_B	1.41	10.3	56.2	600	823	319	0.81	91.2	4.17	80.1	2.99	816
05TS11z_A	0.46	43.8	80.4	294	132	110	0.88	71.2	3.49	68.7	2.64	647
05TS11z_B	0.58	52.8	93.0	202	114	80.2	0.89	72.8	3.51	68.7	2.64	647
05TS12z_A	1.14	20.8	67.0	57.7	64.3	36.7	0.85	110	4.76	40.0	1.62	360
05TS12z_B	0.66	17.7	59.7	111	71.3	71.3	0.84	123	5.63	40.0	1.62	360
04TS12zA	0.72	5.25	43.5	269	188	101	0.77	77.4	2.83	56.4	2.04	702
04TS12zB	0.89	6.78	42.5	194	168	81.5	0.77	83.4	2.94	56.4	2.04	720
04TS15zA	0.27	2.65	40.8	408	108	201	0.75	115	4.44	36.7	1.62	322
04TS15zB	0.32	1.98	40.5	361	111	151	0.73	98.4	3.83	36.7	1.62	322
04TS21zA	0.82	14.6	52.5	78.8	62.7	57.3	0.82	138	4.90	12.4	1.09	73
04TS21zB	1.26	6.96	48.3	61.7	75.6	52.3	0.78	155	5.34	12.4	1.09	73

* Alpha-ejection corrected ages.

†Error includes analytical precision only; in reality, zoning in U and Th and crystal measurement error also likely contribute to uncertainty.

§Depth below paleosurface. Error on this measurement is estimated to be +/- 100 m.

TABLE DR3. $^{40}Ar/^{39}Ar$ DATA FOR VALLEY-FILLING VOLCANIC FLOWS AND HUAYLILLAS IGNIMBRITE

Information on Analysis		Weighted Average Analysis						Inverse Isochron Analysis			
Laser-Fusion		**40(r)/39(k) ± 2σ**	**Age ± 2σ (Ma)**	**MSWD**	**39Ar(k) (%,n)**	**K/Ca**	**40(a)/36(a) ± 2σ**	**40(r)/39(k) ± 2σ**	**Age ± 2σ (Ma)**	
Sample	05TS03	1.360 ± 0.036 ± 2.64%	**1.865 ± 0.050 ± 2.65%**	1.12	84.0 11 of 13	0.746	295.3 ± 16.8 ± 5.69%	1.361 ± 0.081 ± 5.93%	1.867 ± 0.111 ± 5.94%	
Material	Feldspar									
Sample	05TS04	1.413 ± 0.015 ± 1.03%	1.937 ± 0.021 ± 1.07%	1.13	84.4 20 of 23	0.872	327.8 ± 27.6 ± 8.41%	1.387 ± 0.027 ± 1.91%	1.901 ± 0.037 ± 1.94%	
Material	Feldspar									
Sample	05TS04	1.385 ± 0.015 ± 1.06%	1.930 ± 0.021 ± 1.08%	1.04	100.0 16 of 16	1.137	290.7 ± 12.56 ± 4.32%	1.390 ± 0.019 ± 1.40%	1.937 ± 0.027 ± 1.41%	
Material	Feldspar									
		Wtd. Mean Age:	**1.934 ± 0.015 ± 0.78%**	0.05						
Sample	05TS25	2.802 ± 0.008 ± 0.30%	**3.825 ± 0.016 ± 0.42%**	1.49	100.0 18 of 18	14.49	285.7 ± 10.1 ± 3.55%	2.809 ± 0.011 ± 0.37%	3.834 ± 0.018 ± 0.48%	
Material	Sanidine									
Sample	04TS10	4.334 ± 0.008 ± 0.18%	**14.20 ± 0.04 ± 0.27%**	1.29	100.0 12 of 12	70.8	291.1 ± 8.5 ± 2.91%	4.336 ± 0.009 ± 0.21%	14.21 ± 0.04 ± 0.29%	
Material	Sanidine									
Sample	04TS22	4.373 ± 0.010 ± 0.23%	**14.29 ± 0.04 ± 0.30%**	2.00	100.0 11 of 11	50.2	294.3 ± 47.0 ± 16.0%	4.374 ± 0.014 ± 0.31%	14.30 ± 0.05 ± 0.37%	
Material	Sanidine									
Sample	05TS43	11.57 ± 0.013 ± 11.0%	**16.12 ± 0.04 ± 0.23%**	0.82	100.0 20 of 20	59.3	272.1 ± 68.2 ± 25.1%	11.576 ± 0.027 ± 0.23%	16.13 ± 0.05 ± 0.30%	
Material	Sanidine									
Furnace Step-Heating		**40(r)/39(k) ± 2σ**	**Age ± 2σ (Ma)**	**MSWD**	**39Ar(k) (%,n)**	**K/Ca**	**40(a)/36(a) ± 2σ**	**40(r)/39(k) ± 2σ**	**Age ± 2σ (Ma)**	
Sample	05TS08	1.597 ± 0.007 ± 0.44%	**2.196 ± 0.012 ± 0.53%**	0.96	93.7 13 of 17	0.651	295.2 ± 2.5 ± 0.85%	1.598 ± 0.010 ± 0.63%	2.197 ± 0.015 ± 0.69%	
Material	Gndmass									
Sample	05TS38	1.663 ± 0.057 ± 3.42%	2.284 ± 0.079 ± 3.44%	0.78	80.4 12 of 16	0.826	293.7 ± 3.6 ± 1.21%	1.727 ± 0.140 ± 8.13%	2.373 ± 0.193 ± 8.13%	
Material	Gndmass									
Sample	05TS38	1.669 ± 0.041 ± 2.45%	2.249 ± 0.056 ± 2.47%	0.64	84.7 21 of 27	0.799	293.1 ± 2.8 ± 0.97%	1.754 ± 0.106 ± 6.03%	2.363 ± 0.143 ± 6.04%	
Material	Gndmass									
		Wtd. Mean Age:	**2.261 ± 0.046 ± 2.03%**	0.13						

Note: All ages reported relative to TCR-2a Sanidine @ 28.34 Ma

TABLE DR4. LOCATION AND CONTEXT FOR SAMPLES DATED WITH $^{40}Ar/^{39}Ar$

Sample	Description	Age ± 2 σ (Ma)	Ht. above river (m)	Latitude (°S)	Longitude (°W)
05TS03	Feldspar from basal vitrophyre ash; Cotahuasi valley fill	1.865 ± 0.050	400	15°33'48.91"	73°06'16.22"
05TS04	Feldspar from basal vitrophyre obsidian; Cotahuasi valley fill	1.934 ± 0.015	400	15°33'48.91"	73°06'16.22"
05TS25	Sanidine from base of welded tuff in-filling upper Cotahuasi valley	3.825 ± 0.016	450	15°12'41.86"	72°52'49.87"
04TS10	Sanidine from Huaylillas Fm., near town of Aplao	14.20 ± 0.04	n/a	16°14'45.83"	72°30'06.56"
04TS22	Sanidine from Huaylillas Fm., north of Aplao	14.29 ± 0.04	n/a	15°57'20.85"	72°34'59.70"
05TS08	Andesite groundmass, from andesite valley fill near Chaucalla	2.196 ± 0.012	450	15°35'31.51"	73°04'05.70"
05TS43	Sanidine from undeformed ignimbrite crossing range front fault zone 100 km SE of Cotahuasi range front	16.12 ± 0.04	n/a	16°11'16.08"	72°01'36.33"
05TS38	Basaltic andesite groundmass from valley fill near Llauce	2.261 ± 0.056	125	15°39'28.30"	73°04'35.36"

TABLE DR5. PARAMETERS USED IN THERMAL MODEL CALCULATIONS AND RESULTS

Parameter used in model	20°C/km run	30°C/km run
Diffusion radius (micrometers)*:	60	60
Activation energy for closure temperature (kJ/mol)*:	138	138
Normalized frequency factor, $\Omega(s^{-1})$*:	7.64E+07	7.64E+07
Thermal parameters:		
Layer depth to constant temperature (km)†:	60	60
Thermal diffusivity (km^2/my)§:	30	30
Internal heat production (°C/my)§:	8	8
Surface temperature (°C):	10	10
Predicted temperature at base of layer (°C)#:	730	1330
Estimates assuming steady-state heat flux and no erosion:§		
Surface thermal gradient (°C/km):	20	30
Estimate for volumetric heat production (mW/m^3):	0.583	0.583
Estimate for thermal conductivity (W/(m*Kelvin)):	2.186	2.186
Predicted surface heat flux (mW/m^2)#:	43.73	65.59
Crustal avg. product of thermal conductivity and density (kJ/ (Kelvin*m^3))§:	2300	2300
AGE2EDOT results:		
Erosion rate (km/myr):	0.7	0.5
Depth to closure temperature (km):	2.0	1.4
Closure temperature (°C):	72	72

*Farley, K.A., 2000, Helium diffusion from apatite: General behavior as illustrated by Durango fluorapatite: Journal of Geophysical Research, v. 105, no. B2, p. 2903–2914, doi: 10.1029/1999JB900348.

†Beck, S.L., Zandt, G., Myers, S.C., Wallace, T.C., Silver, P.G., and Drake, L., 1996, Crustal-thickness variations in the central Andes: Geology, v. 24, no. 5, p. 407-410.

§Details in Brandon, M.T., Roden-Tice, M.K., Garver, J.I., 1998, Late Cenozoic exhumation of the Cascadia accretionary wedge in the Olympic Mountains, northwest Washington State: GSA Bulletin, v. 110, p. 985-1009.

#Values predicted based on input parameters.

Chapter 3:

Quantifying canyon incision and Andean Plateau surface uplift, southwest Peru: A thermochronometer and numerical modeling approach.

Taylor Schildgen[1]
Todd A. Ehlers[2]
David M. Whipp, Jr.[2]
Kelin Whipple[3]
Kip Hodges[3]
Matthijs van Soest[3]

1. Department of Earth, Atmospheric and Planetary Sciences, Massachusetts Institute of Technology, Cambridge, Massachusetts 02139, USA
2. Department of Geological Sciences, University of Michigan, Ann Arbor, Michigan 48109, USA
3. School of Earth and Space Exploration, Arizona State University, Tempe, Arizona 85287, USA

Abstract

Apatite and zircon (U-Th)/He thermochronometer cooling ages from Cotahuasi-Ocoña canyon at the northwest margin of the Central Andean plateau provide information on rock cooling histories induced by a major phase of canyon incision. In this study we quantify the timing and magnitude of canyon incision by integrating 20 previously published samples from the valley bottom with 26 new samples from five vertical transects. Interpretation of the canyon incision history from cooling ages is complicated by a southwest to northeast increase in temperatures at the base of the crust due to active subduction. Furthermore, the large magnitude of canyon incision in this region leads to additional three-dimensional (3D) variations in sample cooling histories that depend on the style of landscape evolution. We address these complications with a finite-element thermal evolution and thermochronometer age-prediction model to quantify the range of topographic evolution scenarios consistent with observed cooling ages. Geological evidence for early canyon depths of at least 200 m and comparison of 275 model simulations to observed cooling ages and regional heat flow determinations identify a best-fit history with $\leq$ 0.2 km of incision in the forearc region prior to ~14 Ma and up to 3.0 km of incision starting between 8 and 11.5 Ma. Young thermochronometer ages and a $^{40}Ar/^{39}Ar$ age on a valley-filling volcanic flow imply that incision ended by 2.21 $\pm$ 0.02 Ma. Model simulations suggest incision could have ended as early as 6 Ma, but this is not well-constrained by the

results. Better constraints can be derived directly from the age of the youngest apatite sample, 5.24 Ma, as additional incision must have occurred after this time in order to expose the sample. Canyon incision starting at 8 to 11.5 Ma must coincide with or post-date surface uplift, given that incision on the order of several kilometers in magnitude must be driven by surface uplift of at least this magnitude. Contemporaneous surface uplift recorded in the interior and eastern margin of the plateau suggest that uplift was driven by geodynamic mechanisms capable of producing uplift over several hundred kilometers, possibly including delamination of a high-density lithospheric root, lateral flow of lower crust, or subduction zone mechanisms such as thermal weakening and ablative subduction.

1. Introduction

Low-temperature thermochronology can provide a wealth of information reflecting changes in the near-surface thermal field within the crust in response to evolving surface topography (e.g. Ehlers and Farley, 2003; Braun, 2005). Such data have been used to demonstrate the antiquity and evolution of mountain topography (House et al., 1998; 2001; Ehlers et al. 2006; Herman et al., 2007), relief change in landscapes, (e.g., Braun, 2002a; Braun and Roberts, 2005; Shuster et al. 2005), and to record the timing of major canyon incision in southern Peru (Schildgen et al., 2007) and in eastern Tibet (Clark et al., 2005; Ouimet et al., 2007). In many cases, precise interpretations of the data are limited by complications involving the thermal response time to changes in surface topography, lateral and/or temporal variations in crustal thermal properties, and insufficient information on surface morphology prior to major changes.

In this paper we explore how some of these complications affect interpretations of thermochronologic data from southwest Peru, where Schildgen et al. (2007) used a valley-bottom transect of apatite and zircon (U-Th)/He data to decipher the cooling signal induced by a major phase of canyon incision on the western margin of the Central Andean plateau. Canyon incision could coincide with or post-date surface uplift, given that incision on the order of several kilometers in magnitude must be driven by surface uplift of at least this magnitude. However, the time required for an incision signal to propagate through a drainage system implies that the onset of incision provides only a minimum estimate for the onset of surface uplift. Plateau uplift could predate incision by an unknown amount if insufficient discharge is available in rivers for bedrock erosion. As discussed later, in this study we do not believe this is the case and infer incision to be contemporaneous with surface uplift. The lag time between uplift and incision may be on the order of one million years for a detachment-limited system, but at large drainage areas in the trunk stream of major rivers the lag time can be much shorter (Whipple and Tucker, 2002).

Early contributions to the present height of the Central Andes are difficult to constrain, but sedimentary units deposited in the forearc region provide some clues. The regional sedimentary package that blankets the forearc region known as the Moquegua Formation in Peru (Sempere et al., 2004; Roperch et al., 2006) and the Azapa Formation in northern Chile (Wörner et al., 2002) consists of a thick package of siltstone and sandstone red beds that are unconformably overlain by debris flow and fluvial conglomerates. Red beds of the Lower Moquegua Formation are estimated to have been deposited starting at ~50 Ma, and the unconformity beneath the coarser sediments is estimated to be ~30 Ma (Sempere et al., 2004; Roperch et al., 2006), indicating that some inland topography existed prior to that time, and probably grew to more significant heights prior to deposition of the upper Moquegua conglomerates. Later uplift in the region is better constrained. In southern Peru, thermochronology data (Schildgen et al., 2007) and $^{40}Ar/^{39}Ar$ ages on valley-filling volcanic flows (Schildgen et al., 2007; Thouret et al., 2007) suggested that at least 2.4 km of uplift-driven incision started at ca. 9 to 10 Ma. These results agree broadly with uplift estimates from other regions in the Central Andes. These include oxygen- and clumped-isotope data from the Altiplano interior (Ghosh et al., 2006; Garzione et al., 2006; Quade et al., 2007), uplift-induced incision history derived from dated low-relief erosion surfaces on the eastern margin of the plateau (Gubbels et al., 1993; Kennan et al., 1997; Barke and Lamb, 2006), and additional paleoelevation studies based on paleobotany and structural analysis of deformed sediments that are summarized in Table 1. However, in all these cases, uplift estimates are only minima or they are bracketed by large uncertainties. Placing better constraints on the magnitude of uplift during this most recent tectonic phase is of particular importance, because the timing of generation of major topographic barriers such as the Andes has important effects on local and global atmospheric circulation patterns (e.g., Rodwell and Hoskins, 2001; Takahashi and Battisti, 2007). More sophisticated analyses of low-temperature thermochronologic data from southwest Peru can provide the most precise constraints to date on the uplift history of the western margin, and can better inform how topographic evolution of this region relates to development of this major orogenic plateau.

Utilizing a modified version of the three-dimensional finite-element thermal model Pecube (Braun, 2003), we explore what range of topographic evolution scenarios are consistent with thermochronologic data collected from the region. The model tracks the thermal history of rocks as they are advected to the surface through a thermal field that responds to changes in surface topography, and predicts thermochronologic ages of rocks collected at the surface. We compare model results data from 26 new samples collected in five vertical transects in addition to the valley-bottom apatite and zircon (U-Th)/He data previously reported by Schildgen et al. (2007). With new

insights from thermal modeling, we refine previous interpretations of the canyon incision history in southwest Peru.

2. Geologic and Thermal Setting

2.1. Plate tectonic setting

The complex thermal setting of the western margin of the Central Andean plateau poses particular challenges to understanding the thermal evolution of the region. Variations in the convergence rate between the subducting Nazca plate and the South American margin since at least late Cretaceous time (e.g., Pardo-Casas and Molnar, 1987; Somoza, 1998) as well as the absolute westward movement of South America (Silver et al., 1998) are likely related to temporal changes in upper plate shortening and the dip of the descending slab (e.g., Jordan et al., 1983; Sébrier and Soler, 1991; Mercier et al., 1992; Jaillard and Soler, 1996). In northern and central Peru, oblique subduction of the Nazca Ridge generated a pulse of uplift that has propagated southward down the coast but that has not yet affected southwest Peru (e.g., Machare and Ortlieb, 1992; Li and Clark, 1994; Hampel, 2002; Clift et al., 2003).

2.2. Arc volcanism and Heat Flow

Our study is focused on the Cotahuasi-Ocoña drainage in southwest Peru, which cuts through the active volcanic arc lining the western margin of the plateau, and drains ~150 km through the forearc region toward the coast (Fig. 1). Low heat flow measurements from coastal and forearc regions (30 to 60 mW/m^2) increase gradually to higher values (50 to 180 mW/m^2) on the plateau (Henry and Pollack, 1998; Hamza and Muñoz, 1996; Springer and Förster, 1998; Springer, 1999; Hamza et al., 2005). Localized high heat-flow anomalies are generally located within a c. 10 km radius of active volcanoes. As Springer (1999) noted, anomalies of up of 180 mW/m^2 within the volcanic arc region can be explained by shallow magma chambers at 4 to 6 km depth. However, the short-lived nature of such anomalies (generally decreasing to 10 mW/m^2 after 1 million years) imply that they cannot be resolved in long-term thermal field simulations. Even if effects of local arc volcanoes are limited, understanding the effect of spatial variation in geothermal gradients from the coast toward the arc on thermochronologic ages that traverse the forearc region is difficult without explicit modeling.

Subduction-related volcanism has had additional regional and local effects on the thermal history of the region. The early thermal history was likely dominated by cooling of the arc-related Coastal batholith that crops out through much of the western margin in Peru, and locally in the middle reaches of Cotahuasi-Ocoña canyon. Geological maps (INGEMMET, 2001) identify Cretaceous diorites, tonalities, and granodiorites in this region, and new $^{40}Ar/^{39}Ar$ step-heating experiments on

biotite samples from the canyon yielded ages of 137.5 ± 1.8 Ma and 135.7 ± 1.7 Ma (Table 2). Southeast of the canyon, near Arequipa, U/Pb zircon ages demonstrate a long-lived history of plutonism, with ages ranging from 61.0 to 188.4 Ma (Mukasa, 1986). These intrusive bodies that are today between the active arc and the coast give evidence for the inland migration of the active volcanic arc up until ca. 20 Ma when its present position was established (Stern, 2004).

Modern-day arc volcanoes in the region closest to the canyon include Corapuna, Sara Sara, and Solimana, which form a line roughly parallel to the coast at the northeast margin of the intrusive bodies. Volcanic units derived from these centers range in age from ca. 9 to < 1 Ma (Thouret et al., 2007), and cover a radius on the order of 15 to 20 km surrounding the volcanoes. The 14 to 16 Ma Huaylillas-age ignimbrites that blanket the region may have also derived from one or more of these centers. This oldest volcanic unit appears to have pre-dated significant canyon incision, as no place has it been found to outcrop at lower elevations within the canyons. Younger units did enter the canyon, including the 2-km-deep upper reaches of Cotahuasi canyon that were deeply-refilled with volcanic ash at ca. 1 to 2 Ma (Schildgen et al., 2007; Thouret et al., 2007), after the canyon had previously been incised to near its present depth by 3.75 Ma (Schildgen et al., 2007). In the middle and lower reaches of the canyon, however, where themochronologic samples for this study were collected, only a small number of volcanic flows entered from side-valley tributaries. Although these flows are only likely to have caused significant heating in close proximity to the flows, they still may have partially-reset ages on some samples. This highlights the importance of collecting samples far from any volcanic flows to discern robust patterns in cooling related to canyon incision, and of collecting a sufficient number such that any interpretations are not contingent upon a small number samples.

2.3. Regional climate

Extremely low precipitation over most of this region has important implications for bedrock exhumation histories. The Atacama Desert of northern Chile and southwestern Peru is one of the driest regions on earth, due to the combined effects of its position in the descending flow of the atmospheric Hadley cell circulation, the cold oceanic Peru (Humboldt) Current that leads to temperature inversions at the coast, and the orographic barrier created by the Andes that blocks moisture-bearing easterly winds (Abele, 1989). Precipitation in southwest Peru ranges from a hyperarid 2 to 10 mm/yr near the coast, up to a semi-arid 300 to 400 mm/yr in the upper catchments of major rivers (Houston and Hartley, 2003), which leads to very slow modern exhumation rates. Studies of soil development in northern Chile suggest this dry pattern has characterized the western margin since 13 to 19 Ma, and climate was more uniformly semi-arid prior to that time (Rech et al., 2006). In northern Chile, exhumation rates derived from cosmogenic studies were estimated to range from <0.001 mm/yr to

0.05 mm/yr in a transect from the coast to the plateau based on cosmogenic nuclide exposure studies (Kober et al., 2007). This long-term, slow exhumation contrasts dramatically with rapid incision that carved major canyons in the region, which slice down over 3 km below the surrounding surface in the deepest reaches of their path toward the Pacific Ocean. This strong contrast in background and localized erosion rates and the great depth of incision imply a strong potential for rates and timing of canyon cutting to be recorded in low-temperature thermochronology data, as will be described in greater detail below.

3. Thermochronologic data

3.1. Application of low-temperature thermochronology to landscape evolution studies

Both apatite and zircon (U-Th)/He ages are useful to help constrain the thermal and topographic evolution of the region. Because Earth's surface acts as an upper boundary layer to thermal diffusion in the crust, morphology of the surface affects the geometry of near-surface isotherms (e.g., Lees, 1910; Benfield, 1949; Turcotte and Schubert, 1982; Stüwe, 1994; Mancktelow and Grasemann, 1997; Braun, 2002, Ehlers and Farley, 2003). This effect is damped at depth, meaning that higher-temperature thermochronometers reflect cooling resulting only from background exhumation rates. Zircon (U-Th)/He ages are typically set at 7 to 9 km depth (Reiners et al., 2004), where surface effects on isotherm morphology are minimal. In contrast, the relatively shallow, 2 to 3 km depth of the apatite (U-Th)/He closure isotherm (Farley, 2000) is significantly affected by changes in surface topography. Ages can be affected by cooling not only related to background exhumation, and by local movement of isotherms in response to the changing surface. As Schildgen et al. (2007) described in greater detail, (U-Th)/He apatite thermochronologic samples collected from canyon depths exceeding 2 km (depth of the closure temperature isotherm prior to incision) reflect rapid cooling from incision-induced isotherm depression, showing young ages that are distinct from older samples high on canyon walls that were cooled slowly as a result of background exhumation rates (Fig. 2). The rapidly-cooled zone provides an important record of this change in surface morphology, with the age and thickness of the zone reflecting the timing and magnitude of the latest phase of canyon incision.

In this study, 26 new samples collected from 5 vertical transects (Fig. 1, Tables S1-S3) along with samples collected along a valley-bottom transect reported in Schildgen et al. (2007) are interpreted in the context of 3D thermal modeling.

3.2. Analytical methods

Samples were prepared by first crushing all material to less than 500 microns with a jaw crusher only to minimize the number of cracked apatite crystals. Apatite separates were derived through use of a water table, Frantz magnetic separator, and heavy liquid density separations using bromoform. Euhedral apatite crystals were inspected for inclusions under 150x magnification and under cross-polarized light. Inclusion-free grains that exceeded 60 microns in diameter were measured and loaded into platinum tubes as single-grain aliquots. Helium was extracted in an ASI Alphachron U/Th-He dating system by laser heating the samples within a vacuum chamber with a 980nm diode laser for 5 minutes at 9 Amps. The gas was spiked with ^{3}He and exposed to a SAES NP-10 getter for 2 minutes, after which the gas is expanded into a Pfeiffer – Balzers Prisma Quadrupole with a range of 0-100 amu, electron multiplier and a faraday detector. To analyze the $^{4}He/^{3}He$ composition of the gas, four masses were monitored during analysis: Mass 1 as a proxy for homogenous discharge (HD) contributions to the mass 3 peak (contribution is on average 0.03%, but in some cases has been as high as 0.13%.), Mass 3 for ^{3}He, Mass 4 for ^{4}He and Mass 5 for the background. A total of 20 sets of measurements are made in a period of less than 100 seconds. ^{4}He concentrations were calculated by comparing the sample $^{4}He/^{3}He$ to a set of standard analyses run prior to and after the sample analysis. These standard analyses were comprised of adding a known quantity of ^{4}He to the same ^{3}He spike that is used to spike the sample gas. The short-term (5-10 standard analyses) reproducibility is on the order of 0.03-0.05%, while the long-term (complete sample holder run) reproducibility is on the order of 0.05-0.08%. Currently the composition of the ^{4}He standard gas tank is known to 1.18%, which provides the largest contribution to the error in this part of the analytical process. Samples were then retrieved and put into 2 mL high purity polypropylene copolymer (PPCO) vials, into which a 25 microliter ^{235}U and ^{230} Th spike with a concentration of 15 ng/mL and 5 ng/mL respectively was added. The spiked mixtures were then ultrasonically agitated for 15 minutes then left for 4 hours to dissolve the apatite. The solution, diluted with 325 microliter of 18.2MegaOhm water, was analyzed on a Thermo X series quadrupole in the Keck Lab at ASU. Analyses were standardized by analyzing a spiked standard solution to which the same amount of spike was added. For age calculations, Ft corrections were calculated according to procedures outlined in Farley (2002).

3.3. Valley-bottom transect data

Very slow background exhumation rates in the region have preserved a low-relief surface that developed prior to the latest phase of uplift and incision. This surface now forms a gentle ramp from the coast to the volcanic arc, and serves as a common reference level from which depths of incision can be measured for samples collected over wide spatial areas. Schildgen et al. (2007) interpreted

$^{40}Ar/^{39}Ar$ ages of volcanic flows and apatite and zircon (U-Th)/He ages from a 75-km long valley-bottom transect to show at least 2.4 km of incision between ca. 9 and 2.3 Ma. This study differs from that of Schilgen et al. (2007) in that we use new data and a process-based model of sample cooling to improve the interpreted timing and magnitude of topographic development.

On an age versus depth plot of the apatite-He data (Fig. 3), the steep slope shown in the below 9 to 12 Ma reflects rapid cooling induced by canyon incision, while the shallow slope above 9 to 12 Ma reflects slow background denudation. The break in slope shows the onset time of rapid cooling. Schildgen et al. (2007) used the exposed thickness of the rapidly-cooled zone and 1-D thermal modeling of the inferred base of the zone to estimate the total thickness of the rapidly-cooled zone, which implied at least 2.4 km of post-9 Ma incision in the deepest reaches of the canyon.

The conclusions in that paper assumed that there were no substantial lateral variations in the thermal field of the study area. Our purpose here is to further evaluate the robustness of those conclusions in light of the strong lateral gradient in heat flow and possible effects associated with the valley incision process. Long-wavelength topographic effects on geothermal gradients such as compression near the base of a ramp are probably insignificant in this region, as predicted by analytical models for the nearly uniform 2.2° regional slope between the coastal escarpment and the edge of the plateau (Lachenbruch, 1969). Lateral variations in the incision rate, however, can affect the cooling rate of samples and interpretations of the slope on depth versus age plots of data. Incision rates are likely to be slower near the coast, where less than 1 km of incision has occurred, and faster inland, where more than 2.4 km of incision has occurred. With additional samples and three-dimensional thermal modeling, we explore possible implications for data interpretations below.

3.4. Vertical transect data

We collected a series of vertical transects from the middle reaches of Ocoña Canyon, focused around the region where the break in slope occurred in the valley-bottom transect data, at canyon depths of approximately 2 km (Fig. 1). The transect closest to the coast (VT1), which samples depths of 0.8 to 2.3 km, shows relatively old mean ages, ranging from ca. 10 to 55 Ma, and a gentle slope reflecting slow background denudation of approximately 0.025 mm/yr (Fig. 4). The middle transects, VT2 and VT3, sample similar depth ranges of 1.5 to 2.3 km and 1.6 to 2.3 km, and show similar ranges in mean ages from 8 to 20 Ma and 9 to 23 Ma, respectively. Samples from VT4, the transect farthest inland, show a range of ages between 8 and 14 Ma at depths of 2.0 to 2.7 km reflecting faster exhumation of approximately 0.1 mm/yr. In VT2 and VT3, a break in slope appears to occur at 11 to 13 Ma, but is not well-constrained due to limited sampling above the break (Fig. 4).

When compiled in a single plot, the vertical transect data reveal trends similar to that seen in the valley-bottom transect (Fig. 3). Shallow samples are generally old and show a low slope (ca. 0.025 mm/yr), reflecting slow background exhumation rates. Deeper than 2 km below the paleosurface, ages are younger and show better individual-crystal reproducibility, as expected in rapidly-cooled samples. They show a steep slope (ca. 0.18 mm/yr) reflecting fast cooling due to isotherm depression in response to canyon incision. Although the valley-bottom transect showed a sharp break in slope at ca. 9 Ma, vertical transect data show a disperse transition region between ca. 11 and 14 Ma. Apart from this, the main difference between the data sets is that the slope of the older suite of ages from the vertical transects is somewhat steeper and better defined than that of the valley-bottom transect. Such differences are unsurprising given that both transects can lead to biases in the slope of these data (e.g., valley-bottom transect data can be affected by lateral variations in the geothermal gradient as discussed, and vertical transects can be affected by changes in relief through time, e.g., Braun, 2002a).

An additional vertical transect not plotted in Fig. 3 was collected from a side-valley (VT0 in Fig. 1) and showed anomalously young ages compared to the trends shown in the other transects. We later discovered an ignimbrite perched 185 to 235 m above the side-valley floor dated at 2.01 ± 0.03 Ma (Table 2) that may have at least partially reset apatite (U-Th)/He ages in these samples. We also excluded two samples that we suspected may be too close to a volcanic flow farther up the main valley, and one samples we believe was from a landslide block (circled in Fig. 3).

4. Thermal Model of Thermochronometer Cooling Ages

4.1. General Description

We use the finite-element thermal model Pecube (Braun, 2003) to simulate sample cooling and exhumation in the study area (Fig. 1). The model solves the transient three-dimensional advection-diffusion equation with internal radiogenic heat production. We modified the program to account for lateral variations in basal temperature across the domain, and also to predict a wider range of thermochronometer cooling ages. The cooling history of rocks exposed at the surface today were tracked through time and used to predict apatite and zircon (U-Th)/He ages as a function of cooling history (Ehlers et al., 2005), radiation damage (Shuster et al., 2006), and grain size (Farley, 2000). We apply kinetics for helium diffusion in zircon from Reiners et al. (2004) and in apatite from Farley (2000).

4.2. Model Set-up and Parameters

Model set-up entails defining the three-dimensional domain size and resolution, material properties, background exhumation rate, and the style of landscape evolution. The range of model parameters used in this study is summarized in Table 3. Material properties such as heat production and diffusivity are spatially invariant and were not changed in different simulations. Surface temperature is controlled by a specified lapse rate, and temporally varies as topography evolves to different elevations. The temperature pattern at the base of the model domain is held constant. A modification for this work includes the option to increase the temperature linearly at the base of the model up to a maximum temperature, after which it remains constant in order to simulate the thermal field in the overriding plate above a subduction zone. The thermal field within the model domain is controlled by internal heat production, diffusion of heat from a fixed-temperature basal boundary, and advection of heat to the surface resulting from surface denudation. Primary model outputs include a three-dimensional transient temperature field, and predicted apatite and zircon (U-Th)/He cooling ages across the surface topography. Predicted and observed cooling ages were compared for each simulation to identify the range of exhumation histories that could have produced the observed cooling ages.

The simulated region in this work is centered on the middle and lower reaches of Cotahuasi-Ocoña canyon, with dimensions of 215 x 100 km across the surface and 60 km thick (Fig. 5A). This is large enough to prevent boundary effects from biasing heat flow and predicted ages. Based on two-dimensional thermal modeling by Springer (1999) in northern Chile (Fig. 5B), we estimate that basal temperatures at ca. 60 km depth near the coast should be approximately 200°C and increase to a maximum temperature of 1400°C beneath the volcanic arc. For our model simulations, we explored setting basal temperature to be between 100 and 300°C at the edge of the model near the coast (referred to as the T_0 value) and imposed a linear temperature increase between 7 and 11.6°C/km, which placed 1400°C temperatures between ~170 and 100 km from the southern edge of the model domain for a 200°C initial temperature. This range roughly defines the position of volcanic forearc in southwest Peru, which gives an approximate indication of where the tip of the aesthenospheric wedge (and highest temperature) should lie. Farther inland, basal temperature remained at a constant value of 1400°C. In general, our linearly-increasing temperatures are not an ideal match to the apparent non-linear increase modeled by Springer (1999), but did allow us to generate a pattern of increased crustal temperatures between the trench and the arc. Simulated lapse rate was 6.5°C/km with average sea level temperature set to 25°C (Klein et al., 1999). Other material properties and thermal parameters that remained constant are summarized in Table 3.

4.3. Exhumation and Topographic Evolution

Within Pecube, surface topography is defined by digital elevation models (DEMs), and landscape evolution is simulated by morphing from one DEM to another. Two main categories of topographic scenarios that we explored included steady-state topography and canyon incision. For steady-state simulations, the canyon and present day topography existed prior to and throughout the simulation (Fig. 6d). These simulations explored the simplest case of steady-state topography and a spatially and temporally constant exhumation rate. The canyon incision simulations comprised a series of simulations that varied the timing and magnitude of incision into a smooth surface that ramps from the coast up to the plateau. Topography was morphed from the spline DEM (discussed below) (Fig. 6a) to intermediate-relief topography (e.g., Figs. 6b and 6c) and then to the final, high-relief modern topography (Fig. 6d). The timing and rate of incision between individual steps shown in Fig. 6 was treated as free parameters.

The 250-m resolution DEMs used in the simulations were resampled from 30-m resolution DEMs created from Advanced Spaceborne Thermal Emission and Reflection Radiometer (ASTER) imagery (Fig. 6d). Initial topography prior to canyon incision (Fig. 6a) was generated by selecting points on the preserved paleo-surface on canyon interfluves and using a spline interpolation to smooth out canyon relief, but still retain the general morphology of ramping from the coast up toward the plateau (described in greater detail in Schildgen et al., 2007). We refer to this as the "spline DEM." In order to explore the effect of different paleo-canyon depths on predicted thermochronometer age patterns, we created a series of DEMs (e.g., Figs. 6b and 6c) that maintained unchanging elevations for canyon interfluves, but approximated the canyon morphology for earlier stages in the incision history. These DEMs were generated by first multiplying all values in the modern-day DEM by a small fraction (for instance, 0.2), which reduced both total relief and absolute elevation of all points. This layer was then added to a complementary fraction of the spline DEM (for instance, 0.8) in order to create a DEM that maintained the absolute elevation of points on the canyon interfluves while reducing canyon relief. These intermediate layers allowed us to test the effect of differing canyon depths prior to the latest phase of incision.

A uniform background denudation rate was superimposed on the spatially varying exhumation rates that resulted from changing surface morphology. Through these two mechanisms, the model simulates advection of rock toward the surface and changes in surface morphology. For most simulations we investigated background denudation rates between 0.01 and 0.07 mm/yr. This was based on thermochronology data presented in Schildgen et al. (2007) that implied background exhumation rates of 0.015 to 0.02 mm/yr in the southern Peru forearc region from ca. 60 to 10 Ma, as well as cosmogenic data from northern Chile that implied erosion rates of <0.001 to 0.05 mm/yr (Kober et al., 2007).

4.4. Evaluation of Model Results

We conducted 275 simulations to explore a range of incision histories and other model free parameters. Each simulation was compared to several metrics to evaluate if the model produced an acceptable fit to geologic observations. These metrics included (1) a comparison between the range of predicted and observed heat flow, and (2) minimization of the Chi-squared misfit between predicted and observed apatite and zircon (U-Th)/He ages.

Regional heat flow determinations (Henry and Pollack, 1998; Hamza and Muñoz, 1996; Springer and Förster, 1998; Hamza et al., 2005) provided general guidance on the range of reasonable geothermal gradients in the region as well as on the magnitude of lateral changes from near the coast toward the volcanic arc. We also used results of thermal field modeling by Springer (1999) across the subduction zone in northern Chile to verify the general form of lateral thermal field variations. These show that crustal temperatures at ca. 60-km depths increase rapidly from ca. 200°C to 1400°C from the trench to the arc.

To more quantitatively evaluate the quality of fit between our observed thermochronometer ages and model predicted ages and to determine best-fit scenarios, we used a reduced chi-squared goodness-of-fit test. This is a sum of the squared differences between observed thermochronologic ages and expected model ages divided by the variance (Eg. 1).

(1)
$$\sum_{i=1}^{n} \frac{(\mathrm{obs}_i - \mathrm{exp}_i)^2}{\sigma_i^2}$$

For each sample, the standard deviation (σ) was calculated from the range of individual crystal ages. For samples that consisted of only one or two analyzed crystals, we assumed that the standard deviation was equal to 15% of the mean age, as this was the average value for all samples. We compared the chi-squared sum to a critical value that is associated with a 95% confidence level. This is determined by comparison with a chi-squared distribution, typically recorded in tables such as in Pearson and Hartley (1966). The critical value is a function of the number of samples to which model results are compared, as well as the number of free parameters in the model. We consider free parameters to be all the variables that were allowed to change for the different simulations. These include initial basal temperature at the southern edge of the model, lateral basal temperature gradient, maximum temperature, background exhumation rate, onset of canyon incision, and end of canyon incision. If the chi-squared sum is below the critical value, then the model predictions give a good match to the observed ages at the given confidence level. This is probably a reasonable statistic to

assess low-temperature thermochronometry data, where ages generally show poorer reproducibility with increasing age, but the magnitude of error on any particular mean age is difficult to assess (see discussion in Ehlers, 2005). Chi-squared values that fall below the critical value associated with a 95% confidence interval result in model predictions that are predominantly within error of sample mean ages. Lower chi-squared values resulted in even better fits to the mean ages of samples.

5. Model results

In the following sections we describe model simulation results that explored a wide range of parameter space to find both best-fit scenarios and to discern the sensitivity of predicted ages to different exhumation histories. We discuss the quality of fit between model predictions and both apatite and zircon data for simulations that explored background denudation rates and different spatial gradients in basal temperature. However, for simulations that specifically explored details of the canyon incision process, we only discuss the quality of fit for apatite data. This is because the zircon data are unaffected by canyon incision, and hence predicted zircon ages showed no variation in the model runs that only explored details of canyon evolution. Also, for simulations that specifically explore the timing of canyon incision, which has a strong effect only on the youngest set of apatite samples, we compared model results to both the full set of samples as well as a subset of younger samples.

5.1. Steady-state topography

Steady-state topographic simulations started and finished with the modern-day topography DEM. We ran several simulations with a basal temperature varying from 200°C at the southern edge of the model and increasing at a rate of 11.6°C/km toward the arc. The range of denudation rates explored was 0.01 to 0.5 mm/yr. Denudation rates were assumed to be constant over then entire simulation duration of 225 Ma. All other parameters such as material properties are present in Table 3.

Model results indicate that the range in ages predicted for a constant exhumation rate is relatively small, though it increases with slower rates. For example, an exhumation rate of 0.20 mm/yr matches apatite ages from ca. 7 to 9 Ma, a 0.07 mm/yr rate matches a range from ca. 20 to 25 Ma, and a 0.03 mm/yr rate matches ages from ca. 55 to 60 Ma (Fig. 7A). The complete range of observed ages is not produced with any of the constant exhumation rate models. Because of this, results show that a single exhumation rate can match only small ranges of the apatite (U-Th)/He data. Large increases in the lateral basal temperature gradient could help produce a wider spread of ages, but would create lateral variations in heat flow values that exceed modern observations. Model simulations produce better matches to zircon (U-Th)/He data. An exhumation rate of 0.05 mm/yr shows good fits between

predicted and observed ages that are less than 100 Ma, but a slower exhumation rate is needed to match older samples (Fig. 7B).

5.2. Canyon incision

To explore the effect of incision timing and magnitude on predicted ages, we started simulations with the spline DEM (Fig. 6a) and investigated the influence of canyon incision onset between 8 and 12 Ma, incision completion between 2 and 6 Ma, and variations in early canyon maximum depths ranging from 0 to 1120 m, corresponding to 0 to 35% of the modern canyon relief. The following sections describe these topographic scenarios in greater detail and the additional parameters that affect model results.

5.2.1. Background exhumation and basal temperature

We explored the relationship between lateral basal temperature gradient and background exhumation rates to determine a reasonable range of values for these parameters through 40 model simulations. All other parameters were held constant and values used are in Table 3. For the following simulations, we set the initial topography to be the spline DEM (Fig. 6a), set background exhumation rate to be constant over the 225 million year duration of the run, and morphed topography from the spline DEM to the modern-day topography (i.e., incised the canyon) between 11 and 2 Ma.

Model results show that background denudation rate has a strong effect on predicted apatite (U-Th)/He ages. When lateral basal temperature gradient is set to 9.9°C/km and T_0 is 200°C, denudation rates of 0.02 mm/yr produce best fits to the data (Figs. 8A and 8B). Chi-squared misfit values calculated for expected and observed apatite ages over a range of lateral basal temperature gradients and denudation rates are shown in a contour plot in Figure 8C. These illustrate that increasing lateral basal temperature gradients require lower exhumation rates to derive best matches to the data. Denudation rates between 0.024 and 0.015 mm/yr produce best fits for the illustrated range of lateral basal temperature gradients. These simulations produced a range of surface heat flows from near the coast to just south of the volcanic arc of 40 to 50 mW/m^2 for a lateral basal temperature gradient of 7.0°C/km and 40 to 60 mW/m^2 for a gradient of 11.6°C/km. Both are reasonable considering the range of modern-day measurements of ca. 30 to 60 mW/m^2 within the forearc region.

The observed zircon (U-Th)/He data is not well-predicted by uniform background denudation rates (Figs. 8C-E). On both age versus depth (Fig. 8D) and distance from coast versus age (Fig. 8E) plots where the lateral basal temperature gradient is 9.9°C/km, denudation rates of 0.03 mm/yr show a good match to zircon ages less than 120 Ma or closer than 45 km to the coast. Observed ages greater than 120 Ma and farther inland are better matched by a 0.04 mm/yr denudation rate. Simulated heat

flow values of 60 to 80 mW/m^2 across the forearc region resulting from these simulations are higher than modern values. Chi-squared values exceed the critical value of 12.6 (12 samples with 6 free parameters in the model) over all parameter space, suggesting that a uniform background denudation rate is not appropriate for explaining the zircon data. Instead, spatial and/or temporal variations are likely. Alternatively, the data may reflect changing thermal conditions in the crust, possibly related to plutonism.

5.2.2. Incision timing

Although onset of the latest phase of incision should be close to the observed break in slope in the apatite data, imprecision in the data and rounding of the break between older and younger ages due to effects of the helium partial retention zone and lag in thermal response to onset of incision make identification of an onset time difficult. Estimating the timing of incision completion is even more difficult because the base of the rapidly-cooled zone is not exposed, and hence must be inferred from modeling or from other geological constraints. Schildgen et al. (2007) estimated incision completion to be no later than ca. 2.3 Ma, based on the age of a volcanic flow perched within 100 m of the present valley floor. A more precise estimate is no later than 2.21 ± 0.02 Ma, based on a new $^{40}Ar/^{39}Ar$ age of a volcanic flow collected from the present valley floor (Table 2). Onset times of incision that we tested in our simulations ranged from 8 to 12 Ma, and completion times ranged from 2 to 6 Ma. There was no change in topography after the completion time, but background exhumation continued to 0 Ma. In the simulations presented, we show best estimates for incision onset and completion time assuming a range of different T_0 (southern basal edge of model) and lateral basal temperature gradient combinations. For any given combination, the suite of chi-squared values produced from different onset and completion times are sensitive to changes in exhumation rate on the order of 0.0005 mm/yr, often with only one erosion rate producing results that fall below the critical value. Thus, we first identified the exhumation rate that produces minimum chi-squared values, and show how best fits for incision timing are affected with the different combinations. All other parameters were held constant (see Table 3).

Results from 125 simulations illustrate the effects of changing T_0 as well as the effects of changing the lateral basal temperature gradient. In general, minimum chi-squared values cover a shorter range of onset times than completion times, meaning that the former can be determined with greater precision. We discuss results from analyzing the whole sample set as well as a subset of samples that are < 16 Ma. Because there are 27 total samples and 6 free parameters, the critical value associated with a 95% confidence interval when comparing all model results is 32.7. The subset of younger samples consists of 14 samples, and an associated critical value of 15.5.

In the analysis of all samples, with T_0 set to 300°C, increasing temperature gradients from 9.3 to 11.6 generally produces better fits (Fig. 9A-C). Similarly, with the temperature gradient set to 11.6°C/km, increasing T_0 from 100 to 300°C produces a wider region of best fits (Fig. 9C-E). In all plots, chi-squared sums that are below the critical value of 32.7 fall within the range of ca. 8 to 11.5 Ma, and minimum values fall within the range of ca. 9 to 10.5 Ma. Minimum values occur at completion times covering the whole tested range from 2 to 6 Ma, with earlier completion times associated with later onset times. Differences in the quality of fit are also illustrated on an age-depth plot for three simulations (Fig. 10).

Using the same set of exhumation rates and basal temperature patterns, we analyzed a subset of the younger samples to determine if onset and completion times could be determined with higher precision (Fig. 11). However, the range of parameter space explored in all the plots illustrates that chi-squared sums fall below the critical value for the most of the tested range of onset and completion times. Despite the young ages being most significantly affected by changes in the timing of canyon incision, the inclusion of older samples that may reflect characteristics of the partial retention zone allows for the best estimates of incision timing.

5.2.3. Incision magnitude

Simulations to test the effects of different early canyon depths proceeded from the spline DEM to an intermediate layer, and then from the intermediate layer to the modern topography starting at 11 Ma. The spline layer itself contributes relief of approximately 200 m in the deepest reaches of the canyon. We tested two different start times for the generation of higher magnitudes of early canyon incision: 50 to 30 Ma, the estimated time of Lower Moquegua Formation red bed deposition in southern Peru, and 30 Ma to 14 Ma, the time of Upper Moquegua sand/conglomerate deposition (Sempere et al., 2004; Roperch et al., 2004). The former may represent the development of some initial inland topography in the region, while the latter may represent first generation of significant topography. Early canyon relief tested included 10%, 20%, 25%, 30%, and 35% of the modern canyon relief, which corresponds to approximately 320, 640, 800, 960, and 1120 m depths in the deepest reaches of the canyon. Background exhumation rates were set at 0.02 mm/yr, T_0 was set to 200°C, and the range of early canyon depths was tested against a range of lateral basal temperature gradients from 7 to 11.6°C/km.

Model results show significant effects of early canyon relief on predicted ages. For incision occurring from either 50 to 30 Ma or from 30 to 14 Ma, model results are generally much worse than those predicted with no early incision, all far exceeding the critical value, with any significant early relief resulting in over-prediction of sample ages (Fig. 11).

6. Discussion

6.1. Temporal and spatial patterns in background exhumation rates

Understanding temporal and spatial patterns in background exhumation rates is difficult in this region where both are likely to vary. For the steady-state topography simulations, one possible way to match predicted and observed apatite ages is to impose an increasing exhumation rate through time. However, this is an unlikely scenario. First, the required increase in exhumation rates of ca. 0.03 mm/yr to 0.20 mm/yr would demand a change the surface morphology (for example, the sharp edges between canyon walls and the plateau surface are unlikely to be maintained under increasing regional exhumation rates), which would violate the steady-state topographic assumption for the simulation. Additionally, the climate history of the region suggests that exhumation rates are likely to have been slower, not faster, since semi-arid coastal conditions became hyper-arid starting at 19 to 13 Ma (Rech et al., 2006). Finally, geologic relationships indicate little to no canyon incision south of x km from the coast at ~14Ma and that the canyons had been fully cut by 2.2 Ma. The steep gradient in apatite ages is therefore best interpreted as localized cooling resulting from canyon incision.

The role of background exhumation rates is still unclear for canyon incision scenarios. Both apatite and zircon samples near the coast show old ages with low slopes on depth-age plots (e.g. Fig. 3). This shows that coastal regions have experienced low background exhumation throughout the time span recorded by both thermochronometers: ca. 75 to 14 Ma for apatite, and ca. 175 to 75 Ma for zircon. However, younger zircon samples collected from farther inland reflect faster exhumation rates (i.e., steeper slopes) from ca. 75 to 40 Ma on an age-depth plot. These apparent faster exhumation rates can be explained by several alternatives. They may reflect an earlier history of tectonic activity with accompanying faster exhumation in the interior region from 75 to 40 Ma. Alternatively, they may reflect the early establishment of the spatial gradients in precipitation and exhumation that we see today, where higher inland regions experience faster denudation than hyper-arid coastal regions. Finally, they may simply reflect faster cooling that could have been experienced with an identical background exhumation rate but with perturbations to the thermal field, as would be expected from the cooling of Cretaceous age intrusive bodies. Additional data is needed to test which of these possibilities is most likely. For example, vertical transects collected throughout the valley length could discriminate between temporal and spatial changes in the cooling history of zircons.

6.2. Incision history and uplift

Estimating the magnitude of canyon depths prior to the latest phase of incision is one of the biggest challenges in using incision history to learn about past uplift. Early canyon depths give

important information on the likely initial position of near-surface isotherms prior to the latest phase of incision. Such information is critical for assessing the magnitude of the latest phase of incision, but early canyon depths are difficult to determine without clear geologic constraints. In many cases, strath terraces that may record the earliest phases of incision are highly degraded or non-existent. In southwest Peru, depositional records suggest that the major drainages are likely to have experienced a long history of incision that started well before the latest phase of late Cenozoic incision. Cut-and-fill channels up to several hundred meters deep within the ~30 to 14 Ma Upper Moquegua conglomerates (Sempere et al., 2007; Roperch et al., 2006; Thouret et al., 2007) are exposed in smaller drainages such as the Sihuas valley. This points to the early development of a drainage system prior to 14 Ma with depths of at least several hundred meters based on the thickness of exposed cut-and-fill conglomerate packages.

Our model simulations that explored the canyon depths prior to the latest phase of incision produced minimum chi-squared values when the spline topography was used as a starting topography, which consists of approximately 200 m of relief in the deepest reaches. Early incision that exceeded these depths produced fits that far exceeded chi-squared critical values. This interpretation of minimal early canyon relief is supported by the broad, thick Upper Moquegua sand/conglomerate sheets that cover the forearc region from near to coast to elevations as high as 2000 m exposed in the cliffs above the town of Iquipi. Such deposition would not be possible if there were a significant canyon in the region from ca. 30 to 14 Ma, the age range of those sediments. However, in other parts of the forearc, cut-and-fill channels at least 200 m deep in the Upper Moquegua sediments suggests that some relief may have characterized the forearc region at the time. Based on the overall broad distribution of the sediments as well as our model results, we believe early canyons probably did not significantly exceed this depth, though farther inland early canyons may have been deeper. Surface topography that hosted such channels must have reached elevations at least as high, and could feasibly have been in the range of 500 to 1000 m. Because the total depth of the canyon today is ca. 3.2 km at the northern end of our sampled region (in the deepest reaches of the canyon), and early canyon depths were likely not more than ca. 200 m deep, the latest phase of incision was up to 3.0 km in magnitude, decreasing to $\leq$ 1 km at the coast.

6.3. Landscape evolution

One of the main limitations to our topographic simulations is that we use prescribed DEMs to model changes in topography rather than applying exhumation rules that could more accurately portray changes in landscape morphology through time. Propagation of knickpoints through a drainage system could produce incision onset times that differ by several million years between the

outlet and the uppermost catchment. In Cotahuasi-Ocoña canyon, we suspect the propagation time of a knickpoint through the sampled region is likely to be less than one million years (see discussion in Schildgen et al., 2007). However, because onset time has a strong effect on age predictions for the youngest apatite samples, even a one million year difference in onset time can be important.

7. Conclusions

Three-dimensional thermal modeling is a powerful tool for gaining insight into interpretations of thermochronologic data in settings characterized by a spatially variable thermal field, or where major changes in the surface morphology can lead to transient adjustments in the near-surface thermal field. Although our estimates can be further refined with a better understanding of background exhumation rates through space and time, and more accurate representation of topographic evolution, our new interpretations of apatite and zircon (U-Th)/He data from southwest Peru are a significant improvement to earlier estimates of the timing and magnitude of canyon incision.

Results presented here provide new insights into evolution of the western margin of the Altiplano in the context of a major phase of late Cenozoic uplift that has been documented across the Altiplano interior and along the eastern margin in the fold-and-thrust belt known as the Eastern Cordillera. Canyon incision with a magnitude up to 3.0 km starting at 8 to 11.5 Ma requires contemporaneous or preceding surface uplift with at least an equal magnitude. The lag time between the start of uplift and the start of incision may be on the order of one million years for a detachment-limited system, but at large drainage areas in the trunk stream of major rivers, the lag time can be much shorter (e.g., Whipple and Tucker, 2002). The end time of uplift is not well-constrained by association with rapid cooling, as incision can potentially continue long after uplift ends. Our model simulations are also, unfortunately, not very sensitive to the end of incision. Nonetheless, we believe the phase of uplift documented to have started at ca. 10 to 11 Ma in the Altiplano interior and at the eastern margin (evidence summarized in Table 1) is likely to be correlative with uplift that generated the major pulse of incision in Cotahuasi-Ocoña canyon. Such a significant contemporaneous uplift experienced over a 350-km wide orogen is likely to result from a geodynamic process or processes that can affect the whole of an orogenic plateau, rather than isolated regions. The role of upper crustal shortening and thickening is thus less likely to have contributed to this latest phase of uplift, because such deformation is often focused on particular parts of the plateau. Processes occurring deeper within the crust or lithosphere such as lithospheric delamination or regional ductile redistribution of mass through mid- to lower-crustal flow are more likely to affect large regions, and hence are more feasible explanations for the latest phase of plateau uplift.

Acknowledgments

We thank Tyson Smith, Katrina Cornell, and Julie Bradley for help with fieldwork; Will Ouimet, Joel Johnson, and Kristen Cook for discussions. This work was supported by the National Science Foundation Tectonics Division grant no. EAR-0409359.

References

Abele, G., 1989, the influence of age, climate, and relief on the preservation of volcanic landforms in the North Chilean Andes: Bamberger Geographische Schriften, v. 11, p. 45-57.

Arndt, J., Bartel, T., Scheuber, E., and Schilling, F., 1997, Thermal and rheological properties of granodioritic rocks from the Central Andes, North Chile: Tectonophysics, v. 271, p. 75-88.

Barke, R., and Lamb, S., 2006, Late Cenozoic uplift of the Eastern Cordillera, Bolivian Andes: Earth and Planetary Science Letters, v. 249, no. 3-4, p. 350-367.

Benfield, A.E., 1949, The effect of uplift and denudation on underground temperatures: Journal of Applied Physics, v. 20, p. 66-70.

Berry, E.W., 1939, The fossil flora of Potosi, Bolivia: John Hopkins University Studies in Geology, v. 13, p. 1-67.

Braun, J., 2002a, Quantifying the effect of recent relief changes on age-elevation relationships: Earth and Planetary Science Letters, v. 200, p. 331-343.

-, 2002b, Estimating exhumation rate and relief evolution by spectral analysis of age-elevation datasets: Terra Nova, v. 14, p. 210-214.

-, 2003, Pecube: a new finite-element code to solve the 3D heat transport equation including the effects of a time-varying, finite amplitude surface topography: Computers and Geosciences, v. 29, p. 787-794.

Braun, J., and Robert, X., 2005, Quantitative constraints on the rate of landform evolution derived from low-temperature thermochrohonology: Reviews in Mineralogy and Geochemistry, v. 58, no. 351-374.

Čermák, V., and Rybach, L., 1982, Thermal properties, in Hellwege, K.-H., ed., Landolt-Bornstein numerical data and functional relationships in science and technology: New Series, Group V. Geophysics and Space Research, v.1 Physical Properties of Rocks, Subvolume A: Berlin, Springer-Verlag, p. 305-371.

Clark, M.K., House, M.A., Royden, L.H., Whipple, K.X, Burchfiel, B.C., Zhang, X., and Tang, W., 2005, Late Cenozoic uplift of southeastern Tibet: Geology, v. 33, no. 6, p. 525-528.

Clift, P. D., Pecher, I., Kukowski, N., and Hampel, A., 2003, Tectonic erosion of the Peruvian forearc, Lima Basin, by subduction and Nazca Ridge collision: Tectonics, v. 22, no. 3.

Dortman, N.B., 1976, Fizicheskiye Svoystva Gornykh Porod i Poleznykh Iskopaemykh (Physical properties of rocks and minerals): Moscow, Nedra, 527 p.

Ehlers, T. A., and Farley, K.A., 2003, Apatite (U-Th)/He thermochronometry: methods and applications to problems in tectonics and surface processes: Earth and Planetary Science Letters - Frontiers, v. 206, p. 1-14.

Ehlers, T.A., 2005, Crustal thermal processes and the interpretation of thermochronometer data: Reviews in Mineralogy and Geochemistry, v. 58, p. 315-350.

Ehlers, T. A., Farley, K.A., Rusmore, M.E., and Woodsworth, G.J., 2006, Apatite (U-Th)/He signal of large magnitude and accelerated glacial erosion: southwest British Columbia: Geology, v. 34, p. 765-768.

Farley, K.A., 2000, Helium diffusion from apatite: general behavior as illustrated by Durango fluorapatite: Journal of Geophysical Research-Solid Earth, v. 105, no. B2, p. 2903-2914.

Farley, K.A., 2002, (U-Th)/He dating: Techniques, calibrations, and applications: Noble gases in

geochemistry and cosmochemistry, Reviews in Mineralogy and Geochemistry, v. 47, p. 819-844.

Garzione, C.N., and Hoke, G.D., 2006, Paleoelevation and geomorphic constraints on the late Miocene rise of the Andes: geodynamic implications for the growth of orogenic plateaus: Proceedings, Goldschmidt Conference Abstracts 2006, p. A195.

Garzione, C.N., Molnar, P., Libarkin, J.C., and MacFadden, B.J., 2006, Rapid late Miocene rise of the Bolivian Altiplano: Evidence for removal of mantle lithosphere: Earth and Planetary Science Letters, v. 241, no. 3-4, p. 543-556.

Ghosh, P., Garzione, C.N., and Eiler, J.M., 2006, Rapid uplift of the Altiplano revealed through C-13-O-18 bonds in paleosol carbonates: Science, v. 311, no. 5760, p. 511-515.

Graham, A., Gregory-Wodzicki, K.M., and Wright, K.L., 2001, Studies in neotropical paleobotany. XV. A Mio-Pliocene palynoflora from the Eastern Cordillera, Bolivia: implications for the uplift history of the central Andes: American Journal of Botany, v. 146, no. 3, p. 813-826.

Gregory-Wodzicki, K.M., 2000, Uplift history of the Central and Northern Andes: A review: Geological Society of America Bulletin, v. 112, no. 7, p. 1091-1105.

Gubbels, T. L., Isacks, B. L., and Farrar, E., 1993, High-level surfaces, plateau uplift, and foreland development, Bolivian Central Andes: Geology, v. 21, no. 8, p. 695-698.

Haenel, R., Rybach, L., and Stegena, L., 1988, Handbook of terrestrial heat-flow density determination; with guidelines and recommendations of the international heat flow commission, Kluwer-Acad., Dordrecht.

Hampel, A., 2002, The migration history of the Nazca Ridge along the Peruvian active margin: a re-evaluation: Earth and Planetary Science Letters, v. 203, no. 2, p. 665-679.

Hamza, V.M., Dias, F.J.S.S., Gomes, A.J.L., and Terceros, Z.G.D., 2005, Numerical and functional representations of regional heat flow in South America: Physics of the Earth and Planetary Interiors, v. 152, no. 4, p. 223-256.

Hamza, V.M., and Munoz, M., 1996, Heat flow map of South America: Geothermics, v. 25, no. 6, p. 599-646.

Henry, S. G., 1981, Terrestrial heat flow overlying the Andean subduction zone: Ph. D. Thesis, University of Michigan, Ann Arbor, Michigan.

Henry, S.G., and Pollack, H.N., 1988, Terrestrial Heat-Flow above the Andean Subduction Zone in Bolivia and Peru: Journal of Geophysical Research-Solid Earth and Planets, v. 93, no. B12, p. 15153-15162.

Herman, F., Braun, J., and Dunlap, W. J., 2007, Tectonomorphic scenarios in the Southern Alps of New Zealand: Journal of Geophysical Research-Solid Earth, v. 112, no. B4.

Hoke, G.D., and Garzione, C.N., 2006, Late Miocene plateau-wide surface uplift in the Central Andes: an integration of stable isotope paleoaltimetry and geomorphology, in Backbone of the Americas Conference, Mendoza, Argentina.

Hoke, G.D., Isacks, B.L., Jordan, T.E., Blanco, N., Tomlinson, A.J., and Ramezani, J., 2007, Geomorphic evidence for post-10 Ma uplift of the western flank of the central Andes 18°30'-22°S: Tectonics, v. 26, TC5021, doi:10.1029/2006TC002082.

House, M.A., Wernicke, B.P., and Farley, K.A., 1998, Dating topographic uplift of the Sierra Nevada, CA, using apatite (U-Th)/He ages: Nature, v. 396, p. 66-69.

-, 2001, Paleo-geomorphology of the Sierra Nevada, California, from (U-Th)/He ages in apatite: American Journal of Science, v. 301, p. 77-102.

Houston, J., and Hartley, A.J., 2003, The central andean west-slope rainshadow and its potential contribution to the origin of hyper-aridity in the Atacama desert: International Journal of Climatology, v. 23, no. 12, p. 1453-1464.

INGEMMET, 2001, Mapa Geológico del cuadrángulo de Caravelí, Scale 1:100,000, Instituto Geológico Minero y Metalúrgico.

Jaillard, E., and Soler, P., 1996, Cretaceous to early Paleogene tectonic evolution of the northern Central Andes (0-18°S) and its relations to geodynamics: Tectonophysics, v. 259, p. 41-53.

Jordan, T. E., Isacks, B. L., Allmendinger, R. W., Brewer, J. A., Ramos, V. A., and Ando, C. J., 1983, Andean Tectonics Related to Geometry of Subducted Nazca Plate: Geological Society of America Bulletin, v. 94, no. 3, p. 341-361.

Jordan, T.E., Mpodozis, C., Blanco, N., Hoke, G.D., and Nestor, P.L., 2006, Surface uplift of the western slope of the Puna segment of the Central Andean Plateau, in Backbone of the Americas Conference, Mendoza, Argentina.

Kappelmeyer, O., and Haenel, R., 1974, Geothermics with special reference to applications: Berlin, Gebrüder Borntraeger, 238 p.

Kennan, L., Lamb, S., and Hoke, L., 1997, High altitude palaeosurfaces in the Bolivian Andes: Evidence for Late Cenozoic surface uplift, in Widdowson, M., ed., Paleosurfaces: Recognition, Reconstruction and Paleoenvironmental Interpretation: Geological Society Special Publication, Geological Society of London, p. 307–324.

Klein, A.G., Seltzer, G.O., and Isacks, B.L., 1999, Modern and last local glacial maximum snowlines in the Central Andes of Peru, Bolivia and northern Chile: Quaternary Science Reviews, v. 18, p. 63-84.

Kober, F., Ivy-Ochs, S., Schlunegger, F., Baur, H., Kubik, P.W., and Wieler, R., 2007, Denudation rates and a topography-driven rainfall threshold in northern Chile: Multiple cosmogenic nuclide data and sediment yield budgets: Geomorphology, v. 83, p. 97-120.

Lachenbruch, A.H., 1969, The effect of two-dimensional topography on superficial thermal gradients: U.S. Geological Survey Bulletin 1203-E, United States Government Printing Office, Washington, 85 p.

Lees, C.H., 1910, On the shape of the isogeotherms under mountain range in radio-active districts: Proceedings of the Royal Society of London, A, v. 83, p. 339-346.

Li, C., and Clark, A. L., 1994, Tectonic Effects of the Subducting Nazca Ridge on the Southern Peru Continental-Margin: Marine and Petroleum Geology, v. 11, no. 5, p. 575-586.

Machare, J., and Ortlieb, L., 1992, Plioquaternary Vertical Motions and the Subduction of the Nazca Ridge, Central Coast of Peru: Tectonophysics, v. 205, no. 1-3, p. 97-108.

Mancktelow, N.S., and Grasemann, B., 1997, Time-dependent effects of heat advection and topography on cooling histories during erosion: Tectonophysics, v. 270, p. 167-195.

Mel'nikova, N.V., Rzhevskogo, V.V., and Protod'yakonova, M.M., 1975, Spravochnik (Kadastr) Fisicheskikh Svoystv Gornykh Porod (Handbook [Registry] of Physical Properties of Rocks): Moscow, Nedra, 279 p.

Mercier, J. L., Sebrier, M., Lavenu, A., Cabrera, J., Bellier, O., Dumont, J. F., and Machare, J., 1992, Changes in the Tectonic Regime above a Subduction Zone of Andean Type - the Andes of Peru and Bolivia during the Pliocene-Pleistocene: Journal of Geophysical Research-Solid Earth, v. 97, no. B8, p. 11945-11982.

Moiseenko, U.I., Sokolova, L.S., and Istomin, V.E., 1970, Elektricheskie I Teplovye Svoystva Gornykh Porod v Usloviyakh Normal'nykh I Vysokikh Temperatur I Davleniy (Electrical and Thermal Properties of Rocks under Normal and High Temperatures and Pressures): Novosibirsk, Sibirskoe Otdelenie, Nauka, 66 p.

Mukasa, S.B., 1986, Zircon U-Pb ages of super-units in the Coastal batholith, Peru: implications for magmatic and tectonic processes: Geological Society of America Bulletin, v. 97, no. 2, p. 241-254.

Nestor, P.L., Jordan, T.E., Blanco, N., Hoke, G.D., and Tomlinson, A.J., 2006, Evidence for late Miocene uplift by long-wavelength rotation of western flank of Altiplano segment of Central Andes 20°30' – 20°30'S, Chile, in Backbone of the Americas Conference, Mendoza, Argentina.

Ouimet, W., 2007, Dissecting the Eastern Margin of the Tibetan Plateau: A Study of Landslides, Erosion and River Incision in a Transient Landscape: Massachusetts Institute of Technology, Ph.D. Thesis, 197 p.

Pardo-Casas, F., and Molnar, P., 1987, Relative motion of the Nazca (Farallon) and South American plates since late Cretaceous time: Tectonics, v. 6, no. 3, p. 233-248.

Pearson, E.S., and Hartley, H. O., 1966, The Biometrika tables for statisticians: Biometrika, v. 1, 3rd edition,

Pollack, H.N., 1982, The heat flow from the continents: Annual Review of Earth and Planetary Sciences, v. 10, p. 459-481.

Quade, J., Garzione, C., and Eiler, J., 2007, Paleoelevation reconstruction using pedogenic carbonates: Reviews in Mineralogy and Geochemistry, v. 66, p. 53-87.

Rech, J.A., Currie, B.S., Michalski, G., and Cowan, A.M., 2006, Neogene climate change and uplift in the Atacama Desert, Chile: Geology, v. 34, no. 9, p. 761-764.

Reiners, P.W., Spell, T.L., Nicolescu, S., and Zanetti, K.A., 2004, Zircon (U-Th)/He thermochronology: He diffusion and comparisons with 40Ar/39Ar dating: Geochimica Et Cosmochimica Acta, v. 68, no. 8, p. 1857-1887.

Rodwell, M.J., and Hoskins, B.J., 2001, Subtropical anticyclones and summer monsoons: Journal of Climate, v. 14, p. 3192-3211.

Roperch, P., Sempere, T., Macedo, O., Arriagada, C., Fornari, M., Tapia, C., García, M., and Laj, C., 2006, Counterclockwise rotation of late Eocene-Oligocene fore-arc depostis in southern Peru and its significance for oroclinal bending in the central Andes: Tectonics, v. 25.

Schildgen, T.F., Hodges, K.V., Whipple, K.X, Reiners, P.W., and Pringle, M.S., 2007, Uplift of the western margin of the Andean plateau revealed from canyon incision history, southern Peru: Geology, v. 35, no. 6, p. 523-526.

Schön, J.H., 1996, Physical properties of rocks: Fundamentals and principles of petrophysics: Tarrytown, NY, Pergamon, 583 p.

Shuster, D. L., Ehlers, T.A., Rusmore, M.R., and Farley, K.A., 2005, Rapid glacial erosion at 18 Ma revealed by $^{4}He/^{3}He$ thermochronometry: Science, v. 310, p. 1668-1670.

Shuster D.L., Flowers R.M., and Farley K.A., 2006, The influence of natural radiation damage on helium diffusion kinetics in apatite: Earth and Planetary Science Letters, v. 249, no. 3-4, p. 148-161.

Sébrier, M., and Soler, P., 1991, Tectonics and magmatism in the peruvian Andes from late Oligocene time to the present, in Harmon, R. S., and Rapela, C.W., ed., Andean magmatism and its tectonic setting Boulder, Colorado, Geological Society of America Special Paper 265, p. 259-278.

Sempere, T., Fornari, M., Acosta, J., Flores, A., Jacay, J., Peña, D., Roperch, P., and Taipe, E., 2004, Estratigrafía, geochronología, paleogeografía y paleotectónica de los dépositos de antearco del sur del Perú, in XII Congreso Peruano de Geología, Lima, p. 533-536.

Silver, P.G., Russo, R.M.,and Lithgow-Bertelloni, C., 1998, Coupling of South American and African plate motion and plate deformation: Science, v. 279, no. 5347, p. 60-63.

Singewald, J.T., and Berry, E.W., 1922, The geology of the Corocoro copper district of Bolivia: John Hopkins University Studies in Geology, v. 1, p. 1-117.

Somoza, R., 1998, Updated Nazca (Farallon) - South America relative motions during the last 40 My: implications for mountain building in the central Andean region: Journal of South American Earth Sciences, v. 11, no. 3, p. 211-215.

Springer, M., 1999, Interpretation of heat-flow density in the Central Andes: Tectonophysics, v. 306, p. 377-395.

Springer, M., and Forster, A., 1998, Heat-flow density across the Central Andean subduction zone: Tectonophysics, v. 291, no. 1-4, p. 123-139.

Stern, C.R., 2004, Active Andean volcanism: its geologic and tectonic setting: Revista Geológica de Chile, v. 31, p. 161-206.

Stüwe, K., White, L., and Brown, R., 1994, The influence of eroding topography on steady-state isotherms. Application to fission-track analysis: Earth and Planetary Science Letters, v. 124, p. 63-74.

Takahashi, K., and Battisti, D.S., 2007, Processes controlling the mean tropical Pacific precipitation pattern. Part 1: The Andes and the Eastern Pacific ITCZ: Journal of Climate, v. 20, p. 3434-

3451.
Thouret, J.-C., Wörner, G., Gunnell, Y., Singer, B., Zhang, X., and Souriot, T., 2007, Geochronologic and stratigraphic constraints on canyon incision and Miocene uplift of the Central Andes in Peru: Earth and Planetary Science Letters, v. 263, p. 151-166.
Turcotte, D.L., and Schubert, G., 1982, Geodynamics, Applications of Continuum Physics to Geological Problems: New York, John Wiley and Sons, 450 p.
Uyeda, S., Wantanabe, T., Ozasayama, Y., and Ibaragi, K., 1980, Report of heat flow measurements in Peru and Ecuador: Bulletin of the Earthquake Research Institute, v. 55, p. 55-74.
Vorsteen, H.-D., and Schellschmidt, R., 2003, Influence of temperature on thermal conductivity, thermal capacity and thermal diffusivity for different types of rock: Physics and Chemistry of the Earth, v. 28, p. 499-509.
Whipp Jr., D.M., Ehlers, T.A., Blythe, A.E., Huntington, K.W., Hodges, K.V., and Burbank, D.W., 2007, Plio-Quaternary exhumation history of the central Nepalese Himalaya: 2. Thermomkinematic and thermochronometer age prediction model: Tectonics, v. 26, TC3003. doi:10.1029/2006TC001991.
Whipple, K.X, and Tucker, G.E., 2002, Implications of sediment-flux-dependent river incision models for landscape evolution: Journal of Geophysical Research, v. 107, no. B2. doi: 10.1029/2000JB000044.
Wörner, G., Uhlig, D., Kohler, I., and Seyfried, H., 2002, Evolution of the West Andean Escarpment at 18 degrees S (N. Chile) during the last 25 Ma: uplift, erosion and collapse through time: Tectonophysics, v. 345, no. 1-4, p. 183-198.
Yamano, M., and Uyeda, S., 1990, Heat-flow studies in the Peru Trench subduction zone, Proceedings of the Ocean Drilling Program, Scientific Results, p. 653-661.

Figure Captions

Figure 1: Location map showing Cotahuasi-Ocoña Canyon in southwest Peru and thermochronologic sample sites for zircon and apatite (U-Th)/He dating. White box outlines region from which vertical transects were collected and is shown in greater detail in the second frame. Images are created by draping a 30-m resolution semi-transparent digital elevation model (DEM) over a hillshade layer created from the same DEM. The DEM was derived from Advanced Spaceborne Thermal Emission and Reflection Radiometer (ASTER) imagery.

Figure 2: Schematic drawing showing depression of the near-surface 65° (apatite-He closure) isotherm in response to canyon incision. The rapidly-cooled region provides a record of the thermal response to changes in the surface morphology. Modified from Schildgen et al. (2007).

Figure 3: Apatite (U-Th)/He data from valley-bottom and vertical transects in Cotahuasi-Ocoña Canyon plotted against depth beneath reconstructed paleosurface. Black diamonds show the mean ages of valley-bottom transect samples, and white diamonds show mean ages of each sample in four different vertical transects (V1 through V4). Y-axis error bars reflect an estimated ±100m uncertainty

in the depth of samples below the regional paleosurface. X-axis bars show the range of individual crystal ages for each sample.

Figure 4: Vertical transects of apatite (U-Th)/He data. In each plot, the dashed gray line marks the 2-km depth, where we expect to see a transition from the younger to older suite of apatite ages. However, as most transects were limited to under 1000 m in vertical extent, it is difficult to resolve the pattern clearly on a single transect. Black diamonds show individual crystal ages and white diamonds show the mean age for each sample. Uncertainty in the depth plotted is estimated at ±100 m. Transect locations are shown in figure 1.

Figure 5. A: Model set-up and description. Model consists of a 3-dimensional finite element grid that tracks the cooling history of each cell through time and allows for evolving surface topography. Surface temperature is described by a temperature at sea level that changes with elevation according to a defined lapse rate. The surface experiences a uniform background exhumation rate. Topography changes through time by warping from one topographic input file to another. Heat production rate and thermal diffusivity are uniform and specified within the crust (details in Table 3). Temperature at the base of the model domain is defined by a constant value at the southern basal edge (T_0) and a linear lateral basal temperature gradient that increases to a maximum of 1400°C, after which basal temperature remains constant at 1400°C. This provides an approximation of the thermal structure of a subduction zone similar to that modeled in northern Chile by Springer (1999). The position of maximum temperature is controlled by both T_0 and the lateral basal temperature gradient. Because T_0 ranges from 100 to 300°C and the gradient ranges from 7 to 11.6 °C/km, the position of maximum temperatures ranges between 95 and 186 km from the southern edge of the model over the whole range of parameter space. B: Surface heat flow measurements and modeled temperature field (from Springer, 1999).

Figure 6: Examples of the digital elevation models (DEMs) used as input topographies for model simulations. All simulations started with the spline topography (a) and ended with the modern-day topography (d). Additional simulations run to test the effects of different canyon depths prior to the latest phase of incision used additional input topographies such as the middle two frames, which show similar elevations of the canyon interfluves but only a fraction of the modern-day relief on the canyon. Frame b shows 10% of the modern canyon relief, and frame c shows 30% of the modern canyon relief.

Figure 7: Model results for steady-state topographic evolution scenarios. T_0 was set to 200°C, and lateral basal temperature gradient was set to 11.6°C/km. Results plotted show the effect of varying background exhumation rate on predicted apatite and zircon (U-Th)/He ages. Results from all steady-state simulations, including the three plotted here, have a very poor match to observed data. Predicted and observed zircon ages show a better match, but a single exhumation rate does not appear to accurately predict all zircon ages.

Figure 8: Model results for simulations exploring the effects of background exhumation rate and lateral basal temperature gradient on predicted thermochronometer ages, and comparisons with observed ages. Plots A, B, and C show comparisons between model-predicted ages and observed (U-Th)/He ages for apatite samples. For model results shown in plots A and B, parameters held constant include incision onset time (11 Ma), incision completion time (2 Ma), T_0 (200°C), lateral basal temperature gradient (9.9°C/km), and the topographic evolution scenario is from the spline DEM to the modern topography. Plot A shows results on a depth versus age graph, and plot B shows results on a distance from coast versus age graph. Plot C shows a contour plot of chi-squared values that illustrate the misfit between predicted and observed ages over a wide range of lateral basal temperature gradients. Contour intervals are labeled with chi-squared values. The square, circle, and triangle show the exhumation rate and lateral basal temperature gradient values illustrated in plots A and B. Plots D, E, and F are equivalent to plots A, B, and C, respectively, except that they show predicted and observed (U-Th)/He ages for zircon. Fits between predicted and observed zircon ages are generally poor, and probably imply a non-uniform exhumation rate or changes in the thermal field over the time range represented by the zircon data.

Figure 9. Chi-squared plots showing model-predicted incision timing compared to the whole set of apatite samples for various combinations of T_0, lateral basal temperature gradient, and best-fit background exhumation rate. The critical value associated with a 95% confidence interval for the 27 samples and 6 free parameters is 32.7 (highlighted with bold, dashed line).

Figure 10. Age-depth plots of observed and simulated data exploring the timing of canyon incision. Plot A shows results of simulations and observations where T_0 was set at 300°C, lateral basal temperature gradient was set to 11.6°C/km, and background exhumation rate was set to 0.015 mm/yr. The time range listed in the legend refers to the time span of canyon incision. Plot B zooms in to the set of data less than 16 Ma. Plot C is a contour plot of chi-squared values calculated for the whole

sample set, with an associated critical value of 32.7 at a 95% confidence level. The square, circle, and triangle in C illustrate the position within parameter space where the simulations plotted in A lie.

Figure 11. Chi-squared plots showing model-predicted incision timing compared to the whole set of apatite samples for various combinations of T_0, lateral basal temperature gradient, and best-fit background exhumation rate. The critical value associated with a 95% confidence interval for the 14 samples and 6 free parameters is 15.5 (highlighted with bold, dashed line).

Figure 12. Model-predicted ages of various magnitudes of early canyon relief compared to observed apatite data. Percent relief refers to the percentage of modern canyon relief that existed prior to the latest phase of incision. Plot A shows results of simulations and observed data plotted on a age-depth plot where T_0 was set at 200°C, lateral basal temperature gradient was set to 9.3°C/km, background exhumation rate is set to 0.02 mm/yr, early incision occurred between 30 and 14 Ma, and final incision occurred between 9 and 2 Ma. Plots B and C are contour plots of chi-squared misfit values, for early incision generated between 30 and 14 Ma (B) and between 50 and 30 Ma (C). The square, circle, and triangle in plot B illustrate the position within parameter space where the simulations shown in plot A reside. Chi-squared values were calculated using the whole sample set with an associated critical value of 32.7 at a 95% confidence level.

Table 1: Constraints on late Cenozoic uplift in the Central Andes.

Table 2: Age spectra analysis for $^{40}Ar/^{39}Ar$ data.

Table 3: Thermal and material properties for model simulations.

Table S1: Apatite (U-Th)/He individual crystal data.

Table S2: Apatite mean (U-Th)/He ages and sample locations.

Table S3: Zircon-He individual crystal data.

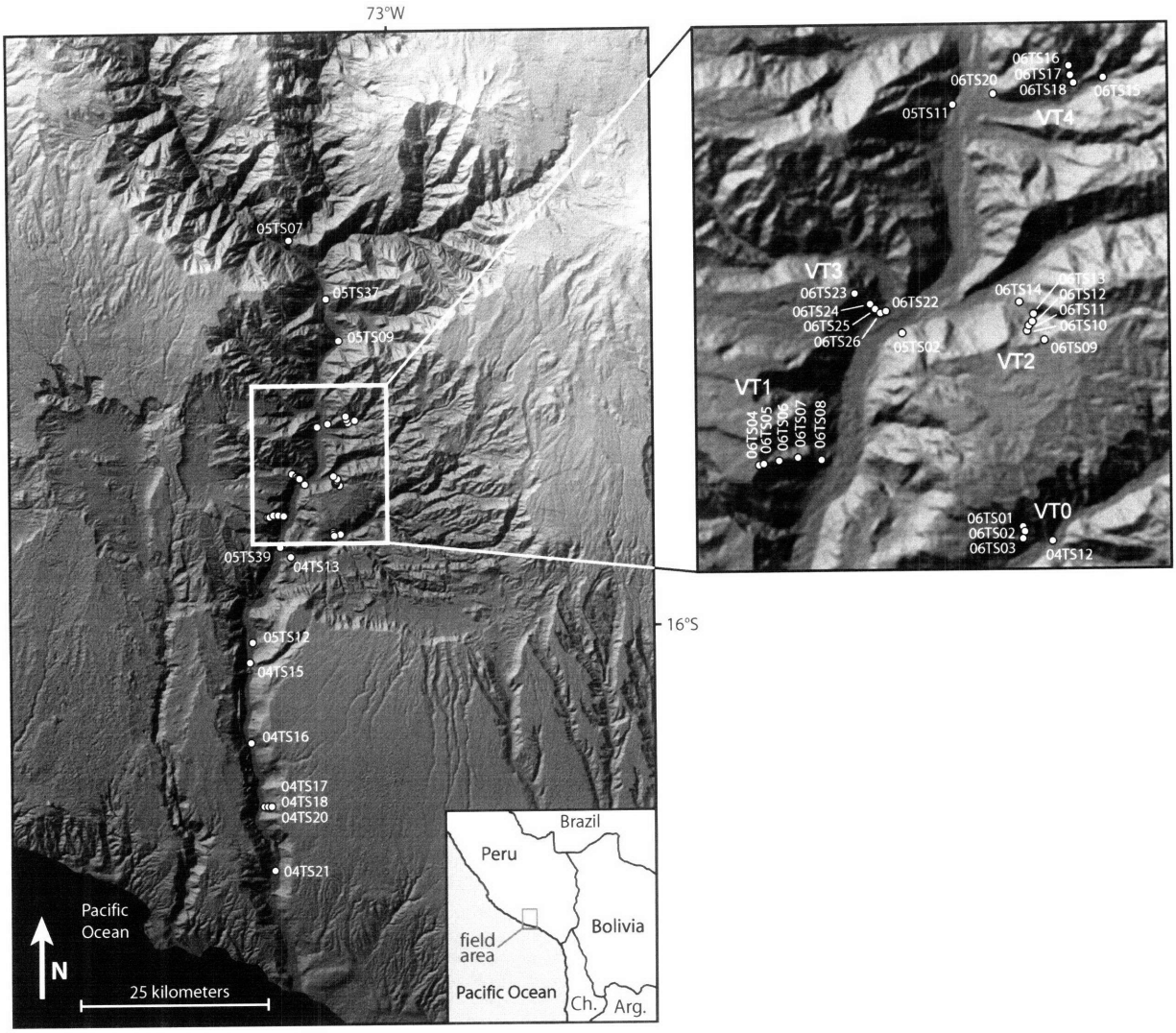
73°W
16°S
05TS07
05TS37
05TS09
05TS39
04TS13
05TS12
04TS15
04TS16
04TS17
04TS18
04TS20
04TS21
Pacific Ocean
N
25 kilometers
Brazil
Peru
Bolivia
field area
Pacific Ocean
Ch.
Arg.
VT4
06TS16
06TS17
06TS18
06TS19
06TS20
05TS11
VT3
06TS23
06TS24
06TS25
06TS26
06TS22
05TS02
VT2
06TS14
06TS13
06TS12
06TS11
06TS10
06TS09
VT1
06TS04
06TS05
06TS06
06TS07
06TS08
VT0
06TS01
06TS02
06TS03
04TS12

Figure 1.

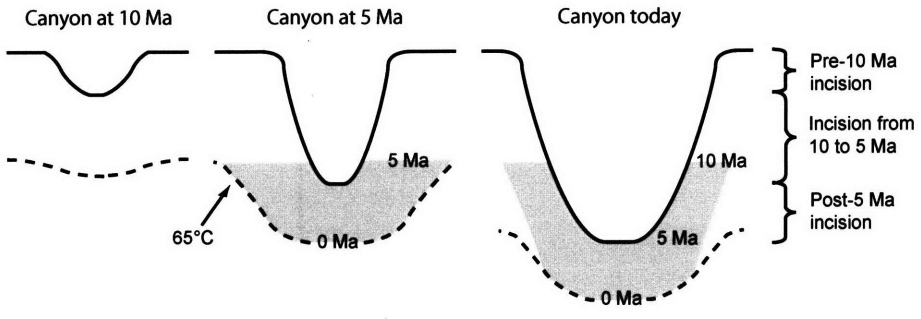
Canyon at 10 Ma
Canyon at 5 Ma
Canyon today
Pre-10 Ma incision
Incision from 10 to 5 Ma
Post-5 Ma incision
5 Ma
10 Ma
65°C
0 Ma
5 Ma
0 Ma

Figure 2.

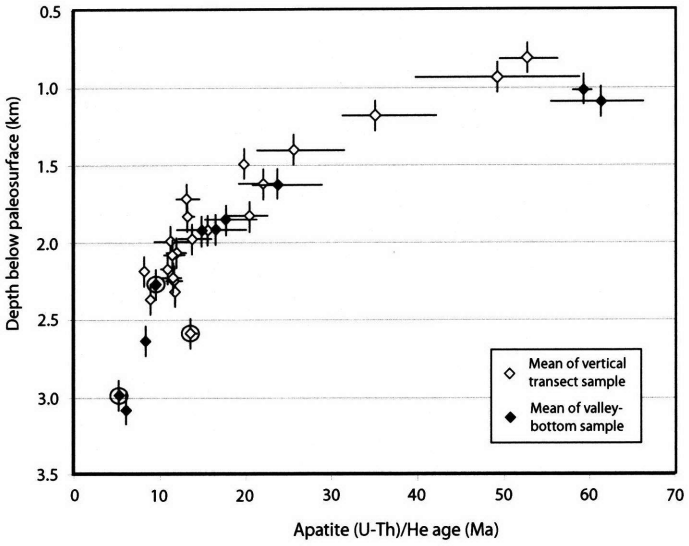
0.5
1.0
1.5
2.0
2.5
3.0
3.5
Depth below paleosurface (km)
0
10
20
30
40
50
60
70
Apatite (U-Th)/He age (Ma)
Mean of vertical transect sample
Mean of valley-bottom sample

Figure 3.

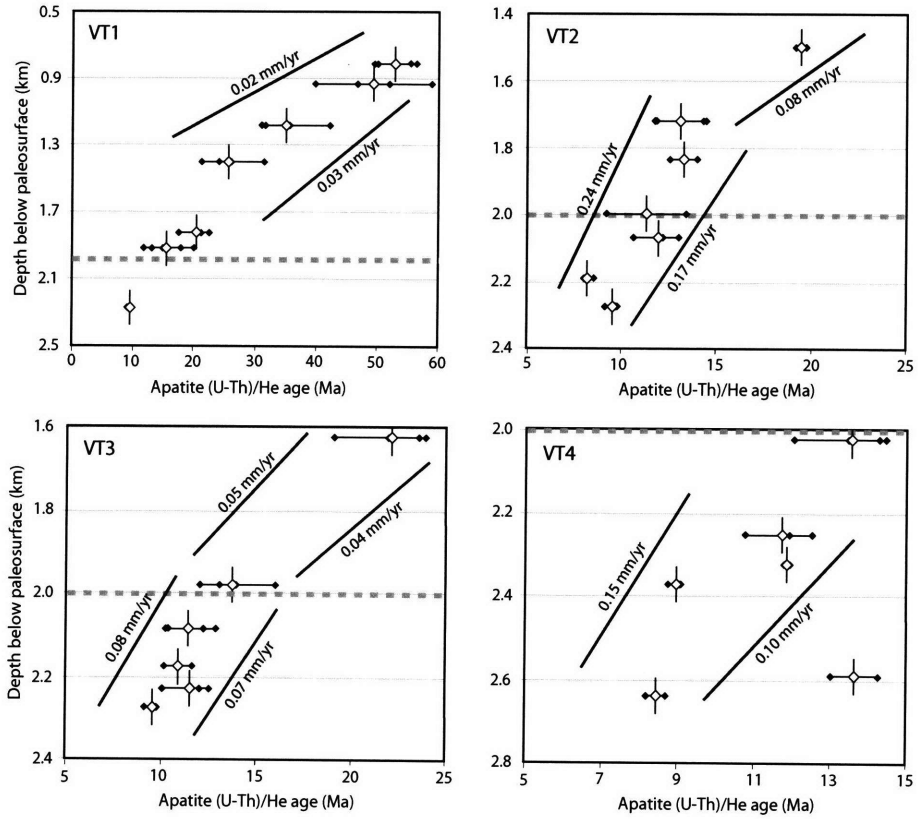
VT1
0.02 mm/yr
0.03 mm/yr
Depth below paleosurface (km)
Apatite (U-Th)/He age (Ma)
VT2
0.24 mm/yr
0.08 mm/yr
0.17 mm/yr
Apatite (U-Th)/He age (Ma)
VT3
0.05 mm/yr
0.04 mm/yr
0.08 mm/yr
0.07 mm/yr
Depth below paleosurface (km)
Apatite (U-Th)/He age (Ma)
VT4
0.15 mm/yr
0.10 mm/yr
Apatite (U-Th)/He age (Ma)

Figure 4.

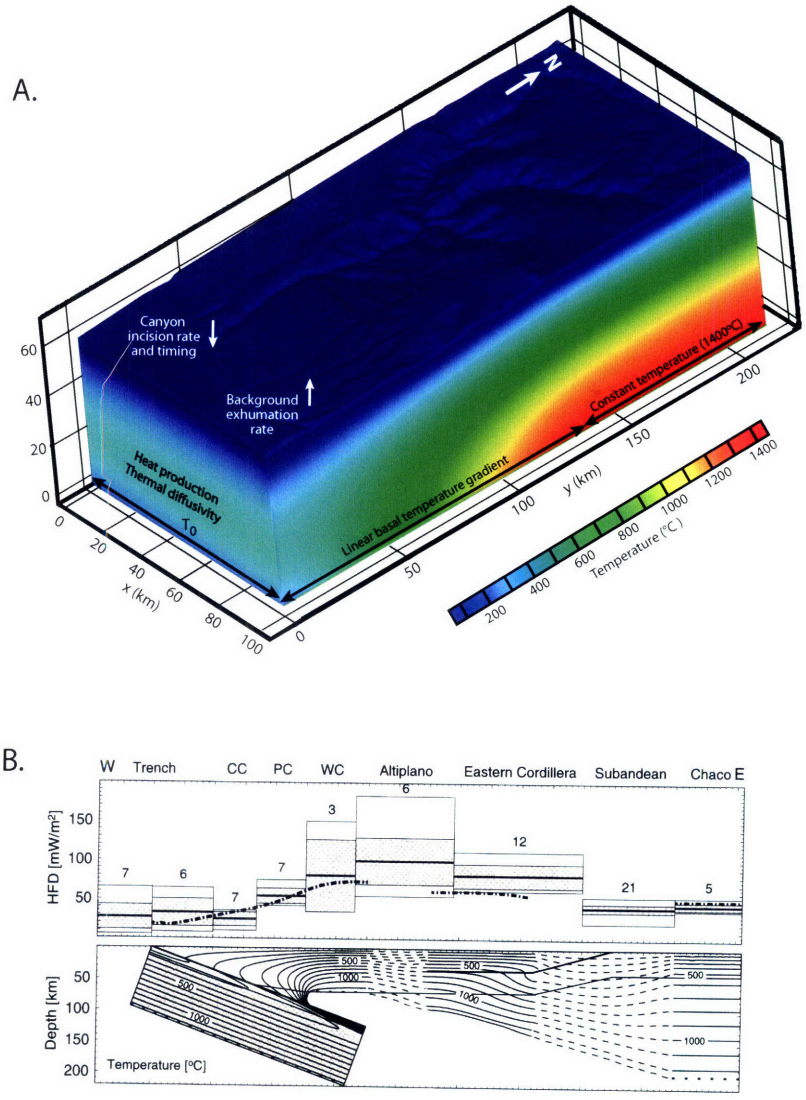
A.
N
Canyon incision rate and timing
Background exhumation rate
Heat production
Thermal diffusivity
T_0
Linear basal temperature gradient
Constant temperature (1400ºC)
x (km)
y (km)
Temperature (ºC)
B.
W
Trench
CC
PC
WC
Altiplano
Eastern Cordillera
Subandean
Chaco E
HFD [mW/m²]
Depth [km]
Temperature [ºC]

Figure 5.

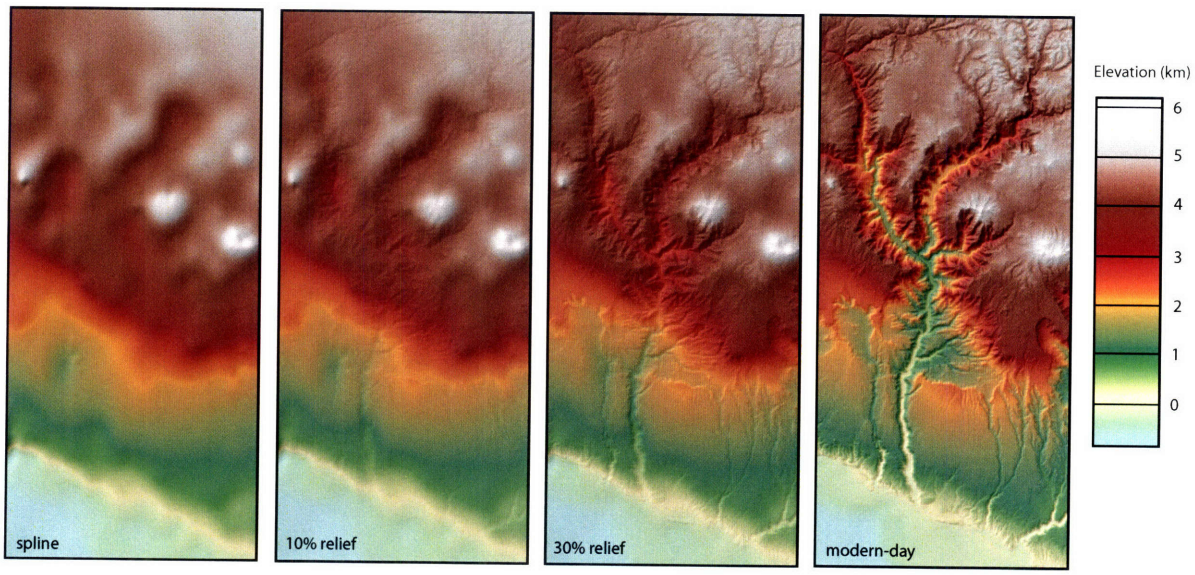

Figure 6.

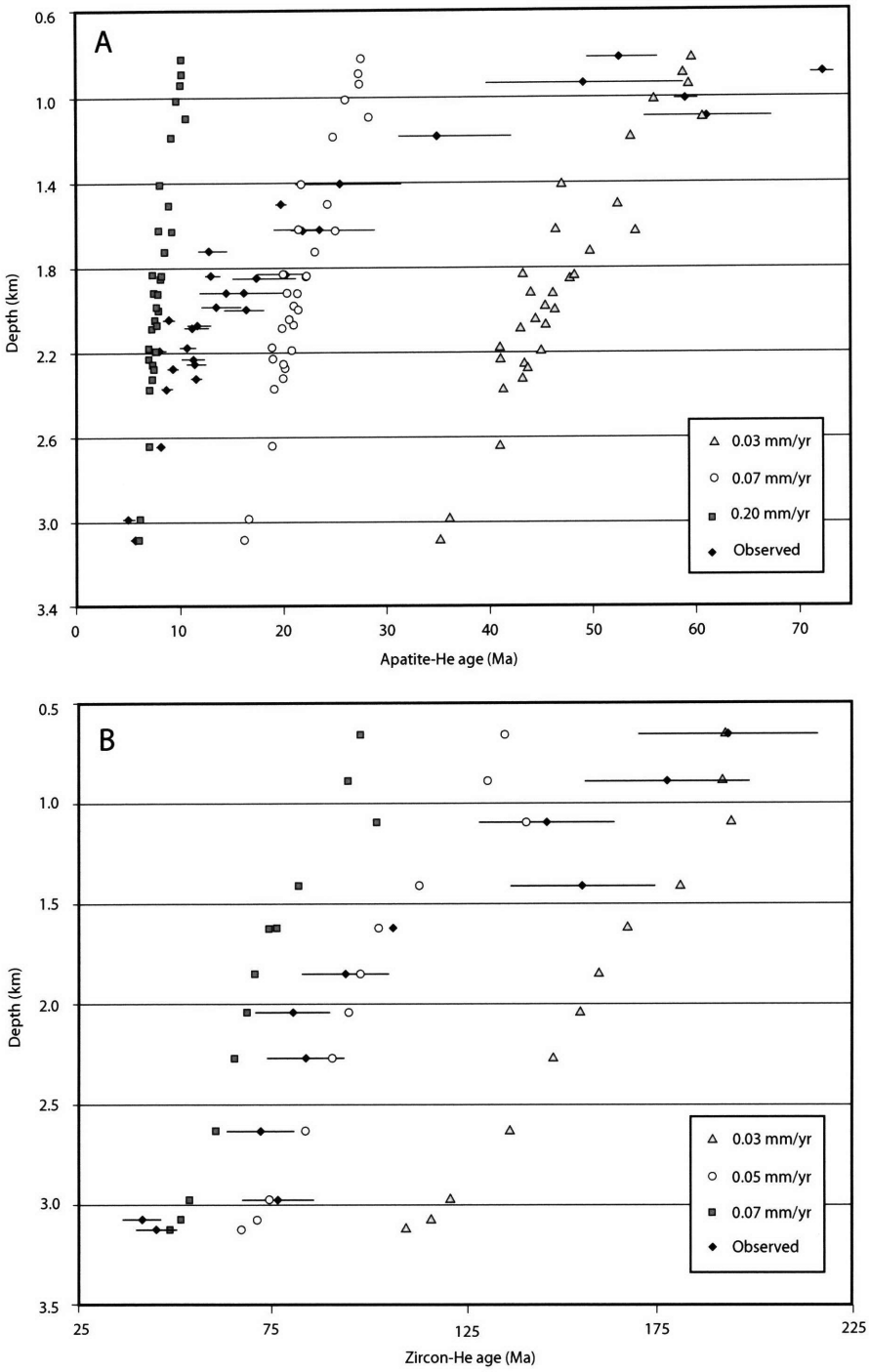
A
Depth (km)
0.6
1.0
1.4
1.8
2.2
2.6
3.0
3.4
0
10
20
30
40
50
60
70
Apatite-He age (Ma)
0.03 mm/yr
0.07 mm/yr
0.20 mm/yr
Observed
B
Depth (km)
0.5
1.0
1.5
2.0
2.5
3.0
3.5
25
75
125
175
225
Zircon-He age (Ma)
0.03 mm/yr
0.05 mm/yr
0.07 mm/yr
Observed

Figure 7.

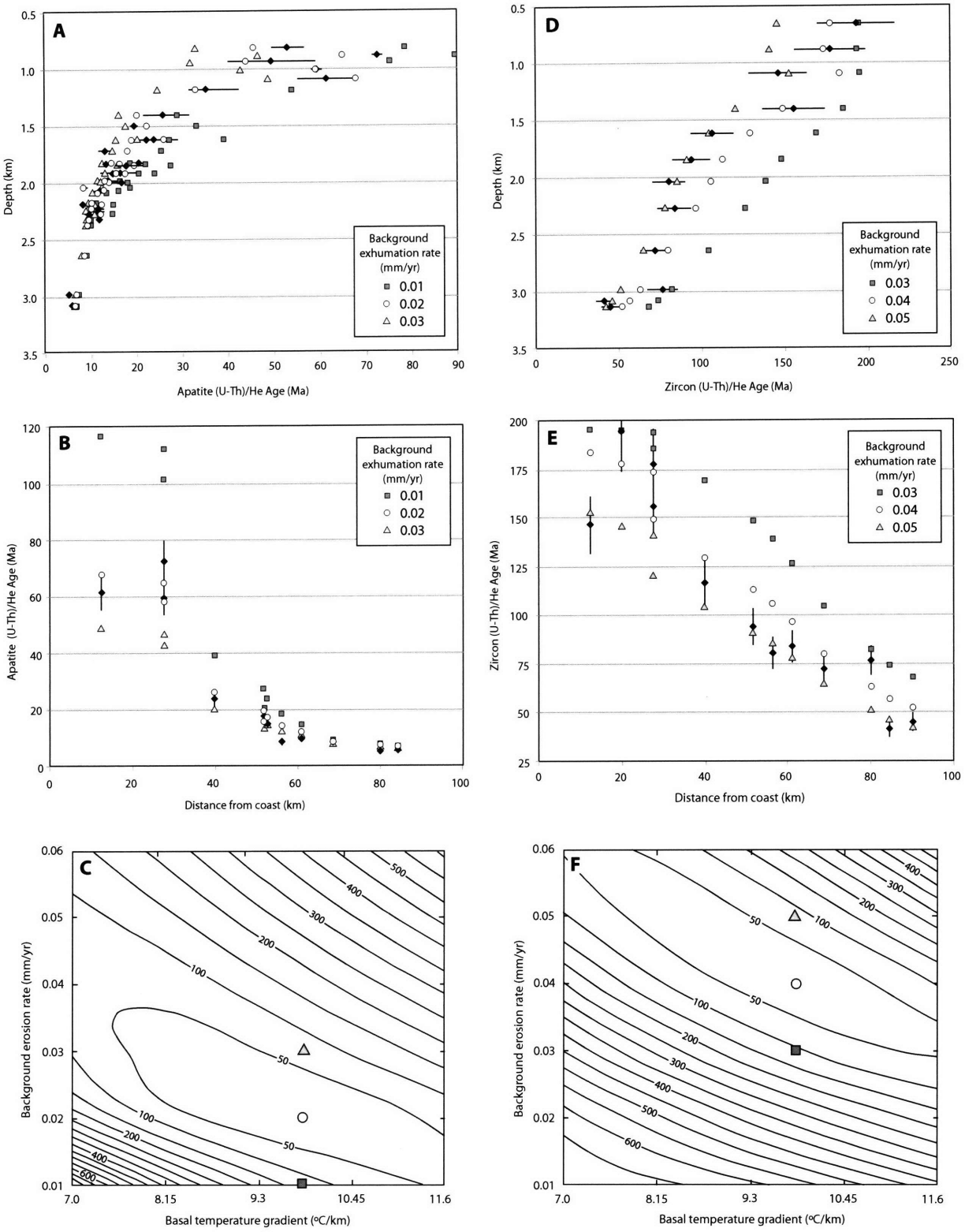
A
Depth (km)
Apatite (U-Th)/He Age (Ma)
Background exhumation rate (mm/yr)
0.01
0.02
0.03
D
Depth (km)
Zircon (U-Th)/He Age (Ma)
Background exhumation rate (mm/yr)
0.03
0.04
0.05
B
Apatite (U-Th)/He Age (Ma)
Distance from coast (km)
Background exhumation rate (mm/yr)
0.01
0.02
0.03
E
Zircon (U-Th)/He Age (Ma)
Distance from coast (km)
Background exhumation rate (mm/yr)
0.03
0.04
0.05
C
Background erosion rate (mm/yr)
Basal temperature gradient (°C/km)
F
Background erosion rate (mm/yr)
Basal temperature gradient (°C/km)

Figure 8.

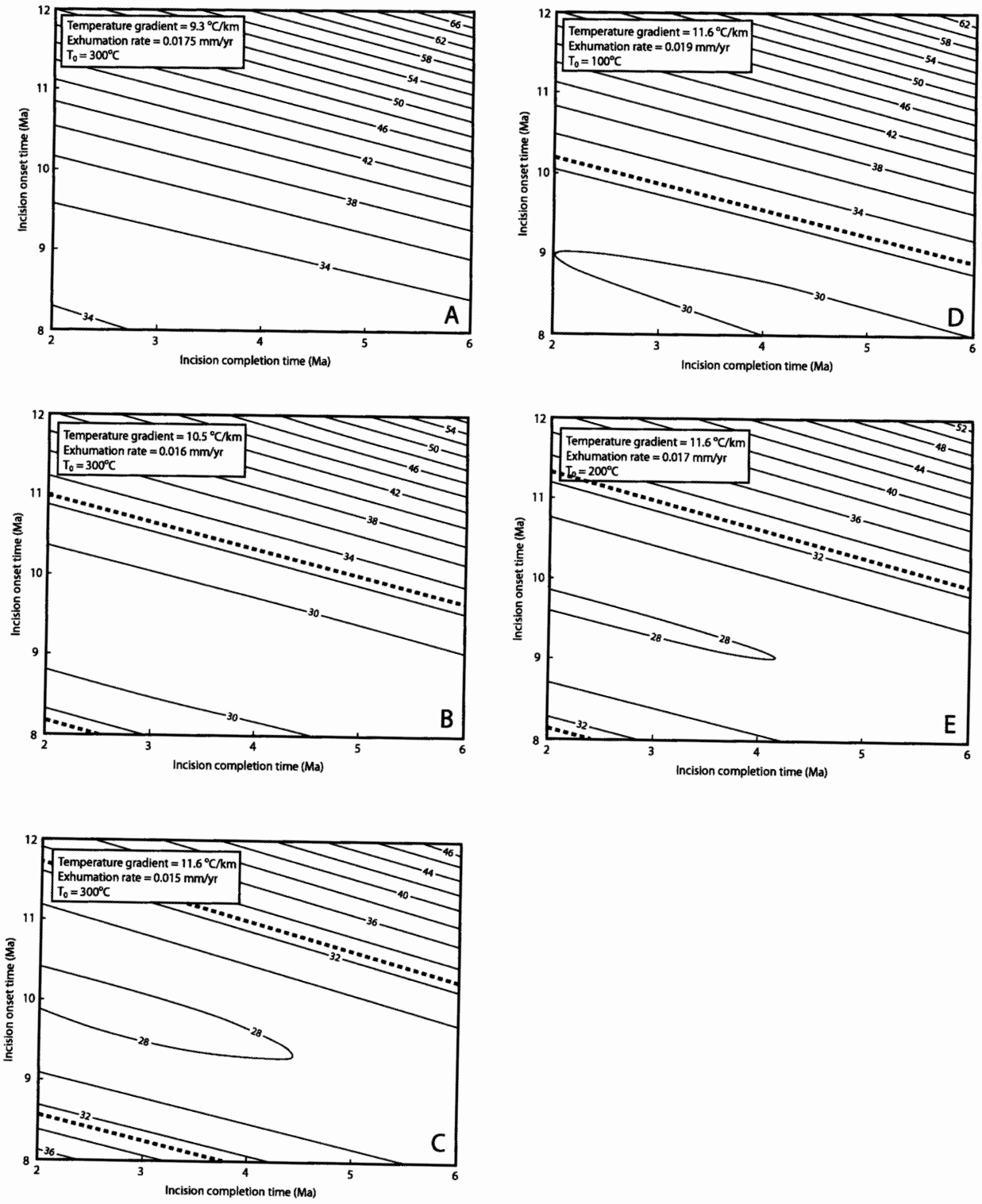
Temperature gradient = 9.3 °C/km
Exhumation rate = 0.0175 mm/yr
T_0 = 300°C
A
Temperature gradient = 11.6 °C/km
Exhumation rate = 0.019 mm/yr
T_0 = 100°C
D
Temperature gradient = 10.5 °C/km
Exhumation rate = 0.016 mm/yr
T_0 = 300°C
B
Temperature gradient = 11.6 °C/km
Exhumation rate = 0.017 mm/yr
T_0 = 200°C
E
Temperature gradient = 11.6 °C/km
Exhumation rate = 0.015 mm/yr
T_0 = 300°C
C
Incision onset time (Ma)
Incision completion time (Ma)

Figure 9.

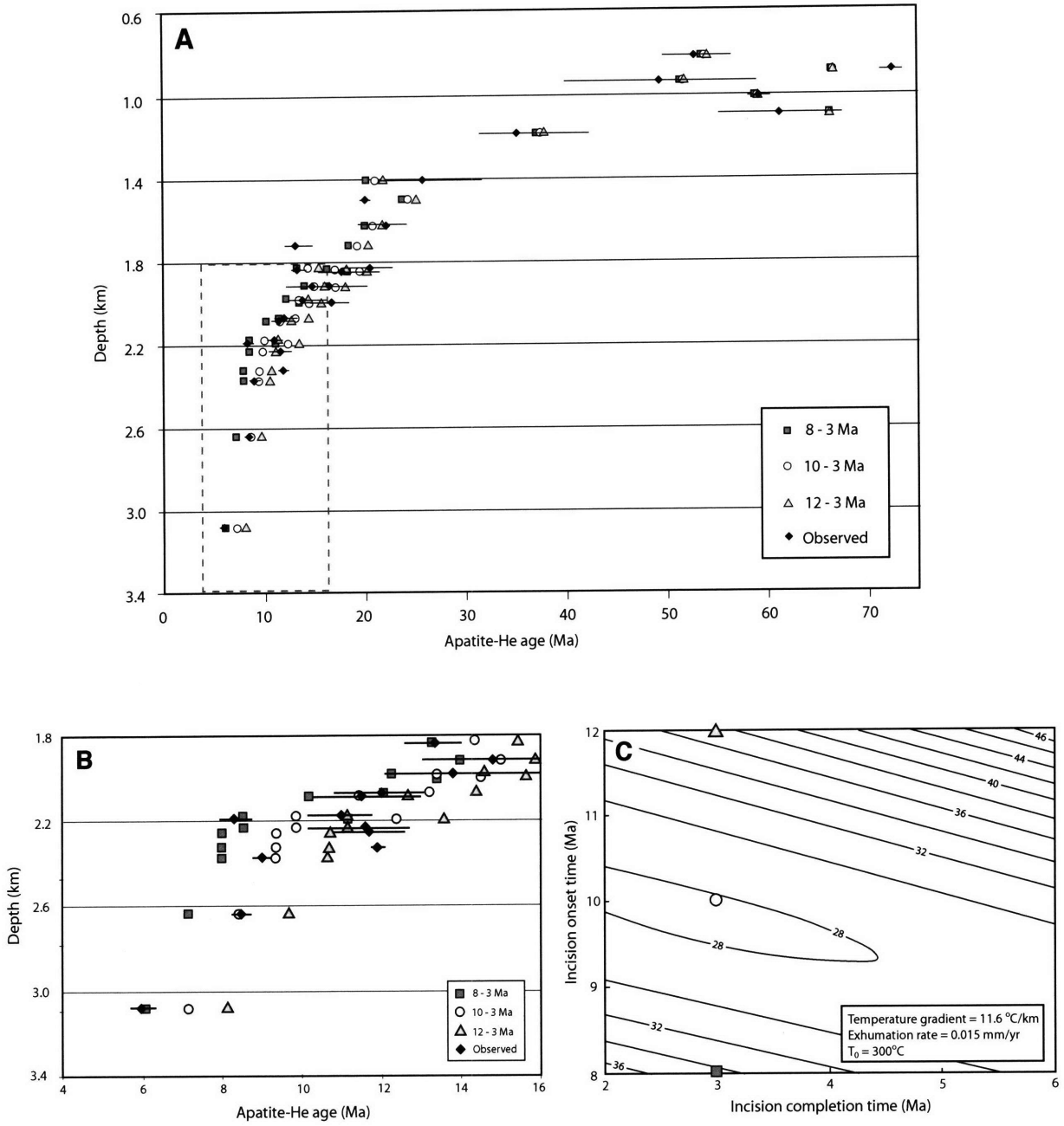
A
Depth (km)
Apatite-He age (Ma)
8 - 3 Ma
10 - 3 Ma
12 - 3 Ma
Observed
B
Depth (km)
Apatite-He age (Ma)
8 - 3 Ma
10 - 3 Ma
12 - 3 Ma
Observed
C
Incision onset time (Ma)
Incision completion time (Ma)
Temperature gradient = 11.6 °C/km
Exhumation rate = 0.015 mm/yr
T_0 = 300°C

Figure 10.

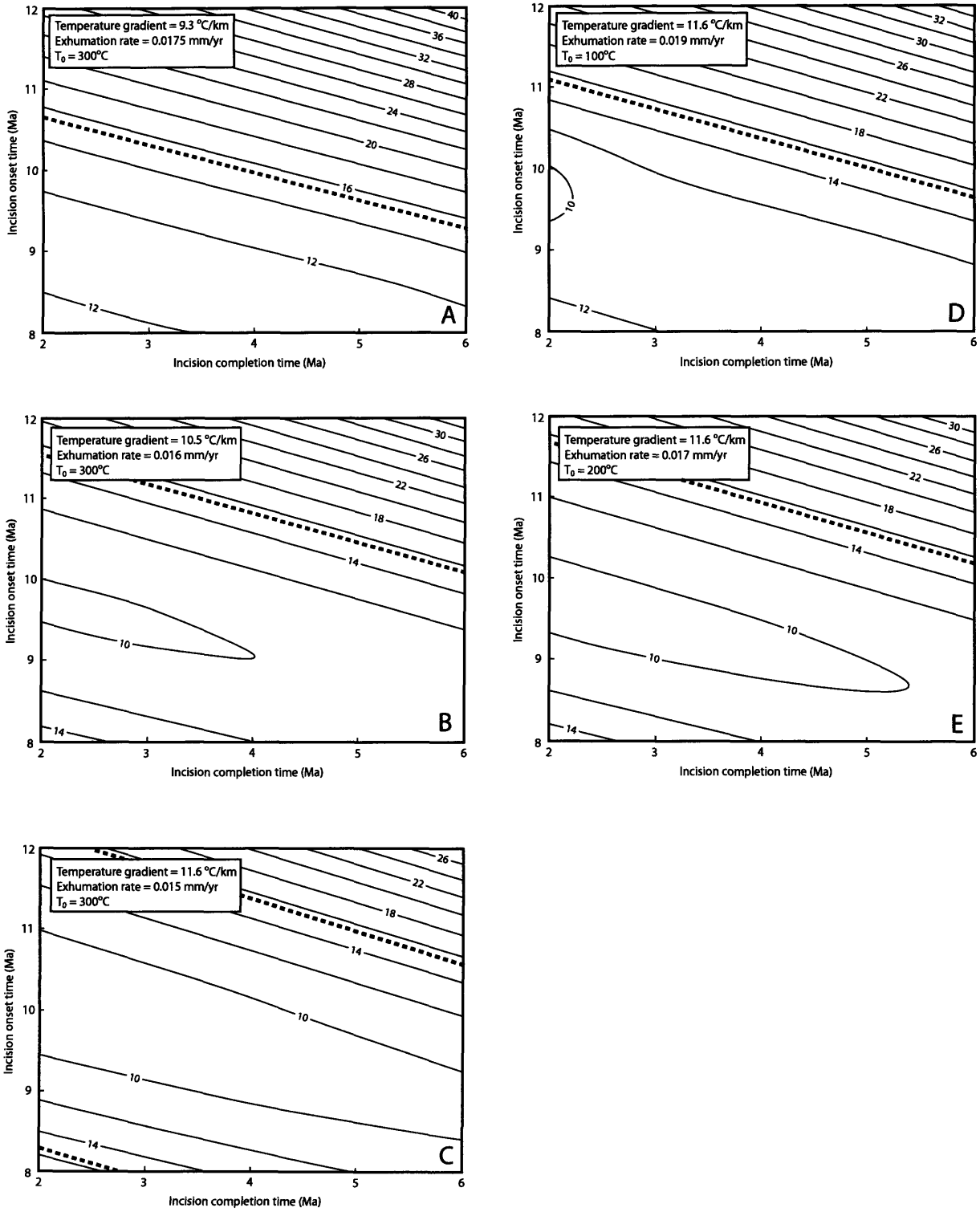
Temperature gradient = 9.3 °C/km
Exhumation rate = 0.0175 mm/yr
T0 = 300°C
A
Temperature gradient = 11.6 °C/km
Exhumation rate = 0.019 mm/yr
T0 = 100°C
D
Temperature gradient = 10.5 °C/km
Exhumation rate = 0.016 mm/yr
T0 = 300°C
B
Temperature gradient = 11.6 °C/km
Exhumation rate = 0.017 mm/yr
T0 = 200°C
E
Temperature gradient = 11.6 °C/km
Exhumation rate = 0.015 mm/yr
T0 = 300°C
C
Incision onset time (Ma)
Incision completion time (Ma)

Figure 11.

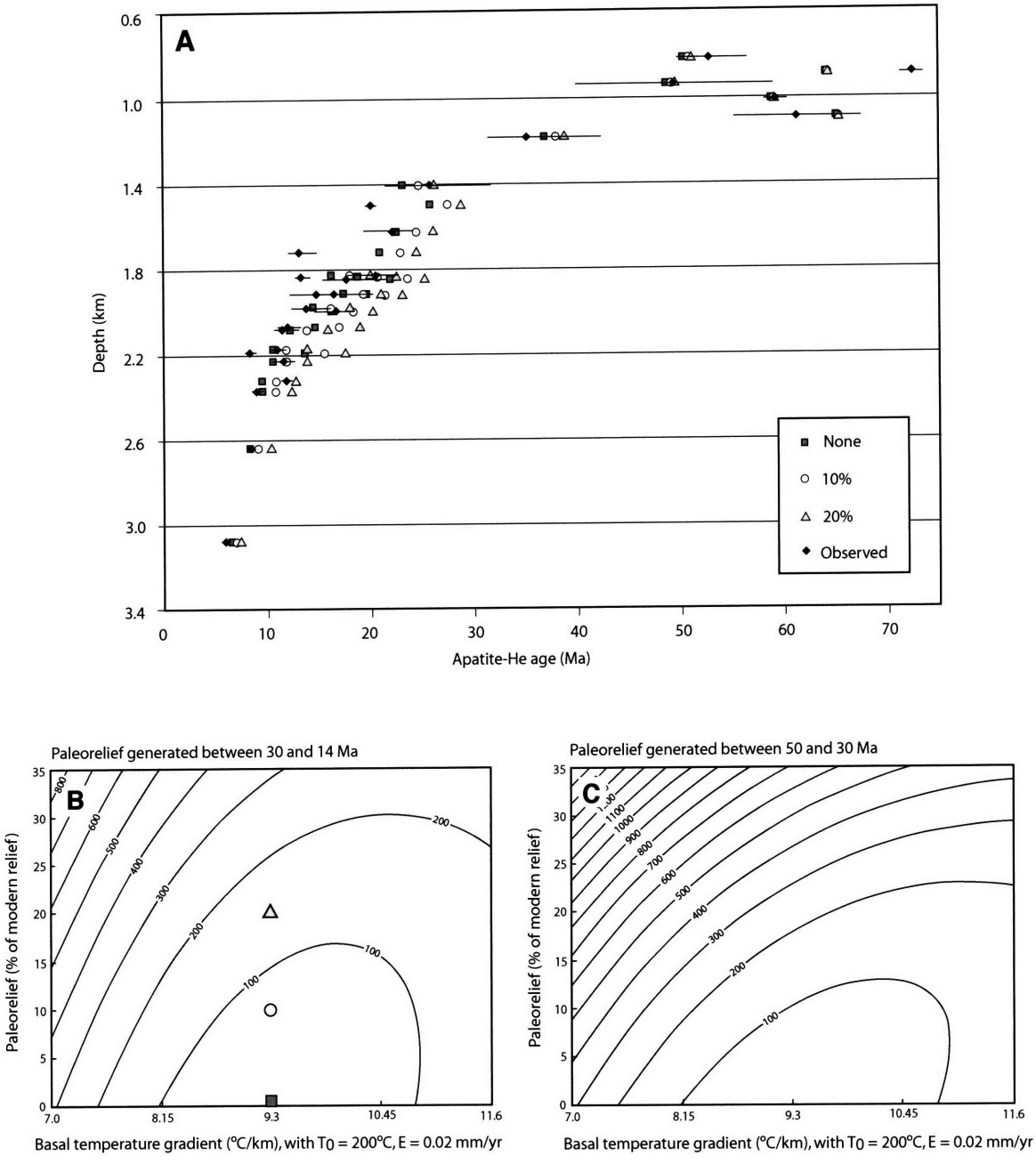
A
Depth (km)
Apatite-He age (Ma)
None
10%
20%
Observed
Paleorelief generated between 30 and 14 Ma
B
Paleorelief (% of modern relief)
Basal temperature gradient (°C/km), with T0 = 200°C, E = 0.02 mm/yr
Paleorelief generated between 50 and 30 Ma
C
Paleorelief (% of modern relief)
Basal temperature gradient (°C/km), with T0 = 200°C, E = 0.02 mm/yr

Figure 12.

TABLE 1. LATE CENOZOIC UPLIFT ESTIMATES FOR THE CENTRAL ANDES

Location	Uplift magnitude (m)	Initiation (Ma)	Method/Evidence	Reference
Corocoro, Altiplano	2000 ± 2000	10 to 15	paleobotany	Singewald and Berry, 1922
Potosi, Altiplano	3040 ± 1260	13.8 to 20.8	paleobotany	Gregory-Wodzicki, 2000
Jakokkota, Altiplano	2535 ± 1405	10 to 11	paleobotany	Gregory-Wodzicki, 2000
Callapa, Altiplano	2500 - 3500	10.3	oxygen isotopes	Garzione et al., 2006
Callapa, Altiplano	3400 ± 600	10.3	clumped isotopes	Ghosh et al., 2006
N. Chile, W. Cordillera	> 1400	10	rotated lake beds	Nestor et al., 2006
N. Chile, W. Cordillera	250 - 1800	10	rotated lake beds	Jordan et al., 2006
N. Chile, W. Cordillera	~ 1000	10	incised paleosurfaces	Hoke and Garzione, 2006
N. Chile, W. Cordillera	1000 - 2000	10	incised paleosurfaces	Garzione and Hoke, 2006
S. Peru, W. Cordillera	> 2400	10	incised canyons	Schildgen et al., 2007
S. Peru, W. Cordillera	2000 - 2500	13 to 9	incised canyons	Thouret et al., in press
Potosi, E. Cordillera	1500 ± 2000	13.8 to 20.8	paleobotany	Berry, 1939
Bolivia, E. Cordillera	1950 ± 1250	12 to 9	incised paleodrainages	Kennan et al.1997
Pislepampa, E. Cordillera	2300 ± 1100	6 to 7	paleobotany	Graham et al.2001
Bolivia, E. Cordillera	1705 +/- 695	12 to 9	incised paleodrainages	Barke and Lamb, 2006

TABLE 2. AGE SPECTRA ANALYSIS FOR $^{40}Ar/^{39}Ar$ DATA

Sample	Material	K/Ca	Age Spectra				Isochron Analysis			Description
			% gas	N*	MSWD	Weighted Age (Ma)	Age (Ma)	40Ar/36Ar intercept	MSWD	
06TS21	groundmass	1.28	50.3	5 of 12	1.62	2.21 ± 0.02	2.23 ± 0.02	292 ± 3.1	0.32	Flow at present valley bottom
04TS12	biotite	n/a	81.7	11 of 18	5.32	137.5 ± 1.76	136.5 ± 2.06	364 ± 302	1.43	Ocoña valleyintrusive bedrock
04TS13	biotite	n/a	55.53	9 of 20	1.77	135.7 ± 1.71	130.4 ± 12.4	927 ± 1505	0.19	Ocoña valleyintrusive bedrock

* Refers to number of steps on age plateau out of total number of steps.

TABLE 3. THERMAL AND MATERIAL PROPERTIES FOR MODEL SIMULATIONS

Parameter or Constant	Range	Reference*	Value/Range used
Thermal conductivity, W/mK			
Gneiss	1.7-8.0 (3.1)	4,6,12	
Granite	2.0-9.0 (3.2)	4,6,12	2.8
Granodiorite	3.3-3.8; 2.6-2.9	16,1	
Quartzite	2.1-4.1 (3.1)	4	
Heat production, uW/m^3			
Granite	2.45-2.5	3,13	
Granodiorite	1.5	13	
Diorite	1.08-1.10	3,13	0.8
Crustal average	0.8-0.9	13,14	
Crustal average, heat flow 50-70 mW/m^2	0.7-0.9	20	
Specific heat capacity, J/kgK			
Gneiss	770-979	2,10,11	
Granite	600-1172	8,9	
Granodiorite	650-1046	1,8,9	800
Diorite	1140	2	
Quartzite	699-1013	2,7	
Thermal Diffusivity, km^2/myr			
Granodiorite	32.8-39.7	1	40
Typical, based on above values	40.1	1	
Range in basal temperature			
At 60 km depth	200-1400	14	200-1400
Density, kg/m^3			
Gneiss	2700	2,10,11	
Granite	2620-2670	8,9,13	
Granodiorite	2700-2840	1,8,9	2750
Diorite	2820-2870	2,13	
Quartzite	2640	2,7	
Lapse Rate, °C/km			
Arid central Andes	6.5	19	6.5
Heat flow, mW/m^2			
Central Peru offshore	30-45	15,14	
South Peru forearc	32-60	5,14	n/a
Peruvian arc and Altiplano	50-180	5,16,17,18	
Geothermal gradients, °C/km			
Peru forearc	12-21	5	n/a

* 1: Arndt et al., 1997; 2: Cermak and Ryback, 1982; 3: Haenel et al., 1988; 4: Hamza et al., 2005; 5: Henry and Pollack, 1988; 6: Ehlers, 2005; 7: Kappelmeyer and Haenel, 1974; 8: Mel'nikova et al., 1975; 9: Moiseenko et al., 1970; 10: Schön, 1996; 11: Dortmund, 1976; 12: Vorsteen and Schellschmidt, 2003; 13: Pollack, 1982; 14: Springer, 1999; 15: Yamano and Uyeda, 1990; 16: Springer and Forster, 1998

TABLE S1. APATITE (U-Th)/He INDIVIDUAL CRYSTAL DATA

Sample	Mass (μg)	Radius (μm)	U (ppm)	Th (ppm)	U/Th	^{4}He (nmol/g)	Ft	Age* (Ma)	2 σ† (Ma)	Depth§ (m)	Elevation (m)	Reference††
06TS01a-A	3.40	47.1	114.7	70.09	1.64	5.08	0.70	10.2	0.25	1692	1045	1
06TS01a-B	2.42	39.2	128.4	77.42	1.66	4.37	0.66	8.31	0.19	1692	1045	1
06TS01a-C	1.95	38.0	141.6	89.36	1.58	6.33	0.64	11.1	0.25	1692	1045	1
06TS01a-D	3.68	47.4	92.78	52.10	1.78	3.58	0.71	8.88	0.22	1692	1045	1
06TS02a-A	4.62	49.4	149.8	91.91	1.63	10.7	0.72	15.9	0.39	1785	936	1
06TS02a-B	2.71	41.6	139.8	80.33	1.74	9.26	0.68	15.9	0.37	1785	936	1
06TS02a-C	3.81	44.4	105.2	63.56	1.66	4.96	0.70	10.8	0.26	1785	936	1
06TS02a-D	2.12	38.0	141.0	77.59	1.82	4.21	0.65	7.49	0.17	1785	936	1
06TS03a-A	2.06	39.6	108.3	58.47	1.85	4.07	0.65	9.40	0.22	1870	851	1
06TS03a-B	3.24	44.8	197.3	123.6	1.60	8.84	0.69	10.4	0.24	1870	851	1
06TS03a-C	2.67	42.1	152.5	95.40	1.60	11.6	0.68		0.41	1870	851	1
06TS03a-D	1.35	34.3	178.6	98.55	1.81	5.17	0.61	7.78	0.18	1870	851	1
06TS04a-A	2.22	40.1	14.52	59.58	0.24	4.96	0.64	49.6	1.16	815	1670	1
06TS04a-B	1.83	35.8	13.58	58.65	0.23	5.09	0.62	55.5	1.49	815	1670	1
06TS04a-C	1.66	37.5	18.11	77.98	0.23	6.12	0.62	50.1	1.30	815	1670	1
06TS04a-D	1.68	35.7	17.12	75.83	0.23	6.53	0.61	56.4	1.23	815	1670	1
06TS05a-A	2.65	42.1	20.58	86.24	0.24	7.63	0.66	52.0	1.20	937	1548	1
06TS05a-B	2.56	42.5	13.84	57.68	0.24	4.60	0.66	46.8	1.11	937	1548	1
06TS05a-C	2.11	35.2	16.28	65.02	0.25	6.28	0.62	58.9	1.30	937	1548	1
06TS05a-D	1.43	34.4	16.68	61.71	0.27	4.02	0.60	39.8	1.00	937	1548	1
06TS06a-A	3.53	44.7	66.30	91.24	0.73	14.0	0.69	42.3	0.96	1185	1336	1
06TS06a-B	3.44	44.1	53.88	72.39	0.74	8.29	0.69	31.2	0.71	1185	1336	1
06TS06a-C	3.56	43.7	30.64	79.05	0.39	5.82	0.69	31.7	0.73	1185	1336	1
06TS06a-D	2.28	38.0	71.19	96.07	0.74	11.8	0.65	35.6	0.77	1185	1336	1
06TS07a-A	6.03	56.3	30.86	64.69	0.48	4.49	0.74	24.1	0.60	1406	1132	1
06TS07a-B	1.99	37.2	23.10	57.74	0.40	3.98	0.63	31.5	0.70	1406	1132	1
06TS07a-C	4.12	47.3	34.28	78.97	0.43	4.31	0.70	21.3	0.50	1406	1132	1
06TS07a-D	2.40	40.9	33.01	67.98	0.49	4.57	0.66	26.1	0.58	1406	1132	1
06TS08a-A	6.31	54.3	97.54	217.6	0.45	20.6	0.74		0.80	1829	743	1
06TS08a-B	3.84	48.4	74.30	120.2	0.62	6.91	0.71	17.6	0.40	1829	743	1
06TS08a-C	3.06	42.8	93.26	195.7	0.48	10.9	0.68	21.3	0.47	1829	743	1
06TS08a-D	3.06	42.8	95.61	202.1	0.47	11.9	0.68	22.5	0.49	1829	743	1
06TS09a-A	1.79	37.8	164.0	186.5	0.88	13.8	0.63	19.2	0.41	1501	1509	1
06TS09a-B	1.37	33.4	86.29	79.78	1.08	6.8	0.60	19.7	0.41	1501	1509	1
06TS10a-A	2.83	42.0	29.34	56.47	0.52	1.85	0.67	11.9	0.30	1722	1267	1
06TS10a-B	2.93	38.9	35.16	76.20	0.46	2.76	0.66	14.5	0.34	1722	1267	1
06TS10a-C	2.84	40.5	26.47	55.08	0.48	1.68	0.67	11.8	0.29	1722	1267	1
06TS10a-D	1.76	36.8	59.40	172.2	0.34	4.84	0.62	14.4	0.31	1722	1267	1
06TS11a-A	4.08	46.8	30.04	69.57	0.43	5.11	0.70		0.68	1836	1171	1
06TS11a-B	3.90	43.8	46.59	96.53	0.48	3.66	0.69	14.0	0.33	1836	1171	1
06TS11a-C	2.06	38.9	50.81	100.2	0.51	2.37	0.64	9.14	0.23	1836	1171	1
06TS11a-D	2.12	39.6	35.12	64.40	0.55	2.23	0.65	12.6	0.31	1836	1171	1
06TS12a-A	3.91	47.3	31.76	70.32	0.45	2.48	0.70	13.5	0.32	1997	1021	1
06TS12a-B	4.10	50.6	45.47	80.24	0.57	2.31	0.71	9.29	0.23	1997	1021	1
06TS12a-C	2.60	41.4	46.97	96.32	0.49	5.60	0.66	22.3	0.50	1997	1021	1
06TS12a-D	2.39	42.1	29.96	45.55	0.66	3.19	0.66	21.8	0.54	1997	1021	1
06TS13a-A	2.00	34.3	96.57	243.4	0.40	5.54	0.62	10.7	0.22	2070	966	1
06TS13a-B	1.84	35.7	139.9	204.5	0.68	27.3	0.63		0.86	2070	966	1
06TS13a-C	3.33	47.7	42.14	83.14	0.51	2.85	0.69	12.2	0.30	2070	966	1
06TS13a-D	2.00	36.7	43.21	86.39	0.50	2.86	0.63	13.1	0.29	2070	966	1

Sample	Mass (μg)	Radius (μm)	U (ppm)	Th (ppm)	U/Th	^{4}He (nmol/g)	Ft	Age* (Ma)	2 σ† (Ma)	Depth§ (m)	Elevation (m)	Reference††
06TS14a-A	7.19	57.0	28.43	67.12	0.42	1.47	0.75	8.14	0.20	2191	852	1
06TS14a-B	5.37	52.8	29.81	67.18	0.44	1.56	0.73	8.63	0.21	2191	852	1
06TS14a-C	4.64	49.7	15.02	23.35	0.64	0.83	0.72	10.4	0.28	2191	852	1
06TS14a-D	2.08	37.3	68.75	172.2	0.40	3.06	0.63	8.13	0.17	2191	852	1
06TS15a-A	5.30	54.5	13.66	42.43	0.32	0.85	0.73	9.06	0.25	2373	1050	1
06TS15a-B	3.85	48.8	10.05	32.24	0.31	0.75	0.70	11.2	0.33	2373	1050	1
06TS15a-C	3.10	43.6	10.83	34.32	0.32	0.61	0.68	8.76	0.68	2373	1050	1
06TS15a-D	2.73	44.0	12.97	39.06	0.33	0.73	0.67	9.09	0.37	2373	1050	1
06TS17a-A	1.38	33.9	23.46	18.69	1.26	1.15	0.61	12.5	0.51	2253	1150	1
06TS17a-B	1.26	32.8	32.95	59.56	0.55	1.61	0.59	10.8	0.25	2253	1150	1
06TS17a-C	1.53	36.1	16.15	25.71	0.63	1.23	0.61	16.6	0.67	2253	1150	1
06TS17a-D	1.24	35.6	29.22	59.61	0.49	1.67	0.59	11.9	0.33	2253	1150	1
06TS18a-A	2.23	42.1	20.72	21.31	0.97	0.67	0.66	7.20	0.24	2324	1079	1
06TS18a-B	2.12	40.5	29.27	30.46	0.96	1.54	0.65	11.9	0.43	2324	1079	1
06TS18a-C	2.19	40.1	21.21	22.81	0.93	2.89	0.66		0.79	2324	1079	1
06TS18a-D	1.39	35.7	29.20	28.12	1.04	1.41	0.61	11.8	0.36	2324	1079	1
06TS20a-A	7.01	58.5	93.13	76.40	1.22	5.95	0.76	13.0	0.33	2594	747	1
06TS20a-B	6.23	55.5	91.57	80.41	1.14	11.2	0.75	24.9	0.61	2594	747	1
06TS20a-C	5.21	51.8	99.66	72.63	1.37	6.62	0.73	14.3	0.36	2594	747	1
06TS20a-D	3.99	48.8	82.73	61.90	1.34	15.3	0.71		0.97	2594	747	1
06TS22a-A	4.37	48.7	32.69	77.99	0.42	2.00	0.71	10.1	0.26	2230	660	1
06TS22a-B	2.89	42.7	38.45	83.87	0.46	3.00	0.67	14.1	0.33	2230	660	1
06TS22a-C	3.16	47.5	30.92	48.78	0.63	1.93	0.69	12.1	0.30	2230	660	1
06TS22a-D	3.01	41.9	36.39	70.14	0.52	2.44	0.67	12.6	0.35	2230	660	1
06TS23a-A	7.01	59.9	20.18	48.71	0.41	3.10	0.75	23.9	0.59	1626	1260	1
06TS23a-B	2.92	45.4	28.87	68.92	0.42	3.19	0.68	19.1	0.47	1626	1260	1
06TS23a-C	2.44	41.5	25.18	60.55	0.42	3.33	0.66	23.6	0.67	1626	1260	1
06TS23a-D	2.52	41.4	27.07	68.07	0.40	3.40	0.66	22.0	0.52	1626	1260	1
06TS24a-A	4.52	50.7	35.63	91.79	0.39	2.92	0.72	13.1	0.32	1981	900	1
06TS24a-B	5.39	53.7	32.15	71.19	0.45	2.72	0.73	14.0	0.34	1981	900	1
06TS24a-C	2.98	45.2	41.33	77.44	0.53	3.55	0.68	16.1	0.37	1981	900	1
06TS24a-D	1.81	38.2	44.03	102.1	0.43	2.82	0.63	12.1	0.27	1981	900	1
06TS25a-A	3.25	44.5	32.05	66.50	0.48	2.18	0.69	12.3	0.30	2086	790	1
06TS25a-B	3.33	48.7	32.63	68.51	0.48	1.93	0.70	10.4	0.25	2086	790	1
06TS25a-C	2.57	40.3	39.05	76.22	0.51	2.11	0.66	10.3	0.25	2086	790	1
06TS25a-D	2.73	45.6	40.02	81.88	0.49	2.82	0.68	12.9	0.30	2086	790	1
06TS26a-A	3.32	45.3	31.36	64.10	0.49	2.03	0.69	11.7	0.29	2176	700	1
06TS26a-B	3.35	46.7	45.51	104.9	0.43	3.83	0.69	14.5	0.34	2176	700	1
06TS26a-C	3.06	46.3	36.07	77.22	0.47	2.07	0.69	10.2	0.25	2176	700	1
06TS26a-D	2.49	43.6	37.47	66.02	0.57	2.11	0.67	11.0	0.27	2176	700	1
05TS37_A	3.57	48.6	10.9	23.3	0.47	0.60	0.73		0.39	3080	852	2
05TS37_B	3.26	42.4	12.6	32.2	0.39	0.48	0.70	6.26	0.24	3080	852	2
05TS37_C	2.81	43.7	13.7	37.2	0.37	0.48	0.70	5.60	0.23	3080	852	2
05TS37_D	1.88	40.8	8.01	15.9	0.50	0.28	0.68	6.42	0.52	3080	852	2

Sample	Mass (μg)	Radius (μm)	U (ppm)	Th (ppm)	U/Th	^{4}He (nmol/g)	Ft	Age* (Ma)	2 σ† (Ma)	Depth§ (m)	Elevation (m)	Reference††
04TS12aA	6.67	63.5	148	106	1.39	6.28	0.79	8.54	0.31	2040	702	2
04TS12aB	2.63	42.8	180	114	1.58	7.33	0.70	9.31	0.34	2040	702	2
04TS12aC	1.15	34.3	174	143	1.21	7.14	0.63	10.1	0.37	2040	702	2
04TS12aD	2.32	44.3	189	115	1.64	5.81	0.70		0.26	2040	702	2
04TS12aE	1.11	32.5	197	107	1.84	6.82	0.62	9.18	0.35	2040	702	2
04TS12aF	1.81	39.8	244	156	1.57	8.07	0.68	7.85	0.29	2040	702	2
04TS13aA	1.08	32.3	84.8	53.8	1.58	7.17	0.62	22.1	0.83	1850	552	2
04TS13aB	1.34	32.3	81.7	49.2	1.66	4.90	0.63	15.5	0.60	1850	552	2
04TS17aA	4.42	47.0	9.39	100	0.09	7.76	0.71	60.0	1.98	1010	290	2
04TS17aB	3.04	41.3	11.2	109	0.10	8.15	0.68	59.2	1.97	1010	290	2
04TS17aC	2.53	45.3	14.7	98.0	0.15	10.1	0.69		2.32	1010	290	2
04TS17aD	2.97	45.8	8.83	94.7	0.09	6.99	0.70	58.7	2.00	1010	290	2
04TS18aA	2.21	40.3	4.72	31.8	0.15	1.31	0.67		1.25	890	415	2
04TS18aB	1.34	36.3	5.33	78.6	0.07	5.92	0.62	72.5	2.98	890	415	2
04TS21aA	1.02	37.3	258	148	1.75	67.6	0.64	66.7	2.48	1090	73	2
04TS21aB	1.57	36.0	22.5	66.3	0.34	7.46	0.64	56.1	1.95	1090	73	2
05TS02_A	2.40	46.7	64.9	140	0.46	3.70	0.71	9.86	0.41	2280	590	2
05TS02_B	1.40	35.6	63.9	114	0.56	2.91	0.64	9.22	0.40	2280	590	2
05TS02_C	1.43	37.1	62.9	113	0.55	3.09	0.65	9.81	0.42	2280	590	2
05TS02_D	2.24	49.2	31.6	47.8	0.66	3.18	0.71		0.82	2280	590	2
05TS09_A	1.86	39.7	111	110	1.01	2.85	0.68	5.68	0.25	2990	816	2
05TS09_B	2.50	43.4	106	118	0.89	2.56	0.70	5.05	0.22	2990	816	2
05TS09_C	1.77	41.1	97.8	85.8	1.14	2.22	0.68	5.11	0.23	2990	816	2
05TS11_A	1.49	37.3	45.1	74.4	0.61	1.87	0.65	8.45	0.38	2640	647	2
05TS11_B	2.11	45.1	74.4	145	0.51	4.57	0.70		0.47	2640	647	2
05TS11_C	1.87	42.5	111	223	0.50	5.25	0.68	8.68	0.36	2640	647	2
05TS11_D	1.27	38.6	126	239	0.53	5.25	0.65	8.19	0.34	2640	647	2
05TS39_A	2.28	44.5	51.9	31.9	1.63	4.54	0.70	20.0	0.92	1920	490	2
05TS39_B	2.47	47.5	90.2	48.3	1.87	5.21	0.72	13.2	0.59	1920	490	2
05TS39_C	3.84	51.1	52.4	28.0	1.88	2.09	0.74		0.33	1920	490	2
05TS39_D	2.48	40.8	84.7	50.9	1.67	5.44	0.69	15.0	0.55	1920	490	2
05TS39_E	3.37	51.9	54.5	35.8	1.52	4.55	0.74	18.0	0.66	1920	490	2
05TS39_F	2.31	48.6	56.7	26.6	2.13	2.90	0.72	11.9	0.56	1920	490	2
05TS40_A	1.03	34.9	108	97.2	1.11	9.42	0.63	21.2	0.79	1920	480	2
05TS40_B	1.40	39.2	119	98.2	1.21	6.82	0.66	13.4	0.49	1920	480	2
05TS40_C	0.87	32.1	143	85.5	1.67	10.1	0.61	18.8	0.71	1920	480	2
05TS40_D	1.12	32.6	141	49.6	2.85	5.24	0.62		0.40	1920	480	2
05TS12_A	1.54	36.9	1.86	23.2	0.08	0.70	0.63	26.1	1.54	1620	360	2
05TS12_B	1.41	40.7	2.79	22.5	0.12	0.36	0.65		0.70	1620	360	2
05TS12_C	1.85	38.9	2.24	15.4	0.14	0.18	0.65		0.62	1620	360	2
05TS12_D	1.80	46.3	2.43	8.24	0.30	0.38	0.69	21.5	1.64	1620	360	2
05TS12_E	2.83	47.9	1.37	13.9	0.10	0.15	0.70		0.77	1620	360	2
05TS12_F	3.12	49.9	3.22	16.9	0.19	0.88	0.72	29.2	1.68	1620	360	2
05TS12_G	2.10	40.7	1.33	6.67	0.20	0.27	0.67	22.0	3.73	1620	360	2
05TS12_H	3.03	50.4	3.37	24.7	0.14	0.91	0.72	24.4	1.23	1620	360	2

*Alpha-ejection corrected age; values shaded gray are outliers not plotted in results.

†Error includes analytical precision only; in reality errors noted previously are likely to contribute to uncertainty.

§Depth below paleosurface. Error on this values is estimated to be +/- 100 m.

**Datum for geographic coordinates WGS1984.

††1: This paper; 2: Schildgen et al., 2007

TABLE S2. APATITE MEAN (U-Th)/He AGES AND SAMPLE LOCATIONS

Sample	Mean Age[1] (Ma)	STDEV[2]	STDEV % of mean age	N[3]	Longitude[4] (W)	Latitude[4] (S)	Depth[5] (m)	Elevation (m)
06TS01	9.6	1.3	13.2	4 of 4	73°3.783"	15°54.359"	1692	1045
06TS02	12.5	4.1	32.9	4 of 4	73°3.749"	15°54.444"	1785	936
06TS03	9.2	1.3	14.3	3 of 4	73°3.782"	15°54.553"	1870	851
06TS04	52.9	3.5	6.7	4 of 4	73°8.701"	15°53.258"	815	1670
06TS05	49.4	8.1	16.4	4 of 4	73°8.621"	15°53.235"	937	1548
06TS06	35.2	5.1	14.6	4 of 4	73°8.329"	15°53.174	1185	1336
06TS07	25.8	4.3	16.8	4 of 4	73°7.973"	15°53.127"	1406	1132
06TS08	20.5	2.6	12.6	3 of 4	73°7.556"	15°53.154"	1829	743
06TS09	19.4	3.0	15.4	2 of 2	73°3.391"	15°51.076"	1501	1509
06TS10	13.1	1.5	11.3	4 of 4	73°3.701"	15°50.898"	1722	1267
06TS11	11.9	2.5	21.1	3 of 4	73°3.666"	15°50.817"	1836	1171
06TS12	16.7	6.4	38.2	4 of 4	73°3.612"	15°50.742"	1997	1021
06TS13	12.0	1.2	10.0	3 of 4	73°3.591"	15°50.605"	2070	966
06TS14	8.8	2.0	22.7	4 of 4	73°3.847"	15°50.392"	2191	852
06TS15	9.5	1.1	12.0	4 of 4	73°2.294"	15°46.457"	2373	1050
06TS17	13.0	2.5	19.6	4 of 4	73°2.908"	15°46.388"	2253	1150
06TS18	10.3	2.7	26.1	3 of 4	73°2.901"	15°46.435"	2324	1079
06TS20	17.4	6.5	37.5	3 of 4	73°4.329"	15°46.718"	2594	747
06TS22	12.2	1.6	13.3	4 of 4	73°6.337"	15°50.558"	2230	660
06TS23	22.2	2.2	9.9	4 of 4	73°6.922"	15°50.242"	1626	1260
06TS24	13.8	1.7	12.2	4 of 4	73°6.631"	15°50.433"	1981	900
06TS25	11.5	1.3	11.4	4 of 4	73°6.521"	15°50.513"	2086	790
06TS26	11.9	1.9	15.7	4 of 4	73°6.382"	15°50.580"	2176	700
05TS37	6.0	1.6	26.4	3 of 4	73°4.437"	15°37.958"	3083	852
04TS12	9.0	1.1	12.2	5 of 6	73°3.235"	15°54.595"	2043	702
04TS13	18.8	4.6	24.5	2 of 2	73°7.068"	15°55.961"	1850	552
04TS17	59.3	0.7	1.1	3 of 4	73°8.979"	16°13.937"	1011	290
04TS18	72.5	11.2	15.4	1 of 2	73°8.855"	16°13.503"	887	415
04TS21	61.4	9.5	15.4	2 of 2	73°8.185'	16°18.122'	1094	73
05TS02	9.6	0.4	3.7	3 of 4	73°6.041"	15°50.925"	2275	590
05TS09	5.3	0.4	6.6	3 of 3	73°3.491"	15°40.872"	2985	816
05TS11	8.4	1.4	16.4	3 of 4	73°5.082"	15°46.908"	2641	647
05TS39	15.6	4.1	26.2	5 of 6	73°7.741"	15°55.161"	1920	490
05TS40	17.8	4.0	22.3	3 of 4	73°7.828"	15°55.467"	1916	480
05TS12	24.6	3.2	12.9	5 of 8	73°9.907"	16°2.112"	1621	360

1 Mean ages calculated based individual ages, excluding outliers.

2 STDEV = standard deviation, based on range of individual crystal ages.

3 Number of individual analyses used in mean age and STDEV calculation out of total individual analyses.

4 Datum used for latitude and longitude is WGS1984.

5 Depth below paleosurface, calculated by method described in Schildgen et al., 2007.

TABLE S3. ZIRCON (U-Th)/He INDIVIDUAL CRYSTAL DATA

Sample	Mass (μg)	Radius (μm)	U (ppm)	Th (ppm)	^{4}He (nmol/g)	Ft	Age* (Ma)	2 σ† (Ma)	Distance (km)	Depth§ (km)	Longitude** (W)	Latitude** (S)	Elevation (m)
04TS13z_B	2.92	38.3	233	106	90.9	0.73	88.9	4.50	51.7	0.19	73°7.068"	15°55.961"	552
04TS13z_A	3.31	37.5	277	169	125	0.73	99.0	4.95	51.7	0.19	73°7.068"	15°55.961"	552
04TS16z_A	14.7	59.8	94.5	257	110	0.82	158	7.28	27.7	0.14	73°10.140"	16°8.762"	225
04TS16z_B	14.7	65.3	170	91.4	134	0.84	153	7.67	27.7	0.14	73°10.140"	16°8.762"	225
04TS18z_A	7.80	56.8	56.5	153	74.3	0.81	182	8.34	27.7	0.89	73°8.855"	16°13.503"	415
04TS18z_B	6.82	57.3	122	156	121	0.81	173	8.23	27.7	0.89	73°8.855"	16°13.503"	415
04TS20z_A	2.22	37.5	200	227	210	0.72	210	9.86	20.0	0.66	73°8.651"	13°13.632"	650
04TS20z_B	4.14	51.5	123	174	123	0.78	177	8.13	20.0	0.66	73°8.651"	13°13.632"	650
05TS02z_A	14.5	54.7	206	166	87.3	0.82	79.9	3.78	61.1	2.28	73°6.041"	15°50.925"	590
05TS02z_B	8.21	50.4	340	160	143	0.80	87.5	4.29	61.1	2.28	73°6.041"	15°50.925"	590
05TS07z_A	13.3	55.3	228	115	53.0	0.82	46.7	2.25	90.2	3.13	73°7.218"	15°33.775"	939
05TS07z_B	12.5	54.3	195	80.8	40.7	0.82	43.1	2.13	90.2	3.13	73°7.218"	15°33.775"	939
05TS09z_A	12.4	63.9	365	223	116	0.83	61.7	2.99	80.1	2.99	73°3.491"	15°40.872"	816
05TS09z_B	10.3	56.2	600	823	319	0.81	91.2	4.17	80.1	2.99	73°3.491"	15°40.872"	816
05TS11z_A	43.8	80.4	294	132	110	0.88	71.2	3.49	68.7	2.64	73°5.082"	15°46.908"	647
05TS11z_B	52.8	93.0	202	114	80.2	0.89	72.8	3.51	68.7	2.64	73°5.082"	15°46.908"	647
05TS12z_A	20.8	67.0	57.7	64.3	36.7	0.85	110	4.76	40.0	1.62	73°9.907"	16°2.112"	360
05TS12z_B	17.7	59.7	111	71.3	71.3	0.84	123	5.63	40.0	1.62	73°9.907"	16°2.112"	360
04TS12zA	5.25	43.5	269	188	101	0.77	77.4	2.83	56.4	2.04	73°3.235"	15°54.595"	702
04TS12zB	6.78	42.5	194	168	81.5	0.77	83.4	2.94	56.4	2.04	73°3.235"	15°54.595"	720
04TS15zA	2.65	40.8	408	108	201	0.75	115	4.44	36.7	1.62	73°10.075"	16°3.508"	322
04TS15zB	1.98	40.5	361	111	151	0.73	98.4	3.83	36.7	1.62	73°10.075"	16°3.508"	322
04TS21zA	14.6	52.5	78.8	62.7	57.3	0.82	138	4.90	12.4	1.09	73°8.185'	16°18.122'	73
04TS21zB	6.96	48.3	61.7	75.6	52.3	0.78	155	5.34	12.4	1.09	73°8.185'	16°18.122'	73

* Alpha-ejection corrected ages.

†Error includes analytical precision only; in reality, zoning in U and Th and crystal measurement error also likely contribute to uncertainty.

§Depth below paleosurface. Error on this measurement is estimated to be +/- 100 m.

**Datum for geographic coordinates WGS1984.

Chapter 4:

Structural and tectonic development of the western margin of the Central Andean Plateau in southwest Peru

Taylor F. Schildgen[1]

Kip V. Hodges[2]

Kelin X Whipple[2]

Matthijs van Soest[2]

Katrina Cornell[1]

1. Department of Earth, Atmospheric and Planetary Sciences, Massachusetts Institute of Technology, Cambridge, Massachusetts 02139, USA

2. School of Earth and Space Exploration, Arizona State University, Tempe, Arizona 85287, USA

Abstract

Structural and thermochronologic studies of the western margin of the Central Andean Plateau, also know as the Western Andean Escarpment (WAE), show changing styles of deformation through time and along strike that give insights into the tectonic evolution of the plateau. In the Cotahuasi-Ocoña and Colca-Majes Valleys in southern Peru, major transverse canyons expose the plateau margin. Within the study area, uplift of the plateau relative to the piedmont region has progressed in at least three phases. First, NW-striking, NE-dipping reverse faults near the WAE accommodated plateau uplift prior to ~14-16 Ma. A second phase of plateau uplift relative to sea level resulted from motion on a system of high-angle, NW-striking, SW-dipping normal faults and subparallel monoclinal folds that together define the modern WAE. Along-strike variations in structural style along the escarpment may reflect the distribution of pre-Tertiary sedimentary strata along this part of the Andean margin, regional crustal heterogeneities mapped out by recent Pb-isotope work, or along-strike changes in the dip angle of the subducting Nazca plate. Thermochronologic studies of the exhumation history of basement rocks across the WAE as well as the $^{40}Ar/^{39}Ar$ age of a young basaltic andesite flow that overlaps a fault segment of the WAE constrain the second phase of uplift to between ~14 and 2.2 Ma. The youngest – but most poorly dated – phase of uplift affected the piedmont region and the plateau margin as a coherent block with no surface-breaking deformational structures to accommodate differential uplift. Although the amount of uplift that can be attributed to Phase I is unknown, the second and third phases resulted in at least 2.5-3.0 km of uplift of the western part of the plateau relative to sea level. As much as 1 km of this may have occurred during Phase III.

The observation that much of the structural relief of the Central Andean Plateau was created between ~14 and 2.2 Ma by high-angle normal faulting and monoclinal folding has important geodynamic implications. Plateau development during this interval was not accommodated by arc-perpendicular shortening on thrust faults, but rather by inflation, or bouyant rise, of the crust with little lateral southwestward expansion of the plateau toward the Peru-Chile trench.

1. Introduction

The Central Andean Plateau is the second largest topographic plateau on Earth, with average elevations of 4000 m extending over a region 300 km wide and ~1500 km long. While many geodynamic models have been proposed to explain the origin of great continental plateaus like the Central Andean Plateau and Tibet, an often-neglected aspect of the debate is that the structural history of plateau margins provides an important constraint on the tectonics processes by which plateaus grow. Our focus in this paper is the western margin of the Central Andean Plateau, where published accounts of the structure of the plateau margin – a topographic feature known as the Western Andean Escarpment (WAE) – are inconsistent. The simple morphology of the WAE led several early researchers to suggest it developed as a result of simple flexure or tilting into a crustal-scale monocline (e.g., Muñoz, 1956; Mortimer, 1973; Isacks, 1988). Wörner et al. (2002) supported this interpretation, but recognized localized normal faulting and late phase of minor reverse faulting. In contrast, several studies in northern Chile have suggested that the margin evolved over a high-angle, west-vergent reverse fault system (e.g., Muñoz and Charrier, 1996; Charrier et al., 2002; Victor et al., 2004; Farías et al., 2005). However, the finding that most of this shortening was finished prior to 10 Ma (e.g., Victor et al., 2004; Farías et al., 2005) implies that it cannot explain the significant post-10Ma uplift of the western margin (e.g., Schildgen et al., 2007; Thouret et al., 2007; Hoke et al., 2007). Based on detailed mapping of some of the more accessible parts of the WAE in southern Peru, this paper aims to evaluate the relative significance of surface faulting and monoclinal deformation in accommodating differential uplift across the WAE. We also explore the role these structures have played in uplift of the Western Cordillera and Central Andean Plateau relative to sea level, and the distribution of that uplift in space and through time.

2. Geologic Setting of the WAE in Southern Peru-Northern Chile

The subduction zone along the western margin of South America has been active since at least Cretaceous time, with periods of tectonism throughout the margin's history correlating broadly with variations in the subduction rate of the Nazca plate beneath the South American plate (e.g., Pardo-Casas and Molnar, 1987; Somoza, 1998), subduction angle (Jordan et al., 1983), and absolute west-

ward drift of South America (Silver et al., 1998). Southern Peru lies at the northern end of the Central Volcanic Zone, which is located above a relatively steeply-dipping (30°) section of the subducting slab. North of approximately 16°S latitude, the subduction zone transitions to a magmatically quiescent "flat-slab" region with a subduction angle of c. 15° (Cahill and Isacks, 1992; Jordan et al., 1983). This transition between a steeply- and shallowly-dipping slab also corresponds to a break in major crustal domains, mapped out by $^{206}Pb/^{204}Pb$ isotope ratios (Mamani-Huisa, 2006).

Between the trench and the WAE that defines the margin of the Central Andean Plateau lies a broad forearc domain which we refer to here simply as the "piedmont" region. Most surface exposures in this region consist of clastic, predominently continental rocks interstratified with ignimbrite sheets that provide valuable time markers. Unfortunately, the stratigraphic nomenclature for these units is inconsistent from one paper to the next. We will generally follow the most recently published chronostratigraphy of Thouret et al. (2007). Of specific interest to us are the Tertiary units in the piedmont region that pre-date incision of the great canyons that drain the Central Andean Plateau. These units will be referred to simply as the Moquegua Group. Clastic rocks in the Moquegua Group were shed from the evolving Andes to the north and east. Deposition of the Moquegua Group began sometime before 30 Ma and perhaps as early as 50 Ma (Sempere et al., 2004; Roperch et al., 2006; Thouret et al., 2007). Early deposition, which we refer to as the "lower Moquegua Group," was dominated by siltstones and sandstones that are preserved today as red beds. An unconformity at ca. 30 Ma (Sempere et al., 2004) marks a transition to coarser sandstones and gravels, which we refer to as the "upper Moquegua Group." Beginning about 24.5 Ma, the upper Moquegua stratigraphy was punctuated by episodic ignimbrite flows. The number and thickness of these flows increase upward in the section. The top of the Moquegua Group corresponds to a thick set of ignimbrite sheets dated at between 14.3 and 13.2 Ma by Thouret et al. (2007). Collectively, the 16.1-13.2 Ma ignimbrites form a regionally extensive caprock, and the dip of this caprock largely defines the topographic slope of the piedmont region, Additional, younger gravels (referred to as the "Moquegua D" unit by some workers; e.g., Sempere et al., 2004) form terraces and pediments that post-date deformation on all faults mapped in the region and often form cut-and-fill channel sequences. Although the age range of these gravels is unknown, a 4.95 ± 0.03 Ma ash layer (Sample 07TS16, Tables 2 and 3) within the gravels suggests a late Miocene to Pliocene age.

The unconformities within the Moquegua Group record the early deformational history of the southwestern Peruvian Andes. The earliest "Incaic" phase, likely responsible for the formation of highlands that were the source region of the lower Moquegua Group, included high-angle, west-vergent reverse faulting prior to 45-40 Ma (Steinmann, 1929; Noble et al., 1979, 1990). High-angle faults that cut strata of the upper Moquegua Group are frequently ascribed to the early Miocene

"Quechua" phase of deformation (Mégard et al., 1984). However, these structures also cut the 16.1-13.2 Ma ignimbrites and thus experienced post-Middle Miocene activity (Schildgen et al., 2007; Thouret et al., 2007). Sebrier et al. (1979) interpreted fine-grained marine sediments of the upper Moquegua Group, found near the town of Iquipi (50 km inland from the coast in the Ocoña Valley), as implying at least 2 km of uplift of the piedmont region subsequent to deposition. In southernmost Peru, near the Locumba and Moquegua Rivers, the "Altos de Camilaca surface", which likely corresponds to the unconformity between the upper and lower Moquegua Groups, provides similar geological evidence for significant post-Middle Miocene uplift. Tosdal et al. (1984) interpreted the surface, which consists of low-relief inland topography and remnants of a regional aggradational fan, as having been close to sea level at the time of deposition. Current elevations of the surface ranging from 1800 to 3500 m imply uplift on the order of 2 to 3 km, with highest magnitudes farther inland.

The northeast margin of the piedmont region is marked by a topographic ramp corresponding to the WAE. The simple morphology of the WAE was first described by Muñoz (1956), and later interpreted by Isacks (1988) as a crustal-scale monocline with > 2km relief and extending along the western margin of the Central Andes. This interpretation was adopted by Wörner et al. (2002) and Hoke et al (2007), who found evidence for uplift and tilting along the western margin in northern Chile in the absence of significant fault activity. In southern Peru, the topographic character of the WAE changes significantly along strike. In the eastern part of our study area, east of the Colca-Majes Valley (Figure 1), the escarpment marks a steep 2-km range front. Topographic swath profiles from the region show that the piedmont region has an average slope of 1.1°, within the range of expected depositional slopes of the sediments covering the area (as determined using the method of Paola and Mohrig, 1996). Slopes steepen abruptly to 6.0° across the escarpment, then decrease again at high plateau elevations. West of the Colca-Majes Valley, the escarpment morphology transitions to a gentle ramp, characterized by a gradual increase in elevation (Fig. 2), and only a slight steepening at the range front. Regionally, this geometry mimics the basal depositional contact of the 16.1-13.2 Ma ignimbrite caprock. The ramp is best exhibited near the Cotahuasi-Ocoña Valley, where the regional slope of 2.2° between the coastal escarpment and the plateau is twice as steep as the alluvial plain in the piedmont region east of the Colca-Majes Valley. In this location there is no clear distinction between the piedmont and the WAE; the WAE effectively extends to the coast. A swath profile parallel to the coast showcases the along-strike variation; piedmont elevations near the Ocoña Valley are c. 700 m higher than at equivalent positions near the Majes Valley. This dramatic change in WAE and piedmont morphology motivated our regional tectonic study. Are the differing morphologies an indication of different structural styles, or could the low slopes to the west simply indicate that the fault system marking the WAE to the east has been obscured by flanking sediments and the overlying

16.1-13.2 Ma ignimbrites? Were the latter interpretation correct, it would provide a minimum age constraint on the age of WAE formation. In the following sections, we describe four transects across the WAE. Geologic mapping, structural observations, bedrock thermochronology, and volcanic geochronology of these areas provide a rich history of the evolution of the WAE in southwestern Peru.

3. Study Areas

Our four study transects coresponded to areas where the WAE is cut by rivers draining nearby highlands of the Western Cordillera (Figure 1). From southeast to northwest, they are the Sihuas Valley, the Molles Valley, the Colca-Majes Valley, and the Cotahuasi-Ocoña Valley. Geological cross-sections (Fig. 3) are based on mapped surface geology with locations shown in Fig. 1. In addition to this, reconnaissance studies of the coastal escarpment provided context for understanding coupled uplift of the piedmont and plateau region relative to sea level.

Basemaps we used in mapping included 1:100,000-scale topographic maps generated by the Instituto Geographico Militar Lima-Peru, 15-m resolution Advanced Spaceborne Thermal Emission and Reflection Radiometer (ASTER) satellite imagery, and shaded relief maps generated from 30-meter-resolution ASTER-derived digital elevation data. This digital elevation model (DEM) was created by merging 32 individual ASTER-derived DEMs in ArcINFO to create a single high-resolution DEM covering the field area. Data drop-outs were filled with 90-m resolution Shuttle Radar Topography Mission (SRTM) digital elevation data. Three-dimensional rendering of 15-m resolution ASTER imagery draped over the DEM provided a useful aid to mapping and morphological analysis. All structural observations and sample locations were georeferenced using ESRI *ArcPad* software running on Compaq-HP *iPAQ* handheld computers coupled with Bluetooth-enabled GPS receivers. Basemaps, structural observations, and sample locations were compiled into a single project in ESRI *ArcMap*. Sample preparation and $^{40}Ar/^{39}Ar$ methods are described in Appendix A.

3.2.1. Sihuas Valley

In the Sihuas Valley, northeast of the town of Pedregal (Fig. 4 and Map A in Fig. 1), a high-angle fault zone separating Moquegua Group sediments in the hanging wall to the south from a complex of Mesozoic intrusive igneous rocks in the footwall to the north marks the base of the WAE. Sébrier et al. (1985) first identified this structure and named it the Lluclla fault; we will refer to it as the Lluclla fault zone. The zone is exposed well near the village of Lluclla, on the northwest side of the Sihuas Valley, where it strikes parallel to the range front (~N35°W) and dips very steeply southwestward. On the southeast side of the valley, the Lluclla fault zone appears to bifurcate into two strands separated by highly deformed Cretaceous granitic rocks. The southern strand maintains the

same steep orientation as the range front fault strand NW of the valley. The northern strand marks the local range front but dips more shallowly (30-40°S). Unfortunately, the intersection of these strands is covered by Quaternary fill in the Sihuas Valley.

In roadcut exposures northwest of the valley (Figure 4b), the Lluclla fault zone intercalates decimeter-scale blocks from the footwall with crushed Moquegua hanging wall sediments (Figure 4b). Cataclastic shear fabrics persist for several hundred meters into the footwall. There are no obvious fault-related ductile fabrics in the footwall, suggesting that all exposed tectonites developed in the upper crust. Although brittle shear orientations vary, the most pronounced shear surfaces strike sub-parallel to the range-front escarpment and dip steeply southwestward or northeastward. Slickenlines are relatively rare on fault surfaces within the shear zone and have a wide variety of orientations. Deformation is more limited in the hanging-wall Moquegua strata. Structures include a series of minor faults with offsets of one to several meters and monoclinal folds dipping up to 10°S with wavelengths of several tens to hundreds of meters. Disturbance of the Moquegua stratigraphy is greatest near the fault zone, where beds have been dragged into orientations dipping up to 35° away from the escarpment. The orientations of these folds, as well as the morphology of the escarpment, imply an important component of normal-sense displacement. Based on stress-inversions of fault and slickenline orientation data from the Lluclla fault zone, Sébrier et al. (1985) inferred NNE-SSW extensional kinematics for the youngest phase of faulting. The total amount of vertical throw on the fault zone is poorly constrained, but must be at least the 500 to 600-m height of the steep mountain front in this area since no units equivalent to the offset Moquegua strata occur in the footwall.

Sébrier et al. (1985) argued that the Lluclla fault zone had a complex deformation history that included an old phase of contractile deformation prior to NNE-SSW extension. We saw no direct evidence of contractile deformation, but there is evidence for multiple phases of extension. On the SE side of the valley, near the valley floor exposures of the Moquegua Group are dominated by redbeds that are lithologically similar to those that characterize the lower Moquegua Group in other regions of southern Peru. At higher elevations up the SE valley wall, these redbeds pass upward into tan conglomerates that are characteristic of the upper Moquegua Group across an angular unconformity. We tentatively correlate this unconformity with the lower-upper Moquegua unconformity elsewhere. At this location, the southern (high-angle) strand of the Llucla fault system cuts the Moquegua red beds but does not disturb supra-unconformity Moquegua Group gravels. A few tens of meters above the unconformity is an interstratified 16.12 ± 0.04 Ma ignimbrite (sample 05TS43, Tables 2 and 3), which limits most recent slip on the high-angle strand to before 16.12 Ma. However, the ignimbrite projects into the escarpment to the northeast, which is a manifestation of the northern (low-angle)

strand of the fault system that cuts gravels underlying the ignimbrite (~20 m below). This implies that the latest slip on the low angle (30-40°) main range front fault postdates 16.12 Ma.

3.2.2. Molles Valley

Published 1:100,000 scale geologic maps of southwest Peru from the Instituto Geológico Minero y Metalúrico (INGEMMET, 2001) suggest that early Andean deformational activity in the Molles Valley (Figure 1) included development of a number of W- to WNW-striking reverse faults and associated fault-propagation folds in pre-Tertiary lithologic units. For example, Figure 3c illustrates a widely-spaced set of imbricate reverse faults that cut both Jurassic sedimentary rocks and underlying Precambrian basement gneisses. The overlying Moquegua sediments exposed in valley walls generally show no deformation or only minor folding into monoclines that is likely related to extensional reactivation of these faults. The contractile deformation was likely related to the Incaic phase of orogenesis (Steinman, 1929; Sebrier, 1985).

Where the WAE crosses the Molles Valley (Fig. 5 and Map B in Fig. 1), the dramatic range front seen today can be attributed to structural uplift of pre-Tertiary igneous units of the Western Cordillera relative to Moquegua strata of the piedmont. Based on satellite imagery, the fault zone responsible for this can be correlated with confidence to the Lluclla fault zone in the Sihuas Valley. Exposure of the fault zone is poorer in the Molles Valley, but the range front geometry suggests a high ($\geq$ 70°) SSW dip. Footwall igneous rocks include relatively coherent structural blocks separated by discrete cataclastic shear zones; typically, these zones strike N40-50°W and dip very steeply southwestward. As was the case in the Sihuas Valley, hanging wall strata here are less penetratively deformed. However, they are deformed into macroscopic drag folds (Figure 5b) consistent with SW-side down (i.e., normal-sense) displacement on the fault zone. Again, rocks in the hanging wall and footwall cannot be matched, such that the local escarpment relief of ~600 m provides a minimum estimate of normal throw.

An undeformed basaltic andesite (sample 04CC12) dated at 0.214 ± 0.044 Ma ($^{40}Ar/^{39}Ar$) has flowed across the fault trace in the Molles Valley, giving a lower-age boundary to range front fault activity. Another constraint comes from a 14.11 ± 0.05 Ma tuff layer (sample 04CC13) within the Moquegua Group two kilometers south of the fault zone; an 18° southerly tilt of this unit demonstrates post-14 Ma deformation of the Moquegua Group. Additional coarse gravels with a regional slope of 1.5 to 2° to the south (within the range of slopes expected for such a deposit) overlie the deformed ignimbrite above an angular unconformity. This implies that tilting occurred before deposition of the post-Moquegua gravels. These gravels are undated locally, but surface remnants project into the regional bajada surface to the south (Fig. 1) that appears to be correlative with the late Miocene to

Pliocene gravels of the Vitor Valley (4.95 Ma, sample 07TS16). This tentative correlation suggests that significant range front deformation was restricted to the period between 14.11 and 4.95 Ma, but that modern canyons in the piedmont region were incised since 4.95 Ma, perhaps in response to regional block uplift (Phase III deformation).

3.2.3. Majes Valley

The Colca-Majes River cuts through the WAE near the town of Aplao with a 2-km-wide alluviated valley (Fig. 6a and Map C in Fig. 1). Topography is dramatic here, exposing what appears to be a 600 to 800 m high fault scarp that comprises much of the lower half of the WAE (Fig. 6b). West of the valley, the 16.1-13.2 Ma ignimbrites cap Moquegua sediments, forming the ramp morphology easily visible in satellite imagery. Schildgen et al. (2007) dated the most prominent capping ignimbrite in this region at 14.29 ± 0.04 Ma.

Existing INGEMMET maps (2001) and our observations reveal that the piedmont region in this valley contains structures related to an early phase of contractile deformation. Several high-angle reverse faults south of the WAE cut both Mesozoic sedimentary bedrock and lower Moquegua red beds that were deposited before ca. 30 Ma (Sempere et al., 2004). Near the town of Aplao, a reverse fault dipping approximately 70° NE places Jurassic bedrock over lower Moquegua red beds, but does not significantly affect upper Moquegua Group strata (Fig. 6c). Two additional high-angle reverse faults 26 km south of the range front (16.202°S, 72.465°W) affect only lower Moquegua Group sediments. An additional reverse fault 45 km south of the range front (16.359°S, 72.494°W) displays similar relationships, but deformation of upper Moquegua strata appears to be on the order of several hundred meters. An ash intercalated in the deformed Moquegua gravels is dated at 16.25 ± 0.10 Ma (Thouret et al., 2007) and 16.26 ± 0.08 Ma (Sample 07TS13). Given their steep dips, total shortening on these early contractile structures must have been limited. We estimate reverse-sense throw of the reverse faults to be on the order of 100 to 200 m.

Much of the later deformation recorded in the region is extensional. Several high-angle normal faults deform upper Moquegua Group and older units in this area. The most dramatic of these is the normal fault that marks the east-west striking range front (Fig. 6b). Exposures of the fault itself are limited, but the 65° dip of the range front escarpment provides an approximate estimate for the fault dip. The total movement on this fault is difficult to assess, but is likely to be at least as great as the scarp height: 600 to 800 m. Although much of the faulted contact between intrusive bedrock to the north and Moquegua Group sediments to the south is buried in landslide debris, limited exposures of upper Moquegua gravels close to the contact show beds dipping up to 30°S, indicating normal sense

slip. Shear fabrics are cataclastic, and show no mylonites or evidence of plastic deformation, indicating shallow, low-temperature deformational conditions.

A second, NW-striking normal fault was mapped south of the range front. This steeply SW-dipping structure cuts lower Moquegua Group sediments and shows drag folds in sediments on the SW side of the fault suggesting normal-sense displacement. Here the total throw on the fault cannot be determined precisely but may be as much as a few hundred meters. The fault continues southeastward, eventually residing entirely within the Moquegua stratigraphy. In this direction along strike, offsets diminish progressively and the fault eventually dies out into a SSW-facing monocline that deforms upper Moquegua sediments. The NW end of the fault is buried beneath Quaternary valley-fill sediments, so its relationship with the range-bounding fault is unclear. If the two merge, its offset may contribute to differential uplift of the Western Cordillera and Central Andean Plateau relative to the piedmont. Alternatively, it may be related to a similarly oriented fault that follows the axis of the Chuquibamba Valley, a large, landslide-filled tributary valley that extends NW of the WAE.

A third extensional structure shown in the Majes map has a very different orientation. Striking NE and dipping steeply NW, this structure marks the southeastern flank of a small graben developed between it and the WAE scarp. Close to the Majes Valley, the NE-striking fault places upper Moquegua gravels dipping ~30°N, over pre-30 Ma lower Moquegua red beds dipping ~10° northward. Total throw in this area is no more than several hundred meters. Farther southwest, this fault also dies out into a monocline facing northwestward that deforms the 16.1-13.2 Ma ignimbrite caprock in this region.

Minimal activity on the range front fault in the western part of this area occurred after 14.29 Ma, as an overlapping ignimbrite sheet of that age shows only minor warping into a monocline. Farther to the east, deformation timing cannot be well-constrained, as datable units have been eroded off the range front. The age of the other NW-and NE-striking normal faults are constrained only to be younger than the upper Moquegua units that they cut/deform.

3.2.4. Ocoña Valley

The Cotahuasi-Ocoña River is the second major river in the region, draining through the 1-km wide Ocoña Valley as it approaches the coast. Although there is no sharp range front in this region, several faults cut through the valley at a roughly equivalent position (Fig. 7 and Map D in Fig. 1).

Similar to the previous three regions described, the Ocoña Valley transect shows some evidence of early contractile deformation. A 70°N-dipping, W-striking shear zone was mapped in Cretaceous granitic rocks in the northern part of this area. Its dip direction and its burial beneath

undeformed Moquegua units to the west (Fig. 7) lead us to interpret it as a reverse fault with unknown throw.

Later activity included slip on the Iquipi fault, an east-west-striking high-angle structure that Roperch et al. (2006) described as accommodating left-lateral motion prior to 15 Ma and probably before 25 Ma. Later movement on this fault also included a north-side-down component, as upper Moquegua Group sediments step down ca. 100 m on the north side of the fault on the western rim of the valley. Total vertical slip on the fault is probably greater, however, as earlier movement likely contributed to the present-day 200 m escarpment in basement rocks (north-side-down) that can be traced along strike on satellite imagery for at least 35 km to the east of the valley and 15 km to the west of the valley.

The Iquipia fault is characterized by a cataclastic shear zone at least several tens of meters thick. There are no obvious fault-related ductile fabrics in the shear zone, suggesting that deformation took place in the upper crust. Shear orientations strike relatively uniformly sub-parallel to the Iquipi fault escarpment, with the differences in orientation possibly related to a rotational component of movement within the shear zone. Slickenlines are relatively rare on fault surfaces, however, this may be related to hydrothermal alteration. Bedrock is hydrothermally altered extending several hundred meters north of the shear zone (and in places has been extensively mined), but any deformation in this region is difficult to discern,

Farther to the east, the fault escarpment is overlapped by the 14.29 Ma ignimbrite caprock dated by Thouret et al. (2007). Although the fault trace is obscured, it projects into the steep range front in the Majes Valley. The fault projects more clearly toward the west on satellite imagery, but is not clear west of the Caravelli Valley. North of the Iquipi fault, a series of flat bedrock benches dominate the interfluve morphology. Elevations range from 1000 to 1800 m, or 500 to 1200 m above river level, and some benches have a thin veneer of sediment that has been mapped as Moquegua Group by others (e.g., Pecho, 1983). The Iquipi fault may represent the southern boundary of a half-graben in the Ocoña Valley. The flat bedrock benches perched at different levels north of the fault may represent smaller blocks that have experienced some movement, but there is no clear northern boundary to the extended region. Hence the deformation may be similar to what is exposed in the Majes Valley, only without a sharp range-front escarpment. Nonetheless, the swath profiles for this region ("ramp" in Fig. 2) suggest broad deformation that extends all the way to coastal regions.

3.2.5. Coastal/Piedmont uplift

Swath profiles through southern Peru illustrate the dramatic rise in elevations to near 1000 m within a few kilometers of the coastline (Fig. 2). Moquegua group and younger gravels grade to and

onlap basement rocks of the beveled Coastal Cordillera at this elevation (Fig. 1), suggesting sea level was not far below at the time of deposition. Fifty kilometers inland, in the region described by Sébrier et al. (1979), Ocoña Canyon cuts to depths of 1.8 km through a 600-m thick pile of Moquegua Group sediments and underlying bedrock of the piedmont region, implying at least 1.8 km of piedmont uplift since deposition of those sediments. Additional evidence of relatively recent uplift comes from the coastal region itself. At the outlet of the Colca-Majes River, near the town of Camaná, a road-cut through fan-delta sediments exposes beds dipping ~ 6° south, and an angular unconformity at 370 m elevation with flat-lying sediments above. We interpret these two units to be the foreset and topset beds of a single fan-delta complex. Given that the contact between the beds was near sea level at the time of deposition and is likely to have experienced post-depositional subsidence and compaction, the coastal region has been uplifted at least 370 m since deposition. The ~1 km high coastal escarpment that is blanketed by Moquegua Group gravel sheets suggests an upper limit for the magnitude of total coastal uplift. Sempere et al. (2004) described what we believe to be the same exposure as two units they named "Camana A" and "Camana B", and dated a tuff above the contact at 20.83 ± 0.06 Ma ($^{40}Ar/^{39}Ar$ on 3 biotite crystals), implying that uplift post-dated deposition of that tuff. The 4.95 Ma coarse gravels deposited at piedmont elevations above the Vitor Valley, which were likely deposited before significant incision of the Vitor River in the piedmont region, suggest a much tighter constraint on the onset of coastal/piedmont uplift that would drive incision. Similar limits for the onset of coastal/piedmont uplift are reported from northern Chile, where coastal rivers cut through piedmont surfaces and high terraces dated at 6 to 6.4 Ma (Sáez et al., 1999; Hoke et al., 2007).

4. Thermochronologic Constraints on WAE Evolution

Thermochronologic samples collected along the axis of the Ocoña Valley also provide insight into the style, magnitude, and timing of recent deformation. Schildgen et al. (2007) presented a valley-bottom transect of (U-Th)/He zircon dates from the Ocoña Valley, which showed no major discontinuities in the inland-younging trend of ages. Large discontinuities would be expected if significant offset were accommodated in a focused region (Fig. 8). Small offsets can, however, be hidden within the data given analytical uncertainties and the spacing of sample locations. Based on an estimated background exhumation rate of 0.02 mm/yr (Schildgen et al., 2007a), we can infer how large of a discontinuity in age could have been produced due to fault movement and put upper bounds on the amount of displacement that could have occurred without perceptible disruption of the observed smooth age trend. A 100-m vertical displacement along a single fault would produce a 5 Ma discontinuity in the pattern of valley-bottom transect data. Such a small change cannot be discerned given the uncertainty of the data and the spacing of samples. A 500-m vertical offset, however, would

produce a 25 million year step, which, if present, would be likely to stand out on the trend. This analysis suggests that the total amount of range front movement in the Ocoña Valley is likely to be less than 500 m subsequent to the helium closure ages of the youngest zircons defining this trend (ca. 45 Ma).

5. Late Cenozoic uplift through regional warping and block uplift

Deformation between the Western Cordillera and the southwest Peruvian coast reflects growth of the western margin of the Central Andean Plateau. Our mapping demonstrates a long history of changing styles of structural accommodation. Early contractile deformation on high-angle reverse faults likely produced the high topography from which many of the major sedimentary units deposited in the piedmont region were derived. The later shift to a dominance of normal and monoclinal structures by Middle Miocene time suggests a fundamental change in the stress regime that accompanied the latest major phase of surface uplift. Long-wavelength warping dominated in the Cotahuasi-Ocoña region, where prior periods of deformation appear to have had limited effects on the Precambrian basement and Cretaceous intrusive rocks that characterize the region (Fig. 2A). In the Colca-Majes region 70 km to the southeast, deformation accommodating latest uplift transitions to steep monoclines and surface-breaking normal faults. This focusing of surface deformation may be related to the depositional patterns of Jurassic-Cretaceous strata, or to pre-Middle Miocene deformational structures developed preferentially in these rocks. (Figs. 2B and 2C). Supporting the notion of a relationship between structural style and pre-existing conditions are Pb isotopic data that suggest a significant change in crustal chemistry (and, perhaps, physical behavior) at approximately 16°S latitude (Mamani-Huisa, 2006). Another possible cause for the northeast-to-southwest transition in structural style may be the dip of the downgoing Pacific plate. The change in subduction angle from 15° to 30° at approximately 16°S latitude (Cahill and Isacks, 1992) is also likely to affect the stress regime in the overlying plate.

5.2. Plateau growth

The observation that late Neogene evolution of the WAE was dominated by steep normal faulting and monoclinal warping has important implications for the growth kinematics of the western flank of the Central Andean Plateau. Any viable model envisioned for plateau uplift must not invoke significant lateral growth of the plateau toward the Peru-Chile trench. Moreover, we note that up to 1 km of the total 2.5 to 3 km of plateau elevation in this region must be attributed to wholesale uplift of the piedmont region plus the plateau in southern Peru. Thus, a significant component of uplift of the Central Andean Plateau relative to sea level was not accommodated by surface deformation at the

plateau margin. It seems unlikely that this broader component of uplift can be attributed to lower crustal flow in response to Brazilian Shield underthrusting beneath the eastern margin (e.g., Isacks, 1988; Allmendinger et al., 1997; Lamb and Hoke, 1997; Wörner et al., 2002, Husson and Sempere, 2003; Gerbault et al., 2005; Hindle et al., 2005) or to catastrophic delamination of a thickened lower lithosphere as has been envisioned for the Central Andean Plateau proper (e.g., Kay and Kay, 1993; Garzione et al., 2006). A better understanding of possible mechanisms must await better constraints on the temporal evolution of piedmont uplift relative to deformation along the WAE, but we speculate that subduction zone processes may have played an under-appreciated role.

Shallowing of the dip of the subducting slab can have several important implications for the overriding plate. One possibility is that progressive subduction erosion of lithosphere beneath the piedmont and Western Cordillera accompanied by thermal thinning can lead to isostatic uplift of the upper crust, as Isacks (1988) envisioned for the early-middle Miocene phases of plateau uplift. Shallowing of the slab dip to less than 20° in the Cotahuasi-Ocoña region relative to areas farther southeast could generate uplift in the overriding plate, particularly in coastal regions. Such a process appears to have occurred in the Pampean flat-slab region of the Central Andes, from 27 to 33.5°S, where the onset of basement block uplift shows remarkable correlation with the eastward migration of the volcanic arc associated with the shallowing slab dip (Ramos et al., 2002). Several studies have similarly noted the spatial correlation between the southern portion of the Peruvian flat slab region (extending from 5 to 16°S) and the current ridge collision zone at 15-16°S (e.g., Nur and Ben-Avraham, 1981; 1983; Pilger, 1981; Mcgeary et al., 1985). Gutscher et al. (1999) attributed the flat slab region to the combined buoyancy of the subducted ridge (a feature almost 250 km wide and rising up to 1600 m above the surrounding sea floor) as well as that of a subducted "Lost Inca Plateau" beneath northern Peru. The oblique subduction angle of the Nazca plate beneath central and southern Peru has lead to a c. 500 km southward migration of the collision zone between the Nazca Ridge and the coast since its initial collision near 11.2°S at c. 11 Ma (Hampel, 2002; Clift et al., 2003). This implies that effects at the current position of the ridge near 16°S are likely to have affected coastal regions only within the past few million years.

7. Conclusions

Structural mapping and thermochronological studies in southwest Peru provide important insights into the history of deformation and its relation to surface uplift between the coast and the western margin of the Central Andean Plateau. Changing stress regimes in the developing plateau led to different generations of reverse faulting, normal faulting, and long-wavelength monoclines that accommodated uplift of the plateau relative to the coast. Early contractile deformation was

accommodated primarily on a series of west-vergent reverse faults that affected Oligocene to Early Miocene sediments as well as older units. In the Ocoña Valley, these structures are dispersed throughout the forearc region and each accommodated uplift on the order of 100 to 300 m. Early movement of structures farther to the east is less well constrained, but is likely to have been more focused along the sharp range front escarpment. By Middle Miocene time, deformation became dominated by normal faulting and broad monoclinal warping. Normal fault movement likely contributed to the sharp morphological expression of the range front seen today in the Majes Valley and to the southeast. On the west side of the Majes Valley and in the Ocoña Valley, extension produced a series of grabens. Total post-16 Ma uplift of inland regions relative to coastal regions accommodated on discrete faults near the WAE is most likely on the order of several hundred meters, but cannot exceed 1 km. This implies that latest uplift of the Western Cordillera to current elevations involved both 1) ~ 1.5 to 2 km of differential uplift of the cordillera relative to the piedmont across the WAE that was accommodated by both monoclinal folding and normal faulting; and 2) ~1 km of coupled uplift of the piedmont and the Central Andean Plateau.

The changes in deformation patterns through time on the western margin of the Central Andean Plateau likely reflect changing dynamics of the evolving plateau. Early contraction in the Central Andes lead to extensive upper crustal shortening and thickening. A major phase of uplift that started at ca. 9 to 10 Ma (Schildgen et al., 2007; Thouret et al., 2007) was accompanied by an apparent change in the style of structural accommodation along the western margin of the plateau in southwest Peru, with uplift of the plateau relative to the piedmont accommodated by structures that resulted in little, if any, propagation of the plateau toward the Peru-Chile trench. Processes that have been envisioned to explain this late Neogene uplift include lower crustal flow into the western part of the Central Andean Plateau, various forms and geometries of lithospheric delamination, and a shallowing of subduction angle. While our results alone do not negate any of these hypotheses, they contribute to a growing knowledge base on the kinematics of plateau margin evolution that will, eventually, inform our understanding of plateau geodynamics.

Acknowledgments

We thank T. Smith and J. Bradley for help with fieldwork; Malcolm Pringle and Bill Olzscheski for help with $^{40}Ar/^{39}Ar$ analyses. This work was supported by the National Science Foundation Tectonics Division grant no. EAR-0409359.

References

Allmendinger, R.W., Jordan, T.E., Kay, S.M., and Isacks, B.L., 1997, The evolution of the Altiplano-Puna plateau of the central Andes: Annual Reviews of Earth and Planetary Sciences, v. 25, p. 139-174.

Baby, P., Rochat, P., Mascle, G., and Herail, G., 1997, Neogene shortening contribution to crustal thickening in the back arc of the Central Andes: Geology, v. 25, no. 10, p. 883-886.

Barke, R., and Lamb, S., 2006, Late Cenozoic uplift of the Eastern Cordillera, Bolivian Andes: Earth and Planetary Science Letters, v. 249, no. 3-4, p. 350-367.

Barnes, J.B., Ehlers, T.A., McQuarrie, N., O'Sullivan, P.B., and Pelletier, J.D., 2006, Eocene to recent variations in erosion across the central Andean fold-thrust belt, northern Bolivia: Implications for plateau evolution: Earth and Planetary Science Letters, v. 248, no. 1-2, p. 118-133.

Beck, S. L., and Zandt, G., 2002, The nature of orogenic crust in the central Andes: Journal of Geophysical Research-Solid Earth, v. 107, no. B10.

Burchfiel, B. C., Chen, Z., Liu, Y., and Royden, L.H., 1995, Tectonics of the Longmen Shan and adjacent regions: International Geological Reviews, v. 37, no. 8, p. 661-736.

Cahill, T., and Isacks, B.L., 1992, Seismicity and shape of the subducted Nazca plate: Journal of Geophysical Research, v. 97, p. 17503-17529.

Clark, M. K., House, M. A., Royden, L. H., Whipple, K. X., Burchfiel, B. C., Zhang, X., and Tang, W., 2005, Late Cenozoic uplift of southeastern Tibet: Geology, v. 33, no. 6, p. 525-528.

Clark, M. K., and Royden, L. H., 2000, Topographic ooze: Building the eastern margin of Tibet by lower crustal flow: Geology, v. 28, no. 8, p. 703-706.

Clift, P. D., Pecher, I., Kukowski, N., and Hampel, A., 2003, Tectonic erosion of the Peruvian forearc, Lima Basin, by subduction and Nazca Ridge collision: Tectonics, v. 22, no. 3.

Echavarría, L., Hernández, R., Allmendinger,R.,and Reynolds, J., 2003, Subandean thrust and fold belt of northwestern Argentina; geometry and timing of the Andean evolution: AAPG Bulletin, v. 87, p. 965-985.

Elger, K., Oncken, O., and Glodny, J., 2005, Plateau-style accumulation of deformation: Southern Altiplano: Tectonics, v. 24, no. 4.

England, P., and Houseman, G., 1985, Role of Lithospheric Strength Heterogeneities in the Tectonics of Tibet and Neighboring Regions: Nature, v. 315, no. 6017, p. 297-301.

Farías, M., Charrier, R., Comte, D., Martinod, J., and Herail, G., 2005, Late Cenozoic deformation and uplift of the western flank of the Altiplano: Evidence from the depositional, tectonic, and geomorphologic evolution and shallow seismic activity (northern Chile at 19 degrees 30' S): Tectonics, v. 24, no. 4.

García, M., and Herail, G., 2005, Fault-related folding, drainage network evolution and valley incision during the Neogene in the Andean Precordillera of Northern Chile: Geomorphology, v. 65, no. 3-4, p. 279-300.

Garzione, C. N., Molnar, P., Libarkin, J. C., and MacFadden, B. J., 2006, Rapid late Miocene rise of the Bolivian Altiplano: Evidence for removal of mantle lithosphere: Earth and Planetary Science Letters, v. 241, no. 3-4, p. 543-556.

Gerbault, M., Martinod, J., and Herail, G., 2005, Possible orogeny-parallel lower crustal flow and thickening in the Central Andes: Tectonophysics, v. 399, no. 1-4, p. 59-72.

Ghosh, P., Garzione, C. N., and Eiler, J. M., 2006, Rapid uplift of the Altiplano revealed through C-13-O-18 bonds in paleosol carbonates: Science, v. 311, no. 5760, p. 511-515.

Gregory-Wodzicki, K. M., 2000, Uplift history of the Central and Northern Andes: A review: Geological Society of America Bulletin, v. 112, no. 7, p. 1091-1105.

Gubbels, T. L., Isacks, B. L., and Farrar, E., 1993, High-Level Surfaces, Plateau Uplift, and Foreland Development, Bolivian Central Andes: Geology, v. 21, no. 8, p. 695-698.

Gutscher, M. A., Olivet, J.L., Aslanian, D., Eissen, J.P., and Maury, R., 1999, The "lost Inca Plateau": cause of flat subduction beneath Peru?: Earth and Planetary Science Letters, v. 171, p. 335-341.

Hampel, A., 2002, The migration history of the Nazca Ridge along the Peruvian active margin: a re-

evaluation: Earth and Planetary Science Letters, v. 203, no. 2, p. 665-679.
Hindle, D., Kley, J., Oncken, O., and Sobolev, S., 2005, Crustal balance and crustal flux from shortening estimates in the Central Andes: Earth and Planetary Science Letters, v. 230, no. 1-2, p. 113-124.
Hoke, G., 2006, The influence of climate and tectonics on the geomorphology of the western slope of the central Andes: Ph.D. Thesis, Cornell University, Ithaca.
Hoke, G.D., Isacks, B.L., Jordan, T.E., Blanco, N., Tomlinson, A.J., and Ramezani, J., 2007, Geomorphic evidence for post-10 Ma uplift of the western flank of the central Andes 18°30'-22°S: Tectonics, v. 26, TC5021, doi:10.1029/2006TC002082.
Houseman, G., and England, P., 1986, Finite strain calculations of continental deformation 1. Method and general results for convergent zones: Journal of Geophysical Research-Solid Earth and Planets, v. 91, no. B3, p. 3651-3663.
Houseman, G. A., McKenzie, D. P., and Molnar, P., 1981, Convective Instability of a Thickened Boundary-Layer and Its Relevance for the Thermal Evolution of Continental Convergent Belts: Journal of Geophysical Research, v. 86, no. NB7, p. 6115-6132.
Husson, L., and Sempere, T., 2003, Thickening of the Altiplano crust by gravity-driven crustal channel flow: Geophysical Research Letters, v. 30, no. 5.
INGEMMET, 2001, Mapa Geológico del cuadrángulo de Caravelí, Scale 1:100,000, Instituto Geológico Minero y Metalúrgico.
Isacks, B. L., 1988, Uplift of the Central Andean Plateau and Bending of the Bolivian Orocline: Journal of Geophysical Research-Solid Earth and Planets, v. 93, no. B4, p. 3211-3231.
Jordan, T. E., Isacks, B. L., Allmendinger, R. W., Brewer, J. A., Ramos, V. A., and Ando, C. J., 1983, Andean Tectonics Related to Geometry of Subducted Nazca Plate: Geological Society of America Bulletin, v. 94, no. 3, p. 341-361.
Kay, R. W., and Kay, S. M., 1993, Delamination and Delamination Magmatism: Tectonophysics, v. 219, no. 1-3, p. 177-189.
Kirby, E., and Whipple, K.X, 2001, Quantifying differential rock-uplift rates via stream profile analysis: Geology, v. 29, no. 5, p. 415-418.
Kley, J., and Monaldi, C.R., 1998, Tectonic shortening and crustal thickness in the central Andes: How good is the correlation?: Geology, v. 26, p. 723-726.
Lamb, S., and Hoke, L., 1997, Origin of the high plateau in the Central Andes, Bolivia, South America: Tectonics, v. 16, no. 4, p. 623-649.
Lamb, S., Hoke, L., Kennan, I., and Dewey, J., 1997, Cenozoic evolution of the central Andes in Bolivia and northern Chile, in Burg, J.-P., and Ford, M., eds., Orogeny Through Time, Geological Society Special Publication, v. 121, p. 237-264.
McQuarrie, N., 2002, The kinematic history of the central Andean fold-thrust belt, Bolivia: Implications for building a high plateau: Geological Society of America Bulletin, v. 114, no. 8, p. 950-963.
Mamani-Huisa, M., 2006, Variations in magma composition in time and space along the Central Andes (13°S-28°S): Ph.D. Thesis, Georg-August-Universität zu Göttingen, Germany, 125 p.
Mcgeary, S., Nur, A., and Benavraham, Z., 1985, Spatial gaps in arc volcanism - the effect of collision or subduction of oceanic plateaus: Tectonophysics, v. 119, p. 195-221.
Megard, F., 1984, The Andean orogenic period and its major structures in central and northern Peru: Journal of the Geological Society of London, v. 141, p. 893-900.
Mortimer, C., 1973, The Cenozoic history of the southern Atacama Desert, Chile: Journal of the Geological Society of London, v. 129, p. 505-526.
Müller, J. P., Kley, J., and Jacobshagen, V., 2002, Structure and Cenozoic kinematics of the Eastern Cordillera, southern Bolivia (21 degrees S): Tectonics, v. 21, no. 5.

Muñoz, J., 1956, Handbook of South American Geology: Memoir Geological Society of America, v. 65, p. 187-214.

Muñoz, N., and Charrier, R., 1996, Uplift of the western border of the Altiplano on a west-vergent thrust system, Northern Chile: Journal of South American Earth Sciences, v. 9, no. 3-4, p. 171-181.

Noble, D. C., Mckee, E. H., and Megard, F., 1979, Early Tertiary Incaic Tectonism, Uplift, and Volcanic Activity, Andes of Central Peru: Geological Society of America Bulletin, v. 90, no. 10, p. 903-907.

Noble, D. C., McKee, E. H., Mourier, T., and Megard, F., 1990, Cenozoic Stratigraphy, Magmatic Activity, Compressive Deformation, and Uplift in Northern Peru: Geological Society of America Bulletin, v. 102, no. 8, p. 1105-1113.

Nur, A. and Ben-Avraham, Z., 1981, Volcanic gaps and the consumption of aseismic ridges in South America: Geological Society of America Memoirs, v. 154, p. 729-740.

-, 1983, Volcanic gaps due to oblique consumption of aseismic ridges: Tectonophysics, v. 99, p. 355-362.

Paola, C., and Mohrig, D., 1996, Palaeohydraulics revisited: palaeoslope estimation in coase-grained braided rivers: Basin Research, v. 8, p. 243-254.

Pardo-Casas, F., and Molnar, P., 1987, Relative motion of the Nazca (Farallon) and South American plates since late Cretaceous time: Tectonics, v. 6, no. 3, p. 233-248.

Pecho, G., 1983, Mapa geológico del cuadrángle de Caravelí, Instituto Geológico Minero y Metalúrgico, scale 1:100,000: INGEMMET.

Pilger, R. H., 1981, Plate reconstructions, aseismic ridges, and low-angle subduction beneath the Andes: Geological Society of America Bulletin, v. 92, p. 448-456.

Rech, J. A., Currie, B. S., Michalski, G., and Cowan, A. M., 2006, Neogene climate change and uplift in the Atacama Desert, Chile: Geology, v. 34, no. 9, p. 761-764.

Ramos, V.A., Cristallini, E.O., and Perez, D.J., 2002, The Pampean flat-slab of the Central Andes: Journal of South American Earth Sciences, v. 15, no. 1, p. 59-78.

Roperch, P., Sempere, T., Macedo, O., Arriagada, C., Fornari, M., Tapia, C., García, M., and Laj, C., 2006, Counterclockwise rotation of late Eocene-Oligocene fore-arc depostis in southern Peru and its significance for oroclinal bending in the central Andes: Tectonics, v. 25.

Royden, L. H., Burchfiel, B. C., King, R. W., Wang, E., Chen, Z. L., Shen, F., and Liu, Y. P., 1997, Surface deformation and lower crustal flow in eastern Tibet: Science, v. 276, no. 5313, p. 788-790.

Schildgen, T. F., Hodges, K.V., Whipple, K.X, Reiners, P.W., and Pringle, M.S., 2007, Uplift of the western margin of the Andean plateau revealed from canyon incision history, southern Peru: Geology, v. 35, no. 6, p. 523-526.

Schildgen, T.F., Hodges, K.V., Whipple, K.X, and van Soest, M., (2007) Changing styles of deformation along the western margin of the Andean Plateau, southern Peru, American Geophysical Union Abstracts with Program.

Schmitz, M., 1994, A Balanced Model of the Southern Central Andes: Tectonics, v. 13, no. 2, p. 484-492.

Schurr, B., Rietbrock, A., Asch, G., Kind, R., and Oncken, O., 2006, Evidence for lithospheric detachment in the central Andes from local earthquake tomography: Tectonophysics, v. 415, no. 1-4, p. 203-223.

Sáez, A.L., Cabrera, L., Jensen, A., and Chong, G., 1999, Late Neogene lacustrine record and palaeogeography in the Quillangua Llamar a basin, central Andean fore-arc (northern Chile): Palaeogr. Palaeoclimatol. Palaeoecol., v. 151, p. 5-37.

Sébrier, M. Marocco, R., Gross, J.J., Macedo, S., and Montoya, R., 1979, Evolución neógena del piedemonte Pacifico de los Andes del sur del Perú, *in* Segundo Congreso Geológico Chileno, Arica, Proceedings, p. 177-188.

Sébrier, M., Mercier, J., Mégard, F., Laubacher, G., and Carey-Gailhardis, E., 1985, Quaternary normal and reverse faulting and the state of stress in the central Andes of south Peru: Tectonics, v. 4, no. 7, p. 739-780.

Sempere, T., Fornari, M., Acosta, J., Flores, A., Jacay, J., Peña, D., Roperch, P., and Taipe, E., 2004, Estratigrafía, geochronología, paleogeografía y paleotectónica de los dépositos de antearco del sur del Perú, in XII Congreso Peruano de Geología, Lima, p. 533-536.

Sheffels, B. M., 1990, Lower Bound on the Amount of Crustal Shortening in the Central Bolivian Andes: Geology, v. 18, no. 9, p. 812-815.

Silver, P. G., Russo, R. M., and Lithgow-Bertelloni, C., 1998, Coupling of South American and African Plate motion and Plate deformation: Science, v. 279, no. 5347, p. 60-63.

Somoza, R., 1998, Updated Nazca (Farallon) - South America relative motions during the last 40 My: implications for mountain building in the central Andean region: Journal of South American Earth Sciences, v. 11, no. 3, p. 211-215.

Steinmann, G., 1929, Geologie von Peru: Heidelberg University, 448 p.

Thouret, J.-C., Wörner, G., Gunnell, Y., Singer, B., Zhang, X., and Souriot, T., 2007, Geochronologic and stratigraphic constraints on canyon incision and Miocene uplift of the Central Andes in Peru: Earth and Planetary Science Letters, v. 263, p. 151-166.

Tosdal, R.M., Clark, A.H., and Farrar, E., 1984, Cenozoic polyphase landscape and tectonic evolution of the Cordillera Occidental, southernmost Peru: Geological Society of America Bulletin, v. 95, p. 1318-1332.

Victor, P., Oncken, O., and Glodny, J., 2004, Uplift of the western Altiplano plateau: Evidence from the Precordillera between 20 degrees and 21 degrees S (northern Chile): Tectonics, v. 23, no. 4.

Vietor, T., and Oncken, O., 2005, Controls on the shape and kinematics of the Central Andean Plateau flanks: Insights from numerical modeling: Earth and Planetary Science Letters, v. 236, no. 3-4, p. 814-827.

Wörner, G., Hammerschmidt, K., Henjes-Kunst, F., Lezaun, J., and Wilke, H., 2000, Geochronology (Ar-40/Ar-39, K-Ar and He-exposure ages) of Cenozoic magmatic rocks from Northern Chile (18-22 degrees S): implications for magmatism and tectonic evolution of the central Andes: Revista Geologica De Chile, v. 27, no. 2, p. 205-240.

Wörner, G., Uhlig, D., Kohler, I., and Seyfried, H., 2002, Evolution of the West Andean Escarpment at 18 degrees S (N. Chile) during the last 25 Ma: uplift, erosion and collapse through time: Tectonophysics, v. 345, no. 1-4, p. 183-198.

Figure Captions

Figure 1. Location map showing simplified geology and regional morphology of southern Peru. Geology layer is draped over both a semi-transparent 30-m resolution digital elevation model derived from Advanced Spaceborne Thermal Emission and Reflection Radiometer (ASTER) imagery and a shaded relief map. Faults are shown as white lines. Dashed rectangles show regions of focused structural mapping. Volcanic cones delineating the Western Cordillera at the western margin of the Altiplano are labeled. White dots show sample locations for zircon (U-Th)/He thermochronology. Dashed-dot white lines show locations of geological cross-sections.

Figure 2. Topographic swath profiles derived from 90-m resolution Shuttle Radar Topography Mission (SRTM) digital elevation data. Swaths selected are 6-km wide and traverse the region

starting from the escarpment morphology east of the Colca-Majes drainage and moving toward the ramp morphology of the Cotahuasi-Ocoña drainage. Light gray lines show the mean elevations from the swaths, and dark gray lines show simplified profiles created by projecting the regional surface across drainages.

Figure 3. Geological cross-sections based on mapped surface geology with locations shown in Figure 1. Cross-section A to A' is west of the Cotahuasi-Ocoña Valley; cross-section B to B' is west of the Colca-Majes Valley; cross-section C to C' is parallel to the Molles Valley. Colors and geological units used are identical to those shown in Figure 1. Vertical exaggeration in all cross-sections is 3:1.

Figure 4. Geological map of Sihuas Valley near range front. Relief is from 15-m resolution band 3N from ASTER imagery. Stereonet plots show contour lines of poles to shear planes (and poles), and white bars indicate region from which shear planes were measured. White dot shows location for sample 05TS43, an undeformed ignimbrite intercalated with Upper Moquegua sediments that cross the main shear zone. Location of field photo is also shown. Field photo reveals a normal fault contact dipping steeply to the southwest between the Moquegua Group and Cretaceous intrusive bedrock. Symbols include: Ks-gr/gd: Cretaceous granite/ granodiorite; O-mo: Oligocene Lower Moquegua; and M-mo: Miocene Upper Moquegua; Q-al: Quaternary alluvium.

Figure 5. Geological map of range front at Molles Valley north of the town of Pedregal. Stereonets show poles and contours of poles of shear fractures north of the contact between intrusive bedrock and Moquegua Group sediments. Location of samples 04CC12 and 04CC13 are shown. Dashed line above sample 04CC13 represents angular unconformity between the tilted ash bed and untilted uppermost Moquegua gravels. Field photo shows red beds of ower Moquegua Group warped upwards as they near the fault zone. People for scale. Symbols in map include Ks-gr/la: Cretaceous granite and latite; O-mo: Lower Moquegua red beds; M-mo: Upper Moquegua sands; Q-al: Quaternary alluvium.

Figure 6. Geology map of range front in Majes Valley and field photos. Shown on map are locations of field photo of range front escarpment (photo 4b), field photo of the high-angle thrust fault near Aplao (photo 4c) and sample 04TS22, an ignimbrite boulder derived from the Huaylillas Ignimbrite. Map symbols represent the following units: PC-gr: Precambrian granite; Js-gr/la: Jurassic granites and latites; Ks-gd: Cretaceous granodiorite; O-mo: Oligocene Lower Moquegua Group red beds; M-mo: Miocene Upper Moquegua Group conglomerates and gravels; Q-al: Quaternary alluvium.

Figure 7. Ocoña Valley geology map. Stereonet plots show contour lines of poles to shear planes (and poles), and white bars indicate region from which shear planes were measured. Sample PIG-03-126 was from a rhyolite capping the Upper Moquegua sediments dated at 13.20 Ma (Thouret et al., 2007). Unit symbols include: N-mo: Neogene Upper Moquegua Group, P-mo: Lower Moquegua Group, Ks-an: Cretaceous andesite; Ks-gd: Cretaceous granodiorite; Q-al: Quaternary alluvium; and PC-gn: Precambrian gneiss.

Figure 8. Schematic drawing of thermochronometer data collected along a valley cutting through a deformed margin and zircon (U-Th)/He data collected along a valley-bottom transects in Ocoña Valley. Drawing illustrates how uplift accommodated on a major surface-breaking fault produces a clear discontinuity in the pattern of thermochronologic data crossing the fault zone, which contrasts with the pattern of smooth decrease in ages collected through a monocline. Data from Ocoña Valley shows increasingly young ages farther inland, with no clear discontinuities in age that would be indicative of significant movement on surface-breaking faults.

Table 1. Constraints on late Cenzoic uplift for the Central Andes.

Table 2. $^{40}Ar/^{39}Ar$ sample description and context.

Table 3. Age spectra analysis for $^{40}Ar/^{39}Ar$ data.

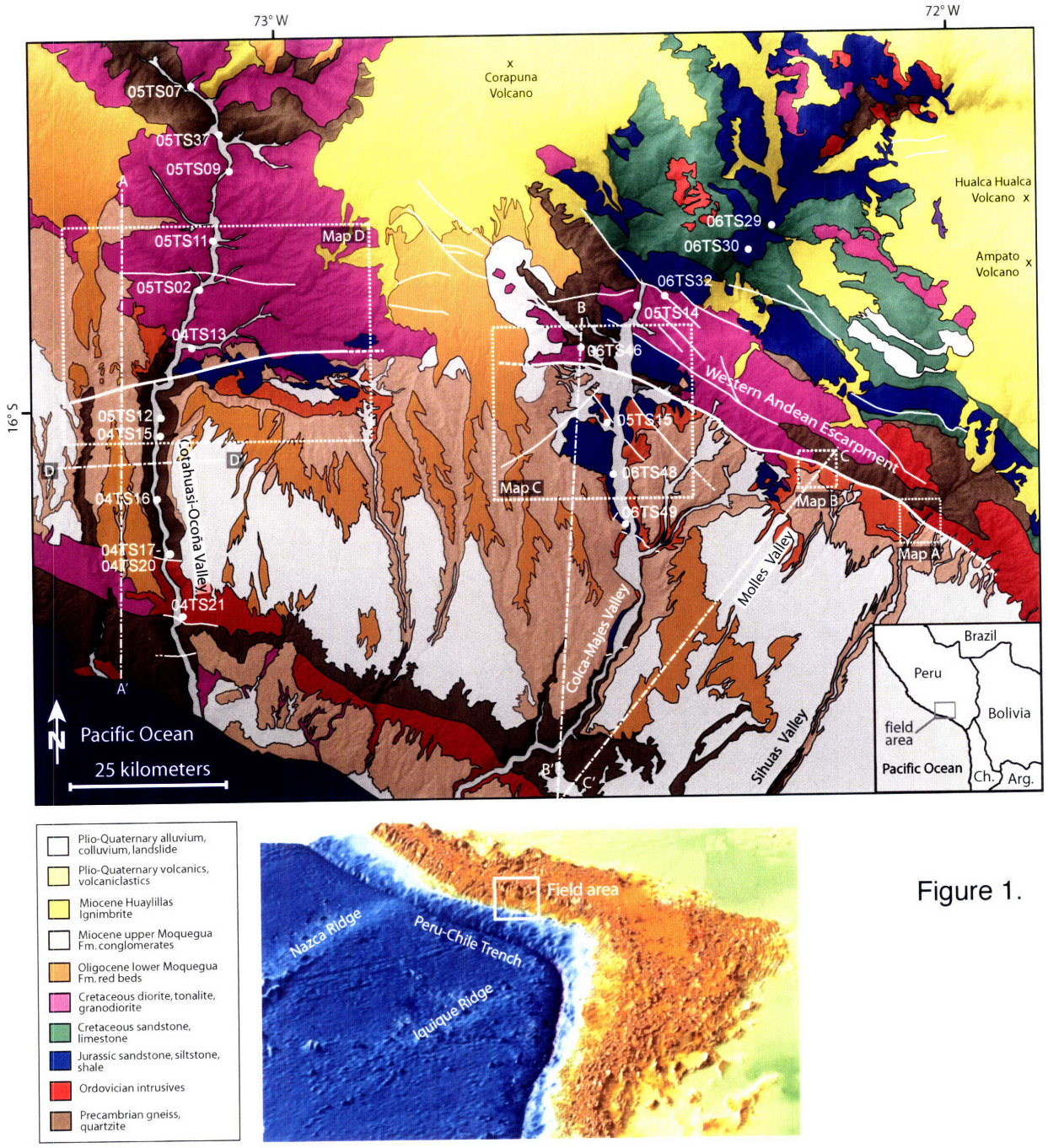
73° W
72° W
16° S
Corapuna Volcano
Hualca Hualca Volcano
Ampato Volcano
05TS07
05TS37
05TS09
05TS11
05TS02
04TS13
05TS12
04TS15
04TS16
04TS17-04TS20
04TS21
06TS29
06TS30
06TS32
05TS14
06TS46
05TS15
06TS48
06TS49
Map D
Map C
Map B
Map A
Western Andean Escarpment
Cotahuasi-Ocoña Valley
Colca-Majes Valley
Molles Valley
Sihuas Valley
Pacific Ocean
25 kilometers
Brazil
Peru
Bolivia
field area
Pacific Ocean
Ch.
Arg.
Plio-Quaternary alluvium, colluvium, landslide
Plio-Quaternary volcanics, volcaniclastics
Miocene Huaylillas Ignimbrite
Miocene upper Moquegua Fm. conglomerates
Oligocene lower Moquegua Fm. red beds
Cretaceous diorite, tonalite, granodiorite
Cretaceous sandstone, limestone
Jurassic sandstone, siltstone, shale
Ordovician intrusives
Precambrian gneiss, quartzite
Nazca Ridge
Peru-Chile Trench
Iquique Ridge
Field area

Figure 1.

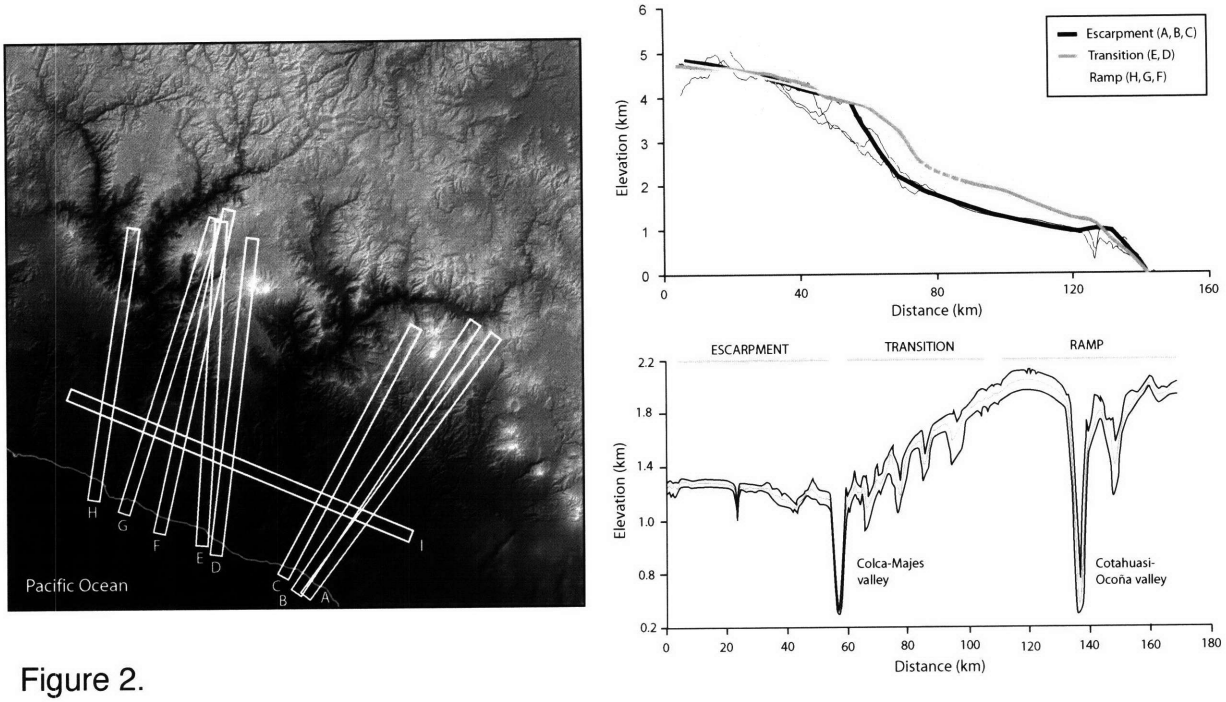
Pacific Ocean
H
G
F
E
D
C
B
A
I
Escarpment (A, B, C)
Transition (E, D)
Ramp (H, G, F)
Elevation (km)
Distance (km)
ESCARPMENT
TRANSITION
RAMP
Colca-Majes valley
Cotahuasi-Ocoña valley

Figure 2.

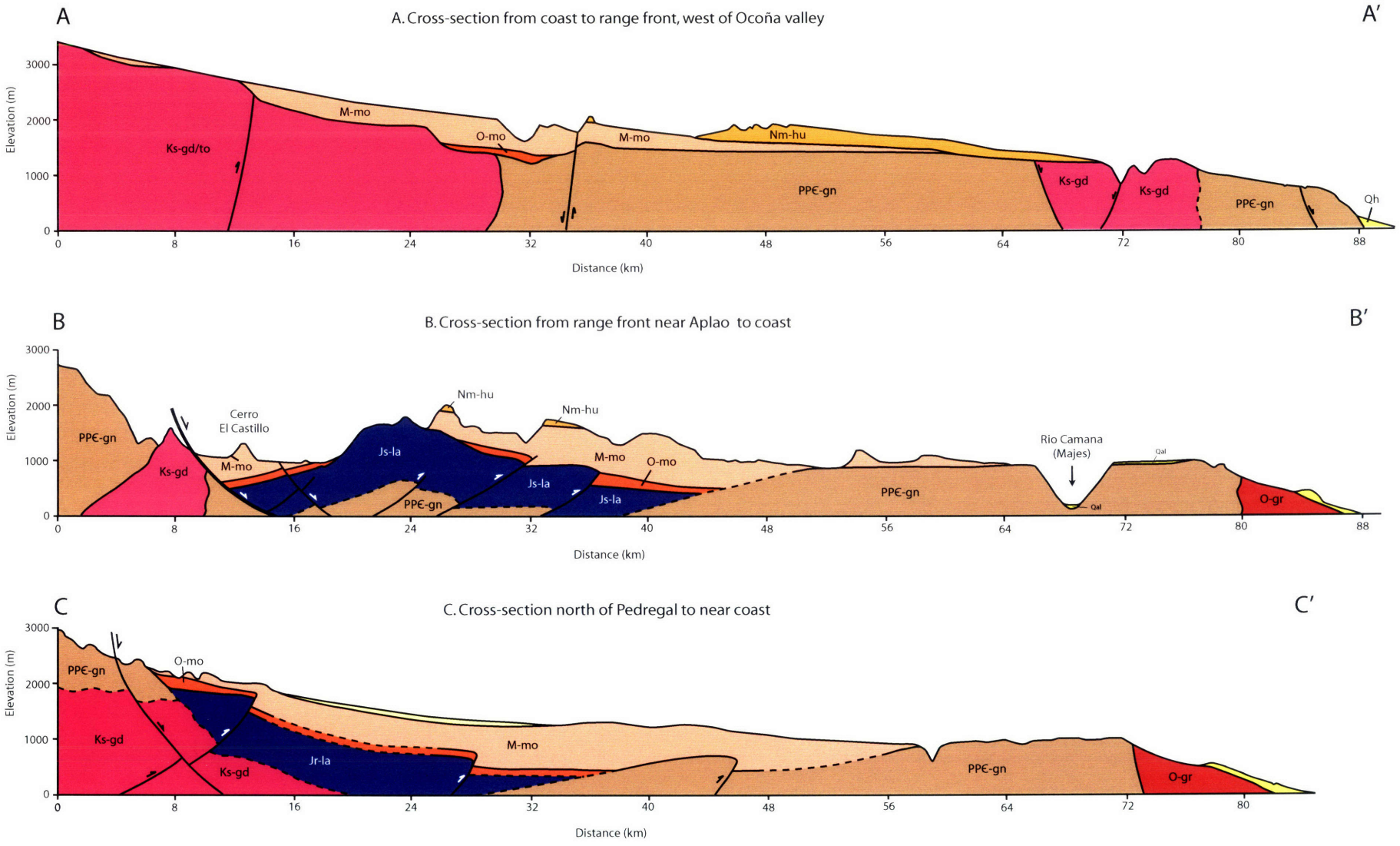
A
A. Cross-section from coast to range front, west of Ocoña valley
A′
Elevation (m)
3000
2000
1000
0
Ks-gd/to
M-mo
O-mo
M-mo
Nm-hu
PPЄ-gn
Ks-gd
Ks-gd
PPЄ-gn
Qh
0
8
16
24
32
40
48
56
64
72
80
88
Distance (km)
B
B. Cross-section from range front near Aplao to coast
B′
Elevation (m)
3000
2000
1000
0
PPЄ-gn
Ks-gd
Cerro
El Castillo
M-mo
Js-la
Nm-hu
Nm-hu
M-mo
O-mo
Js-la
Js-la
PPЄ-gn
Rio Camana
(Majes)
Qal
Qal
PPЄ-gn
O-gr
0
8
16
24
32
40
48
56
64
72
80
88
Distance (km)
C
C. Cross-section north of Pedregal to near coast
C′
Elevation (m)
3000
2000
1000
0
O-mo
PPЄ-gn
Ks-gd
Jr-la
Ks-gd
M-mo
PPЄ-gn
O-gr
0
8
16
24
32
40
48
56
64
72
80
Distance (km)

Figure 3.

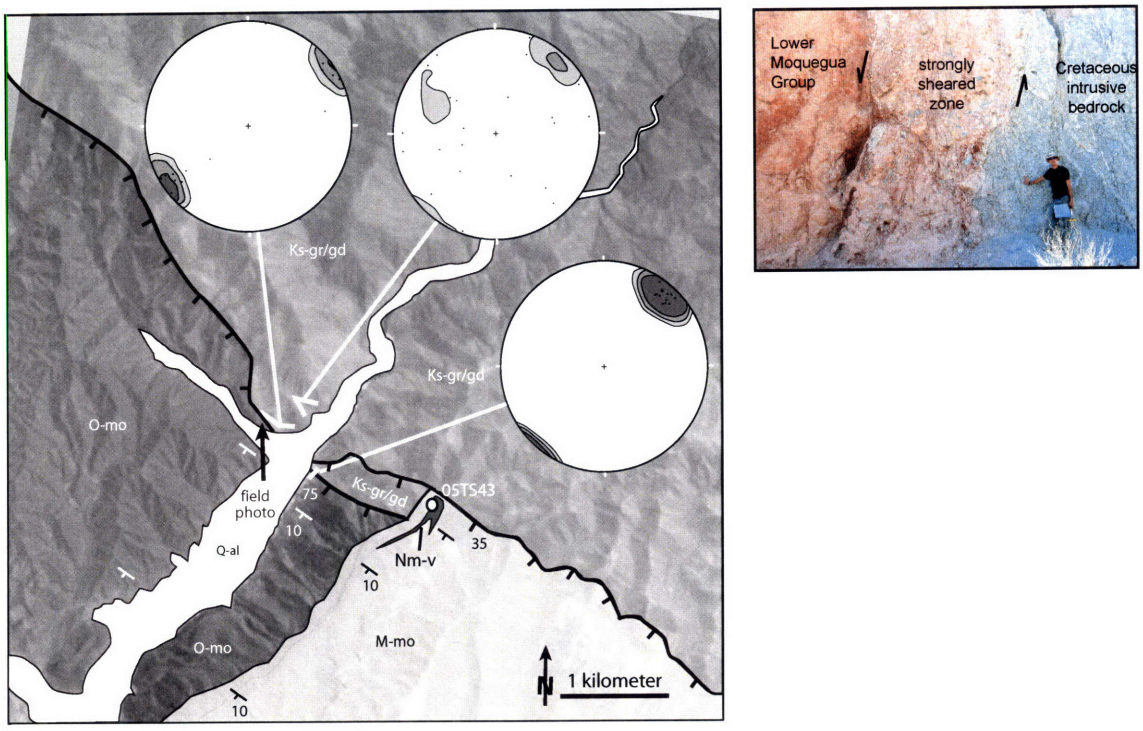
Ks-gr/gd
Ks-gr/gd
O-mo
field
photo
75
10
Ks-gr/gd
05TS43
35
Q-al
Nm-v
10
O-mo
M-mo
10
1 kilometer
Lower
Moquegua
Group
strongly
sheared
zone
Cretaceous
intrusive
bedrock

Figure 4.

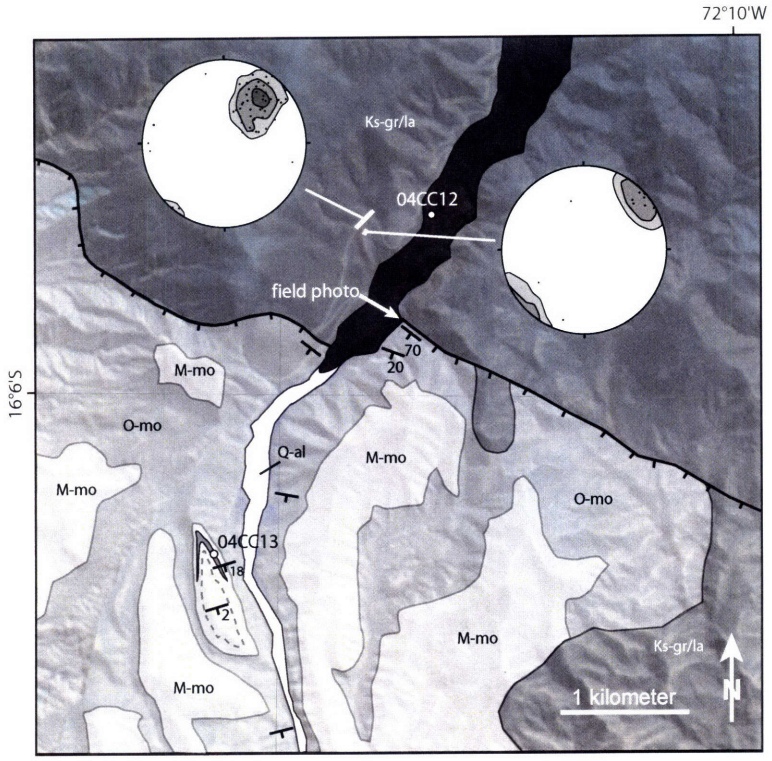
72°10'W
16°6'S
Ks-gr/la
04CC12
field photo
70
20
M-mo
O-mo
Q-al
M-mo
M-mo
O-mo
04CC13
18
12
M-mo
M-mo
Ks-gr/la
1 kilometer
N

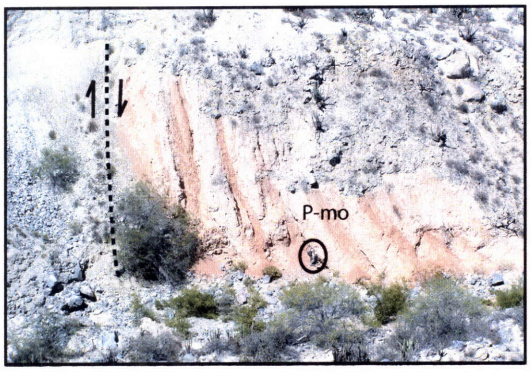
P-mo

Figure 5.

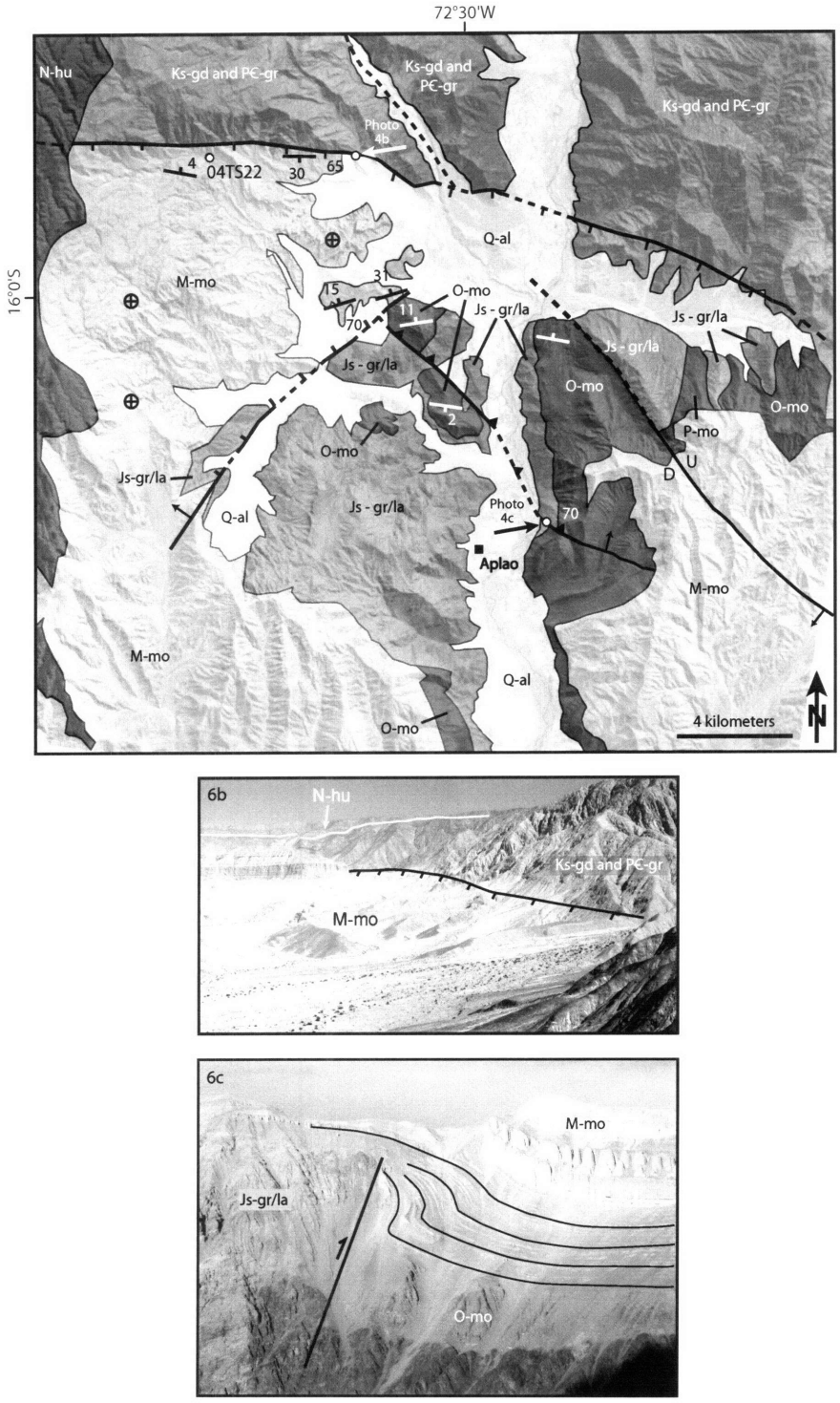
72°30'W
16°0'S
N-hu
Ks-gd and P€-gr
Ks-gd and P€-gr
Ks-gd and P€-gr
Photo 4b
4
04TS22
30
65
Q-al
M-mo
15
3
O-mo
11
Js - gr/la
70
Js - gr/la
Js - gr/la
Js - gr/la
O-mo
O-mo
2
P-mo
U
D
O-mo
Js-gr/la
Q-al
Js - gr/la
Photo 4c
70
Aplao
M-mo
M-mo
Q-al
O-mo
4 kilometers
N
6b
N-hu
Ks-gd and P€-gr
M-mo
6c
M-mo
Js-gr/la
O-mo

Figure 6.

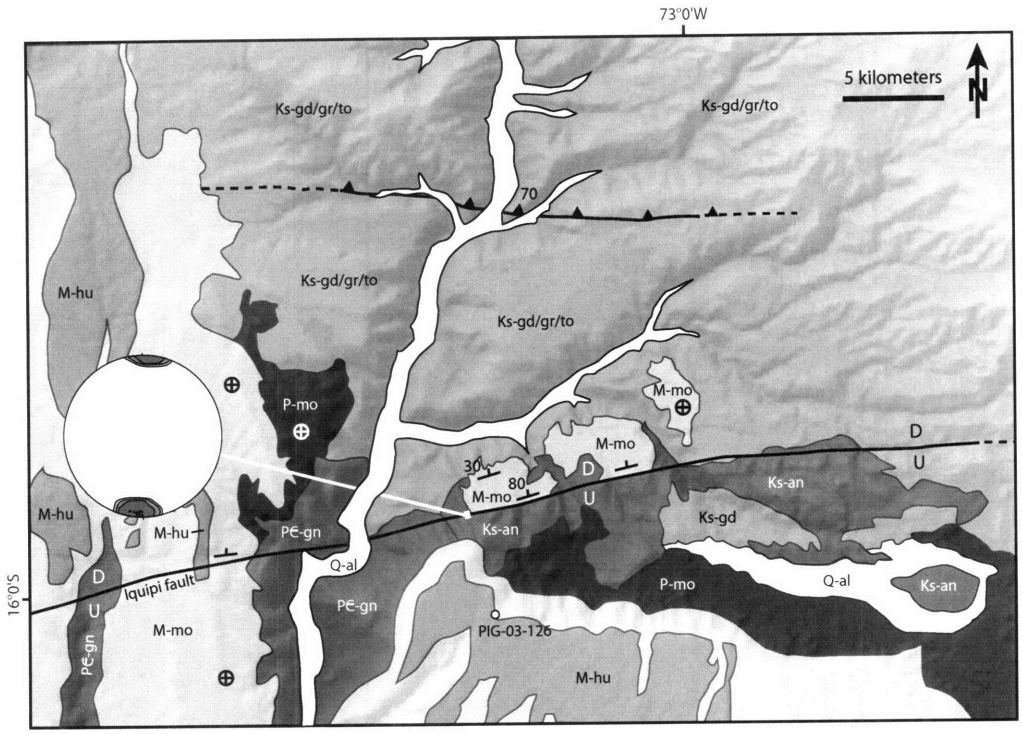
73°0'W
16°0'S
5 kilometers
N
Ks-gd/gr/to
Ks-gd/gr/to
70
Ks-gd/gr/to
Ks-gd/gr/to
M-hu
P-mo
M-mo
M-mo
D
U
30
80
M-mo
D
U
Ks-an
Ks-gd
M-hu
M-hu
PЄ-gn
Ks-an
Q-al
P-mo
Q-al
Ks-an
D
U
Iquipi fault
PЄ-gn
M-mo
PIG-03-126
PЄ-gn
M-hu

Figure 7.

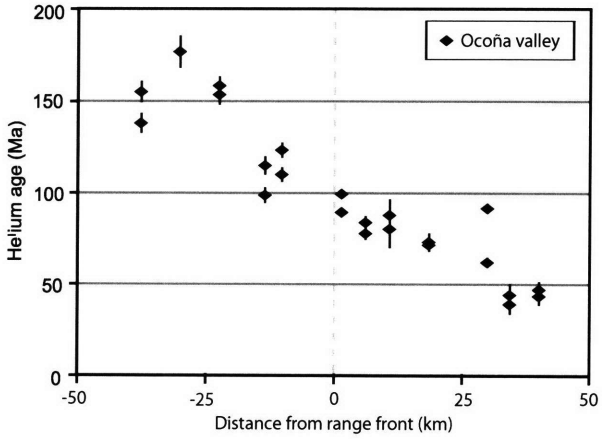
Ocoña valley
Helium age (Ma)
200
150
100
50
0
-50
-25
0
25
50
Distance from range front (km)

Figure 8.

TABLE 1. LATE CENOZOIC UPLIFT ESTIMATES FOR THE CENTRAL ANDES

Location	Uplift magnitude (m)	Initiation (Ma)	Method/Evidence	Reference
Corocoro, Altiplano	2000 ± 2000	10 to 15	paleobotany	Singewald and Berry, 1922
Potosi, Altiplano	3040 ± 1260	13.8 to 20.8	paleobotany	Gregory-Wodzicki, 2000
Jakokkota, Altiplano	2535 ± 1405	10 to 11	paleobotany	Gregory-Wodzicki, 2000
Callapa, Altiplano	2500 - 3500	10.3	oxygen isotopes	Garzione et al., 2006
Callapa, Altiplano	3400 ± 600	10.3	clumped isotopes	Ghosh et al., 2006
N. Chile, W. Cordillera	> 1400	10	rotated lake beds	Nestor et al., 2006
N. Chile, W. Cordillera	250 - 1800	10	rotated lake beds	Jordan et al., 2006
N. Chile, W. Cordillera	~ 1000	10	incised paleosurfaces	Hoke and Garzione, 2006
N. Chile, W. Cordillera	1000 - 2000	10	incised paleosurfaces	Garzione and Hoke, 2006
S. Peru, W. Cordillera	> 2400	10	incised canyons	Schildgen et al., 2007
S. Peru, W. Cordillera	2000 - 2500	13 to 9	incised canyons	Thouret et al., in press
Potosi, E. Cordillera	1500 ± 2000	13.8 to 20.8	paleobotany	Berry, 1939
Bolivia, E. Cordillera	1950 ± 1250	12 to 9	incised paleodrainages	Kennan et al.1997
Pislepampa, E. Cordillera	2300 ± 1100	6 to 7	paleobotany	Graham et al.2001
Bolivia, E. Cordillera	1705 +/- 695	12 to 9	incised paleodrainages	Barke and Lamb, 2006

TABLE 2. DESCRIPTION AND CONTEXT FOR $^{40}Ar/^{39}Ar$ SAMPLES

Sample	Description	Latitude (S)	Longitude (W)	Age ± 2σ (Ma)
05TS43	Undeformed ignimbrite crossing range front fault zone near Llucila	16° 11' 16.08"	72° 01' 36.33"	16.12 ± 0.04
04TS10	Huaylillas Ignimbrite near Toro Muerto (south of Aplao)	16° 14' 45.83"	72° 30' 06.56"	14.20 ± 0.04
04TS22	Huaylillas Ignimbrite near range front north of Aplao	15° 57' 20.85"	72° 34' 59.70"	14.29 ± 0.04
04CC13	Warped ash unit within Moquegua Fm. south of range front north of Pedregal	16° 06' 42.93"	72° 12' 18.51"	14.11 ± 0.05
04CC12	Undeformed basaltic andesite crossing range front fault zone north of Pedregal	16° 05' 45.72"	72° 11' 47.54"	0.214 ± 0.044

TABLE 3. AGE SPECTRA ANALYSIS FOR $^{40}Ar/^{39}Ar$ DATA

Sample	Material	K/Ca	Age Spectra				Isochron Analysis			Reference**
			% gas	N*	MSWD	Weighted Age (Ma)	Age (Ma)	40Ar/36Ar intercept	MSWD	
05TS43	Sanidine	59.3	100	20 of 20	0.82	16.12 ± 0.04	16.13 ± 0.05	272 ± 68	0.85	1
04TS10	Sanidine	70.8	100	12 of 12	1.29	14.20 ± 0.04	14.21 ± 0.04	291 ± 9	1.28	1
04TS10	Biotite	12.1	95.9	9 of 18	1.68	14.32 ± 0.05	14.32 ± 0.20	296 ± 20	1.93	this paper
04TS22	Sanidine	50.2	100	11 of 11	2.00	14.29 ± 0.04	14.30 ± 0.05	294 ± 47	2.21	1
04TS22	Biotite	10.8	90.7	9 of 19	1.46	14.35 ± 0.05	14.31 ± 0.21	300 ± 19	1.62	this paper
04CC13	Sanidine	84.1	100	10 of 10	0.73	14.11 ± 0.05	14.07 ± 0.14	330 ± 236	0.72	this paper
04CC13	Biotite	9.68	100	10 of 10	0.66	14.39 ± 0.12	14.2 ± 0.83	323 ± 145	0.60	this paper
04CC12	Groundmass	0.388	68.6	6 of 14	2.13	0.214 ± 0.044	n/a ± n/a	n/a ± n/a	n/a	this paper
PIG-03-126	Feldspar	n/a	n/a	n/a	n/a	13.21 ± 0.53	n/a ± n/a	n/a ± n/a	n/a	2
PIG-03-126	Biotite	n/a	n/a	n/a	n/a	13.19 ± 0.07	n/a ± n/a	n/a ± n/a	n/a	2

* Refers to number of steps on age plateau out of total number of steps, or number of grains analysed for single-grain analyses.

** References are 1: Schildgen et al., 2007; 2: Thouret et al., 2007;

Chapter 5:
Synthesis

The surface and deep-crustal processes responsible for orogenic plateau development operate over spatial scales that can reach hundreds of kilometers and span tens of millions of years. Analyzing the contribution of different geodynamic processes to plateau growth requires wide representation of studies that can assess the development of surface topography through time and can place constraints on potential driving forces. Canyons that cut through the western margin of the Central Andean plateau in southwest Peru document 2.6 to 3.0 km of incision induced by late Cenozoic surface uplift. By combining low-temperature thermochronologic records of the incision-induced cooling signal with canyon depth constraints from dated valley-filling volcanic flows, we derived a detailed record of surface response to the most significant phase of uplift in the development of the Central Andean plateau. We placed these results in the context of the evolving plateau margin by analyzing the structures that accommodated uplift. Considering our results along with uplift studies from the plateau interior and the eastern margin suggests that the geodynamic processes responsible for plateau growth likely operated throughout the plateau region during the late Cenozoic. Comparisons of our work to studies in eastern Tibet highlight some similar evolutionary features of these two major plateaus, and support the notion of a common set of geodynamic processes that govern the growth of orogenic plateaus.

Low-temperature thermochronology is one of the most effective tools for recording major phases of canyon incision. Apatite (U-Th)/He data from vertical and valley-bottom transects in Cotahuasi-Ocoña and Colca-Majes canyons reveal patterns of upper crustal cooling that were induced by near-surface isotherm depression beneath the incising canyons. Lithologies favorable to yielding pristine apatite grains dominate the middle reaches of Cotahuasi-Ocoña canyon, which allowed us to make our most detailed estimates of incision history from this drainage. Initial estimates of a minimum of 2.4 km of incision starting at ca. 9 Ma (Schildgen et al., 2007) were refined in Chapter 3 by applying three-dimensional thermal modeling to explore what range of topographic evolution scenarios were consistent with the thermochronologic data. An updated version of the finite-element model Pecube (Braun, 2003; Whipp et al., 2007) provided a mechanism to more accurately interpret the canyon-induced cooling signal from a complex thermal field background that is typical of actively subducting margins. Analysis of valley-bottom and vertical transects revealed that at least 2.6 km of incision occurred in the deepest reaches of the canyon, starting at 10 to 11 Ma, and finishing by no earlier than 3.5 Ma. $^{40}Ar/^{39}Ar$ dates on valley-filling volcanic flows helped better constrain the end of

incision to no later than 2.2 Ma. Geological evidence for cut-and-fill channels up to several hundred meters deep that pre-dated the latest phase of incision suggests that the total magnitude of late Cenozoic incision is likely to be at least 200 m less that the total 3.2 km depth of the canyon. In summary, between 2.6 and 3.0 km of down-cutting occurred in the deepest reaches of the canyon starting at 10 to 11 Ma and ending between 2.2 and 3.5 Ma.

Our analyses of vertical and valley-bottom transects with three-dimensional thermal modeling provided us with several insights into some of the important features of low-temperature thermochronology data collected from regions that have experienced transient cooling, such as that induced by major canyon incision. Understanding the factors that can affect age patterns from different sampling transects is particularly important for making reasonable interpretations of data, particularly where sampling density is limited, or in cases where three-dimensional thermal modeling is beyond the scope of the study. Our data from southwest Peru showed that estimates for the onset of a transient cooling signal can be accurately revealed in valley-bottom transects when such transects traverse regions of variable exhumation depth. Slopes of these data on age-depth plots, however, can be affected by lateral variations in the thermal field, topography, or regional exhumation rates. Vertical (or near-vertical) transects from valley walls are generally unaffected by these potential lateral variations, however, they can be strongly affected by changes in topographic relief. The oversteepening effects on age-elevation data induced by decreased surface relief described by Braun (2002) may be further complicated in regions where the surface does not closely approximate sinusoidal topography. In these regions, only parts of the vertical transect data may be oversteepened, and can show misleading patterns that resemble transitions from slow to fast exhumation.

Constraining the phase of uplift that likely induced canyon incision is primarily limited by our ability to quantify the lag time between tectonic forcing and geomorphic response. Whipple and Tucker (2002) noted that at high drainage areas where transport-limited conditions are likely to dominate, channel response sweeps upstream from the outlet in a diffuse manner, and all points along the channel progressively adjust to new conditions. This would imply nearly simultaneous onset of incision throughout the middle and lower reaches of the canyons, which are characterized by wide alluvial channels and perennial discharge. However, incision magnitudes on the multi-kilometer scale require substantial bedrock incision, which may be more likely to generate knickpoints even at large drainage areas.

Attempting to quantify geomorphic response times in field settings is difficult. Within a single drainage, knowledge of the timing of an event that generates a geomorphic response and preservation of knickpoints that have propagated up the drainage system can provide an excellent estimate for the response time of that particular drainage. Applying such an estimate to other

drainages is very difficult though, due to strong dependences on climate or erosivity of the drainage network. Our investigations of landslides and potential triggering mechanisms through time, may be an important first step in more detailed future studies of geomorphic response times in the region. The strong correlation between El Niño Southern Oscillation (ENSO) activity and increased precipitation and mass-wasting events suggests that short-term climate variations play a significant role in the pace of landscape evolution in this otherwise hyper- to semi-arid region (e.g., Quinn and Neal, 1992; Ortlieb, 2000; Vargas et al., 2000; Keefer et al., 2003; Houston, 2006; Haylock et al., 2006). Unfortunately, very few studies have cataloged an older record of mass-wasting events, making inferences about ENSO activity in the geologic past very difficult. Using $^{40}Ar/^{39}Ar$ ages of volcanic flows that bracket landslide deposits and cosmogenic exposure ages of landslide surfaces, we documented landslides ranging from Holocene age to several millions of years old throughout the Cotahuasi-Ocoña and Colca-Majes region. Much more work to date and map mass wasting events from the region is required before more substantial conclusions can be drawn about climate over the time span of the latest phase of late Cenozoic uplift, and how this may have affected the geomorphic response times of major drainages.

Studies of the retreat rate of Sipia Falls in the upper Cotahuasi catchment provide a very localized (500 m) and short-term (ca. 10 ka) estimate for how quickly the river can incise bedrock. Given these limitations, waterfall retreat rates still support the notion that response times of large drainages in arid environments can be relatively fast, particularly when the uppermost catchments tap into semi-arid climates and point water sources such as snowmelt from nearby volcanic peaks. However, better estimates of the lag time between onset of uplift and onset of incision requires substantial future work in order to better understand how local variations in erosivity and temporal changes in climate can affect the rate at which rivers incise major canyons. One possibility may be to investigate changes in the onset of incision time recorded in different vertical transects along the length of the valley. Unfortunately, temporal resolution of the transition between the slowly- and rapidly-cooled suite of apatite samples is not better than approximately one to two million years. Resolving differences in incision onset time that may only be on the order of one million years through low-temperature thermochronology requires substantial improvements in our ability to decipher transient cooling signals.

The structural evolution of the western margin in southwest Peru includes temporally and spatially varying styles of deformation. Early compressional deformation produced discrete reverse faults that deformed Oligocene and older units, and also generated disperse low-angle shear zones east of the Colca-Majes valley. Later (post-14 to 16 Ma) activity that accommodated uplift of the plateau relative to the coast is dominated by long-wavelength warping and kinematic normal faulting. In the

region around the Cotahuasi-Ocoña valley, the predominantly crystalline bedrock appears to have been resistant to rupture, and instead uplift was accommodated through long-wavelength warping of the piedmont region. This contrasts with late-stage deformation east of the Colca-Majes valley, where sandstones overlain by a thick package of sediments show a combination of shorter-wavelength warping near the range front escarpment, as well as post-14 to 16 Ma kinematic normal movement on high-angle structures. Likely superimposed on the differential uplift between the coast and the plateau was a component of block uplift. This is shown in the dramatic sea cliffs that line the coast, and is loosely constrained by a 20.83 ± 0.06 Ma biotite age for an ash within uplifted deltaic sediments (Sempere et al., 2004).

Geodynamic processes responsible for this latest uplift must be consistent with the stress regime implied by these late-stage structures on the western margin. They must also probably explain uplift on a plateau-wide scale, as evidence presented here from southwest Peru, from farther south in northern Chile, from the plateau interior, and from the eastern plateau margin all suggest a significant period of uplift starting at 10 to 11 Ma (Singewald and Berry, 1922; Berry, 1939; Gregory-Wodzicki, 2000; Graham et al., 2001; Kennan et al.1997; Barke and Lamb, 2006; Garzione et al., 2006; Ghosh et al., 2006). The two most likely candidates include delamination of a high-density lithospheric root, and ductile redistribution of material resulting from underthrusting of the Brazilian Shield beneath the eastern plateau margin. The former is most likely to explain block uplift of crust where it is cool and thin near the trench, while the latter would most likely contribute to differential uplift of the plateau relative to the coast. Better constraints on the timing and magnitude of coastal uplift and geodynamic modeling of how effectively these mechanisms can produce the pattern of deformation recorded on the western margin will likely contribute substantially to this remaining open question.

Late-stage uplift is not unique to the Central Andean plateau. Similarities between uplift timing, magnitude, and style of structural deformation between the western margin of the Central Andean plateau and the eastern margin of the Tibetan plateau suggest that similar geodynamic processes are likely to control late-stage plateau evolution. Crustal thickening through compression likely dominates much of the evolutionary history of major orogenic plateaus. This is commonly aided by thick sedimentation that occurs as a result of drainage isolation behind growing plateau margins. However, once thresholds in crustal and lithospheric thickness/density are exceeded, geodynamic processes related to the plateau itself such as delamination and mid- to lower-crustal flow can take over the later stages of plateau growth and expansion. Despite the difficulty of documenting these processes directly, continued work on understanding the development of surface topography coupled with geochemical and seismic studies that can potentially provide windows in deeper crustal

processes will continue to refine our understanding of how orogenic plateaus evolve through space and time.

References

Barke, R., and Lamb, S., 2006, Late Cenozoic uplift of the Eastern Cordillera, Bolivian Andes: Earth and Planetary Science Letters, v. 249, no. 3-4, p. 350-367.

Berry, E. W., 1939, The fossil flora of Potosi, Bolivia: John Hopkins University Studies in Geology, v. 13, p. 1-67.

Braun, J., 2002, Quantifying the effect of recent relief changes on age-elevation relationships: Earth and Planetary Science Letters, v. 200, p. 331-343.

-, 2003, Pecube: a new finite-element code to solve the 3D heat transport equation including the effects of a time-varying, finite amplitude surface topography: Computers and Geosciences, v. 29, p. 787-794.

Garzione, C. N., Molnar, P., Libarkin, J. C., and MacFadden, B. J., 2006, Rapid late Miocene rise of the Bolivian Altiplano: Evidence for removal of mantle lithosphere: Earth and Planetary Science Letters, v. 241, no. 3-4, p. 543-556.

Ghosh, P., Garzione, C. N., and Eiler, J. M., 2006, Rapid uplift of the Altiplano revealed through C-13-O-18 bonds in paleosol carbonates: Science, v. 311, no. 5760, p. 511-515.

Graham, A., Gregory-Wodzicki, K.M., and Wright, K.L., 2001, Studies in neotropical paleobotany. XV. A Mio-Pliocene palynoflora from the Eastern Cordillera, Bolivia: implications for the uplift history of the central Andes: American Journal of Botany, v. 146, no. 3, p. 813-826.

Gregory-Wodzicki, K. M., 2000, Uplift history of the Central and Northern Andes: A review: Geological Society of America Bulletin, v. 112, no. 7, p. 1091-1105.

Haylock, M. R., Peterson, T. C., Alves, L. M., Ambrizzi, T., Anunciacao, Y. M. T., Baez, J., Barros, V. R., Berlato, M. A., Bidegain, M., Coronel, G., Corradi, V., Garcia, V. J., Grimm, A. M., Karoly, D., Marengo, J. A., Marino, M. B., Moncunill, D. F., Nechet, D., Quintana, J., Rebello, E., Rusticucci, M., Santos, J. L., Trebejo, I., and Vincent, L. A., 2006, Trends in total and extreme South American rainfall in 1960-2000 and links with sea surface temperature: Journal of Climate, v. 19, no. 8, p. 1490-1512.

Houston, J., 2006, The great Atacama flood of 2001 and its implications for Andean hydrology: Hydrological Processes, v. 20, p. 591-610.

Keefer, D. K., Moseley, M. E., and deFrance, S. D., 2003, A 38 000-year record of floods and debris flows in the Ilo region of southern Peru and its relation to El Nino events and great earthquakes: Palaeogeography Palaeoclimatology Palaeoecology, v. 194, no. 1-3, p. 41-77.

Kennan, L., Lamb, S., and Hoke, L., 1997, High altitude palaeosurfaces in the Bolivian Andes: Evidence for Late Cenozoic surface uplift, in Widdowson, M., ed., Paleosurfaces: Recognition, Reconstruction and Paleoenvironmental Interpretation: Geological Society Special Publication, Geological Society of London, p. 307–324.

Ortlieb, L., 2000, The documentary historical record of El Niño events in Peru: an update of the Quinn record (sixteenth through nineteenth centuries), in Diaz, H., and Markgraf, V., ed., El Niño and the Southern Oscillation: Multiscale Variability and Global and Regional Impacts: Cambridge, Cambridge University Press, p. 207-295.

Quinn, W. H., and Neal, V.T., 1992, The historical record of El Niño events, in Bradley, R. S., and Jones, P.D., ed., Climate Since A.D. 1500: London, Routledge, p. 623-648.

Schildgen, T. F., Hodges, K.V., Whipple, K.X, Reiners, P.W., and Pringle, M.S., 2007, Uplift of the western margin of the Andean plateau revealed from canyon incision history, southern Peru: Geology, v. 35, no. 6, p. 523-526.

Sempere, T., Fornari, M., Acosta, J., Flores, A., Jacay, J., Peña, D., Roperch, P., and Taipe, E., 2004, Estratigrafía, geochronología, paleogeografía y paleotectónica de los dépositos de antearco del sur del Perú, in XII Congreso Peruano de Geología, Lima, p. 533-536.

Singewald, J. T., and Berry, E.W., 1922, The geology of the Corocoro copper district of Bolivia: John Hopkins University Studies in Geology, v. 1, p. 1-117.

Vargas, G., Ortlieb, L., and Rutllant, J., 2000, Alluviones históricos en Antofagasta y su relación con eventos El Niño/Oscilación del Sur. Historic mudflows in Antofagasta, Chile, and their relationship to the El Nino/Southern Oscillation events: Revista Geológica de Chile, v. 27, no. 2, p. 157-176.

Whipp Jr., D. M., Ehlers, T.A., Blythe, A.E., Huntington, K.W., Hodges, K.V., and Burbank, D.W., 2007, Plio-Quaternary exhumation history of the central Nepalese Himalaya: 2. Thermomkinematic and thermochronometer age prediction model: Tectonics, v. 26, TC3003.

Whipple, K. X., and Tucker, G.E., 2002, Implications of sediment-flux-dependent river incision models for landscape evolution: Journal of Geophysical Research, v. 107, no. B2, p. doi: 10.1029/2000JB000044.

Appendix:

Temporal and spatial patterns of Holocene and Pleistocene landslides in southern Peru: implications for local lithologic controls and past climate changes

Taylor F. Schildgen[1]
Kelin X Whipple[2]
Kip V. Hodges[2]
Mariela Perignon[1]
Arjun Heimsath[2]

1. Department of Earth, Atmospheric and Planetary Sciences, Massachusetts Institute of Technology, Cambridge, Massachusetts 02139, USA
2. School of Earth and Space Exploration, Arizona State University, Tempe, Arizona 85287, USA

Abstract

Landslides and landslide-related deposition dominate many high-relief regions in southern Peru. The highest concentration of mass wasting events occurs at high elevations and in close proximity to volcanic cones and associated thick ash deposits, which suggests that key factors controlling mass wasting are the integrity of the failing material and high run-off from precipitation and snowmelt. Some landslide-choked valleys also align with mapped faults, suggesting that seismic activity contributed to headwall collapse and retreat through time. Landslides in the upper Cotahuasi valley range in age from 10 -8 ka, and 5-1 ka based on ^{10}Be cosmogenic exposure dating. These fall within wetter climate periods in the high Central Andes based on paleoclimate reconstructions. The predominance of Holocene-age deposits suggests that the valley has evolved in pulses, with drier periods slowly excavating out landslide material, and wetter periods allowing a thick accumulation of debris in valley bottoms. Other landslides dated at greater than 100 ka in deep river valleys suggest a potential regional climate signal, but at this time the record is too sparse and dates too imprecise to make firm conclusions on potential triggering mechanisms for these older landslides.

Interactions between landslides and rivers are an important area of investigation, both for understanding the potential impacts of landslides on the evolution of river profiles through time and the possible long-term record of landsliding that fluvial processes may help preserve. Landforms dated at Sipia Falls, a 100-m waterfall generated after a landslide forced the river to cut a new bedrock

gorge into a valley sidewall, has migrated 490 m upstream migration since ca. 10 ka is roughly half the future length of the new gorge, implying a life time of 20,000 years for this local bedrock knickpoint. This implies a horizontal waterfall retreat rate of 5 cm/yr, and a vertical retreat rate up a 0.04 gradient of 0.2 cm/yr. At Sipia Falls and at other sites of major landslides, both extensive upstream deposition and new gorge incision that can result from landslide damming provide many more options for dating mass-wasting events than the landslide material alone. This implies a promising area of exploration for studies of paleoclimate and paleoseismicity that hope to extend records of mass-wasting events to pre-Holocene times.

1. Introduction

Landslides provide a dramatic record of both local factors that predispose a landscape to catastrophic failure as well as time-variant triggering mechanisms. Morphologic and lithologic controls include the relief of a landscape, rock strength, and any pre-existing anisotropy relative to adjacent valleys (e.g., Eisbacher and Clague, 1984; Hermanns and Strecker, 1999). Within areas susceptible to failure, primary triggering mechanisms include seismic shaking and climate changes that increase the sapping potential of groundwater flowing out of springs, produce high-intensity rainfall events, and/or lead to rapid snowmelt (e.g., Costa and Schuster, 1988). Deciphering which of these triggers is likely to have been important in a region is a complicated task, requiring spatial and temporal mapping of landslide deposits, landslide headwalls and surrounding bedrock, fault zones, and potential sources of water, all over regions large enough to discern local from regional effects. This, combined with proxy records of past climate change, can provide us with the best possible context in which to understand past and future patterns of mass wasting.

Hundreds of landslides and debris flows in the Central Andes reveal landscape responses to Holocene climate changes (e.g., Grosjean et al., 1997; Keefer et al., 1998; 2003; Truath et al., 2000; 2003; Vargas et al., 2006). In the Central Andes, a few studies have deciphered relationships between climate and landsliding as early as 30 ka (e.g., Bookhagen et al., 2001; Keefer et al., 2003; Trauth et al., 2000). However, only a small number of landslides from much earlier times, which tend to be exceptionally large, have been described in the literature. These include the >2.5-Ma, 24-km^3 Lluta collapse in northern Chile (Wörner et al., 2002; Strasser and Schlunegger, 2005), and a series of mountain front failures in northwest Argentina with ^{21}Ne exposure ages between 130 and 430 ka (Hermanns et al., 2000; 2001). The dominance of young deposits in the geologic record is likely related to the limited preservation potential of many landslides, which often consist of unconsolidated sediment and weak/altered rock clasts. However, there may be additional avenues to pursue in documenting a longer record of landslides and exploring their triggering mechanisms. In particular,

interactions of landslides with rivers can result in incision of new bedrock gorges in river channels, which can be dated back to several hundreds of thousands of years with cosmogenic exposure dating methods. Other datable features may also persevere longer in the geologic record, such as volcanic flows that overlie landslides or landslide-associated fluvial deposits.

In this paper we present a series of geomorphic studies of areas in southern Peru (Fig. 1) where landslides and their steep headwall escarpments dominate the landscape morphology, and discuss relationships with mapped fault zones, local geology, groundwater sources, and local relief. New cosmogenic exposure ages on samples collected from several landslides and associated deposits as well as $^{40}Ar/^{39}Ar$ ages on bracketing volcanic flows provide a temporal context for these events. We anticipate that these results will contribute to a growing body of literature documenting the age of landslides throughout a much larger region than the one described here. This will eventually allow for an assessment of whether landslides in southern Peru are predominantly a local phenomenon driven by seismic shaking or local storms, a widespread phenomenon driven by major changes in regional climate, or a combination of both.

We also discuss some of the important implications for landsliding in the region, in particular how they interact with fluvial systems through time. The latter is a subject of particular interest, because river longitudinal profiles have proven to be useful records of fluvial responses to external forcing, such as from changes in climate or tectonic regime (e.g., Whipple and Tucker, 1999, 2002; Snyder et al., 2000; Kirby and Whipple, 2001; Lague and Davy, 2003; Wobus et al., 2006). Landslides, however, can complicate interpretations of profiles by creating dams and associated deposition that locally perturbs the channel form (e.g., Dethier and Reneau, 1996; Reneau and Dethier, 1996; Korup, 2006; Ouimet et al., 2007). Understanding the timescale over which such features can persist in a given system provides us with perspective on the importance of these localized perturbations for interpreting river profiles. The perturbations can in turn provide opportunities to date landslides, particularly in cases where the effects on the fluvial system outlast the landslide material itself. We present results from two areas that address this particular issue.

2. Geological Setting

In southern Peru, landslides play a major role in surface evolution. Tributary valleys are often characterized by cirque-shaped headwalls and wide floors filled with hummocky landslide debris. Main valleys show both recent and old evidence of landslide damming, with lacustrine deposition in terraces stranded up to 600 m above present valley floors, and locals reporting landslide-dammed, 7-km-long lakes in the trunk stream valleys that existed for only a few years (GianMarco Vellutino, personal communication). Roads and trails throughout the region often take advantage of the lower

hillslopes and weaker material found in major landslide deposits, particularly in regions where steep, rocky canyon walls would prevent any other means of access.

Seismic shaking is likely a prime trigger for landslides in southern Peru. The area is seismically active as a result of both deep, large earthquakes that have occurred near the Wadati-Benioff zone of the subducting Nazca plate beneath the western margin of South America, as well as shallower intraplate earthquakes that tend to produce major tsunamis. Convergence rates between the plates has varied between 7 and 15 cm/yr since 40 Ma, and presently is measured to be 8 cm/yr (Pardo-Casas and Molnar, 1987; Somoza, 1998). Subduction-related earthquakes with magnitudes exceeding 8 have devastated the western margin of South America throughout historic times, including the 1960 magnitude 9.5 earthquake in central Chile (Beck and Ruff, 1989). Such large earthquakes can trigger landslides up to several hundred kilometers away from the epicenter (Keefer, 2002), and can prime the landscape for future failures through widespread "shattering" of the ground surface (Keefer and Moseley, 2004; Loveless et al., 2005). In southern Peru, the recurrence interval of large subduction-related earthquakes appears to be ca. 100-yr, as documented through major events in 1604 (Mw 8.7), 1687 (Mw 8.4), 1784 (Mw 8.4), 1868 (Mw 8.8) and 2001 (Mw 8.4) (Dorbath et al. 1990).

Although seismic shaking can have devastating effects on the landscape, landslides tend to occur most often in steep terrain where lithologic and structural factors predispose the landscape to failure (e.g., Hermanns and Strecker, 1999; Strecker and Marrett, 1999; Hermanns et al., 2000, 2001; Roering et al., 2005). The Cotahuasi-Ocoña and Colca-Majes canyons cut gorges over 3 km deep into the surround plateau surface. Canyon walls are steep, with slopes most commonly between 30 and 50 degrees. High local relief within the catchments is maintained by a hyper- to semi-arid climate that prevents hillslope processes from effectively smoothing the landscape, and instead leads to surface evolution through catastrophic failure events. Hoke et al. (2005) believed that similar landscapes in northern Chile evolved through groundwater sapping and periodic failures. This is most likely to occur where a less-permeable interface leads to a concentration of groundwater in a single plane. In southern Peru, high-relief regions are particularly susceptible to failure where canyons cut through weakly welded volcanic ash. Such areas can be found in upper regions of the canyons, where ignimbrite eruptions filled previously-cut valleys with deposits up to 2-km thick that are presently being re-incised (e.g., Schildgen et al., 2007; Thouret et al., 2007). Surface and groundwater run-off varies throughout the region, and may play a role in weathering, sapping, or destabilizing these volcanic-dominated areas, particularly at the interfaces between ignimbrites and underlying bedrock.

3. Regional climate

Despite high relief, seismic activity, and lithologic factors that all favor mass wasting processes, some arid regions may still require higher than average precipitation to induce failures (e.g., Keefer and Moseley, 2004). Understanding the climate setting of southern Peru is therefore critical for assessing landslide triggers through time.

The Cotahuasi-Ocoña and Colca-Majes Rivers have cut some of the deepest canyons in the world on their course from their headwaters in the Central Andes, through the Western Escarpment of the Altiplano and associated forearc region, and finally to the Pacific Ocean. Despite these impressive fluvially-carved features, the region itself receives very little precipitation. This is a combined result of its geographic position in the descending flow of the atmospheric Hadley cell, the cold Peru (Humboldt) Current that creates a strong atmospheric temperature inversion, and the Central Andean orographic barrier that blocks moisture-bearing easterly winds (Abele, 1989). Historical data from the World Meteorological Organization show that coastal regions are hyper-arid, receiving only a few millimeters of precipitation per year on average. Rainfall increases in an exponential fashion (Houston and Hartley, 2003) to 100 to 300 mm/yr up the Western Escarpment, and greater than 400 mm/yr in the high plateau regions (Fig. 1). Most precipitation occurs during the austral summer months, however perennial flow in these major rivers implies that considerable run-off is generated as a result of snowmelt from nearby volcanoes.

3.1. Paleoclimate

Reconstructions of past climate conditions are complicated by several factors. First, climate changes in coastal regions do not track changes in high-elevation regions, implying that records from high-elevation ice cores and lakes cannot be directly compared to proxy records from coastal areas. This dichotomy is reflected in modern weather station records also, as the Atacama and Central Andes wet seasons are poorly correlated (Holmgren et al., 2001). Second, proxy records show relatively high spatial variability in the onset of wetter and drier conditions. Abbott et al. (2003), for example, found a 2000-year difference in the onset of wet mid-Holocene conditions recorded in high-elevation lake core sediments between 14 and 20°S latitude, which they believed was a result of southward migration of the zone of intense summer convection called the Intertropical Convergence Zone. Vargas et al. (2006) also noted that a prolonged mid-Holocene wet period recorded by debris flows in coastal regions of southern-most Peru coincided with an arid period in coastal northern Chile. Similarly, a high-stand in the water levels of Lake Aricota at 17.3°S at 6100 ^{14}C yr BP (Placzek et al., 2001) coincided with a low-stand of water level in Lake Titicaca (e.g., Baker et al., 2001). These observations stress the importance of obtaining proxy climate data near to an area of interest.

Generally, however, most proxy records suggest that southern Peru was characterized as having a wet period from ca. 12.5 to 8 ka, a mid-Holocene dry period from ca 8 ka to ca. 5 ka, and a wetter late Holocene period (e.g., Keefer et al., 1998, 2003; Fontugne et al., 1999; Baker et al., 2001; Vargas et al., 2000; 2006; Haylock et al., 2006).

3.2. El Niño Southern Oscillation

Superimposed on these general trends are changes in the variability of seasonal rainfall and frequency of major rainfall events. The El Niño Southern Oscillation (ENSO) creates variations in SST that induce greater yearly variability in precipitation. El Niño periods (warmer than average SSTs) are correlated with greater than average austral summer precipitation in coastal regions of southern Peru, while La Niña periods (cooler than average SSTs) are associated with greater than average precipitation in the Western Cordillera and Altiplano (Houston, 2002; 2006). Extremes in SST related to ENSO are associated with some of the highest precipitation events on record in South America (e.g., Quinn and Neal, 1992; Ortlieb, 2000; Vargas et al., 2000; Keefer et al., 2003; Houston, 2006; Haylock et al., 2006). Debris flow deposits and lake core sediments provide proxy evidence that the ENSO has been affecting the Central Andes since ca. 5 ka (Grosjean et al., 1997; Keefer et al., 1998;Vargas et al., 2006; Truath et al., 2000), although some workers interpret proxy records as showing ENSO-related variability as early as 17 to 30 ka (e.g., Truath et al., 2000; Keefer et al., 2003; Rein et al., 2005).

4. Detailed description and dates on selected landslides

In the following section, we describe field sites in southern Peru where landslides appear to dominate geomorphic processes in the region, affecting both valley morphology and stream profile evolution. We also discuss what factors in each region may be likely to contribute to failure events, and in this way explore what patterns exist and which factors are most important on a regional scale. In each region, we dated landslides directly with cosmogenic exposure age methods (see reviews in Lal, 1991; Bierman, 1994; Gosse and Phillips, 2001, and sample preparation protocols outlined in Kohl and Nishiizumi, 1992, and Ditchburn and Whitehead, 1994), or we dated volcanic flows that bracket landslide ages with $^{40}Ar/^{39}Ar$ geochronology. Input data for calculating exposure ages and dates for all samples are summarized in Tables 1 through 3. Exposure ages are calculated using the CHRONOS-Earth exposure age calculator version 2.0 (Balco et al, submitted, and available at http://hess.ess.washington.edu/math/). Although a wide range of model ages is presented depending on which spallation scaling scheme is assumed, we use ages calculated from the time-invariant Lal (1991)/Stone (2002) scheme and "internal" errors which include analytical errors only (no uncertainty

in nuclide production rates) for the purposes of discussion. Although "external" errors are more appropriate for assessing the accuracy of exposure ages and comparing ages different parts of the world, internal errors are more appropriate for directly comparing exposure ages from a single study region (Balco et al., submitted).

4.1. Chuquibamba Valley

The morphology of the middle reaches of the Colca-Majes canyon showcase the dominance of landsliding in controlling the development of tributary valleys. The headwall of the southernmost tributary, Chuquibamba valley, forms a dramatic cirque-like escarpment (Fig. 2). This escarpment is cut into the 14- to 16-Ma weakly welded Huaylillas ignimbrite, which blankets the region up to several hundred meters thick (Thouret et al., 2007; Schildgen et al., 2007). Below the uppermost headwalls are a series of slump blocks, which form an irregular inner ring below the surrounding plateau surface. More mobile material appears to have traveled farther down the tributary valley, accumulating into a stack of multiple landslides. The valley has a "stumpy" appearance with little variation in width except near the confluence with the main valley, where it narrows considerably. Through the narrow outlet, the toes of several landslides have spilled out into the main valley in several lobes (Fig. 2).

Clasts within the landslide are predominantly ignimbrite blocks, though small cobbles of intrusive, gneissic, and quartzite bedrock also appear. The valley walls are mostly buried in either landslide material plastered up onto the walls, or colluvium from intrusive and gneissic bedrock, so determining whether or not the valley has cut significantly into the non-volcanic bedrock is difficult. The small component of non-volcanic material within the slide, however, suggests minimal excavation into bedrock from mass-wasting processes. A small stream runs through this tributary valley perennially (most likely sourced from Corapuna snowmelt), and has in one location incised through a 120-m thick section of landslide material down to bedrock of the valley sidewall. Assuming a triangular cross-section to the landslide fill in the valley and a maximum depth of 120 m, we estimate a minimum 1.4 km^3 volume of landslide material in the valley today.

Although the slump blocks below the base of the headwall escarpment obscure any potential evidence for sapping, the perrenial water source may play an important role in maintaining a steep headwall this tributary. The concentration of groundwater between the crystalline bedrock surface and the overlying porous ignimbrite blanket on the plateau may facilitate failures between these two units during seismic events. A high-angle fault system projects up through the valley, suggesting that the valley orientation and evolution may be related to activity on these structures. The contrast in morphology between the Chuquibamba valley and the tributary valley to its north, Pampacolca valley,

is striking, and may provide additional hints as to how each has evolved. Pampacolca valley is deeply incised throughout its length, and has little resemblance to a cirque-shaped headwall. Instead, individual fingers of v-shaped valleys fan out at the tributary head, much more similar to the type of tributary morphology typically encountered in more humid regions. The main difference between the two valleys is the underlying bedrock. Pampacolca valley is cut into a steeply folded section of Jurassic sediments, through which water is likely to permeate readily. This, and the lower contrasting strength between the bedrock and the regionally-blanketing ignimbrites, implies that there is less likely to be a clear basal plane along which failure events would occur, and instead both ignimbrite and sandstone erode relatively easily.

We collected three samples for cosmogenic exposure dating from the surface of the landslide in Chuquibamba valley (Fig. 3). Samples collected from the top surfaces of two large boulders yielded relatively old ^{10}Be exposure ages of 86.5 ± 2.6 ka (06TS42) and 118.9 ± 3.6 ka (06TS45). Dissolution pits on the surface of 06TS42 suggested that the boulder hadn't experienced recent spallation, but both boulders may have experienced some erosion since they first exposed. A quartzite clast collected from the top of a hummock mound (06TS44) had sharp edges and appeared uneroded, however its small size means it was likely to have originally been buried beneath landslide surface, hence the sample provides a minimum estimate for the landslide age. As expected, it yielded a significantly younger age of 29.2 ± 1.0 ka. Although the samples show a wide range in ages and the landslide has likely experienced a complex history of multiple failures, it appears as if the uppermost surface is of late Pleistocene age.

4.2. Sipia Falls

The Cotahuasi river flowing over Sipia Falls in the upper reaches of Cotahuasi canyon cascades down over 100 m in three closely-spaced steps, representing the most dramatic knickpoint on rivers in the region. Above the highest exposed bedrock on the north side of the valley is an extensive exposure of landslide material, up to several hundred meters thick. Approximately 500 m both downstream and upstream from Sipia Falls are landslide-filled paleovalleys exposed on the northeastern wall of the present valley. The upstream fill is capped by both lacustrine and fluvial sediment, the latter of which has been carved into a series of fluvial terraces (Fig. 4). These relationships suggest that Sipia Falls was created after a landslide filled the original valley, temporarily dammed the river to form a lake, then forced the river to carve out a new bedrock channel as it cut a new valley through the landslide fill, south of its original valley location (Fig. 5). This example of an "epigenetic gorge" was described by Ouimet et al. (2007), who noted that such gorges form in a wide variety of landscapes throughout the world when landslide damming or other major

aggradational events lead to major river diversions. Sipia Falls, however, is rare in that it represents a transient form prior to complete gorge formation. An age for the landslide that led to river damming and bedrock incision would provide insight into the timescale of epigenetic gorge formation in general, as well as a specific example of how quickly this river system adjusts to a major perturbation in its river profile.

We collected several samples from the landslide and associated fluvial deposits for cosmogenic exposure dating to constrain the age of the landslide (Table 1). Because landslide dams tend to be breached and fail soon after dammed lakes overtop the landslide (particularly with unconsolidated, weak volcaniclastic material), we expected that exposure ages of the alluvium dammed behind the landslide would be similar to ages for the landslide itself. Two large, fluvially-polished granodiorite boulders partially buried within alluvium immediately upstream from the landslide (Fig. 6) yielded ^{10}Be ages of 9.7 ± 0.5 ka (05TS18) and 9.6 ± 0.4 ka (05TS19). From the landslide itself, one amalgamated sample of quartzite clasts from the top of the landslide yielded ages of 9.5 ± 0.4 and 9.0 ± 0.5 ka (replicate analyses for 05TS20), and the surface of one quartzite boulder yielded ages of 12.7 ± 0.5 ka and 11.5 ± 0.4 ka (replicate analyses for 05TS21). Because the landslide samples derived from the alluvial material and from the amalgamated quartzite sample cluster around 10 ka, we believe this is the likely age of the landslide. A small amount of cosmogenic inheritance may explain the slightly older age for the quartzite boulder sampled from the top of the landslide.

Because Sipia Falls has retreated 490 m upstream from the original downstream position of the paleovalley, we can calculate horizontal and vertical retreat rates for the waterfall. Assuming a 10 ka age for the landslide and associated initiation of gorge incision, the horizontal retreat rate is 5 cm/yr, and the vertical retreat rate up a graded gradient estimated to be 0.04 is 0.2 cm/yr. These data also imply that a landslide of these dimensions that causes a diversion in the main channel valley is likely to create a knickpoint in the river profile for roughly 20,000 years. Cosmogenic samples collected from the gorge itself could have provided similar information. Important to recognize though is the time-transgressive nature of gorge incision. The best estimates for the landslide age would then be on walls at the downstream end of the gorge, where incision first started.

4.3. Upper Cotahuasi valley

Although the landslide dam at Sipia Falls is an impressive feature in the landscape, it is only one of many similarly immense deposits that characterize the upper Cotahuasi valley. Additional landslides also produced dams and associated fluvial and lacustrine deposition, but upstream of Sipia Falls none appear to have diverted the river into a new bedrock channel. The town of Sancay, 6 km downstream of Sipia Falls, is built on a high terrace 600 m above the present valley floor. Near the

top of the terrace, a ca. 20 m think section of lake beds are exposed, which are capped by a disperse layer of rounded pebbles and cobbles. A landslide dam that is no longer preserved is the likely explanation for this high terrace. In addition, in the region upstream from Sipia Falls, the valley bottom is wide (300 to 500 m) and alluviated over a 25-km reach. This contrasts with the valley widths upstream and downstream of this region, which are generally less than 100 m. Given the height of the landslide dam at Sipia Falls, it is only likely that 4 to 5 km worth of upstream back-filling can be related to that landslide dam. Hence, a number of additional landslides are likely to have affected the valley farther upstream. The scalloped rims of the canyon that cut through weak volcanic rock (Fig. 7) show likely head scarps for these slides.

Within 10 to 20 km of the southern wall are Sabancaya volcano and Nevado Firura (5888 and 5498 m, respectively). Lakes on the surface of the plateau near volcanic peaks and springs that emerge within nearby valley headwalls suggest snowmelt-sourced groundwater is an important component of the hydrologic system. Floors below headwall-cirques tend to lie at similar elevations, suggesting a common basal failure plane that is most likely the top of an underlying, more resistant lithologic unit. Compared to the weakly-welded volcanic ash, this is likely to be a less-permeable layer above which springs emerge. Escarpments on the northern wall of the main valley also include some cirque-like forms cut into ignimbrites, but they are far fewer and less well-formed. Although there are some lakes on the plateau north of the valley, there are no large peaks nearby to accumulate a substantial snowpack. These observations suggest that a series of factors are important for developing and maintaining the cirque-like headwalls in the upper Cotahuasi valley: weak volcanic rock over a more resistant and less-permeable bedrock layer, a significant supply of groundwater, and deeply incised valleys into which debris may empty upon failure.

Geochronological data from the valley suggests that it experienced a dynamic history of multiple incision and volcanic refilling events. The original valley was incised to within 400 m of its present depth by no later than 3.75 Ma (Schildgen et al., 2007; Thouret et al., 2007) based on the age of an ignimbrite that flowed deep into the valley. Thouret et al (2007) suggested that ignimbrite deposits probably refilled the valley at 1.4 Ma based on the presence of thick young ignimbrites along the plateau edges. (U-Th)/He apatite dates from bedrock in the valley floor dated at 1 to 2 Ma (Schildgen et al., 2007) support the theory that these young volcanics filled the valley to considerable depth in order to reset the thermochronometer ages. The latest espisode of incision thus represents at least the second time that the valley has been incised.

We collected samples for cosmogenic exposure age modeling on a few of these deposits. Amalgamated quartzite clasts collected from the tops of landslide hummocks near the bottom of the Cotahuasi valley yielded ages of 8.1 ± 0.4 ka, 5.6 ± 0.2 ka, and 8.2 ± 0.3 ka (samples 05TS34,

05TS35, and 05TS36). The deposit associated with this surface caps an older landslide with an irregular contact. Although we found no material to date from the older landslide, good exposure of multiple landslide units in this valley offers promise for future work. At higher elevation in a tributary valley, we collected samples from the surfaces of large ignimbrite boulders that had collapsed from the cirque-shaped headwalls. These yielded younger ages of 5.2 ± 0.2 ka, and 1.3 ± 0.1 ka (samples 05TS37 and 05TS38). We have no clear evidence that the boulder surfaces have been free from erosion over the past several thousand years, yet they are large enough that they are likely to have been exposed since deposition. As a result, these samples likely provide minimum age estimates for the landslide deposit in the upper portion of the valley. Although we only sampled a small selection of landslides in the upper Cotahuasi valley, similarly morphologies of other landslides in the valley suggest that they are also likely to be Holocene in age.

Holocene mass-wasting events that affected the upper Cotahuasi valley also may have occurred farther downstream in the Ocoña valley. A boulder with a 6.9 ± 0.3 ka ^{10}Be exposure age from a fluvial terrace stranded 40 m above the present valley floor suggests significant aggradation downstream, either from an unmapped landslide or more wide-spread aggradation throughout the valley. Extensive fill terraces line the valley for stretches up to several kilometers long, but ages for these features have not yet been determined. A bedrock strath terrace stranded 7 m above the present valley floor on both sides of the canyon floor and dated at 3.3 ± 0.3 ka records a late pulse of valley incision. If it were related to landslide damming, the damming must have occurred on the 1-km wide Ocoña valley, because the bedrock strath extends up both major tributaries to the Ocoña: the Cotahuasi and the Maran. A likely source area would be from the southern flanks of Solimana volcano, which is mostly collapsed into the wide tributary valley below it, though no clear evidence for the collapse material remains in the main Ocoña valley.

4.4. Upper Colca valley

The upper Colca valley cuts down over 1500 m below the gentle topography of the surrounding 5000-m plateau surface. Vocanic peaks exceeding 6000 m built on the plateau provide perennial groundwater through snowmelt. Initial incision in this region was likely similar to that of Cotahuasi canyon to the west, which was cut to near its present depth between ca. 9 and 2.3 Ma (Schildgen et al., 2007). Ignimbrites dated at 2.2 Ma blanket the upper Colca region, which lead Thouret et al. (2007) to believe that the valley was refilled by young ignimbrites at that time, and since then has been re-incised in multiple stages. Initial re-incision must have been rapid, as a bedrock-capping younger ignimbrite dated at 1.82 +/- 0.02 Ma (sample 04CC10, Table 3) reaches to within 80 m of the present valley floor.

Since that time, the valley has evolved in a complicated fashion involving multiple incisional and depositional periods. The valley walls today are flanked by an extensive set of terraces, which generally consist of interfingered coarse river cobbles, lake sediments, colluvium, and landslide deposits. Deposition in the valley is primarily upstream from a major knickpoint on the river profile, which also corresponds to the location of the collapsed northern flank of Hualca Hualca volcano (Fig. 8). Where exposed on the north side of the valley, the indurated material of the flank collapse consists of extrusive and intrusive andesitic clasts with diameters ranging from several centimeters to several meters. This flank collapse most likely dammed the valley and led to extensive upstream fluvial and lacustrine deposition. Subsequent depositional, mass wasting, and erosional events modified this fill and shaped the terraces that we see today.

Eash and Sandor (1995) described seven levels of geomorphic surfaces in the valley based on field mapping and air photo analysis. They described well-developed soils on the uppermost terraces (up to 500 m above the present valley floor), which they estimated to be Pleistocene in age. They reported radiocarbon dates on organic material in one of the lowest terraces of 1610 +/- 70 yr B.P., and they reported K/Ar dates on two andesite flows of 64 +/- 14 ka and 172 +/- 14 ka overlying higher fluvial sediments. We report new $^{40}Ar/^{39}Ar$ dates on andesite flows that bracket the oldest lake sediments in the valley, which we infer were deposited in response to the Hualca Hualca flank collapse (Table 2). One flow that underlies lake sediments is dated at 636 +/- 45 ka (sample 04CC09). A second flow that overlies lake sediments is dated at 622.7 +/- 6.1 ka (sample 04CC05, Fig. 9). Although the initial timing of lacustrine deposition is not tightly constrained, the latter date shows that sediments had started filling the lake by c. 620 ka.

4.5. Old landslides preserved in steep canyons

Older landslides are also preserved in the deepest reaches of Cotahuasi and Colca Canyons. In general, the steep canyon walls would seem to provide poor preservation potential for landslides along the river. Fortunately, many basaltic andesite flows entering from tributary valleys flowed over landslide deposits, preserving them today within thick sections of sediment- and volcanic-filled paleovalleys. In the middle reaches of Cotahuasi canyon, a ca. 25-m thick basaltic andesite overlies lake sediments that in turn overlie a landslide deposit. Most likely, the lake deposits were related to valley damming from the landslide. Lake sediments appear to have been injected into the base of the flow as flame structures, suggesting that the lake sediments were wet at the time the volcanic flow buried them (Fig. 10). Because of this, we believe the age of the flow gives a very good estimate for the age of the sediments and landslide. Two splits of groundmass from the flow yielded $^{40}Ar/^{39}Ar$ dates of 139 ± 3 ka and 141 ± 5 ka (sample 05TS27).

Other volcanic flows provide only minimum ages for the landslides they bury, as we didn't see clear evidence that the sediments were buried soon after deposition. Farther downstream in Cotahuasi Canyon, a 633 ± 84 ka volcanic flow buries a 20-m thick landslide deposit. In the middle reaches of Colca Canyon, numerous volcanic flows bury landslide deposits, but few are accessible due to the steep inner gorge in this section of the river. Four pieces of float from a flow perched above (but not directly over) a landslide deposit yielded ages between 170 and 178 ka (samples 06TS31a through d), giving a minimum age for the underlying landslide.

5. Discussion and Conclusions

5.1. Spatial and temporal landslide patterns

Landslides in southern Peru are clustered in areas where lithologic and topographic characteristics favor mass wasting erosional processes. The most extensive landslide deposition is in the upper Colca and upper Cotahuasi valleys, both of which were refilled by volcanic ignimbrites in the last several million years. Cirque-shaped headwalls in these regions expose weakly welded ignimbrites up to several hundred meters thick, and the ignimbrite-dominated clast lithology within landslide deposits showcase the facility with which these cliffs tend to collapse. The high density of headwall escarpments near volcanic cones suggests that the perennial source of meltwater from these snow-capped peaks is another key factor for failure events. Because we rarely see water flowing on the surface over the plateau or the valley walls, we suspect groundwater is funneled through to the interface between ignimbrites and underlying bedrock, and facilitates failure along this basal plane when seismic shaking or a particularly wet climate period triggers mass movements.

Understanding the relationship between landslides and temporally-varying triggers, such as seismic shaking and climate change, is complicated by limitations in the temporal resolution of dating landslide deposits, sparse preservation of these features in the geologic record, and imperfect records of how climate and seismicity have varied through time. Historical records of earthquakes, however, suggest that seismic shaking along this active margin is widespread and significant, with short recurrence intervals of major events when compared to multi-millennial variations in Holocene precipitation. Limited resolution of dating techniques will likely prevent us from resolving whether or not certain mass-wasting clusters are related to particular earthquake events, but resolving climate-related millennial variations seems to be a reasonable goal. Broad correlations that we see between the timing of landslide clustering in the river valleys of southern Peru with clusters in northern Chile and northwest Argentina lend further support to our interpretation of regional climate creating major pulses of landslides in southern Peru, rather than local seismic shaking.

5.2. Old landslide and paleoclimate implications

Beyond relationships with triggering mechanisms, the pattern of landslide preservation in the geologic record may tell us more about the dynamics of landscape evolution in regions where mass-wasting is a dominant erosional process. Holocene-age deposits in the upper Cotahuasi valley dominate the depositional record, and have ages that tend to cluster around wetter periods documented for this part of the Andes (8 to 10 ka and after 5 ka). However, their combined volume makes up only a small fraction of the total amount of volcanic material that was removed to carve out the valleys since the time they were filled, between 1 and 2 million years ago. This suggests that the upper valleys in these regions have evolved in pulses. Older landslides that initially carved out a new canyon into the volcanic rock have likely been excavated from the depths of the upper canyon, and are only preserved in a few places farther downstream where volcanic flows overrode them or where scraps of landslide or lake sediment deposition were stranded high on the canyon walls. Excavation periods are likely to have occurred when runoff in the channel bottom sourced from high-elevation snowmelt was sufficient to transport the weak, unconsolidated landslide material, but precipitation and runoff on hillslopes was still minimal, preventing additional failures. The Holocene-debris-choked valley today is likely a reflection of a generally wetter late Holocene period that continues to produce hillslope failure events faster than the valleys can be excavated. Older landslides preserved farther downstream may signal that similar variations in precipitation lead to landslide-choked valleys as far back as 600 ka, and possibly earlier. In northwest Argentina, Trauth et al. (2003) drew similar conclusions, as they found that despite the pulsed nature of landslide events, changes in the sedimentary budget recorded in basins downstream were minimal. Instead, they believed, the landslide material accumulated in upper catchment basins, and arid conditions precluded rapid removal of the sediment from the system. In their study as well as ours, we see that through changes in upper catchment storage volume, a relatively steady pace of sediment removal from the system can proceed, despite the episodic nature of events that deliver unconsolidated material to the fluvial system.

5.3. Developing a pre-Holocene landslide inventory

Further analysis of clustering for pre-Holocene landslides requires a much more extensive catalogue of old landslides. Preservation of these unconsolidated deposits is one of the biggest obstacles in this goal, but some of the approaches used in this study are likely to be fruitful in other regions as well. Volcanic flows often provide resistant covers that can often be easily dated with high precision back to many millions of years with $^{40}Ar/^{39}Ar$ geochronology. Older deposits can be dated directly by measuring cosmogenic burial ages on landslide surfaces that immediately underlie the

flows. Although precision on burial ages is generally low, they do provide a means of directly dating landforms that are up to several millions of years old (Granger and Muzikar, 2001). Another approach is to take advantage of the interactions between landslides and fluvial systems. Landslide dams lead to upstream deposition of alluvial and lake sediments that have a higher chance of preservation simply as a function of their wide spatial extent. After rivers breach landslide dams, new incision into valley sidewalls can lead to rapid exposure of bedrock, which can be dated by measuring the accumulation of cosmogenic isotopes. Focused research on dating older landslides and similar mass-wasting deposits has great promise for providing new insights into variations in climate far beyond the extensively-studied Holocene period.

Acknowledgments

We thank W. Ouimet and J. Johnson for discussions; K. Cornell, J. Bradley and T. Smith for help with field work; M. Goddard, G.M. Vellutino, and J. Bustamante for logistical support; J. Dixon for guidance on cosmogenic sample preparation; M. Pringle and W. Olszewski for help with $^{40}Ar/^{39}Ar$ analyses; M. Caffee and S. Ma for running cosmogenic samples at the PRIME Laboratory at Purdue University.

References

Abbott, M. B., Wolfe, B. B., Wolfe, A. P., Seltzer, G. O., Aravena, R., Mark, B. G., Polissar, P. J., Rodbell, D. T., Rowe, H. D., and Vuille, M., 2003, Holocene paleohydrology and glacial history of the central Andes using multiproxy lake sediment studies: Palaeogeography Palaeoclimatology Palaeoecology, v. 194, no. 1-3, p. 123-138.

Abele, G., 1989, the influence of age, climate, and relief on the preservation of volcanic landforms in the North Chilean Andes: Bamberger Geographische Schriften, v. 11, p. 45-57.

Baker, P. A., Seltzer, G. O., Fritz, S. C., Dunbar, R. B., Grove, M. J., Tapia, P. M., Cross, S. L., Rowe, H. D., and Broda, J. P., 2001, The history of South American tropical precipitation for the past 25,000 years: Science, v. 291, no. 5504, p. 640-643.

Balco, G., Stone, J.O., Lifton, N.A., Dunai, T., submitted, A complete and easily accessible means of calculating surface exposure ages or erosion rates from ^{10}Be and ^{26}Al measurements: Quaternary Geochronology.

Beck, S. L., and Ruff, L. J., 1989, Great Earthquakes and Subduction Along the Peru Trench: Physics of the Earth and Planetary Interiors, v. 57, no. 3-4, p. 199-224.

Bierman, P. R., 1994, Using in-Situ Produced Cosmogenic Isotopes to Estimate Rates of Landscape Evolution - a Review from the Geomorphic Perspective: Journal of Geophysical Research-Solid Earth, v. 99, no. B7, p. 13885-13896.

Bookhagen, B., Haselton, K., and Trauth, M.H., 2001, Hydrological modelling of a Pleistocene landslide-dammed lake in the Santa Maria Basin, NW Argentina: Palaeogeography Palaeoclimatology Palaeoecology, v. 169, p. 113-127.

Costa, J. E., and Schuster, R.L., 1988, The formation and failure of natural dams: Geological Society of America Bulletin, v. 100, no. 7, p. 1054-1068.

Desilets, D., and Zreda, M., 2003, Spatial and temporal distribution of secondary cosmic-ray nucleon intensities and applications to in situ cosmogenic dating: Earth and Planetary Science Letters, v. 206, no. 1-2, p. 21-42.

Desilets, D., Zreda, M., and Prabu, T., 2006, Extended scaling factors for in situ cosmogenic nuclides: New measurements at low latitude: Earth and Planetary Science Letters, v. 246, no. 3-4, p. 265-276.

Dethier, D. P., and Reneau, S. L., 1996, Lacustrine chronology links late pleistocene climate change and mass movements in northern New Mexico: Geology, v. 24, no. 6, p. 539-542.

Ditchburn, R. G., and Whitehead, N.E., 1994, The separation of 10Be from silicates, in 3rd Workshop of the South Pacific Environmental Radioactivity Association, p. 4-7.

Dorbath, L., Cisternas, A., and Dorbath, C., 1990, Assessment of the Size of Large and Great Historical Earthquakes in Peru: Bulletin of the Seismological Society of America, v. 80, no. 3, p. 551-576.

Dunai, T. J., 2001, Influence of secular variation of the geomagnetic field on production rates of in situ produced cosmogenic nuclides: Earth and Planetary Science Letters, v. 193, no. 1-2, p. 197-212.

Eash, N. S., and Sandor, J.A., 1995, Soil chronosequence and geomorphology in a semi-arid valley in the Andes of southern Peru: Geoderma, v. 65, p. 59-79.

Eisbacher, G. H., and Clague, J.J., 1984, Destructive mass movements in high mountains: Hazard and management: Geological Survey of Canada Paper, v. 84-16, p. 230.

Fontugne, M., Usselmann, P., Lavallee, D., Julien, M., and Hatte, C., 1999, El Nino variability in the coastal desert of southern Peru during the mid-Holocene: Quaternary Research, v. 52, no. 2, p. 171-179.

Gosse, J. C., and Phillips, F. M., 2001, Terrestrial in situ cosmogenic nuclides: theory and application: Quaternary Science Reviews, v. 20, no. 14, p. 1475-1560.

Granger, D. E., and Muzikar, P. F., 2001, Dating sediment burial with in situ-produced cosmogenic nuclides: theory, techniques, and limitations: Earth and Planetary Science Letters, v. 188, no. 1-2, p. 269-281.

Grosjean, M., Núñez, L., Cartajena, I., and Messerli, B., 1997, Mid-Holocene climate and culture change in the Atacama Desert, northern Chile: Quaternary Research, v. 48, p. 239-246.

Haylock, M. R., Peterson, T. C., Alves, L. M., Ambrizzi, T., Anunciacao, Y. M. T., Baez, J., Barros, V. R., Berlato, M. A., Bidegain, M., Coronel, G., Corradi, V., Garcia, V. J., Grimm, A. M., Karoly, D., Marengo, J. A., Marino, M. B., Moncunill, D. F., Nechet, D., Quintana, J., Rebello, E., Rusticucci, M., Santos, J. L., Trebejo, I., and Vincent, L. A., 2006, Trends in total and extreme South American rainfall in 1960-2000 and links with sea surface temperature: Journal of Climate, v. 19, no. 8, p. 1490-1512.

Hermanns, R. L., Niedermann, S., Garcia, A. V., Gomez, J. S., and Strecker, M. R., 2001, Neotectonics and catastrophic failure of mountain fronts in the southern intra-Andean Puna Plateau, Argentina: Geology, v. 29, no. 7, p. 619-622.

Hermanns, R. L., and Strecker, M. R., 1999, Structural and lithological controls on large Quaternary rock avalanches (sturzstroms) in arid northwestern Argentina: Geological Society of America Bulletin, v. 111, no. 6, p. 934-948.

Hermanns, R. L., Trauth, M. H., Niedermann, S., McWilliams, M., and Strecker, M. R., 2000, Tephrochronologic constraints on temporal distribution of large landslides in northwest Argentina: Journal of Geology, v. 108, no. 1, p. 35-52.

Hoke, G. D., Isacks, B. L., Jordan, T. E., and Yu, J. S., 2004, Groundwater-sapping origin for the giant quebradas of northern Chile: Geology, v. 32, no. 7, p. 605-608.

Holmgren, C. A., Betancourt, J.L., Rylander, K.A., Roque, J., Tovar, O., Zeballos, H., Linares, E., Quade, J., 2001, Holocene vegetation history from fossil rodent middens near Arequipa, Peru: Quaternary Research, v. 56, p. 242-251.

Houston, J., 2002, Groundwater recharge through an alluvial fan in the Atacama Desert, northern Chile: mechanisms, magnitudes and causes: Hydrological Processes, v. 16, no. 15, p. 3019-3035.

-, 2006, The great Atacama flood of 2001 and its implications for Andean hydrology: Hydrological Processes, v. 20, p. 591-610.

Houston, J., and Hartley, A. J., 2003, The central andean west-slope rainshadow and its potential contribution to the origin of hyper-aridity in the Atacama desert: International Journal of Climatology, v. 23, no. 12, p. 1453-1464.

Keefer, D. K., 1994, The Importance of Earthquake-Induced Landslides to Long-Term Slope Erosion and Slope-Failure Hazards in Seismically Active Regions: Geomorphology, v. 10, no. 1-4, p. 265-284.

-, 2002, Investigating landslides caused by earthquakes - A historical review: Surveys in Geophysics, v. 23, no. 6, p. 473-510.

Keefer, D. K., deFrance, S. D., Moseley, M. E., Richardson, J. B., Satterlee, D. R., and Day-Lewis, A., 1998, Early maritime economy and EL Nino events at Quebrada Tacahuay, Peru: Science, v. 281, no. 5384, p. 1833-1835.

Keefer, D. K., and Moseley, M. E., 2004, Southern Peru desert shattered by the great 2001 earthquake: Implications for paleoseismic and paleo-El Nino-Southern oscillation records: Proceedings of the National Academy of Sciences of the United States of America, v. 101, no. 30, p. 10878-10883.

Keefer, D. K., Moseley, M. E., and deFrance, S. D., 2003, A 38 000-year record of floods and debris flows in the Ilo region of southern Peru and its relation to El Nino events and great earthquakes: Palaeogeography Palaeoclimatology Palaeoecology, v. 194, no. 1-3, p. 41-77.

Kirby, E., and Whipple, K.X, 2001, Quantifying differential rock-uplift rates via stream profile analysis: Geology, v. 29, no. 5, p. 415-418.

Kohl, C. P., and Nishiizumi, K., 1992, Chemical Isolation of Quartz for Measurement of In situ-Produced Cosmogenic Nuclides: Geochimica Et Cosmochimica Acta, v. 56, no. 9, p. 3583-3587.

Korup, O., 2006, Rock-slope failure and the river long profile: Geology, v. 34, no. 1, p. 45-48.

Lague, D., and Davy, P., 2003, Constraints on the long-term colluvial erosion law by analyzing slope-area relationships at various tectonic uplift rates in the Siwaliks Hills (Nepal): Journal of Geophysical Research-Solid Earth, v. 108, no. B2.

Lal, D., 1991, Cosmic-Ray Labeling of Erosion Surfaces – In-situ Nuclide Production-Rates and Erosion Models: Earth and Planetary Science Letters, v. 104, no. 2-4, p. 424-439.

Lifton, N. A., Bieber, J. W., Clem, J. M., Duldig, M. L., Evenson, P., Humble, J. E., and Pyle, R., 2005, Addressing solar modulation and long-term uncertainties in scaling secondary cosmic rays for in situ cosmogenic nuclide applications: Earth and Planetary Science Letters, v. 239, no. 1-2, p. 140-161.

Loveless, J. P., Hoke, G. D., Allmendinger, R. W., Gonzalez, G., Isacks, B. L., and Carrizo, D. A., 2005, Pervasive cracking of the northern Chilean Coastal Cordillera: New evidence for forearc extension: Geology, v. 33, no. 12, p. 973-976.

Nishiizumi, K., Caffee, M. W., Finkel, R. C., Brimhall, G., and Mote, T., 2005, Remnants of a fossil alluvial fan landscape of Miocene age in the Atacama Desert of northern Chile using cosmogenic nuclide exposure age dating: Earth and Planetary Science Letters, v. 237, no. 3-4, p. 499-507.

Ortlieb, L., 2000, The documentary historical record of El Niño events in Peru: an update of the Quinn record (sixteenth through nineteenth centuries), in Diaz, H., and Markgraf, V., ed., El Niño and the Southern Oscillation: Multiscale Variability and Global and Regional Impacts: Cambridge, Cambridge University Press, p. 207-295.

Pardo-Casas, F., and Molnar, P., 1987, Relative motion of the Nazca (Farallon) and South American plates since late Cretaceous time: Tectonics, v. 6, no. 3, p. 233-248.

Placzek, C., and Quade, J., 2001, Holocene lake-level fluctuations of Lake Aricota, southern Peru: Quaternary Research, v. 56, p. 181-190.

Ouimet, W., Whipple, K., Royden, L., Sun, Z., and Chen, Z., 2007, The influence of large landslides on river incision in a transient landscape: eastern margin of the Tibetan plateau (Sichuan, China): Geological Society of America Bulletin, v. 119, no. 11, p. 1462-1476.

Quinn, W. H., and Neal, V.T., 1992, The historical record of El Niño events, in Bradley, R. S., and Jones, P.D., ed., Climate Since A.D. 1500: London, Routledge, p. 623-648.

Reneau, S. L., and Dethier, D. P., 1996, Late Pleistocene landslide-dammed lakes along the Rio Grande, White Rock canyon, New Mexico: Geological Society of America Bulletin, v. 108, no. 11, p. 1492-1507.

Roering, J. J., Kirchner, J.W., and Dietrich, W.E., 2005, Characterizing structural and lithologic controls on deep-seated landsliding: Implications for topographic relief and landscape evolution in the Oregon Coast Range, USA: Geological Society of America Bulletin, v. 117, no. 5/6, p. 654-668.

Schildgen, T. F., Hodges, K.V., Whipple, K.X, Reiners, P.W., and Pringle, M.S., 2007, Uplift of the western margin of the Andean plateau revealed from canyon incision history, southern Peru: Geology, v. 35, no. 6, p. 523-526.

Snyder, N. P., Whipple, K. X., Tucker, G. E., and Merritts, D. J., 2000, Landscape response to tectonic forcing: Digital elevation model analysis of stream profiles in the Mendocino triple junction region, northern California: Geological Society of America Bulletin, v. 112, no. 8, p. 1250-1263.

Somoza, R., 1998, Updated Nazca (Farallon) - South America relative motions during the last 40 My: implications for mountain building in the central Andean region: Journal of South American Earth Sciences, v. 11, no. 3, p. 211-215.

Stone, J. O., 2000, Air pressure and cosmogenic isotope production: Journal of Geophysical Research-Solid Earth, v. 105, no. B10, p. 23753-23759.

Strasser, M., and Schlunegger, F., 2005, Erosional processes, topographic length-scales and geomorphic evolution in arid climatic environments: the "Lluta collapse", northern Chile: Geologische Rundschau, v. 94, no. 3, p. 433-446.

Strecker, M. R., and Marrett, R., 1999, Kinematic evolution of fault ramps and its role in development of landslides and lakes in the northwestern Argentine Andes: Geology, v. 27, no. 4, p. 307-310.

Thouret, J.-C., Wörner, G., Gunnell, Y., Singer, B., Zhang, X., and Souriot, T., 2007, Geochronologic and stratigraphic constraints on canyon incision and Miocene uplift of the Central Andes in Peru: Earth and Planetary Science Letters, v. 263, p. 151-166.

Trauth, M. H., Alonso, R. A., Haselton, K. R., Hermanns, R. L., and Strecker, M. R., 2000, Climate change and mass movements in the NW Argentine Andes: Earth and Planetary Science Letters, v. 179, no. 2, p. 243-256.

Trauth, M. H., Bookhagen, B., Marwan, N., and Strecker, M. R., 2003, Multiple landslide clusters record Quaternary climate changes in the northwestern Argentine Andes: Palaeogeography Palaeoclimatology Palaeoecology, v. 194, no. 1-3, p. 109-121.

Vargas, G., Ortlieb, L., and Rutllant, J., 2000, Alluviones históricos en Antofagasta y su relación con eventos El Niño/Oscilación del Sur. Historic mudflows in Antofagasta, Chile, and their relationship to the El Nino/Southern Oscillation events: Revista Geológica de Chile, v. 27, no. 2, p. 157-176.

Vargas, G., Rutllant, J., and Ortlieb, L., 2006, ENSO tropical-extratropical climate teleconnections and mechanisms for Holocene debris flows along the hyperarid coast of western South America (17°-24°S): Earth and Planetary Science Letters, v. 249, no. 3-4, p. 467-483.

Whipple, K. X., and Tucker, G.E., 1999, Dynamics of the stream-power river incision model: Implications for height limits of mountain ranges, landscape response timescales, and research needs: Journal of Geophysical Research, v. 104, p. 17,661-17,674.

-, 2002, Implications of sediment-flux-dependent river incision models for landscape evolution: Journal of Geophysical Research, v. 107, no. B2, p. doi: 10.1029/2000JB000044.

Wobus, C., Whipple, K.X, Kirby, E., Snyder, N., Johnson, J., Spyropolou, K., Crosby, B., and Sheehan, D., 2006, Tectonics from topography: procedures, promise, and pitfalls: Geological Society of America Special Paper 398, p. 55-74.

Wörner, G., Uhlig, D., Kohler, I., and Seyfried, H., 2002, Evolution of the West Andean Escarpment at 18°S (N. Chile) during the last 25 Ma: uplift, erosion and collapse through time: Tectonophysics, v. 345, no. 1-4, p. 183-198.

Figure Captions

Figure 1. Location map showing field area in southern Peru. Topography is shown as a semi-transparent 30-m resolution digital elevation model (DEM) derived from 15-m resolution Advanced Spaceborne Thermal Emission and Reflection Radiometer (ASTER) imagery draped over shaded relief generated from the same DEM. Volcanic peaks are marked with black triangles and labeled with names and elevations. White dots with black outlines show weather stations with yearly average precipitation (in mm) labeled.

Figure 2. Chuquibamba valley and landslide morphology. A: Regional view of Chuquibamba valley as a tributary to the Colca-Majes drainage. B: Shaded relief map of Chuquibamba valley created from 30-m resolution digital elevation model derived from 15-m resolution Advanced Spaceborne Thermal Emission and Reflection Radiometer (ASTER) imagery. Slump blocks in the upper tributary are easily visible, as is the composite toe near the confluence with the main valley. Thin black lines show positions of mapped faults. C: 15-m resolution ASTER image (band 3N) showing composite toe of landslides at the bottom of Chuquibamba valley.

Figure 3. Boulders sampled for cosmogenic exposure age modeling from surface of landslide in Chuquibamba valley. Sample 06TS42 is from boulder in photo A, and sample 06TS45 is from boulder in photo B. Both boulders show evidence of spallation on their sides, and may have been affected on their top surfaces from which samples were collected. The upper surface of the boulder in photo A, however, shows evidence of surface weathering, such as the 2-cm-scale dissolution pits in photo C (mechanical pencil for scale). This suggests there as been no recent spallation on the top of that boulder.

Figure 4. Sipia falls overview pictures. Top photo and diagram show view of Sipia Falls and landslide from upstream view. Middle photo and diagram show view of landslide from downstream view. Left photo shows upper part of the falls with people for scale. Photo above shows the series of benches that

have been cut into alluvium that accumulated behind the landslide dam. The uppermost bench sits 160 m above the river on the upstream side of Sipia Falls. In the distance, a series of high benches show the level to which side valleys built alluvial fans. These may also be related to the lake that was dammed behind the landslide at Sipia Falls.

Figure 5. Schematic valley-long cross-section through Sipia Falls region. The bold line shows the active channel profile.

Figure 6. Samples collected for cosmogenic dating from Sipia Falls region. Samples 05TS18 and 05TS19 (photos A and B) were collected from the surfaces of granodiorite boulders within alluvial sediments dammed behind the landslide. Both boulders exhibited polished surfaces that are unlikely to have eroded significantly since deposition. Light-colored terrace in background of photos is top of lake sediments. Darker, hummocky surface immediately behind the lake sediments is the top of the landslide. Sample 05TS21 (photo C) was collected from the surface of a quartzite boulder on top of the landslide. Centimeter-scale bar on white board for scale.

Figure 7. Three-dimensional rendition of upper Cotahuasi valley showing cirque-shaped tributary headwalls and landslide debris in valley bottom. Image created by draping 15-m resolution ASTER imagery (bands 3N,2,1) over 30-m resolution digital elevation model. Vertical exaggeration is 1.5 times.

Figure 8. Shaded relief map of upper Colca valley derived from 30-m digital elevation data from ASTER imagery. Dashed black line shows the head scarp of the collapsed north flank of Hualca Hualca volcano. Most likely several generations of collapses have contributed to valley damming and upstream lacustrine and fluvial deposition. White dots show locations of dated volcanic units (see Table 1).

Figure 9. Contact between basaltic andesite flow (site of sample 04CC05) and underlying lake sediments. Dashed white line shows position of contact. Age of flow provides a minimum constraint on the timing of valley damming and subsequent lacustrine deposition.

Figure 10. Photos showing sample site 05TS27, where basaltic andesite flowed over a thin layer of lake sediments that blanket a landslide deposit. Photo on left shows volcanic flow over the landslide. Lake sediments can be seen as a thin, light-colored band in between. Photo on right shows "flame

structures" where lake sediments form a highly irregular contact with the volcanic flow. Most likely this is because the lake sediments were still wet at the time lava flowed over them.

Table 1. Summary of cosmogenic exposure age calculations.

Table 2. Sample descriptions and input data for exposure age calculations.

Table 3. $^{40}Ar/^{39}Ar$ sample description and dates.

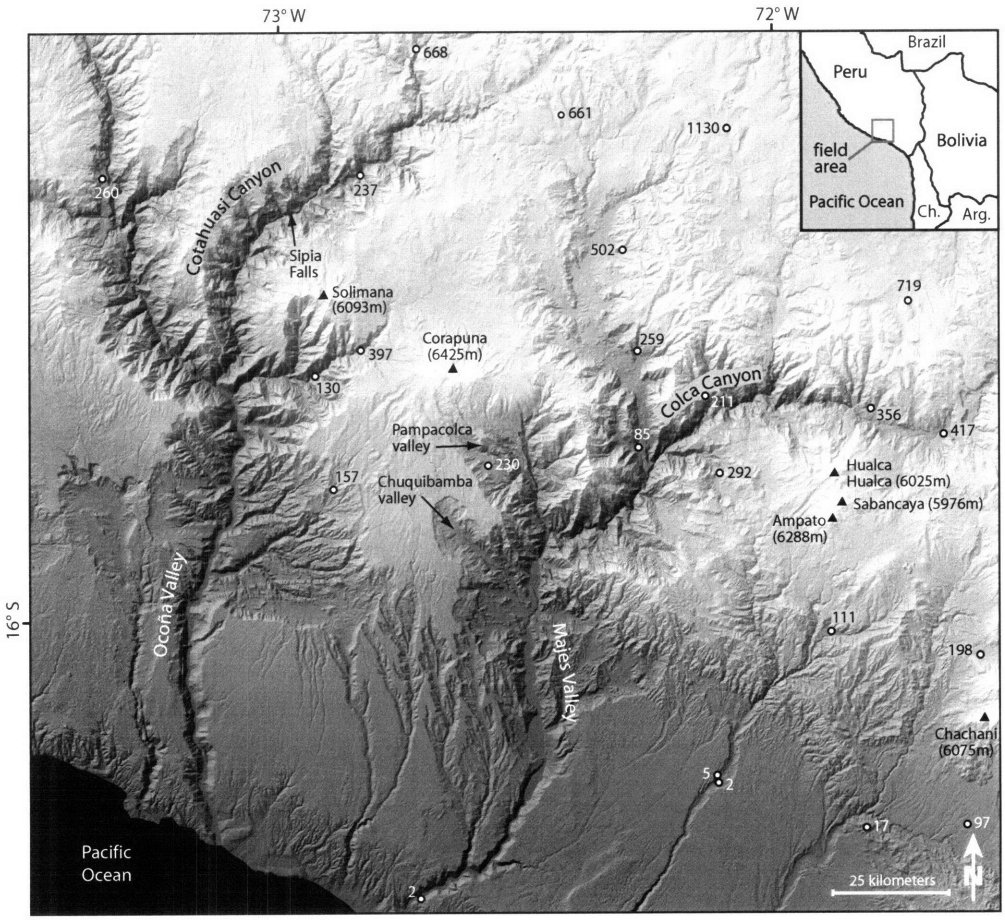
73° W
72° W
16° S
668
661
1130
260
237
502
719
259
397
130
211
356
417
85
230
292
157
111
198
5
2
17
97
2
Brazil
Peru
Bolivia
field area
Pacific Ocean
Ch.
Arg.
Cotahuasi Canyon
Sipia Falls
Solimana (6093m)
Corapuna (6425m)
Colca Canyon
Pampacolca valley
Chuquibamba valley
Hualca Hualca (6025m)
Sabancaya (5976m)
Ampato (6288m)
Ocoña Valley
Majes Valley
Chachani (6075m)
Pacific Ocean
25 kilometers
N

Figure 1.

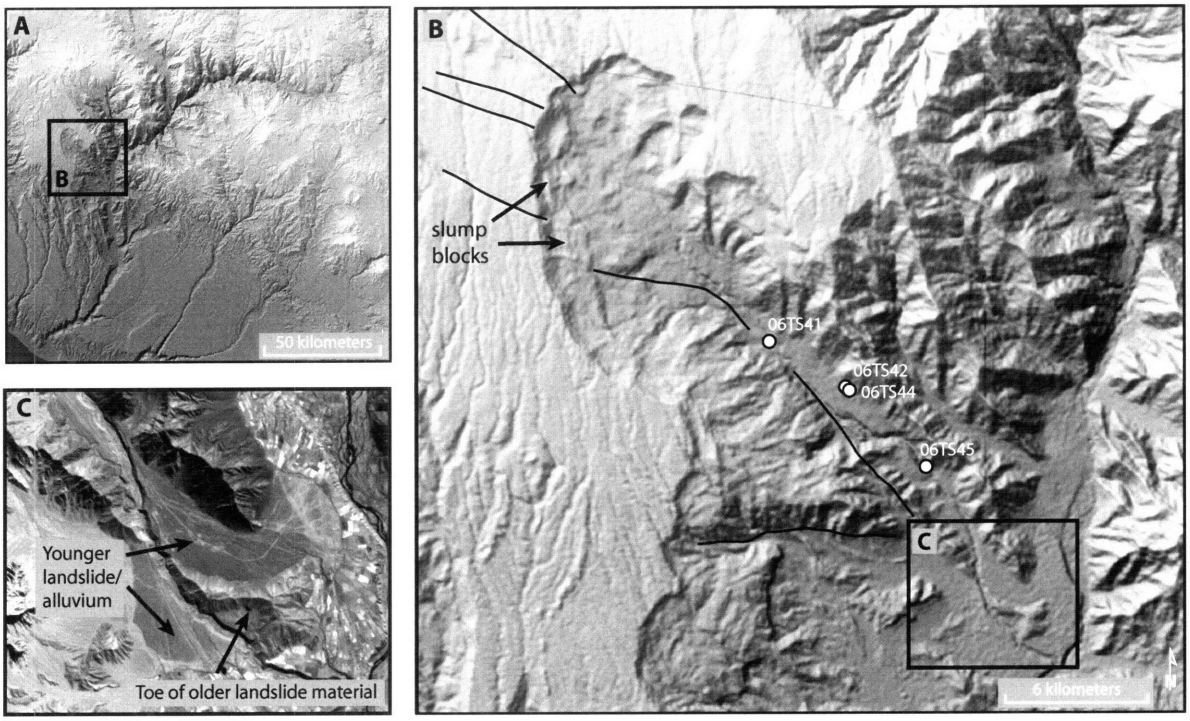
A
B
50 kilometers
C
Younger
landslide/
alluvium
Toe of older landslide material
B
slump
blocks
06TS41
06TS42
06TS44
06TS45
C
6 kilometers
N

Figure 2.

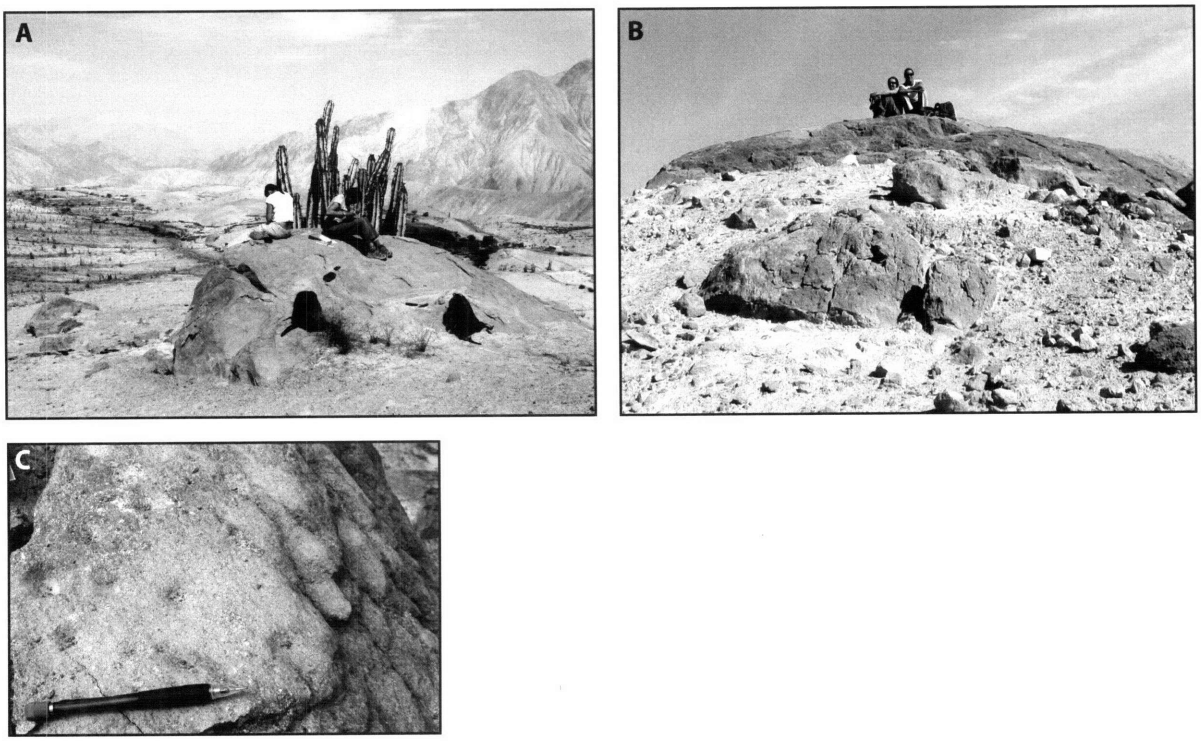

Figure 3.

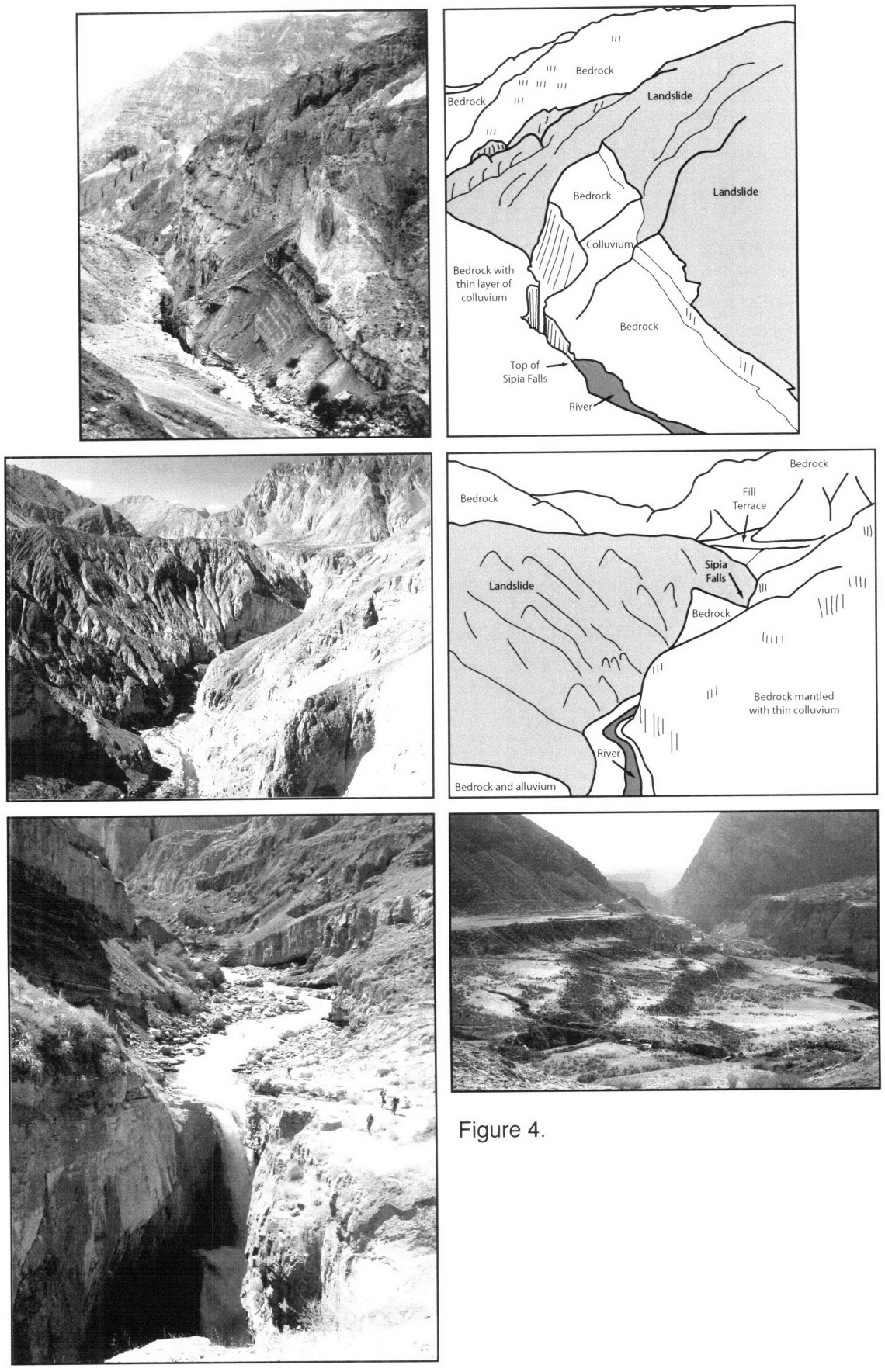
Bedrock
Bedrock
Landslide
Bedrock
Landslide
Colluvium
Bedrock with thin layer of colluvium
Bedrock
Top of Sipia Falls
River
Bedrock
Bedrock
Fill Terrace
Sipia Falls
Landslide
Bedrock
Bedrock mantled with thin colluvium
River
Bedrock and alluvium

Figure 4.

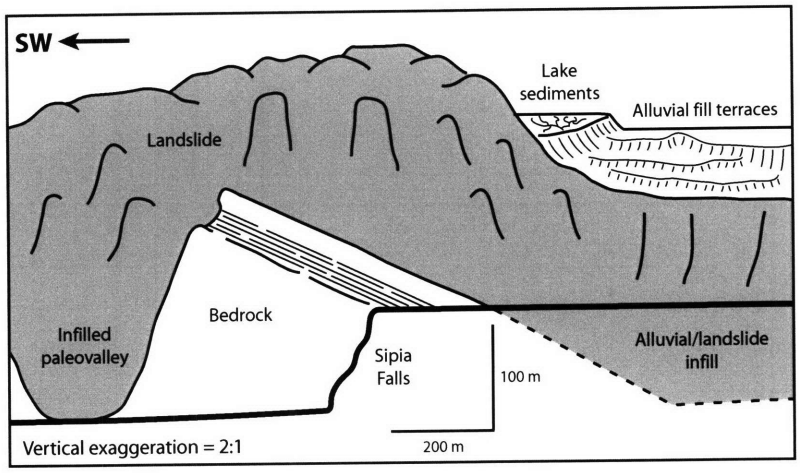
SW
Lake
sediments
Alluvial fill terraces
Landslide
Bedrock
Infilled
paleovalley
Sipia
Falls
100 m
Alluvial/landslide
infill
Vertical exaggeration = 2:1
200 m

Figure 5.

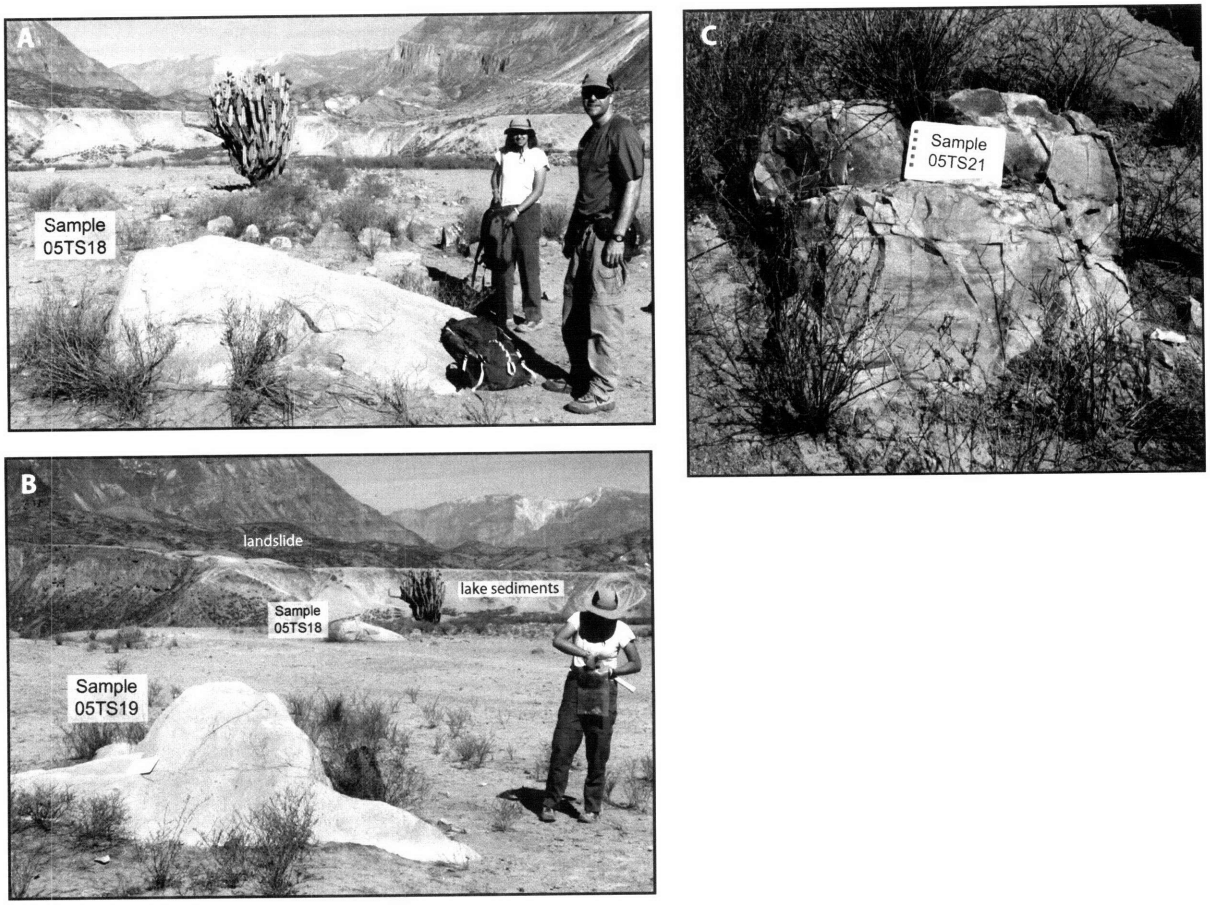
A
Sample
05TS18
B
landslide
lake sediments
Sample
05TS18
Sample
05TS19
C
Sample
05TS21

Figure 6.

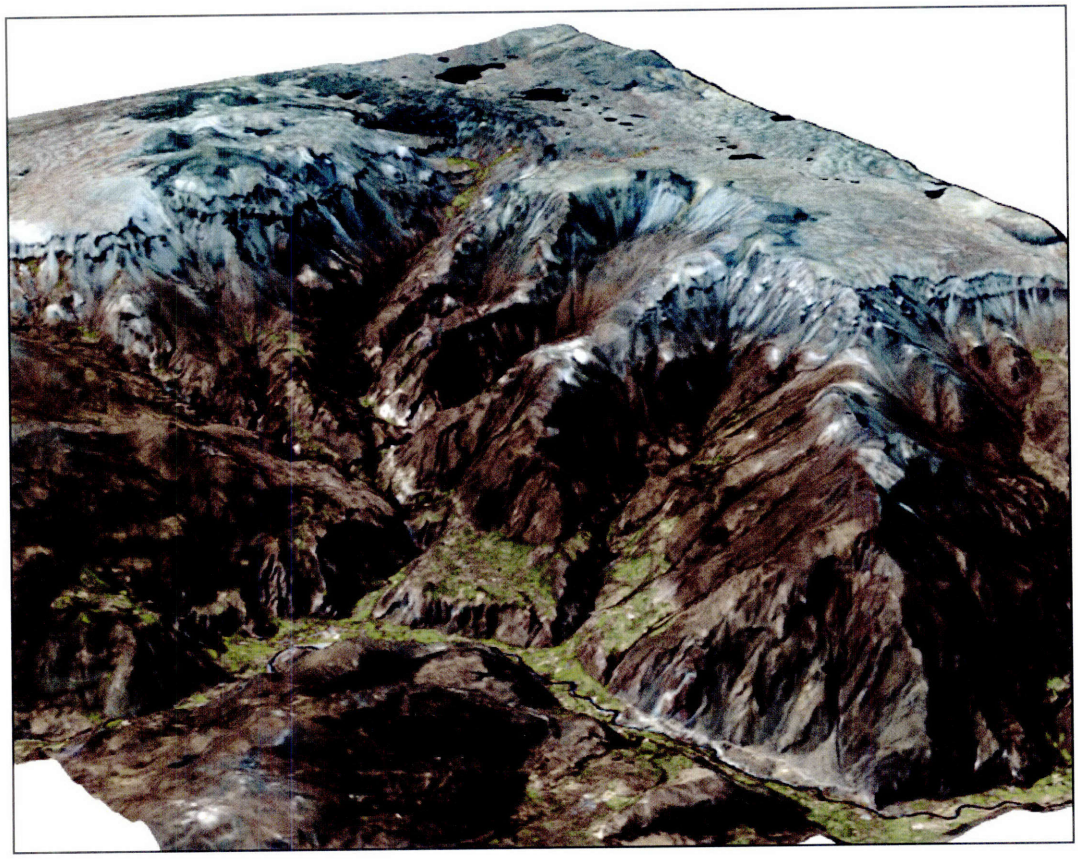

Figure 7.

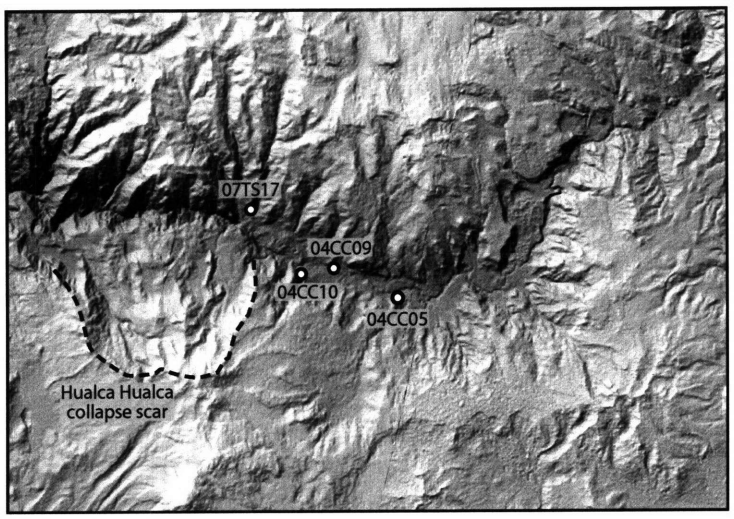

Figure 8.

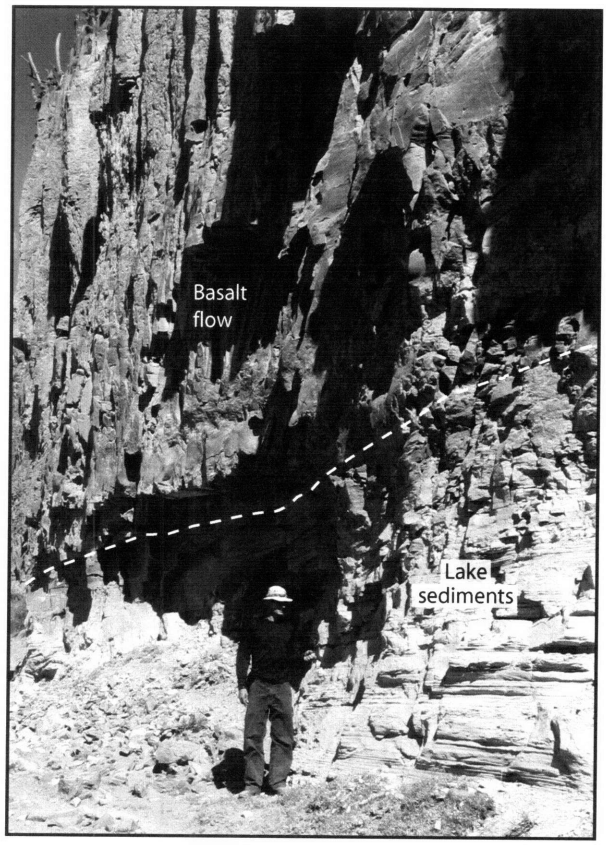

Figure 9.

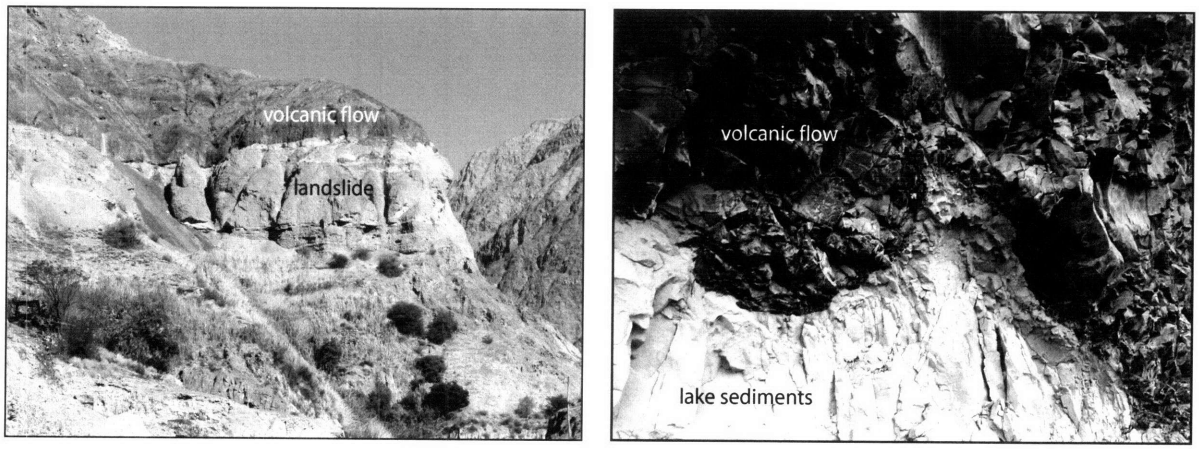

Figure 10.

TABLE 1. SUMMARY OF COSMOGENIC EXPOSURE AGE CALCULATIONS

Scaling scheme:	Desilets and others (2003, 2006)	Dunai (2001)	Lifton and others (2003, 2006)	Time-dependent Lal (1991)/Stone (2000)	Time-independent Lal (1991)/Stone (2000)
Sample	Age ± Error[1] (ka) (ka)	Age ± Error[1] (ka) (ka)	Age ± Error[1] (ka) (ka)	Age ± Error[1] (ka) (ka)	Age ± Error[1] ± Error[2] (ka) (ka) (ka)
05TS18	9.2 ± 1.2	9.2 ± 1.2	9.2 ± 1.1	9.5 ± 1.0	9.7 ± 1.0 ± 0.5
05TS19	9.1 ± 1.2	9.1 ± 1.2	9.1 ± 1.0	9.4 ± 0.9	9.6 ± 1.0 ± 0.4
05TS20	8.9 ± 1.2	8.9 ± 1.2	9.0 ± 1.0	9.3 ± 0.9	9.5 ± 1.0 ± 0.4
05TS20B	8.4 ± 1.1	8.4 ± 1.1	8.4 ± 1.0	8.7 ± 0.9	9.0 ± 0.9 ± 0.5
05TS21	12.1 ± 1.6	12.1 ± 1.6	12.1 ± 1.3	12.4 ± 1.2	12.7 ± 1.3 ± 0.5
05TS21B	10.9 ± 1.4	10.9 ± 1.4	10.9 ± 1.2	11.3 ± 1.1	11.5 ± 1.1 ± 0.4
06TS34	7.4 ± 1.0	7.5 ± 1.0	7.5 ± 0.8	7.9 ± 0.8	8.1 ± 0.8 ± 0.4
06TS35	5.5 ± 0.7	5.5 ± 0.7	5.6 ± 0.6	5.6 ± 0.5	5.6 ± 0.6 ± 0.2
06TS36	7.5 ± 1.0	7.5 ± 1.0	7.5 ± 0.8	8.0 ± 0.8	8.2 ± 0.8 ± 0.3
06TS37	4.8 ± 0.6	4.8 ± 0.6	4.9 ± 0.5	5.3 ± 0.5	5.2 ± 0.5 ± 0.2
06TS38	1.2 ± 0.2	1.1 ± 0.1	1.2 ± 0.1	1.4 ± 0.1	1.3 ± 0.1 ± 0.1
06TS42	74.4 ± 9.6	74.8 ± 9.6	73.3 ± 8.0	72.4 ± 6.9	86.5 ± 8.5 ± 2.6
06TS44	27.4 ± 3.5	27.5 ± 3.5	27.2 ± 2.9	26.9 ± 2.6	29.3 ± 2.8 ± 1.0
06TS45	102.7 ± 13.3	102.5 ± 13.2	101.3 ± 11.1	98.7 ± 9.5	118.9 ± 11.7 ± 3.6
05TS06	3.7 ± 0.6	3.5 ± 0.5	3.7 ± 0.5	3.5 ± 0.5	3.3 ± 0.4 ± 0.3
05TS10	6.9 ± 0.9	6.7 ± 0.9	6.9 ± 0.8	6.7 ± 0.7	6.9 ± 0.7 ± 0.3

1: External uncertainty; includes uncertainties in nuclide measurement, reference nuclide production rate, and scaling scheme.

2: Internal uncertainty; includes uncertainty in nuclide measurement only.

TABLE 2. SAMPLE DESCRIPTIONS AND INPUT DATA FOR EXPOSURE AGE CALCULATIONS

Sample	Latitude (S)	Longitude (W)	Thickness (cm)	Thickness scaling	Shielding factor	Elevation (m)	^{10}Be conc. (atoms/g)	Error	Density (g/cm^3)	Description
05TS18	15°13'46.95"	72°57'05.69"	2.5	0.979	0.964	2250	148025	7742	2.7	Granodiorite boulder in alluvium behind Sipia falls
05TS19	15°13'46.22"	72°57'04.47"	1.0	0.992	0.964	2250	148004	6138	2.7	Granodiorite boulder in alluvium behind Sipia falls
05TS20	15°14'10.26"	72°57'19.15"	3.0	0.975	0.985	2350	156853	6604	2.7	Quartzite clasts on landslide surface Sipia falls
05TS20B	15°14'10.26"	72°57'19.15"	3.0	0.975	0.985	2350	148049	7595	2.7	Replicate analysis of above
05TS21	15°14'17.78"	72°57'35.03"	2.0	0.983	0.985	2340	209904	7841	2.7	Ignimbrite boulder on landslide surface Sipia falls
05TS21B	15°14'17.78"	72°57'35.03"	2.0	0.983	0.985	2340	190216	7296	2.7	Replicate analysis of above
06TS34	15°12'14.85"	72°54'39.13"	1.0	0.992	0.999	2585	159610	7781	2.7	Quartzite pieces on landslide surface Cotahuasi valley
06TS35	15°12'08.52"	72°54'34.64"	1.0	0.992	0.999	2590	110213	4263	2.7	Quartzite pieces on landslide surface Cotahuasi valley
06TS36	15°11'57.75"	72°54'40.54"	1.0	0.992	0.999	2590	161826	5838	2.7	Quartzite pieces on landslide surface Cotahuasi valley
06TS37	15°14'51.23"	72°50'58.40"	3.0	0.975	0.986	3900	202238	9133	2.0	Ignimbrite boulder surface upper Cotahuasi valley
06TS38	15°14'50.44"	72°50'59.72"	3.0	0.975	0.986	3900	49983	2349	2.0	Ignimbrite boulder surface upper Cotahuasi valley
06TS42	15°54'04.24"	72°33'34.92"	3.0	0.975	0.987	1675	928974	27665	2.0	Ignimbrite boulder from Chuquibamba slide
06TS44	15°54'04.26"	72°33'34.94"	3.0	0.975	0.987	1675	316379	10264	2.7	Quartzite vein clast from Chuquibamba slide
06TS45	15°55'33.40"	72°31'58.13"	3.0	0.975	0.987	1300	971701	28641	2.0	Ignimbrite boulder from Chuquibamba slide
05TS06	15°34'17.36"	73°07'08.37"	5.0	0.959	0.965	950	20499	2057	2.7	7-m bedrock strath, Maran-Cotahuasi confluence
05TS10	15°40'52.32"	73°03'37.22"	3.5	0.971	0.926	790	36630	1660	2.7	Granodiorite boulder in 40-m alluvial strath, Ocona valley

TABLE 3. AGE SPECTRA ANALYSIS FOR $^{40}Ar/^{39}Ar$ DATA

Sample	Material	K/Ca	Age Spectra				Isochron Analysis			Description
			% gas	N*	MSWD	Weighted Age (Ma)	Age (Ma)	40Ar/36Ar intercept	MSWD	
04CC05	groundmass	1.79	62.8	6 of 14	0.99	0.622 ± 0.006	0.624 ± 0.008	294 ± 5.0	1.18	overlies lake sediments
04CC05	groundmass	1.76	69.1	6 of 13	2.08	0.622 ± 0.008	0.623 ± 0.012	294 ± 6.5	2.43	overlies lake sediments
04CC09	groundmass	0.59	66.5	6 of 14	2.38	0.636 ± 0.045	0.708 ± 0.089	290 ± 6.2	1.70	underlies lake sediments
04CC10	feldspar	0.09	79.2	9 of 10	0.92	1.79 ± 0.32	1.695 ± 0.557	301 ± 35	1.03	flows into upper Colca valley
04CC10	feldspar	0.10	72.8	6 of 7	1.6	2.04 ± 0.33	1.865 ± 0.533	333 ± 101	1.70	flows into upper Colca valley
05TS36	groundmass	0.81	83.8	6 of 11	1.00	0.633 ± 0.084	0.753 ± 0.138	292 ± 3.3	0.12	caps landslide deposit
05TS27	whole rock	0.54	94.4	4 of 15	2.06	0.141 ± 0.005	0.148 ± 0.022	286 ± 41	4.14	caps landslide deposit
05TS27	whole rock	0.54	100.0	6 of 6	1.06	0.139 ± 0.003	n/a ± n/a	n/a ± n/a	n/a	caps landslide deposit
06TS31a	groundmass	0.82	76.9	7 of 13	0.87	0.177 ± 0.007	0.172 ± 0.022	298 ± 7.2	0.97	caps landslide deposit
06TS31b	groundmass	1.14	87.7	7 of 13	1.01	0.170 ± 0.007	0.172 ± 0.021	295 ± 5.2	1.21	caps landslide deposit
06TS31c	groundmass	1.20	95.2	8 of 13	1.96	0.171 ± 0.011	0.156 ± 0.023	300 ± 5.6	1.58	caps landslide deposit
06TS31d	groundmass	1.58	76.9	8 of 10	1.19	0.178 ± 0.012	0.045 ± 0.036	306 ± 14	0.95	caps landslide deposit

* Refers to number of steps on age plateau out of total number of steps, or number of grains analysed for single-grain analyses.